UC Santa Barbara
UC Santa Barbara Electronic Theses and Dissertations

Title

Geochemistry of Molybdenum and Other Variably Chalcophile Elements

Permalink

https://escholarship.org/uc/item/2cq885fk

Author

Greaney, Allison Talbott

Publication Date

2018

Peer reviewed|Thesis/dissertation

UNIVERSITY OF CALIFORNIA

Santa Barbara

Geochemistry of Molybdenum and Other Variably Chalcophile Elements

A dissertation submitted in partial satisfaction of the

requirements for the degree Doctor of Philosophy

in Earth Science

by

Allison Talbott Greaney

Committee in charge:

Professor Roberta L. Rudnick, Chair

Professor Matthew G. Jackson

Professor Frank J. Spera

December 2018

The dissertation of Allison Talbott Greaney is approved.

_____

Frank J. Spera

_____

Matthew G. Jackson

_____

Roberta L. Rudnick, Committee Chair

December 2018

ACKNOWLEDGEMENTS

I dedicate this dissertation to my mom and dad, Melissa Talbott and Dennis Greaney, who instilled a sense of curiosity and independence in me from an early age. From talking me through my first elementary school homework assignments that left me in tears, to sharing words of encouragement when grad school finances got tight ("When I was in grad school I just shared peanut butter with the dog at the end of the month when I ran out of money"), my mom and dad taught me the persistence and resilience needed to be successful in a PhD program. They have shaped me into the person I am today, and I truly could not have gotten to where I am without them. Similarly, I've treasured the support and comedic relief from my sister Sam throughout the years.

I met John during my first year of graduate school at Maryland, and although our relationship took a turn we didn't anticipate as I moved across the country, he has been my constant motivator and support system. From striking up our first conversation over a pallasite meteorite to proposing to me on the Old Rag Granite, he has graciously allowed geology to permeate his life. I am so grateful for his patience as I pursued my PhD 2700 miles away, and for being my rock when things got tough.

Roberta has been a wonderful advisor and mentor who expertly guided me through the world of geochemistry while letting me maintain independence in my research. She has always been supportive, whether analyses went right or wrong, and she always had ideas for the "next step" whenever I got stuck. Under her guidance I developed from a *very* green researcher, fresh out of undergrad, into an established scientist with the ability to independently design and execute a research project. I also want to thank her for allowing me to attend conferences (and dance at conference banquets) all over the world, which were all

unforgettable experiences. I mostly appreciated that she let me be a normal human throughout grad school – from supporting me to take weekends off, to encouraging my science outreach efforts, to betting bottles of wine on research outcomes. I am forever grateful to her for guiding my scientific and professional development.

My committee members: Matt Jackson and Frank Spera, my collaborators Rich Gaschnig, Steve Romaneillo, Ariel Anbar, and Aleisha Johnson, and my co-authors from around the world all provided crucial lab training and feedback to this research. Their suggestions for project ideas, modeling calculations, and writing tips helped me develop into a better scientist. I learned a great deal from everyone involved in these projects.

Finally, I would like to thank the staff, faculty, and graduate students at the University of Maryland and the University of Santa Barbara. This includes the lab managers Richard Ash, Phil Piccoli, Igor Puchtel, Andrew Kylander-Clark, and Gareth Seward who contributed significantly to the analytical portion of these studies. Additionally, the professional support from the administrative staff at both institutions was crucial for my success. Lastly, I want to personally acknowledge the "first years" at UMD who got me through my first two years of graduate school, and my dear friends at UCSB: Julie, Mareike, Drew, and many others who helped me temporarily forget molybdenum with an episode of the Bachelor or bottle of champagne on the Mesa.

"But what are young men to rocks and mountains?"

- Jane Austen

VITA OF ALLISON TALBOTT GREANEY

December 2018

<u>EDUCATION</u>

Doctor of Philosophy in Earth Science   December 2018
       University of California Santa Barbara
       Advisor: Dr. Roberta Rudnick
       Dissertation: "Geochemistry of Molybdenum and Other Variably Chalcophile
           Elements"

Bachelor of Science in Geology   August 2014
       University of Illinois Urbana – Champaign

<u>PROFESSIONAL APPOINTMENTS</u>

Graduate Student Researcher, University of California Santa Barbara   2016-2018
Graduate Student Researcher, University of Maryland College Park   2014-2016
Undergraduate Research Assistant, University of Illinois Urbana – Champaign   2013-2014

<u>PUBLICATIONS</u>

Greaney A.T., Rudnick R.L, Helz R.T., Gaschnig R.M., Ash R.D., Piccoli P. (2017) The
      behavior of chalcophile elements during magmatic differentiation as observed in
      Kilauea Iki lava lake, *Geochimica et Cosmochimica Acta*, **210**, 71-96

Greaney A.T., Rudnick R.L, Gaschnig R.M., Whalen J.B., Luais B., Clemens J.D.
      (2018) The Geochemistry of Molybdenum in the Continental Crust, *Geochimica et
      Cosmochimica Acta* **238**, 36-54

<u>CONFERENCE ORAL PRESENTATIONS</u>

Greaney A.T. and Rudnick R.L. (2018) Completing the molybdenum isotope mass balance
      in subduction zones, *Goldschmidt Conference Abstract #1568*

Greaney A.T., Rudnick R.L., Romaniello S.J., Johnson A.C., Gaschnig R.G., Anbar A.D.
      (2017) Molybdenum isotopes reveal oxidation of Earth's continental crust during the
      2.4 Ga Great Oxidation Event, *AGU Fall Meeting Abstract #210147*

Johnson A.C., Reinhard C.T., Romaniello S.J., **Greaney A.T.,** Garcia-Robledo E., Revsbach
      N.P., Canfield D.E., Lyons T.W., Anbar A.D. (2017) Quantifying Archean
      Oxygenation – Insights from Sulfide Oxidation Experiments at Low PO2, *GSA
      Abstract #294-3*

Greaney A.T., Rudnick R.L, Gaschnig R.M. (2016) "Crustal Sources of Molybdenum" *Goldschmidt Conference Abstract #1754*

Greaney A.T., Rudnick R.L, Helz R.T., Gaschnig R.M. Ash, R.D. Piccoli, P. (2015) "The behavior of chalcophile elements during magmatic differentiation as observed in Kilauea Iki Lava Lake", *AGU Fall Meeting Abstract #70008*

CONFERENCE POSTER PRESENTATIONS

Toc M., Rudnick R.L., **Greaney A.T.** (2018) Causes of Molybdenum Depletion in Granites, *Goldschmidt Conference Abstract*

Greaney A.T., Rudnick R.L (2017) Chalcophile elements in the mantle, *International Kimberlite Conference, Abstract #4473*

Greaney A.T., Rudnick R.L., Gaschnig R.M. (2016) Molybdenum cycling during Crust Formation and Destruction*, AGU Fall Meeting Abstract #134671*

Johnson A.C., Reinhard C.T., Romaniello S.J., **Greaney A.T.,** Garcia-Robledo E., Revsbach N.P., Canfield D.E., Lyons T.W., Anbar A.D. (2016) Reconciling "Whiffs" of O2 with the Archean MIF S Record: Insights from Sulfide Oxidation Experiments, AGU Fall Meeting

Greaney A.T., Rudnick, R.L Helz R.T., Gaschnig R.M., Ash R.D., Piccoli P. (2015) "The behavior of chalcophile elements during magmatic differentiation as observed in Kilauea Iki Lava Lake", *GSA Fall Meeting Abstract #262233*

TEACHING

Instructor, Physical Geology, EARTH 2, UCSB, Summer 2018
TA, Physical Geology, EARTH 2, UCSB, Winter 2017
TA, High Temperature Geochemistry, GEOL 445, UMD, Fall 2015
TA, Igneous and Metamorphic Petrology, GEOL 443, UMD, Spring 2015

AWARDS AND GRANTS

G.K. Gilbert Award for Best Department Seminar, UCSB, 2018
Harry Glicken Award for Volcanology, UCSB, 2018
Alumni Graduate Award for Research Excellence, UCSB, 2017
Doctoral Student Travel Grant, UCSB, 2017
International Kimberlite Conference Student Travel Grant, 2017
NSF Graduate Research Fellowship – Honorable Mention, 2016
Best Graduate Talk Award, UMD, 2016
Earth Research Institute Travel Grant, UCSB, 2016
Graduate Student Assoc. Travel Grant, UCSB, 2016
Goldschmidt-NASA Student Travel Grant, 2016
International Conference Student Support Award, UMD, 2016

Earth System Science Interdisciplinary Center (ESSIC) Travel Grant, 2016
Jacob K. Goldhaber Travel Grant, UMD, 2015
Flagship Fellowship, UMD, 2014
Outstanding Senior in Geology, UIUC, 2014
Franklin Fund Award, UIUC 2014
National Association of Geoscience Teachers Field Study Scholarship, 2014
L. Austin Weeks Undergraduate Grant, AAPG, 2014

ABSTRACT

"Geochemistry of Molybdenum and Other Variably Chalcophile Elements"

by

Allison Talbott Greaney

This research began with a simple question: Is molybdenum a chalcophile element – i.e., is it hosted in sulfides? I began to answer this question with three granites at the University of Maryland, then followed Mo through the Archean continental crust, Hawaiian lavas, subducted oceanic crust, the lithospheric mantle, glacial sediments, and ultimately weathering profiles at the University of California Santa Barbara. Each measurement prompted new questions about the geochemical behavior of Mo in different reservoirs. Along the way, we explored other nominally chalcophile elements like Ga, Ge, Mo, Ag, Cd, In, Sn, Sb, W, Tl, and Bi. Partitioning and isotope fractionation studies of several of these elements (e.g., Cd, Sn, Tl, W) are some of the newest frontiers in geochemistry, as their behavior has the potential to inform us of geological processes that shape our crust and mantle.

Nevertheless, molybdenum remained the central theme of these research projects. Using a combination of laser ablation ICP-MS, standard addition single collector ICP-MS and isotope dilution multi collector ICP-MS, I present six studies on the geochemistry of Mo. In the first two chapters we establish that Mo is *not* hosted in sulfides in the granitic upper crust and in basaltic to intermediate magmas of Kilauea Iki lava lake in Hawaii. We also find that Mo is systematically depleted from each granite analyzed, relative to the LREE, which led to the establishment of three hypotheses: 1) Mo is fractionated during igneous differentiation, 2) Mo is retained in the slab during subduction, or 3) Mo is removed from cooling granite plutons during fluid exsolution to eventually precipitate as molybdenite (MoS_2) in epithermal

veins. The first hypothesis was the basis for an undergraduate research project that refuted the idea (Appendix G), the second hypothesis formed Chapter III, and the results of these studies ultimately support hypothesis 3, suggesting that, on average, 60% of the Mo delivered to the upper crust in plutons forms MoS_2.

Chapters III and VI follow Mo into the lithospheric mantle and lower crust where we find that Mo isotopes are fractionated during subduction, as isotopically light Mo is incorporated into rutile and isotopically heavy Mo is transported into the mantle wedge. This may partially explain why the continental crust is isotopically heavier than peridotites and basalts. Additionally, we find that Mo is added via metasomatic fluids or melts to residual peridotites where it is ubiquitous along grain boundaries. Molybdenum is enriched in metasomatically deposited sulfides, however its abundance in "primary" mantle sulfides is similar to that measured in crustal sulfides. Mo and W-rich fluids derived from subducted slabs may be the metasomatic agent that infiltrated these peridotites.

Finally, Chapters IV and V explore "low-temperature" isotopic fractionation of Mo during continental weathering at the Earth's surface. We find that Mo isotopes in glacial diamictites that record weathering of the crust over the last three billion years become progressively lighter with time. We hypothesize that this is due to the onset of oxidative weathering at the Great Oxidation Event (2.4 Ga) and test this hypothesis with studies of modern weathering profiles. Data from saprolites and bauxites confirm that when Mo is lost during continental weathering, it is fractionated, and the light Mo isotopes are retained in the regolith, as observed in the diamictites. We conclude that Mo isotopes record the onset of oxidative weathering at ~ 2.4 Ga, and therefore the rise of oxygen in our atmosphere.

TABLE OF CONTENTS

Chapter I. The behavior of chalcophile elements during magmatic differentiation as observed at Kilauea Iki lava lake, Hawaii

As published in Geochimica et Cosmochimica Acta in 2017

With co-authors Roberta L. Rudnick[1,2], Rosalind T. Helz[3], Richard M. Gaschnig[1,4], Philip M. Piccoli[1], Richard D. Ash[1]

[1]University of Maryland College Park, Department of Geology, College Park, MD 20742

[2]University of California Santa Barbara, Department of Earth Science, Santa Barbara, CA 93106

[3]United States Geological Survey, Reston, VA, 20192

[4]University of Massachusetts Lowell, Department of Earth Sciences, Lowell, MA 01854

Author Contributions

R.L. Rudnick conceived the study, aided in data interpretation, and provided comments and edits on the manuscript.

A.T. Greaney carried out the analyses and data interpretation and wrote the manuscript.

R. Helz provided samples, aided in data interpretation, and provided edits on the manuscript.

R.M. Gaschnig, R.D. Ash, and P.M. Piccoli provided analytical assistance and edits on the manuscript.

ABSTRACT

We quantify the behavior of Cu, Ga, Ge, As, Mo, Ag, Cd, In, Sn, Sb, W, Tl, Pb, and Bi during the differentiation of a picritic magma in the Kilauea Iki lava lake, Hawaii, using whole rock and glass differentiation trends, as well as partition coefficients in Cu-rich sulfide blebs and minerals. Such data allow us to constrain the partitioning behavior of these elements between sulfide and silicate melts, as well as the chalcophile element characteristics of the mantle source of the Kilauea lavas. Nearly all of the elements are generally incompatible on a whole-rock scale, with concentrations increasing exponentially below ~6 wt% MgO. However, in-situ laser ablation data reveal that Cu, Ag, Bi, Cd, In, Pb, and Sn are chalcophile; As, Ge, Sb, and Tl are weakly chalcophile to lithophile; and Mo, Ga, and W are lithophile. The average $D^{\text{sulfide/silicate melt}}$ values are: $D_{Ag} = 1252 \pm 1201$ (2SD), $D_{Bi} = 663 \pm 576$, $D_{Cd} = 380 \pm 566$, $D_{In} = 40 \pm 34$, $D_{Pb} = 34 \pm 18$, $D_{Sn} = 5.3 \pm 3.6$, $D_{As} = 2.4 \pm 7.6$, $D_{Ge} = 1.6 \pm 1.4$, $D_{Sb} = 1.3 \pm 1.5$, $D_{Tl} = 1.1 \pm 1.7$, $D_{Mo} = 0.56 \pm 0.6$, $D_{Ga} = 0.10 \pm 0.3$, and $D_W = 0.11 \pm 0.1$. These findings are consistent with experimental partitioning studies and observations of Ni-rich sulfide liquid in mid-ocean ridge basalts (MORB), despite the different compositions of the KI sulfides. The KI glasses and whole rocks are enriched in As, Ag, Sb, W, and Bi, relative to elements of similar compatibility (as established by abundances in MORB), mimicking enrichments found in basalts from the Manus back arc basin (Jenner et al., 2012) and the upper continental crust (UCC). These enrichments suggest the presence of terrigenous sediments in the Kilauea mantle source. The KI source is calculated to be a mixture of depleted MORB mantle (DMM) and 10–20% recycled crust composed of MORB and minor terrigenous sediments.

1.1 INTRODUCTION

Elements can be categorized into four major groups according to their geochemical behavior: lithophile (rock/silicate-loving), siderophile (iron-loving), chalcophile (sulfur-loving), and atmophile (gas-loving) (Goldschmidt, 1937). These classifications offer only the broadest descriptions of the behavior of an element, as composition (including oxygen and sulfur fugacity), temperature, and pressure all affect the partitioning of elements in a given environment. The elements Cu, Ga, Ge, As, Mo, Ag, Cd, In, Sn, Tl, Pb, and Bi may be considered nominally chalcophile, as they form or preferentially partition into sulfides in surface environments (e.g., sedimentary basins, low T hydrothermal and epithermal systems), however their behavior in the core, mantle, and crust can vary quite dramatically. Elements like Cu and Ag behave as chalcophile elements in nearly all studied crystallizing environments. The remaining elements Ga, Ge, As, Mo, Cd, In, Sn, Sb, Tl, Pb, and Bi have been observed to either behave as structural components in sulfide phases (e.g., molybdenite MoS_2, galena PbS, stibnite Sb_2S_3, bismuthinite Bi_2S_3) or may substitute for the metal cation or anion (e.g., Ga, Ge, Cd and In replace Zn in sphalerite, ZnS). Their behavior in igneous systems, where magmatic sulfides crystallize or form immiscible liquids may be different, however, because element solubility as a cation or anion into a sulfide liquid can vary dramatically from its partitioning into a crystalline phase (Helmy et al., 2010). Many of these elements have been classified as lithophile elements in the bulk silicate Earth (e.g., Ga, Ge, Mo, In, Sn, Sb, Pb: Yi et al., 1995; Jochum and Hoffmann, 1997; Kuroda and Sandell, 1954; Shaw, 1957). Tungsten is generally considered to be moderately siderophile (Walker, 2016), but it is included in this study given its geochemical similarity to Mo.

4

A primary motivation for our study is to understand the partitioning behavior of Mo during igneous differentiation. Molybdenum is considered to be moderately siderophile during core formation (Walker, 2016), but is also found in the mantle, making it partially lithophile (Newsom and Palme, 1984). Molybdenum can also be chalcophile in low-temperature hydrothermal or sedimentary environments where it is concentrated in the ore mineral molybdenite and into syngenetic or diagenetic Mo-Fe-S phases formed in euxinic waters (Erickson and Helz, 2000; Helz et al., 2011; Gregory et al., 2015). Molybdenite is occasionally present as an accessory phase in rhyolite (Audétat et al., 2011). This variable behavior is driven by redox reactions. Molybdenum has garnered special interest because it is one of the most important tracers of atmospheric oxygen in the Precambrian due to its unique weathering properties that are dependent on its redox state – Mo is insoluble in the tetravalent state but it is soluble when oxidized to its hexavalent state. Therefore, Mo is thought to remain reduced, insoluble, and thus sequestered in the Archean crust before the 2.4 Ga Great Oxidation Event (GOE). Once the atmosphere became oxygenated, however, it is suggested that Mo was released from sulfides or other phases, oxidized to its soluble state, and washed into the oceans where it is concentrated in black shales. The Mo abundance in black shales has been one of the key observations used to determine exactly when O_2 rose in the atmosphere (Anbar et al., 2007; Scott et al., 2008). Thus, one of our aims is to test the hypothesis that Mo is primarily hosted in sulfides that will break down in the presence of atmospheric oxygen to release Mo. Because the Archean continental crust was likely significantly more mafic than the present-day crust (Taylor and McLennan, 1985; Condie, 1993; Tang et al., 2016; Gaschnig et al., 2016), studying Mo concentrations in sulfides blebs

and other basaltic minerals provides a first-order approximation of the Mo distribution in Archean basalts and their differentiates that would have been weathered during the GOE.

A second motivation for this study is to use chalcophile element concentrations to gain insight into igneous petrogenesis and the nature of the Kilauea mantle source. Recent studies have provided better understanding of the formation of sulfides and the distribution and behavior of chalcophile elements during mantle melting and crust formation in MORB (Patten et al., 2013), arcs, and back arc basins (Jenner et al., 2010 and 2012; Jenner, 2015; Lee et al., 2012) and. However, the behavior of many of these chalcophile elements during magmatic differentiation is less constrained, save for a few (e.g., Ga, Kato et al. (2017); Mo Yang et al. (2015) Mo; Cd, In, and Sn,Yi et al (2000) and Jochum et al. (1993); Sb, Jochum and Hofmann (1997); W, Arevalo and McDonough (2008); Tl, Prytulak et al. (2013), and Pb, Hofmann (1988)). In these element-specific studies, the mineralogical hosts were not empirically determined. Differentiation trends for these elements can be used to infer mantle source compositions. The nature of the mantle source of the Hawaiian hot-spot is debated, however many researchers argue for a depleted mantle source containing varying proportions of recycled oceanic crust, as initially proposed by White and Hofmann, 1982. By documenting the behavior of variably chalcophile elements during differentiation in the Kilauea Iki lava lake, we can identify their mineralogical hosts and estimate the mantle source abundances, as done previously for platinum group elements (Puchtel et al., 2004) and W (Ireland et al., 2009), to gain insights into its formation.

We present data for Cu, Ga, Ge, As, Mo, Ag, Cd, In, Sn, Sb, W, Tl, Pb, and Bi in the Kilauea Iki lava lake. This includes whole rock analyses, in-situ mineral analyses, and determination of partition coefficients between the melt and sulfides, silicates, and oxides.

1.2 KILAUEA IKI LAVA LAKE

The Kilauea Iki lava lake formed when picritic lava ponded in a pre-existing crater during the 1959 eruption of Kilauea volcano. The lava was emplaced in seventeen eruptive phases over the course of four weeks (Richter and Moore, 1966), and subsequently cooled and differentiated as a closed system over the following decades, thus providing an excellent natural laboratory to study magmatic differentiation. The eruption was well documented and several drilling excursions from 1960 to 1988 have provided numerous cores that have been extensively analyzed. Data for major elements (Helz and Taggert, 2010, Helz et al., 1994), lithophile trace elements (Helz, 2012), highly siderophile trace elements (Pitcher et al., 2009), and numerous stable isotope systems (Tomascak et al. 1999, Teng et al. 2007, Teng et al. 2008, Chen et al. 2013, Savage et al., 2015) have been published.

The Kilauea Iki core samples are dominated by picrite and basalt, but also contain internal differentiates resulting from discontinuous fractionation processes (Helz, 1987). The picrites and basalts range in whole rock (WR) MgO content from 27 wt% (olivine cumulates) to 7.5 wt% and contain varying proportions of olivine and chromite as well as occasional plagioclase, augite, and Fe-Ti oxides. The average composition of the lave lake is around 15 wt% MgO_{WR} (Wright, 1973). The majority of the internal differentiates are ferrodiabasic segregation veins (< 6 wt% MgO_{WR}, up to 57 wt% SiO_{2WR}) that formed as evolved residual liquid segregated from the surrounding crystal mush by flowing into cracks created in the cooling lake. The segregation veins contain plagioclase, augite, Fe-Ti oxides, minor acicular apatite, an immiscible sulfide, and silicate glass that is quite felsic (between 56 and 74 wt% SiO_{2glass}), relative to most quenched basalts. Fe-Ni-Cu sulfide blebs were previously documented within melt inclusions hosted in olivine in the picrite and basalt samples (Helz

and Wright, 1992; Stone and Fleet, 1991) and Cu-rich sulfide blebs have been previously documented in the groundmass of the more evolved samples (Helz, 1987; Stone and Fleet, 1991; Pitcher et al., 2009). Because parts of the lake were still molten during drilling, melt was quenched upon extraction, preserving glass in many samples. Glass quenching temperatures in drill cores range from ~1150°C in the most mafic rocks to ~900°C in the more evolved samples (Helz and Thornber, 1987), although most samples were completely cooled and solidified by the time they were drilled. Oxygen fugacities in the lake were determined using the oxide oxybarometer of Ghiorso and Evans (2008) and evolve from $\Delta NNO+1.5$ to $\Delta NNO-1$, which corresponds to different stages of crystallization (supplementary figures). A complete thermal history of the lake from the 1981 drill-core is documented in Helz and Thornber (1987).

Thirty-six samples ranging from 26.9 to 2.4 wt% MgO_{WR} (Table 1) were analyzed for whole rock and/or in-situ chalcophile element data. Samples were chosen based on previous characterization, MgO content, thermal history, and mineralogy. The modal mineralogy of select samples was determined by point counting and can be found in the Table A7.

Sample	Rock type	Analysis	MgO WR	MgO glass	Temp, C°	fO2, ΔNNO	Sulfides
67-2-83.7	andesite	LA	*nd*	1.77	*1015*		none
67-3-70.0	ferrodiabase vein	LA	*nd*	0.09	972		gmass
67-3-75.0	ferrodiabase vein	LA	*9.47*	0.51	990		gmass
67-3-75.7	ferrodiabase vein	LA	*nd*	0.49	1000	-0.57	gmass
67-3-76.2	ferrodiabase vein	LA	*5.14*	0.66	1015	-0.66	gmass
75-1-125.0	ferrodiabase vein	LA	*5.94*	0.09	975	-0.91	gmass
75-1-130.5	andesite	LA	*9.73*	0.40	980	0.44	gmass, incl
75-1-134.4/133.4	olivine basalt	LA, SA	*10.65*	2.01	1037		gmass
79-1R1-170.9	ooze from vein	LA, SA	*3.48*	1.78	*110*		gmass
79-3-150.4	olivine basalt	LA, SA	*13.51*	no glass	*825*		gmass, incl
79-3-158.0	ferrodiabase vein	LA, SA	*4.5*	0.37	*990*	-0.45	gmass
79-3-160.6/160.3	olivine basalt	LA, SA	*16.11*	0.61	*110*	1.53	inclusion
79-3-171.9/172.8	olivine basalt	LA, SA	*18.8*	4.32	*110*	1.38	none
81-2-88.6	vein within a vein	LA, SA	*2.37*	no glass	*110*	-0.89	gmass
81-1-169.9	segregation vein	LA	*nd*	0.14	970		gmass
81-1-178.9b	andesite	LA	*nd*	0.79	995		gmass
81-1-178.9sv	ferrodiabase vein	LA	*nd*	0.52	995		gmass
81-1-210.0/209.8	olivine basalt	LA, SA	*24.53*	6.09	*1135*		none
81-1-294.7	olivine basalt	LA, SA	*14.3*	5.03	1105		none
Iki 58	eruption pumice	SA	*8.08*	*nd*	*1144*		*nd*
Iki 22	eruption pumice	SA	*19.52*	*nd*	*1216*		*nd*
Iki 3	eruption pumice	SA	*17.2*	*nd*	*1213*		*nd*
67-2-85.7	ooze from vein	SA	*2.6*	*nd*	*1060*		*nd*
67-3-6.8	chilled upper crust	SA	*25.83*	*nd*	*110*		*nd*
67-3-27.5	chilled upper crust	SA	*12.01*	*nd*	*110*		*nd*
75-1-38.9	chilled upper crust	SA	*10.73*	*nd*	110		*nd*
75-1-75.2	ferrodiabase vein	SA	*5.77*	*nd*	110		*nd*
75-1-121.5	olivine poor basalt	SA	*7.77*	*nd*	*850*		*nd*
81-1-119.2	olivine basalt	SA	*6.74*	*nd*	*110*		*nd*
81-1-169.9x	ferrodiabase vein	SA	*26.87*	*nd*	*975*		*nd*
81-1-239.9	olivine basalt	SA	*26.55*	6.13	*1140*		*nd*

Table 1.1 Sample Data. Italicized MgO content and temperatures from work of R. Helz.

1.3 METHODS

1.3.1 Whole Rock Analyses

Twenty-one whole rock powders, four USGS standard reference materials (BHVO-1, W-2, AGV-2, and GSP-1), and a total analytical blank (TAB) were analyzed using standard addition solution inductively coupled mass spectrometry (ICP-MS) and externally calibrated solution ICP-MS. Fifty milligrams of powder were dissolved in Savillex beakers for the KI samples, BHVO-1, and W-2. High-pressure Teflon© Parr bombs were used to digest the more felsic standards (AGV-1 and GSP-1) to ensure dissolution of resistant phases. One mL of concentrated HNO_3 and 3 mL of concentrated HF were added to the beakers and bombs, which were then placed on a hotplate (150°C) or in an oven (180°C), respectively, for ≥72 hours. The solutions were then evaporated to dryness on a hotplate and 2 mL of concentrated HNO_3 were added and subsequently evaporated before adding 1 mL of HNO_3 and 2 mL of 18Ω MilliQ H_2O, resealing the beakers/bombs, and replacing them on the hotplate/furnace overnight (≥12 hours). The beakers/bombs were removed the next day and "master solutions" were made, consisting of the dissolved solution (sample + 1 mL of HNO_3 + 2 mL of MilliQ H_2O) diluted to 15mL with 2% HNO_3 and trace HF. Sample dissolution and standard addition procedures follow the procedures of Gaschnig et al. (2015).

The standard addition technique involves spiking the solution of unknown concentration with known concentrations of the element of interest, and using the spiked samples to create a calibration curve. Two spikes were prepared: Spike A contains Ag, Cd, In, Sb, Tl, and Bi and Spike B contains Ga, Ge, Sn, Mo, and W. For the most accurate results, the spikes were prepared so that they contain roughly double the concentration expected in the samples. Three solutions were created for each sample + spike combination. Solution one contains

1mL of master solution and 1 mL of a purified Rh solution in 2% HNO_3 (~75 ppb) to be used as a drift corrector. Solution two contains 1 mL of master solution, 1 mL of Rh, and 0.5 mL of spike. Solution three contains 1 mL of master solution, 1 mL of Rh, and 1 mL of spike. The three aliquots were diluted to a total volume of 10 mL with 2% HNO_3 then vigorously shaken to homogenize the solution.

Additionally, a separate 1mL aliquot of the master solution was spiked with 1mL of ~800ppb In (drift corrector) and diluted to 15 mL with 2% HNO_3 for Cu, Pb and other trace element analyses. These data were reduced with an external calibration curve created with the USGS standards. The standard addition and In-spiked solutions were run on a Thermo-Finnigan Element2 HR-ICP-MS at the University of Maryland within a week of solution preparation. The instrument was tuned to keep oxide production below 0.8% $^{238}U^{16}O/^{238}U$. Multiple isotopes of most elements were run in low (LR) and some were run in medium (MR) resolution to reduce polyatomic and isobaric interferences. For the suite of chalcophile elements, the following isotopes were measured: ^{69}Ga (MR), ^{71}Ga (MR), ^{73}Ge (MR), ^{74}Ge (MR), ^{75}As (MR), ^{95}Mo (LR, MR), ^{97}Mo (LR, MR), ^{98}Mo (LR, MR), ^{107}Ag (LR, MR), ^{109}Ag (LR, MR), ^{111}Cd (LR, MR), ^{115}In (LR, MR), ^{117}Sn (LR, MR), ^{118}Sn (LR, MR), ^{119}Sn (LR, MR), ^{121}Sb (LR, MR), ^{182}W (LR, MR), ^{183}W (LR, MR), ^{205}Tl (LR), and ^{209}Bi (LR). The ^{115}In data were corrected for interferences by ^{115}Sn (resulting in a 10% difference, on average). Copper-63, ^{65}Cu, ^{206}Pb, and ^{208}Pb were analyzed with the external calibration method. Precision was determined using replicate analyses of BHVO-1 and AGV-2 (Table A1 and supplementary figures). The standard addition data were reduced using an in-house Excel macro created by Ming Tang.

1.3.2 In-Situ Analyses

In-situ analyses of glass, silicates, oxides, and sulfide blebs were carried out on eighteen petrographic thin sections. The phases were analyzed for major element compositions using WDS on a JEOL JXA-8900 Electron Probe Micro Analyzer (EPMA) at the University of Maryland. Between 8 and 10 points were measured on glass per sample and a mean was calculated for each sample showing homogeneous glass composition (all glasses were homogeneous except for 67-3-83.7 and 75-1-130.5, which contain less than 5% glass). A total of ~245 EPMA point analyses were made on ~190 sulfides from 13 thin sections. At least two points were analyzed on sulfides that were larger than 10 µm to check for compositional heterogeneity due to exsolution. Many sulfides showed multiple regions of heterogeneous exsolution, making it nearly impossible to extrapolate the data collected from a 2-dimensional cross section of the sulfide sphere to what may lie below or above the plane of the thin section. Therefore, the true major element composition of the sulfide blebs is uncertain. Such heterogeneity was taken into consideration when reducing the laser ablation (LA) ICP-MS data. All EPMA analyses were performed with a 5 µm beam, 15 kV accelerating voltage, and 25 nA probe current.

Trace element abundances were determined using LA-ICP-MS at the University of Maryland. The phases were ablated in a He atmosphere using a New Wave UP 213 nm wavelength laser and the resulting sample plume was analyzed with a Thermo-Finnigan Element2 HR-ICP-MS. The instrument was tuned so that the $^{238}U^{16}O/^{238}U$ ratio was below 0.8%. All substrates were ablated with a laser frequency of 7 Hz and fluence was kept between 2.5 and 4 J/cm^2, depending on the substrate being analyzed. The isotopes measured were: ^{63}Cu, ^{65}Cu, ^{69}Ga, ^{71}Ga, ^{73}Ge, ^{74}Ge, ^{75}As, ^{95}Mo, ^{97}Mo, ^{98}Mo, ^{107}Ag, ^{109}Ag, ^{111}Cd, ^{113}In, ^{115}In, ^{117}Sn, ^{119}Sn, ^{121}Sb, ^{123}Sb, ^{184}W, ^{205}Tl, ^{208}Pb, and ^{209}Bi. The In data were corrected for

interferences by [113]Cd and [115]Sn. Glass, silicate, and oxide analyses were performed using a laser spot size between 55 to 80 µm, and sulfide analyses were performed with a spot size of 25 to 80 µm, depending on the size of the phase being ablated. Between 6 and 10 glass points were measured per thin section and then averaged for a sample mean. Samples that contain heterogeneous glasses were not used in D value calculations. Thirty-two sulfides (> 25 µm) within six thin sections were ablated, but because of the small size of the sulfide blebs it was not possible to ablate distinct unmixed regions within a bleb. Data reduction for LA-ICP-MS was performed using NIST 610 as the external calibration standard and the Iolite software created at the University of Melbourne (Paton et al., 2011). Silicon was used as an internal standard for silicate phases, Cu for sulfides, and Mn for oxides. Only sulfides that were in contact with homogeneous glass were targeted for LA-ICP-MS analysis. Because several sulfides have heterogeneous major element abundances, the raw sulfide ablation data was reduced twice: once using the highest Cu content measured by EPMA and once using the lowest Cu content. Of the 32 sulfides ablated, only five were compositionally heterogeneous enough to yield two reduction values that varied by more than 10%. The two reduction values for the 27 homogeneous sulfides were then averaged to give a single concentration for each trace element in each sulfide. For example, two distinct unmixed regions of a sulfide may contain 42 wt% and 50 wt% Cu each, so the resulting ablation data

was reduced once using the 42 wt% Cu endmember and a then re-reduced using the 50 wt% Cu end member. These two reduction schemes gave two separate endmember values for the trace elements of interest, which were then averaged if they varied by less than 10%. Reference materials BHVO-2g, NIST-612, and JB sulfide (a reference sulfide created by James Brenan at the University of Toronto, Mungall and Brenan, 2014) were used as

secondary standards during laser ablation analyses. Values determined for standard reference materials are provided in Table A1.

1.4 SULFIDES

1.4.1 Sulfide Textures and Composition

Visible sulfides in the samples form round droplets between one and 200 µm in diameter. These immiscible sulfide phases are common in basaltic melts and are often referred to as "blebs" as they are near-spherical in shape. Within the lake, the sulfides are found in the groundmass of the most evolved basalts and segregation veins, and occasionally within melt inclusions in olivine phenocrysts of the more primitive samples. Here we focus on the groundmass sulfides in the most evolved samples with quite felsic (nearly rhyolitic) glass, as opposed to other studies (Patten et al., 2013) where sulfides blebs were in contact with basalt glass.

In reflected light, most sulfides appear to be composed of a yellow, relatively Cu-poor phase and an orange, Cu-rich phase. However, the exact abundance of Cu, Fe, and S in these exsolved regions varies from sulfide to sulfide. Native Cu is observed in several sulfides (Fig. 1a), and rare Fe-oxides are found as inclusions within some blebs. Exsolution textures range from simple to complex, including very fine-grained, acicular lamellae, and massive exsolution features, as shown in Fig. 1. The groundmass sulfide blebs are all Cu-Fe-S phases that form a solid solution between isocubanite, $CuFe_2S_3$, and bornite, Cu_5FeS_4 (Fig. 2) with rare Ni present. Complete major and trace element data for the sulfides can be found in Table A6.

The blebs likely represent immiscible sulfide melt droplets that unmixed following quenching to subsolidus temperatures, with crystallization towards bornite and isocubanite

14

endmembers. The textures of sulfide blebs suggest sulfide liquid immiscibility and the Cu-rich composition is likely reflective of formation by in-situ crystallization in an evolved, Cu-rich melt. In samples with abundant glass, roughly half of the sulfides are surrounded by glass while the other half appear to have nucleated onto another phase (typically Fe-Ti oxides, Fig. 1a,b,c). In samples with minor glass (< 8 volume %), sulfides are found as interstitial phases sandwiched between olivine, augite, and plagioclase (Fig. 1d). A complete list of sulfide textures, size, and composition is provided in Table A6.

The sulfides that are found in the eruption sample Iki-22 and within melt inclusions in olivine phenocrysts are compositionally distinct from the groundmass sulfides in the evolved samples, as they contain significantly more Ni. Up to 11 wt% Ni was measured in this study, however a previous study found up to 31 wt% in the sulfide blebs in Iki-22 which were determined to be either pentlandite or MSS (Stone and Fleet, 1991).

Table 1.2	MgO wt%	Cu	Ga	Ge	As	Mo	Ag
Iki 58	8.08	132	24	1.97	0.63	1.13	0.18
2s		31.1	4.3	0.43	0.1	0.27	0.08
Iki 22	19.5	111	19.9	1.94	0.5	0.94	0.17
2s		27.6	3.6	0.42	0.08	0.22	0.08
Iki3	17.2	103	15.8	1.47	0.32	2.19	0.1
2s		3.4	2.8	0.32	0.05	0.52	0.04
81-2-88.6	2.37	537	39.6	1.98	2.2	4.7	0.53
2s		40.2	7.1	0.43	0.36	1.11	0.23
67-2-85.7	2.72	539	43.2	2.17	2.31	4.55	0.66
2s		40.5	7.8	0.47	0.38	1.07	0.29
79-1R1-170.9	3.48	459	40.9	2.09	2.35	3.61	0.49
2s		35.5	7.4	0.45	0.38	0.85	0.21
79-3-158.0	4.5	260	29.5	1.7	1.03	2.3	0.28
2s		20.3	5.3	0.37	0.17	0.54	0.12
75-1-75.2	5.77	167	33.9	2.22	0.86	2.04	0.4
2s		43.8	6.1	0.48	0.14	0.48	0.17
75-1-121.5	7.77	139	27.9	2.03	0.65	1.33	0.22
2s		33.5	5	0.44	0.11	0.31	0.1
67-3-27.5	12	125	24.2	2.04	0.45	1.14	0.15
2s		9.12	4.3	0.44	0.07	0.27	0.07
75-1-38.9	12.5	94.4	23.2	1.99	0.42	1.03	0.21
2s		22.3	4.2	0.43	0.07	0.24	0.09
79-3-150.4	13.5	81.8	22.2	1.97	0.44	1.03	0.15
2s		20.3	4	0.42	0.07	0.24	0.07
81-1-210.0	24.5	60.7	12.7	1.65	0.21	0.57	0.06
2s		4.51	2.3	0.36	0.04	0.14	0.03
67-3-6.8	25.8	102	15.2	1.67	0.33	0.71	0.09
2s		25.6	2.7	0.36	0.05	0.17	0.04
81-1-239.9	26.6	52.9	12.4	1.66	0.21	0.56	0.05
2s		3.86	2.2	0.36	0.04	0.13	0.02
81-1-169.9x	26.9	91.9	16	1.78	0.39	0.95	0.11
2s		6.85	2.9	0.38	0.06	0.22	0.05
81-1-119.2	6.74	141	22.6	1.58	0.74	1	0.14
2s		8.93	4.1	0.34	0.12	0.24	0.06
75-1-134.4	10.9	126	19	1.52	0.74	1.42	0.09
2s		7.99	3.4	0.33	0.12	0.34	0.04
79-3-160.3	16.1	105	17.5	1.56	0.66	0.91	0.13
2s		6.61	3.2	0.34	0.11	0.21	0.06
79-3-172.8	18.71	95.3	14	1.38	0.61	0.85	0.46
2s		6.02	2.51	0.3	0.1	0.2	0.2
81-1-294.7	14.3	109	17	1.47	0.58	0.72	0.11
2s		6.87	3.06	0.32	0.09	0.17	0.05

Table 1.2 cont…

Table 1.2	Cd	In	Sn	Sb	W	Tl	Pb	Bi
Iki 58	0.18	0.11	2.75	0.09	0.68	0.03	1.18	0.03
2s	0.05	0.02	0.78	0.04	0.59	0.01	0.12	0.01
Iki 22	0.16	0.09	4.66	0.09	0.36	0.02	7.48	0.03
2s	0.04	0.01	1.33	0.04	0.31	0.01	0.74	0.01
Iki3	0.2	0.06	1.3	0.15	0.32	0.02	1.73	0.03
2s	0.05	0.01	0.37	0.07	0.28	0.01	0.09	0
81-2-88.6	0.3	0.13	7.11	0.3	1.04	0.08	4.82	0.08
2s	0.08	0.02	2.02	0.15	0.91	0.03	0.15	0.01
67-2-85.7	0.33	0.18	7.27	0.3	1.28	0.1	5.42	0.07
2s	0.08	0.03	2.07	0.15	1.12	0.04	0.17	0.01
79-1R1-170.9	0.29	0.17	5.44	0.28	0.93	0.08	6.54	0.07
2s	0.07	0.03	1.55	0.14	0.81	0.03	0.21	0.01
79-3-158.0	0.17	0.11	3.57	0.14	0.52	0.04	2.45	0.02
2s	0.04	0.02	1.02	0.07	0.45	0.01	0.08	0
75-1-75.2	0.23	0.14	3.34	0.13	0.41	0.04	1.38	0.05
2s	0.06	0.02	0.95	0.07	0.36	0.01	0.13	0.01
75-1-121.5	0.17	0.12	2.3	0.09	0.35	0.03	1.18	0.02
2s	0.04	0.02	0.65	0.05	0.31	0.01	0.12	0
67-3-27.5	0.16	0.09	1.67	0.13	0.22	0.03	1.08	0.01
2s	0.04	0.01	0.47	0.06	0.19	0.01	0.03	0
75-1-38.9	0.17	0.1	1.8	0.08	0.49	0.01	1.99	0.01
2s	0.04	0.02	0.51	0.04	0.42	0.01	0.19	0
79-3-150.4	0.14	0.1	1.65	0.06	0.52	0.02	0.74	0.01
2s	0.04	0.02	0.47	0.03	0.45	0.01	0.07	0
81-1-210.0	0.09	0.05	0.77	0.03	0.07	0.01	0.64	0.01
2s	0.02	0.01	0.22	0.02	0.06	0	0.02	0
67-3-6.8	0.11	0.07	1.34	0.05	0.18	0.01	0.83	0.02
2s	0.03	0.01	0.38	0.02	0.16	0	0.08	0
81-1-239.9	0.08	0.05	0.69	0.03	0.06	0.01	0.42	0.01
2s	0.02	0.01	0.2	0.01	0.05	0	0.01	0
81-1-169.9x	0.11	0.07	1.25	0.05	0.17	0.02	0.81	0.03
2s	0.03	0.01	0.36	0.02	0.15	0.01	0.03	0
81-1-119.2	0.12	0.09	1.99	0.07	0.26	0.02	1.41	0.01
2s	0.03	0.01	0.57	0.03	0.23	0.01	0.07	0
75-1-134.4	0.13	0.08	1.62	0.05	0.51	0.02	1.55	0.01
2s	0.03	0.01	0.46	0.03	0.45	0.01	0.08	0
79-3-160.3	0.1	0.06	1.24	0.05	0.21	0.01	1.01	0.02
2s	0.02	0.01	0.35	0.02	0.19	0	0.05	0

79-3-172.8	0.1	0.06	1.06	0.04	0.16	0.01	1.02	0.01
2s	0.02	0.01	0.3	0.02	0.14	0	0.05	0
81-1-294.7	0.11	0.08	1.32	0.05	0.19	0.02	0.89	0.02
2s	0.03	0.01	0.37	0.02	0.17	0.01	0.05	0

Table 1.2. Variably chalcophile element abundances in the whole rock (ppm).
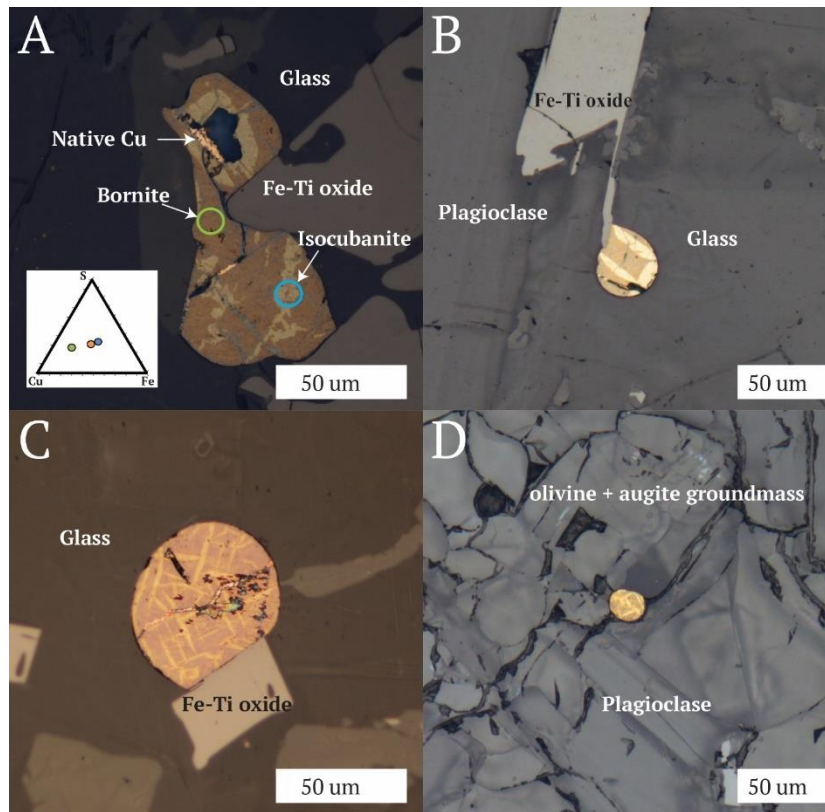
Figure 1.1. Photomicrographs of typical sulfides found in the KI groundmass. A) An irregular shaped sulfide with complex exsolution textures. Four points measured with EPMA display four distinct phases: chalcopyrite, bornite, isocubanite, and native Cu. Normalized EPMA analyses are shown on the inset ternary diagram. B) "Simple" massive exsolution texture on a sulfide that likely nucleated onto an Fe-Ti oxide. C) Lamellar/acicular exsolution texture. D) An interstitial sulfide found in a sample with minor glass. The sulfide still retains its rounded shape and displays exsolution lamellae. Interstitial sulfides like this were not analyzed using laser ablation ICP-MS because they are not in direct contact with glass. All photos taken in reflected light.

1.4.2 Sulfide Equilibrium

In order for partition coefficients to be valid, the sulfides must be in equilibrium with the glass, and the glass must be homogenous. While equilibrium can be difficult to establish in natural systems, sulfide-glass equilibrium can be evaluated in the KI samples from the following criteria set by Peach et al. (1990), Li and Audétat (2015), and this study: 1) there is no correlation between sulfide size and composition; 2) the sulfides are compositionally

homogeneous; and 3) the sulfides are in direct contact with the glass. The first requisite is met, as there is no correlation observed between sulfide diameter and major or trace element composition. This implies that the surrounding silicate melt did not significantly change in composition during sulfide growth as would be the case if larger (older) sulfides were enriched in silicate-incompatible chalcophile elements compared with the smaller (younger) sulfides. This also suggests that the surrounding melt was not chemically isolated (i.e., interstitial) during sulfide growth. The second criterion is difficult to evaluate given the exsolved nature of the sulfides, but they all form Cu-Fe-S solid solutions between isocubanite and bornite, and the Cu content of all sulfides in the same thin section varies by less than 30%. Finally, while many occurrences of sulfides are found throughout the KI samples, only those in direct contact with glass were analyzed using LA-ICP-MS (see Fig. 1a,b,c). All of these samples have greater than 15% glass by volume, with the exception of one (sample 81-1-169.9, which is at a higher risk for disequilibrium). It can thus be inferred that the melt was interconnected and grain boundaries were likely wetted in these glassy samples, implying sulfides were in direct contact with the melt until the molten rock was quenched (Miller et al., 2014). Additionally, only samples with relatively homogeneous glass were used in D value calculation where the 2 sigma RSD calculated on multiple point analyses of glasses was less than 25% for all elements except Ag, Cd, In, Sb, and Bi (the least abundant elements in the glasses, so their large RSD is a function of difficulty measuring ppb-level abundances with LA-ICP-MS). In summary, although caution should be taken when claiming true equilibrium in a crystallizing system, the criteria above suggests the sulfides equilibrated with the evolved, intermediate silicate melt. Thus, this study provides an assessment of partitioning behavior in a natural system.
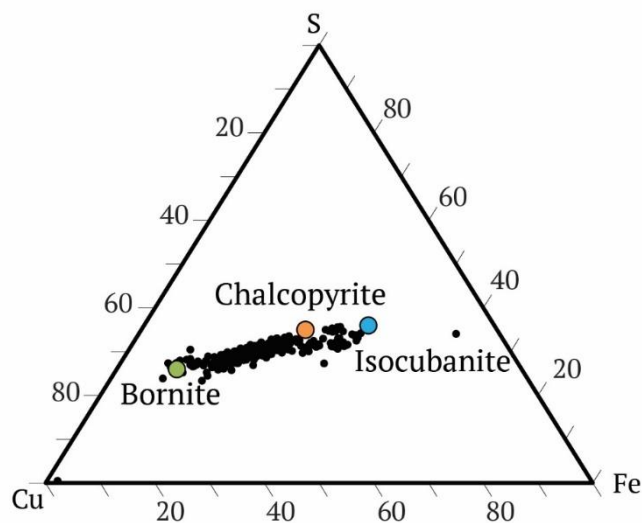
Figure 1.2. Ternary diagram of ~245 EPMA point analyses measured on ~180 sulfides. The green symbol represents bornite, the orange chalcopyrite, and the blue is isocubanite, showing that the KI sulfide blebs found within the glass form a solid solution between the bornite and isocubanite endmembers.

1.5 REULTS

1.5.1 Whole Rock Differentiation Trends

In the whole rocks, all elements (except for Ge) become more concentrated with increasing differentiation (Fig. 3, Table 2). Because the concentrations of many of the elements of interest increase nearly exponentially with decreasing MgO content, it can be inferred that they behave incompatibly on a whole rock scale during differentiation of the lava lake. By contrast, Ge maintains a relatively constant concentration in all of the Kilauea samples.

The erupted pumice samples Iki-3 (17.2 wt% MgO$_{WR}$) and Iki-22 (19.5 wt% MgO$_{WR}$) show anomalous enrichments in several elements (Sn, Pb, Mo, Bi, Cd, Sb) that cannot be explained given the observed mineralogy of the samples in thin sections. Similar anomalous enrichments were found in KI eruption pumice and basalt analyzed by Pitcher et al. (2009)

where spikes in some PGEs (especially Pt in Iki-22 and Ru and Ir in the glass separate, Iki-22g) were attributed to precipitation of metal or alloy "micro-nuggets" that were not visible in thin section but may impart a "nugget effect" on the whole rock data. The origin of these enrichments is further discussed in section 6.1.
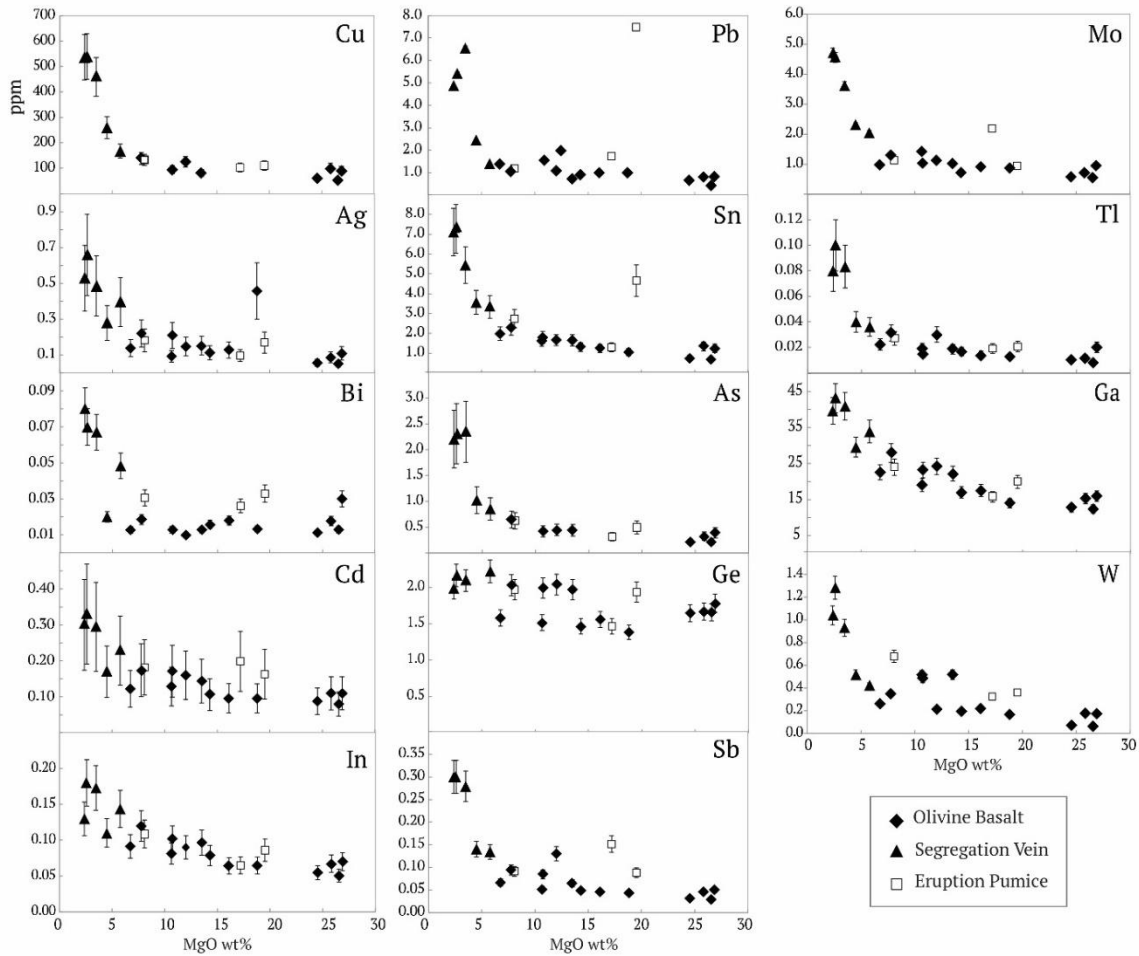
Figure 1.3 MgO variation diagrams displaying chalcophile element differentiation trends in the whole rock powders. All trace elements are measured in ppm. Error bars denote 2SD as determined by replicate analyses of BHVO-1 (MgO = 7.2 wt%) and may be an overestimate for the segregation vein samples that are more enriched in the chalcophile elements.

Table 1.3	MgO	Cu	Ga	Ge	As	Mo	Ag
67-3-75.0	0.51	291	61	10.8	13.9	6.36	0.12
2s	0.1	100	24.6	8.96	9.34	2.66	0.37
79-3-160.6	0.61	133	44.9	4.45	7.72	7.75	0.12
2s	0.06	18.8	11.3	1.95	2.37	2.48	0
79-3-171.9	4.32	319	33.4	4.23	10.2	2.46	0.11
2s	0.18	38.5	3.4	1.15	6.45	0.23	0.05
79-1R1-170.9	1.78	333	35.1	5.63	6.68	3.06	0.11
2s	0.22	68.7	1.83	0.61	1.72	0.64	0.03
81-1-209.8	6.09	193	25.5	3.4	2.74	1.36	0.07
2s	0.15	35.7	4.02	0.84	1.25	0.39	0.03
81-1-294.7	5.03	314	33.9	4.36	4.22	2.15	0.14
2s	0.39	24.5	3.79	0.76	1.39	0.37	0.02
81-1-169.9*	0.14	18.6	32.8	3.11	15.8	8.29	0.06
2s	0.06	1.23	7.16	1.62	ND	1.22	ND
79-3-158*	0.37	67.3	38.3	4.95	6.77	4.43	0.09
2s	0.12	11.1	6.27	1.7	2.06	1.27	0.01
67-3-75.7	0.58	162	44.7	6.76	ND	4.73	0.09
2s	0.13	21.5	3.94	1.33	ND	0.44	0.02
67-3-75.7b*	0.49	122	36.7	5.65	9.18	4.18	0.12
2s	0.13	12.6	3.51	0.74	2.29	1.51	0.04
75-1-134.4	2.01	225	54.6	8.69	11.9	5.17	0.11
2s	0.07	36.2	8.41	3.21	4.68	0.56	0.06
81-1-178.6b	0.79	189	69.8	7.73	6.39	8.23	0.25
2s	0.18	26.9	24	6.2	1.13	1.18	ND
81-1-178.6sv	0.52	119	17.9	6.53	ND	3.78	0.15
2s	0.04	53.9	30.9	2.86	2.86	1.08	0.03
67-3-70.0	0.09	116	44.1	5.79	8.64	5.1	0.18
2s	0.05	100	12.1	4.29	5.6	3.31	ND
67-3-83.7	1.77	344	63.1	10.4	ND	7.53	0.15
2s	0.81	119	17.9	6.53	ND	3.78	ND
67-3-76.2*	0.66	193	60	9	12.5	6.26	0.06
2s	0.2	79	23.9	3.9	8.97	3.13	0.06
75-1-130.5	0.4	75.4	44.5	4.95	14.8	8.55	0.1
2s	0.07	10.7	22.1	5.02	ND	2.39	0.03
75-1-125.0*	0.09	29.1	34.9	3.29	6.08	3.77	0.13
2s	0.04	4.21	3.64	1.77	1.96	1.9	0.01
79-3-160.6i	3.24	32.8	23.3	2.69	6.1	0.88	0.08
2s	0.31	7.07	0.57	0.25	ND	0.18	0.13
79-3-171.9i	5.06	148	23.1	2.8	4.96	0.88	0.08
2s	0.25	32.4	3.38	0.69	3.92	0.25	0.11
81-1-209.8i	6.06	191	25.2	2.4	3.2	1.45	0.07
2s	0.08		*1 analysis*				

Table 1.3 cont.

Table 1.3 cont	Cd	In	Sn	Sb	W	Tl	Pb	Bi
67-3-75.0	0.21	0.07	9.45	0.29	1.82	0.22	10.1	0.07
2s	0.33	0.02	2.17	0.33	0.7	0.09	1.53	0.04
79-3-160.6	0.22	0.23	7.36	0.36	2.12	0.22	7.62	0.06
2s	0.32	0.49	2.35	0.35	0.81	0.09	1.54	0.02
79-3-171.9	0.11	0.13	2.54	0.12	0.6	0.04	ND	0.03
2s	0.07	0.05	0.66	0.08	0.21	0.04	ND	0.01
79-1R1-170.9	0.21	0.15	3.85	0.15	0.82	0.07	6.15	0.04
2s	0.15	0.02	0.66	0.17	0.2	0.04	0.98	0.03
81-1-209.8	0.2	0.1	1.68	0.04	0.34	0.03	1.7	0.01
2s	0.13	0.06	0.84	0.06	0.14	0.03	0.54	0.03
81-1-294.7	0.11	0.13	3.11	0.05	0.53	0.06	2.72	0.04
2s	0.24	0.05	0.89	0.13	0.11	0.04	0.06	0.03
81-1-169.9*	0.17	0.06	6.44	0.9	2.39	0.32	ND	0.03
2s	0.34	0.02	2.09	0.44	0.65	0.13	ND	0.02
79-3-158*	0.15	0.1	7.07	0.24	1.58	0.15	7.74	0.04
2s	0.19	0.03	1.54	0.14	0.37	0.04	1.04	0.02
67-3-75.7	ND	0.22	7.22	0.3	1.47	0.15	ND	0.04
2s	ND	0.18	1.56	0.12	0.29	0.05	ND	0.03
67-3-75.7b*	0.21	0.09	7.3	0.45	1.4	0.1	7.38	0.05
2s	0.16	0.06	1.99	0.82	0.8	0.1	ND	0.03
75-1-134.4	0.23	0.14	6.05	0.23	1.26	0.13	6.37	0.05
2s	0.17	0.03	1.05	0.09	0.27	0.04	0.86	0.03
81-1-178.6b	0.12	0.08	8.8	0.45	2.16	0.26	ND	0.04
2s	0.03	0.06	5.21	0.23	0.72	0.03	ND	0.04
81-1-178.6sv	ND	0.11	3.63	1.71	0.92	0.15	ND	0.06
2s	ND	0.04	1.42	0.17	0.23	0.03	ND	ND
67-3-70.0	0.16	0.06	8.32	0.33	1.75	0.15	ND	0.03
2s	0.14	0.06	4.12	0.26	1.21	0.13	ND	0.04
67-3-83.7	ND	0.15	8.48	0.92	2.18	0.16	ND	0.09
2s	ND	0.06	3.63	1.71	0.92	0.15	ND	0.06
67-3-76.2*	0.24	0.1	7.97	0.28	1.91	0.17	8	0.05
2s	0.31	0.04	2.11	0.17	1.13	0.11	2.53	0.05
75-1-130.5	0.24	0.06	8.42	0.42	2.51	0.21	ND	0.06
2s	0.23	0.02	2.57	0.31	0.89	0.08	ND	0.05
75-1-125.0*	0.1	0.09	10.1	0.37	2.15	0.2	ND	0.04
2s	0.08	0.02	1.81	0.21	0.44	0.08	ND	0.02
79-3-160.6i	0.05	0.26	1.11	0.15	0.21	0.01	ND	0.01
2s	ND	0.03	0.45	0.08	0.12	0	ND	0
79-3-171.9i	0.24	0.21	1.26	0.07	0.21	0.02	ND	0.03
2s	0.23	0.21	0.58	0.13	0.2	0.04	ND	0.02

81-1-209.8i	0.33	0.23	2.87	0.07	0.3	0.02	ND	0.04
2s								

Table 1.3. Glass major element data for the Kilauea Iki lava lake samples.

1.5.2 Glass Analyses

While the chalcophile elements appear to behave incompatibly on a whole rock scale, glass analyses better reflect the partitioning of several elements due to the saturation and/or fractionation of various phases. Variation diagrams of the glass trace element analyses are displayed in Fig. 4 and the data can be found in Table 3. The most primitive glass measured in this study contains 6.1 wt% MgO. The average MgO content of the parental erupted melt was between 8.5 and 9.0 wt% as determined by scoria glasses (Helz et al., 2017). The majority of the glasses analyzed here are from segregation veins where the glass is actually quite felsic (between 0.2 and 3.0 wt% MgO_{glass}), as these are the samples where sulfide is most easily found.

We have demonstrated the highly chalcophile nature of Cu in this system, hence we can use it as a proxy for S since the latter is compromised by degassing during eruption and drilling (Helz and Wright, 1983). Copper abundance in the glass steadily increases from 6 to 2 wt% MgO_{glass} and then abruptly falls, consistent with sulfide saturation at around 2 wt% MgO_{glass} (Fig. 4). Because the melt saturates with respect to sulfides, but sulfide droplets do not physically segregate from the magma, these decreases in abundances are not observed in the whole rock data. Other chalcophile elements that show a drop in overall abundance below 2 wt% MgO_{glass} are Ag, Cd, In, and Bi.

Arsenic, Ga, and Ge appear to decrease in abundance at around 1 wt% MgO. The abundances of Mo, Sn, Sb, W, Tl, and Pb in the glass all increase, to varying degrees, with increasing differentiation, suggesting that these elements behave relatively incompatibly in the system and they are not significantly influenced by sulfide formation. This is further

supported by an inverse relationship between the glass abundance of a sample and the

concentrations of elements Mo, Sn, Sb, W, and Tl, suggesting they are strongly concentrated

into the last vestiges of melt.
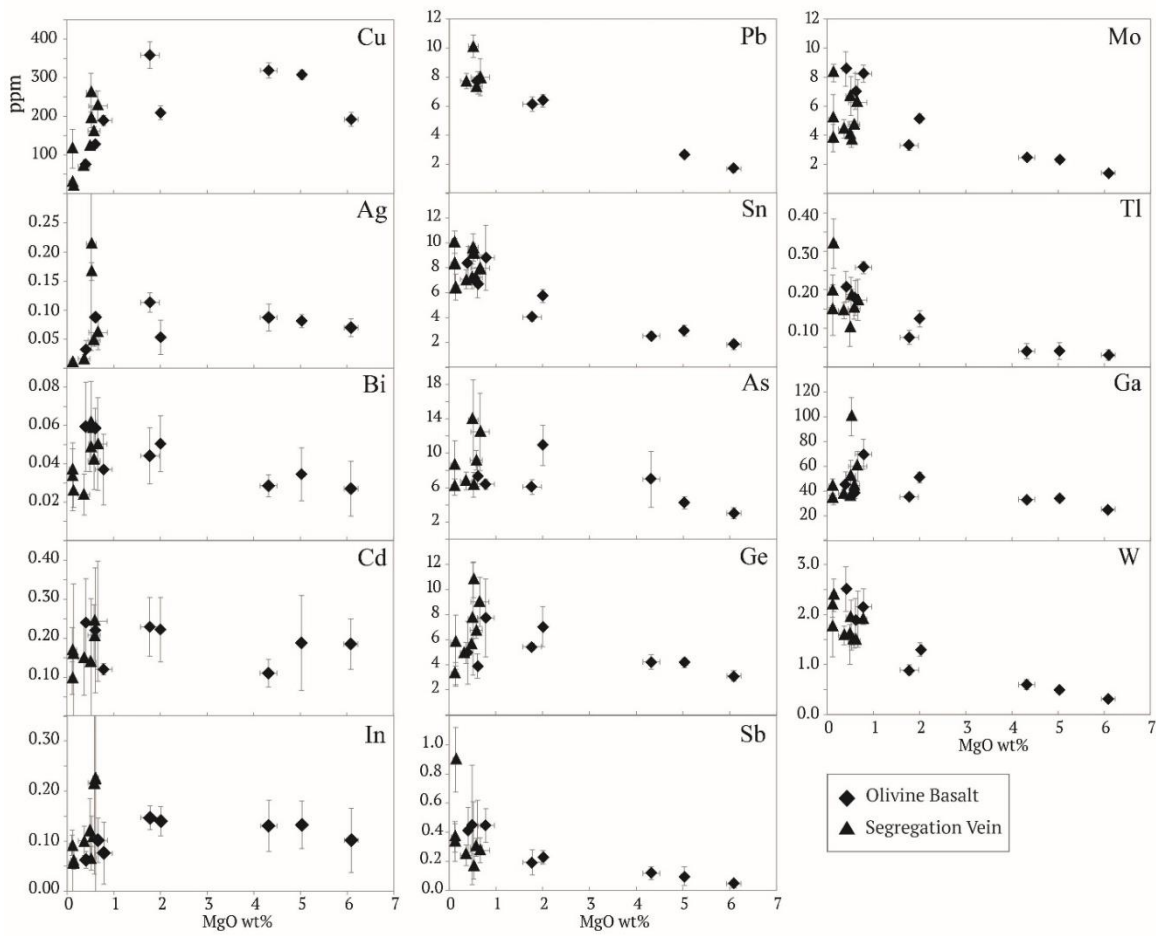
Figure 1.4. Glass MgO variation diagrams displaying trace element differentiation patterns. All trace elements are reported in ppm. Each point represents a sample average of 6-10 laser ablation point analyses. Error bars represent 1σ of the mean of replicate analyses.

Sulfide	Ga	Ge	As	Mo	Ag	Cd	In	Sn	Sb	W	Tl	Pb	Bi
Sample 67-3-75.7b													
75.7b_S02b	0.18	6.50	200	2.56	70.1	30.7	2.78	27.7	0.23	0.10	0.03	320	32.2
2s	0.52	1.48	47.0	0.70	6.86	4.88	0.40	5.27	0.47	0.12	0.04	19.4	3.36
75.7b_S03	0.26	8.85	104	1.46	40.6	24.6	1.46	25.0	0.18	bdl	bdl	257	21.0
2s	0.34	1.38	20.2	0.44	4.49	3.25	0.30	4.28	0.18	0.71	0.01	16.6	1.59
75.7b_S04	0.34	6.63	83.0	1.92	104	32.0	2.87	22.1	0.39	0.02	0.20	342	21.5
2s	0.09	0.58	14.5	0.27	9.55	1.70	0.24	1.77	0.08	0.02	0.04	13.1	0.88
75.7b_S08	4.51	5.45	95.0	1.40	93.0	20.5	3.22	24.6	0.51	0.09	0.09	334	8.89
2s	0.69	0.71	19.1	0.39	8.49	1.63	0.27	2.72	0.11	0.05	0.06	13.1	0.70
75.7b_S11b	3.98	5.21	22.4	2.25	83.8	30.4	2.68	25.8	0.46	0.21	0.19	318	27.8
2s	0.66	0.61	5.94	0.33	5.94	2.12	0.20	1.87	0.08	0.06	0.04	12.4	1.31
75.7b_S12a	0.40	8.56	89.0	1.69	169	61.5	3.05	39.7	0.64	0.02	0.32	311	30.1
2s	0.07	0.61	13.8	0.24	6.93	2.83	0.17	2.44	0.10	0.01	0.05	11.0	1.27
75.7b_S13b	2.59	9.40	71.0	1.54	108	6.40	2.17	20.0	0.81	0.12	0.20	247	10.5
2s	0.54	1.20	14.1	0.36	7.78	1.27	0.25	2.83	0.23	0.08	0.07	13.4	0.71
75.7b_S14	0.47	8.70	8.70	1.16	85.3	49.7	2.39	32.7	0.54	0.02	0.17	274	25.6
2s	0.14	0.81	0.92	0.24	3.64	3.08	0.19	2.51	0.13	0.02	0.05	12.0	1.20
Sample 75-1-125.0													
125.0_S02	1.70	14.9	10.3	7.40	110	76.0	3.93	78.0	1.06	bdl	0.53	909	33.2
2s	0.92	2.76	2.55	2.19	21.9	11.3	0.78	12.7	0.48	0.71	0.30	57.3	3.54
125.0_S05		6.35	4.85	0.49	47.0	65.0	3.53	5.35	0.33	bdl	0.05	314	35.3
2s		1.13	1.13	0.31	3.54	8.49	0.31	1.52	0.18	0.71	0.05	13.8	2.37
125.0_S08	1.04	7.40	11.6	4.55	95.0	71.0	4.67	76.5	0.77	bdl	bdl	970	38.4
2s	0.47	1.56	2.37	1.41	12.7	11.0	0.50	12.0	0.48	0.71	0.71	84.9	5.06
125.0_S12	0.25	6.75	6.90	1.36	115	52.0	3.96	55.0	0.30	0.22	bdl	636	20.9
2s	0.30	1.67	1.95	0.61	15.6	8.14	0.53	8.85	0.20	0.22	0.71	40.4	1.74
125.0_S13	0.35	5.60	3.01	0.53	30.7	44.3	2.53	2.11	0.10	bdl	bdl	27.6	3.54
2s	0.23	0.95	0.78	0.23	2.57	5.39	0.22	0.95	0.08	0.71	0.71	1.86	0.38
125.0_S15a	1.12	8.00	12.8	5.05	86.5	92.0	7.33	101	0.46	0.15	0.02	911	26.3
2s	0.64	1.80	2.05	1.34	5.41	10.6	0.78	11.7	0.27	0.21	0.03	51.3	3.85
125.0-S17	1.35	7.00	2.70	0.39	44.9	47.5	3.83	2.25	0.06	0.02	bdl	19.1	1.89
2s	0.56	1.48	0.85	0.22	4.95	7.43	0.46	0.92	0.06	0.03	0.71	1.87	0.31
125.0_S27	1.95	8.95	10.6	bdl	33.1	38.4	4.46	4.00	bdl	bdl	bdl	25.8	6.30
2s	1.23	3.13	2.84		6.13	9.53	0.73	2.39				2.80	1.23
125.0_S34	2.90	10.2	16.0	3.85	114	80.0	8.32	88.0	0.61	bdl	0.46	818	26.3
2s	1.70	3.51	3.79	1.06	9.92	15.9	0.85	16.7	0.48	0.71	0.31	57.8	3.08

Sample 67-3-76.2

76.2_S04	9.80	8.10	8.40	1.36	94.0	34.8	3.21	27.3	0.44	0.30	0.23	227	26.5
2s	2.44	1.38	2.19	0.45	9.55	5.06	0.30	5.06	0.19	0.19	0.13	18.7	3.61
76.2_S05	0.29	10.1	9.50	0.79	89.0	42.1	3.27	36.0	0.36	bdl	0.19	245	26.2
2s	0.11	0.88	1.42	0.22	7.43	3.29	0.21	8.14	0.10	0.71	0.04	11.3	3.22
76.2_S06	0.18	5.61	4.05	0.63	81.1	26.8	1.26	13.0	0.18	bdl	bdl	125	10.8
2s	0.08	0.80	0.58	0.20	6.82	2.62	0.14	2.28	0.09	0.71	0.71	5.26	0.81
76.2_S13	0.62	6.15	3.38	0.65	168	22.8	1.95	28.9	0.39	0.03	bdl	156	15.8
2s	0.21	0.83	0.55	0.21	19.2	2.42	0.19	4.63	0.15	0.03	0.71	6.58	1.99
76.2_S01	0.27	5.13	6.21	1.14	96.2	34.5	1.29	43.5	0.43	0.01	0.14	375	18.6
2s	0.08	0.50	0.55	0.14	5.23	2.19	0.13	2.62	0.10	0.01	0.04	12.0	0.99

Sample 81-1-169.9

169.9_S05	22.30	5.70	9.20	8.35	76.4	49.3	4.35	73.9	0.72	0.93	1.75	994	23.2
2s	6.12	1.49	2.27	1.67	5.31	5.31	0.35	6.48	0.23	0.34	0.38	38.9	1.95
169.9_S09	1.15	7.05	2.35	0.90	70.5	33.4	3.68	25.0	0.12	0.06	bdl	350	17.3
2s	1.30	2.48	0.90	0.67	13.0	8.99	0.33	6.19	0.17	0.08	0.71	23.0	1.86

Sample 79-3-158.0

|													
158_S28	0.52	4.50	6.00	1.91	112	73.0	2.97	31.9	0.45	bdl	0.16	nd	37.9
2s	0.69	3.70	2.40	0.82	18.0	14.00	0.94	5.80	0.42		0.12		6.30
158_S30		12.5	7.60	3.30	291	217	6.51	78.0	bdl	bdl	bdl	nd	29.4
2s	0.83	9.30	5.50	2.40	40.0	57.0	2.80	18.0					5.70
158_S23	0.20	4.70	3.20	7.20	158	95.0	2.19	34.2	0.15	bdl	bdl	nd	59
2s	0.75	5.30	3.30	3.70	31.0	26.0	1.20	9.30	0.39				20.0
158_S20	0.14	5.60	1.60	2.81	80.0	59.0	2.20	33.4	0.30	bdl	0.03	nd	23.5
2s	0.25	2.30	1.80	0.85	12.0	10.0	0.79	5.30	0.33		0.05		3.80
158_S22	0.19	8.80	4.20	4.00	124	108	3.38	58.0	1.80	bdl	bdl	nd	35.9
2s	0.60	4.50	2.70	1.90	21.0	21.0	1.00	17.0	1.10				9.90
158_S11	5.00	10.9	9.40	7.80	355	127	4.32	69.2	0.67	0.24	0.13	nd	58.1
2s	1.20	2.50	2.40	1.50	65.0	11.0	0.76	7.60	0.33	0.15	0.07		5.50
158_S12		4.90	3.30	3.11	148	80.0	4.53	29.1	0.22	bdl	bdl	nd	26.9
2s	0.21	2.50	1.80	0.90	26.0	16.0	0.62	8.70	0.25				9.50

Table 1.4 Trace element concentrations in sulfides in ppm

1.5.3 Partition Coefficients

Partition coefficients (D values) and chalcophile element abundances for the sulfides are presented in Tables 4 and 5, and D values for other oxides and silicates can be found in Tables 6 and 7, respectively. Partition coefficients were calculated as C^{phase}/C^{glass} using the mean glass composition for a given sample.

1.5.3.1 Sulfides

Partition coefficients were calculated for each sulfide in a thin section (between 1 and 9 per section) by taking the mean sulfide composition divided by the mean glass composition for the sample. Taking the mean of the $D^{sulfide/silicate}$ values for the five samples measured gives $D_{Ag} = 1252 \pm 1201$ (2σ), $D_{Bi} = 663 \pm 576$, $D_{Cd} = 380 \pm 566$, $D_{In} = 40 \pm 34$, $D_{Pb} = 34 \pm 18$, $D_{Sn} = 5.3 \pm 3.6$, $D_{As} = 2.4 \pm 7.6$, $D_{Ge} = 1.6 \pm 1.4$, $D_{Sb} = 1.3 \pm 1.5$, $D_{Tl} = 1.1 \pm 1.7$, $D_{Mo} = 0.56 \pm 0.6$, $D_{Ga} = 0.10 \pm 0.3$, and $D_W = 0.11 \pm 0.1$. The partition coefficients span nearly six orders of magnitude between the elements of interest (Fig. 5), so they are divided up into three categories: 1) chalcophile elements, average $D \geq 5$: Ag, Bi, Cd, In, Pb, and Sn; 2) weakly chalcophile elements, average $D \sim 1$: As, Ge, Sb, and Tl; and 3) non-chalcophile elements, $D < 1$: Mo, Ga and W. Within the chalcophile elements, subgroups could be created for strongly chalcophile (Ag, Bi, Cd, In) and chalcophile (Pb and Sn) elements. This is because Pb and Sn do not decrease in abundance in the glasses after sulfide saturation, showing that sulfide saturation does not completely control their behavior. Partition coefficients are not plotted for Cu because it is an essential structural constituent of the sulfides, ranging between 25 and 58 wt%; D_{Cu} can reach up to 19,000.
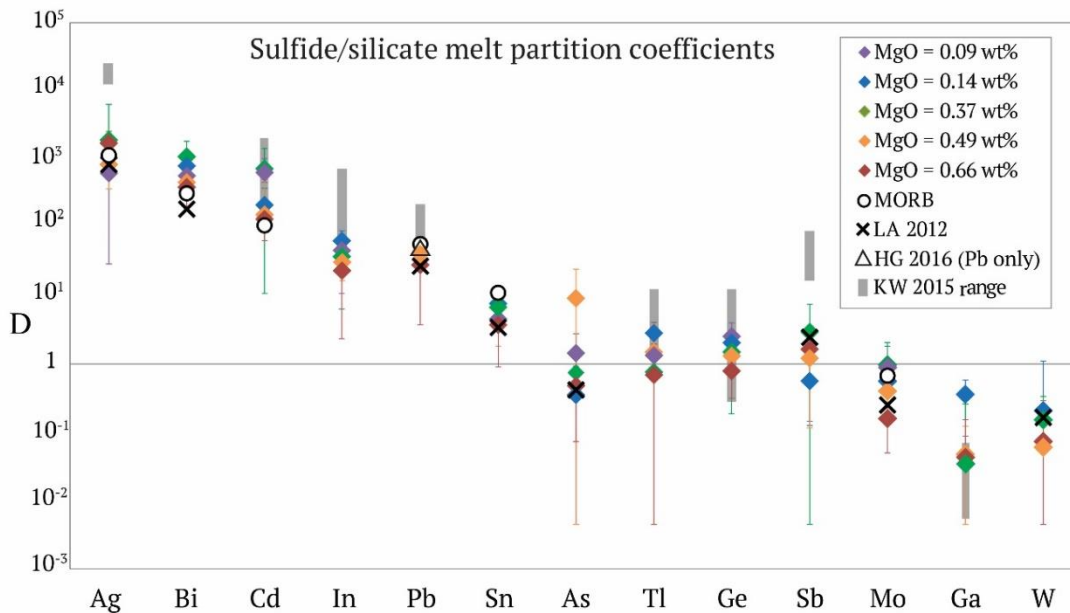
Figure 1.5. Partition coefficients measured in five KI samples (colored diamonds). Error bars represent 2 standard deviations of the mean of multiple sulfide-silicate analyses per sample. The different colored diamonds represent KI glasses with different MgO contents, as labelled in the symbol key; purple diamond corresponds to sulfides in sample 75-1-125.0, blue is 81-1-169.9, green is 79-3-158.0, orange is 67-3-75.7, and red is 67-3-76.2. The mean glass composition for each sample was used to calculate the D values. Average $D^{\text{sulfide liquid/silicate melt}}$ values from Li and Audetat (2012) at FMQ>0 are represented by an X. MORB values from Patten et al., (2013) are represented by open circles and Pb values expected in MORB, as measured by Hart and Gaetani (2016), is represented with a triangle. Cu is not plotted because it is a main structural component to the sulfides. The gray bar represents the range of $D^{\text{sulfide/silicate}}$ that were calculated using the Kiseeva and Wood (2015) equation at 1050°C, average Cu (45 wt%) and Ni (0.7 wt%) abundances, and FeO content of the silicate melt between 7.3 and 1.3 wt%.

Sulfide	Ga	Ge	As	Mo	Ag	Cd	In	Sn	Sb	W	Tl	Pb	Bi
Sample 67-3-75.7b													
75.7b_S02b	0.00	1.15	21.8	0.61	567	148	30.9	3.79	0.51	0.07	0.31	43.3	662
2s	0.01	0.30	7.47	0.28	520	826	11.9	1.26	1.41	0.10	0.46	6.60	354
75.7b_S03	0.01	1.57	11.3	0.35	328	118	16.2	3.42	0.39	nd	nd	34.8	431
2s	0.01	0.32	3.58	0.16	302	661	6.3	1.10	0.82			5.36	229
75.7b_S04	0.01	1.17	9.04	0.46	837	154	31.8	3.02	0.86	0.01	1.94	46.3	442
2s	0.00	0.18	2.75	0.18	768	861	12.3	0.86	1.57	0.01	1.92	6.70	233
75.7b_S08	0.12	0.96	10.3	0.33	752	99	35.8	3.36	1.12	0.06	0.85	45.3	183
2s	0.02	0.18	3.32	0.15	690	551	13.8	0.99	2.06	0.05	1.00	6.57	97
75.7b_S11b	0.11	0.92	2.43	0.54	678	147	29.8	3.53	1.01	0.15	1.86	43.0	572
2s	0.02	0.16	0.89	0.21	620	819	11.5	1.00	1.85	0.10	1.84	6.24	302
75.7b_S12a	0.01	1.51	9.69	0.40	1369	296	33.9	5.43	1.41	0.02	3.14	42.1	618
2s	0.00	0.23	2.85	0.16	1250	1655	13.1	1.52	2.58	0.01	3.08	6.07	326
75.7b_S13b	0.07	1.66	7.73	0.37	874	31	24.1	2.74	1.80	0.09	2.00	33.5	216
2s	0.02	0.30	2.47	0.16	800	172	9.3	0.84	3.32	0.07	2.04	5.02	114
75.7b_S14	0.01	1.54	0.95	0.28	690	239	26.5	4.47	1.19	0.01	1.65	37.1	526
2s	0.00	0.25	0.26	0.12	630	1337	10.2	1.27	2.19	0.01	1.66	5.44	277
Sample 75-1-125.0													
125.0_S02	0.05	4.54	1.69	1.96	848	779	42.7	7.76	2.88	nd	2.64	nd	893
2s	0.03	2.58	0.69	1.15	1060	682	9.3	1.88	2.09		1.85		521
125.0_S05	0.00	1.93	0.80	0.13	362	666	38.4	0.53	0.88	nd	0.24	nd	948
2s		1.09	0.32	0.10	447	581	8.4	0.18	0.71		0.25		547
125.0_S08	0.03	2.25	1.91	1.21	733	727	50.8	7.61	2.09	nd	nd	nd	1033
2s	0.01	1.30	0.73	0.71	909	638	11.0	1.82	1.76				607
125.0_S12	0.01	2.05	1.14	0.36	883	533	43.1	5.47	0.80	0.10	nd	nd	562
2s	0.01	1.22	0.49	0.24	1096	467	9.4	1.32	0.71	0.11			326
125.0_S13	0.01	1.70	0.49	0.14	236	454	27.6	0.21	0.27	nd	nd	nd	95.2
2s	0.01	0.96	0.21	0.09	*292*	395	6.0	0.10	0.27				55.5
125.0_S15a	0.03	2.44	2.10	1.34	667	943	79.7	10.0	1.24	0.07	0.11	nd	708
2s	0.02	1.42	0.76	0.76	824	821	17.3	2.15	1.02	0.10	0.17		418
125.0-S17	0.04	2.13	0.44	0.10	346	487	41.7	0.22	0.15	0.01	nd	nd	50.9
2s	0.02	1.23	0.20	0.08	428	427	9.1	0.10	0.17	0.01			30.3
125.0_S27	0.06	2.72	1.74	0.00	255	393	48.6	0.40	nd	nd	nd	nd	170
2s	0.04	1.75	0.73		*318*	353	10.6	0.25					103
125.0_S34	0.08	3.09	2.62	1.02	875	820	90.6	8.76	1.66	nd	2.29	nd	706
2s	0.05	1.97	1.05	0.59	1082	726	19.7	2.28	1.60		1.81		413
Sample 67-3-76.2													
76.2_S04	0.16	0.90	0.67	0.22	1522	142.8	31.6	3.42	1.58	0.15	1.30	28.3	526

2s	0.08	0.42	0.51	0.13	1493	182	104	1.10	1.18	0.13	1.08	9.24	511
76.2_S05	0.00	1.12	0.76	0.13	1441	173	32.2	4.52	1.30	0.00	1.08	30.6	520
2s	0.00	0.49	0.56	0.07	1411	219	106	1.57	0.89		0.71	9.77	504
76.2_S06	0.00	0.62	0.32	0.10	1313	110	12.4	1.62	0.65	0.00	0.00	15.7	215
2s	0.00	0.28	0.24	0.06	1286	139	40.8	0.52	0.51			5.0	208
76.2_S13	0.01	0.68	0.27	0.10	2721	93.5	19.2	3.62	1.41	0.01	0.00	19.5	313
2s	0.01	0.31	0.20	0.06	2672	119	63.0	1.12	1.03	0.02		6.2	304
76.2_S01	0.00	0.57	0.50	0.18	1558	142	12.7	5.46	1.56	0.00	0.82	46.9	370
2s	0.00	0.25	0.36	0.09	1522	179	41.7	1.48	1.02	0.00	0.55	14.9	356
Sample 81-1-169.9													
169.9_S05	0.68	1.83	0.58	1.01	1273	290	69.0	11.5	0.80	0.39	5.46	nd	911
2s	0.24	1.07	0.44	0.25	1249	579	20.3	3.86	0.47	0.18	2.51		581
169.9_S09	0.04	2.27	0.15	0.11	1175	196	58.5	3.87	0.13	0.02	nd	nd	681
2s	0.04	1.43	0.11	0.08	1152	395	17.2	1.58	0.20	0.04			436
Sample 79-3-158.0													
158_S28	0.01	0.91	0.89	0.43	1227	488	29.5	4.51	1.86	nd	1.10	nd	1585
2s	0.02	0.81	0.45	0.22	1025	632	8.48	1.28	2.05		0.88		1446
158_S30	nd	2.52	1.12	0.74	3189	1451	64.5	11.03	0.00	nd	nd	nd	1230
2s		2.07	0.88	0.58	2663	1896	18.6	3.50					1128
158_S23	0.01	0.95	0.47	1.62	1732	635	21.7	4.84	0.62	nd	nd	nd	2468
2s	0.02	1.12	0.51	0.96	1446	831	6.25	1.68	1.65				2365
158_S20	0.00	1.13	0.24	0.63	877	395	21.8	4.72	1.24	nd	0.23	nd	983
2s	0.01	0.61	0.28	0.26	732	509	6.28	1.27	1.54		0.32		895
158_S22	0.00	1.78	0.62	0.90	1359	722	33.5	8.20	7.42	nd	nd	nd	1502
2s	0.02	1.09	0.44	0.50	1135	935	9.65	2.99	6.30				1409
158_S11	0.13	2.20	1.39	1.76	3890	849	42.8	9.79	2.76	nd	0.87	nd	2430
2s	0.04	0.91	0.55	0.61	3249	1089	12.3	2.38	2.12	0.10	0.53		2191
158_S12	0.00	0.99	0.49	0.70	1622	535	44.8	4.11	0.91	nd	nd	nd	1125
2s		0.61	0.30	0.29	1354	693	12.9	1.52	1.16				1084

Table 1.5 Trace element partition coefficients in sulfides

1.5.3.2 Oxides

The crystallizing oxides (pseudobrookite and ilmenite) contain minor amounts of Cu, Ga, Mo, Ag, Cd, and In and have partition coefficients ($D^{\text{oxide/silicate melt}}$) greater than or equal to one, so the oxides can be considered as minor-mineralogical hosts (Table 6, chalcophile element abundances in Table A4). Ilmenite contains Ag (D~4), Cd (D~1), and In (D~3). Pseudobrookite contains Cu (D~1), Ga (D~1), Mo (D~1), Ag (D~3), Cd (D~1), and In (D~2). Oxide fractionation does not significantly deplete these elements in the melt, as there is no decrease in overall abundance below ~5 wt% MgO_{glass} (Fig. 4).

1.5.3.3 Silicates

Olivine and augite are the only two silicates analyzed in this study, but neither are significant hosts of the elements investigated here. The D values calculated for all of the elements are below one (Table 7, chalcophile element abundances in Table A5). Plagioclase was not analyzed, as it was not expected to be a significant host of any of these elements with the exception of Ga and Ge, which may substitute for Al and Si, respectively.

	Cu	Ga	Ge	As	Mo	Ag	Cd	In	Sn	Sb	W	Tl	Pb	Bi
pseudobrookite	1.08	1.12	0.24	0.14	1.40	3.06	1.05	2.44	0.61	0.18	0.13	0.20	0.03	0.33
2s	1.79	1.08	0.23	0.26	3.37	5.89	1.23	4.69	0.91	0.29	0.21	0.73	0.09	0.33
ilmenite	0.47	0.38	0.24	0.25	0.53	3.59	0.97	2.95	0.63	0.27	0.12	0.11	0.00	0.39
2s	0.51	0.32	0.82	0.92	0.57	7.12	1.96	4.48	0.76	1.15	0.21	0.23	0.01	0.50

Table 1.6 Trace element partition coefficients in oxides

	Cu	Ga	Ge	As	Mo	Ag	Cd	In	Sn	Sb	W	Tl	Pb	Bi
olivine	0.10	0.01	0.34	0.01	0.03	0.06	0.83	0.14	0.02	0.02	bdl	bdl	bdl	0.27
2s	0.08	0.00	0.03	0.01	0.06	na		0.16	0.01	na				
augite	0.21	0.04	0.30	0.04	0.01	bdl	0.34	0.11	0.00	bdl	bdl	bdl	bdl	bdl
2s	0.21	0.04	0.30	0.04	0.01		0.34	0.11	0.00					

Table 1.7 Trace element partition coefficients in silicates

1.6 DISCUSSION

1.6.1 Element Volatility

Anomalous spikes of Mo, Cd, Sn, Sb, Pb, Bi in the whole rock data are present in two of the three eruption pumice samples and one of the eighteen drill core basalts (Fig. 3). Given that the enrichments are primarily concentrated in the eruption phases and similar anomalies are observed in the PGEs (Pitcher et al., 2009), we propose that some chalcophile elements and PGEs partition into a vapor phase during eruption and precipitated in condensates from this vapor.

Rhenium volatility during basaltic volcanism is well documented (Pitcher et al., 2009; Sun et al., 2003; Lassiter, 2003; Norman et al., 2004) and it has been suggested that vapor-phase Re is deposited in Re-sulfides (Korzhinsky et al., 1994) or Mo- and Bi-bearing phases in fumarolic fields (Tessalina et al., 2008). Enrichments in Cu, As, Sb, Te, Tl, and Pb have also been documented in condensed vapor from fumarole gas jets (Korzhinsky et al., 1994). Thus, vaporization during eruption and subsequent precipitation is a possible cause of the enrichments seen in the KI pumice.

The potential loss of volatile elements from the lava lake could decrease their concentrations in the glasses and whole rocks. For example, Yi et al. (2000) showed that subaerial outgassing lowers Cd abundances in basalts, and Norman et al. (2004) calculated that Cd outgassing, alongside Re and S, may lower Cd concentrations in volcanic glass by a factor of 2-5. Bismuth may also be slightly affected by this process, however, significant depletions of the volatile elements In, Sn, Cu and Pb due to outgassing is considered unlikely (Yi et al., 2000; Norman et al., 2004). To our knowledge, the influence of volatility on Mo and Sb concentrations in whole rock and glass has not been determined. We conclude that

36

Mo, Cd, Sn, Sb, Pb, Bi may have partitioned into a vapor phase to varying degrees, however the extent of their possible depletion from the lava lake is unknown. The results of previous work on Cd and Bi outgassing prompt us to take caution when interpreting the absolute abundances of these elements in the KI magma.

1.6.2 Sulfide Genesis and Evolution

The Cu-rich groundmass-hosted sulfides in the Kilauea Iki drill core samples are compositionally distinct from those found in other studies of basalts. Immiscible sulfide blebs that have been found in MORB (Patten et al., 2013; Peach et al., 1990), arc-related basalts (Jenner et al., 2015), and those experimentally synthesized in silicate melts (Li and Audétat, 2012 and 2015; Kiseeva and Wood, 2015) are Fe- and Ni-rich and composed of mono-sulfide solution (MSS), pentlandite, and/or pyrrhotite compositions that were in equilibrium with more primitive magmas. By contrast, the Kilauea Iki groundmass sulfides are different in this respect because they are Cu-rich phases that are surrounded by an intermediate to felsic melt. Rare Ni-rich MSS sulfides are found as occasional inclusions in olivine and in the Iki-22 pumice groundmass, which likely originated deep in Kilauea's magma system. Sulfur analyses from scoria glasses suggest that the initial magma was not sulfide saturated (Helz et al., 2017).

Magnetite crystallization is proposed to cause sulfide saturation in basalts from the Lau and Manus back arc basins by redox reactions (Jenner et al., 2010: 2012; Jenner, 2015). In these magmas, sulfides form immediately following magnetite saturation at ~6 and 3 wt% MgO_{glass}, in the two basins, respectively. In KI, Fe-Ti oxides (titaniferous-magnetite, ilmenite, and pseudobrookite) crystallize and fractionate between 5 and 3 wt% MgO_{glass}, as evidenced by the decrease in Ti and Fe on whole rock and glass MgO variation diagrams

(supplementary figures) and the appearance of these phases in thin section. This precedes

sulfide saturation at 2 wt% MgO_{glass}. The incorporation of Fe^{3+} into magnetite and

pseudobrookite will reduce the residual melt and drive sulfur reduction (S^{6+} to S^{2-}), leading to

the formation of sulfides. Oxygen fugacities calculated using the Fe-Ti oxide oxy-

thermobarometer of Ghiorso and Evans (2008) indicate that at the onset of magnetite

crystallization, the fO$_2$ of the system was around NNO+1.5 (or roughly FMQ+2.3). No

sulfides are observed in the groundmass of the more primitive samples as the oxygen

fugacity is too high for sulfide to saturate (Jugo 2009); this is also consistent with the sulfide

undersaturation inferred for the primary magma (Helz et al., 2017). The oxygen fugacity falls

to NNO-1 after the onset of the magnetite fractionation in the more evolved samples

(supplementary figures). We propose that this process of magnetite-induced sulfide

saturation, which has been termed the "magnetite crisis" (Jenner et al., 2010), contributes to

sulfide saturation in KI.

In KI, the Cu-rich sulfides are present in even the most evolved samples, implying that

they did not physically segregate from the differentiating magma. This suggests that the lava

lake was effectively a closed system at this stage of its evolution such that the sulfide blebs

were trapped within a semi-rigid crystal network (Fig. 1).

1.6.3 Behavior of Nominally Chalcophile Elements

1.6.3.1 Chalcophile Elements

We observed that Ag, Bi, Cd, and In are strongly chalcophile because their abundance in

the melt is entirely controlled by sulfide saturation, i.e., they fractionate out of the evolving

melt when sulfides form. By contrast, Pb and Sn concentrations continue to increase in the

evolving melt (Fig. 4), so their behavior in the magma is not entirely controlled by sulfide

saturation. This is due to the lower $D^{sulfide/silicate\ melt}$ of Pb and Sn and exceedingly small volume of sulfides that precipitate in this system. The sulfides are abundant enough to deplete the concentrations of the strongly chalcophile elements from the silicate melt, but not Pb and Sn. Lead analyses were added to the study late, thus not all glass samples plotted in Fig. 4 have corresponding Pb data. This may potentially skew interpretations because the absolute lowest MgO samples were not analyzed for Pb – missing data could reveal that Pb does drop in abundance in the most evolved samples. The average Nd/Pb ratio of the whole rock samples is 19 (± 9 2SD) which is consistent with an average of 15 for OIB (Hofmann 2003; Hart and Gaetani 2006). This ratio does not change systematically with differentiation in either the whole rock or glass data, suggesting that Pb and Nd (and Ce) do behave similarly, consistent with Pb not being strongly influenced by sulfide saturation.

In sulfides found in MORB (Patten et al., 2013), Ag, Bi, Cd, Pb, and Sn were also found to be chalcophile and calculated D values agree with those determined here (Fig. 5, enclosed circles, In was not measured in the Patten et al. study). This is an interesting observation given the differing melt composition, sulfide composition, and intensive variables (T, P, and fO$_2$) between the Kilauea Iki lava and MORB. MORBs saturate Ni-rich sulfides at around 10 wt% MgO$_{glass}$ which is not induced by magnetite saturation (Jenner and O'Neill, 2012, Patten et al., 2013). Hart and Gaetani (2016) experimentally determined Pb $D^{sulfide\ liquid/silicate\ melt}$ values to be between 4 and 66, dependent on T and FeO$_{glass}$, with expected MORB D~45. Additionally, Li and Audétat (2012) produced experimental $D^{sulfide\ liquid/silicate\ melt}$ that match those calculated for Ag, Bi, Pb, and Sn in KI (Fig. 5, X's, no Cd or In data are available in the Li and Audétat study; data were selected from runs having the composition, fO$_2$, and P and T conditions near those of KI; the sulfide composition has between 1.8 and 3.0 wt% Cu).

Finally, the experimental work of Kiseeva & Wood (2013, 2015) produced an algorithm that incorporates temperature, sulfide composition, and melt composition to calculate $D^{sulfide/silicate\ melt}$; D values calculated from this equation at the range in T, $Cu_{sulfide}$, and FeO_{glass} found in KI generally reproduce the KI partition coefficients quite well (gray bars, Fig 5). In KI, there is no correlation between $D^{sulfide/silicate\ melt}$ and MgO_{glass} or FeO_{glass} (which is directly related to the oxygen content of the sulfide, Kiseeva and Wood, 2015). However, the samples that contain sulfides cover a small range of MgO_{glass} or FeO_{glass} so trends may not be observable given the limited range of melt compositions. Additionally, there is no correlation between sulfide compositions (Cu, Fe, S, Ni, Mn, or Co content) and $D^{sulfide/silicate\ melt}$.

1.6.3.2 Weakly Chalcophile and Non-Chalcophile Elements

Arsenic, Ge, Sn, Tl, Mo, Ga, and W are weakly chalcophile to non-chalcophile (i.e., lithophile) in this igneous system (Fig. 5). Of these elements, Mo was also measured in MORB sulfides and found to be weakly chalcophile (Patten et al., 2013). KI D values for As, Sb, Mo, and W agree with those determined in the Li and Audétat (2012) study. Germanium, Tl, and Ga partition coefficients are in agreement (within error) with those predicted by the Kiseeva & Wood calculation, however the KI D_{Sb} falls significantly below the predicted values.

The abundance of Ga, Ge, and As appear to drop in the glasses at around 2 wt% MgO_{glass} (Fig. 4). This drop may be partially attributed to partitioning into sulfides for As and Ge, but Ga would not be affected by sulfide saturation. Instead, we propose that these elements, specifically As, may partition into apatite, where they substitute for P. While apatite is a common accessory phase in the evolved samples, it forms thin (<5 µm wide) needles that are too small for laser ablation analyses to confirm the presence of these elements. Additionally,

40

minor Ga substitutes for Al and Ge may substitute for Si in late fractionating plagioclase or augite. Scatter in the Mo and Ga abundances in evolved samples (Fig. 4) is likely caused by partitioning into Fe-Ti oxides. Antimony, Tl, Mo, and W are not significantly affected by sulfide saturation and instead behave as overall incompatible, lithophile elements during differentiation from mafic to felsic magmas. Octahedrally coordinated Mo and W have ionic radii that differ by only 1%, so their substitution for Ti in Ti-oxides is expected to be roughly equal, however Mo is significantly more abundant in oxides than W. The reason for this difference in partitioning into oxides is unknown, however it may simply be attributed to Mo being more abundant in the system than W (Mo/W ratios vary between 2 and 4 in the glass). Additionally, Mo is slightly more chalcophile than W. Despite this, Mo and W generally behave as incompatible lithophile elements in this system.

1.6.4 Molybdenum in Basalts

Molybdenum is an element of special interest because of its redox-sensitivity, suggested chalcophile behavior, and use as a paleo-redox indicator for Precambrian surface and ocean environments. Molybdenum is a chalcophile element in hydrothermal/epithermal systems that carry sufficient quantities of reduced S (MoS_2 formation) and in anoxic marine environments where it is sequestered in authigenic Fe-Mo-S phases (Helz et al., 2011) or converted to tetrathiomolybdate particles (MoS_4^{2-}) that settle out of solution (Erickson and Helz, 2000). However, in the KI magmatic system it shows incompatible, lithophile behavior and is more heavily concentrated in glass (average 5 ppm) and Fe-Ti oxides (average 6.4 ppm) than sulfides (average 2.6 ppm). Considering the abundances of these different phases, the glass accounts for the majority of the Mo in the samples (between ~50 and ~90%). The Mo $D^{sulfide/silicate}$ values measured here corroborate those from a study of MORB that found

Mo concentrations in sulfides were often below the detection limit of LA-ICP-MS (Patten et al, 2013). Molybdenum occurs primarily in its oxidized, hexavalent state in the basaltic glass (Eggins and O'Neill, 2002), making it generally incompatible in most silicates and incapable of bonding with S^{2-} to form MoS_2. Hexavalent Mo likely substitutes for octahedrally coordinated tetravalent Ti^{4+} in ilmenite as well as tetrahedrally coordinated Ti^{4+} in pseudobrookite, given similar ionic radii. Hexavalent Mo substitution into Fe-Ti-oxides would need to be charge balanced to maintain electrical neutrality.

A crustal sulfide host of Mo has been invoked in paleo-atmosphere studies (Anbar et al., 2007) where oxidative weathering of pyrite and molybdenite is suggested to release Mo from the continental crust at the time of the Great Oxidation Event (GOE). Here we show that sulfide blebs comprising three common igneous sulfides – chalcopyrite, isocubanite, and bornite – do not host significant Mo. In fact, mass balance calculations suggest that the sulfides typically host less than 5% of the total Mo budget of the samples in Kilauea Iki. We conclude that sulfides are not a significant host of Mo in basalts (MORB) and andesites (evolved KI), while glass and, to a lesser extent, magnetite and ilmenite are. Thus, the oxidation of igneous sulfides is likely not an important source of Mo to the oceans. This has significance for the use of Mo as a paleo-redox proxy as the Archean upper continental crust was significantly more mafic (Taylor and McLennan, 1985; Tang et al., 2016: Gaschnig et al., 2016) and the felsic continents were likely smaller (Cawood et al., 2013) and basalt was probably a much more common crustal lithology. The weathering properties of Mo-rich basaltic to komatiitic glass should be investigated in order to understand Mo removal from the crust at the time of the GOE.

1.6.5 Enrichments of As, Ag, Sb, W, and Bi

In KI whole rock powders and glasses, several chalcophile and lithophile elements are systematically enriched relative to elements of similar compatibility, as determined by their anomalous peaks on a primitive mantle-normalized spider diagram (supplementary figures) and cross plots (Fig. 6). Enriched lavas plot in the upper right quadrant of Fig. 6, while MORB data (Jenner and O'Neill, 2012) plot around or slightly below one. Also shown in the cross plots are primitive glasses from the Eastern Manus back arc basin and Northwest Lau spreading center from Jenner et al. (2012). Interestingly, the subduction-influenced Manus BAB shares As, Sb, and Bi enrichments with Kilauea, while the NW Lau spreading center basalts lack signatures of subduction-influenced magmatism, and are not enriched in As or Bi. Thus, the As, Sb, and Bi budget of KI shares similarities with basalts influenced by recycling in subduction zones, however the W enrichment observed in KI lavas is not found in either back arc basin. The enrichment in Bi is especially striking considering its abundance may have been affected by degassing (Norman et al., 2004; and section 6.1). In arc settings, enrichments in As, Sb, Tl, Pb, and Bi have been attributed to the influence of hydrothermally altered oceanic crust that concentrates these elements into low-temperature sulfides (Jenner et al., 2012). The sulfides then break down during subduction and release these elements into the mantle wedge (Noll et al., 1996). The formation of hydrothermal sulfides seems to be the best way to concentrate the elements that are enriched in KI, but these sulfides would need to survive subduction to be incorporated into the KI source.

Ireland et al. (2009) found that W enrichments in several Hawaiian basalts could be explained by the mixing of 3 - 20% recycled oceanic crust and sediments into a depleted mantle source. Pursuing this hypothesis further, we modeled the source composition for the Kilauea Iki picrites to understand the origin of these enrichments.

Figure 1.6 Enrichments observed in Kilauea Iki lavas. Each element is normalized to an interpolated value (denoted with a star), which is the expected concentration of that element if it partitions the same as similarly compatible elements, as observed in MORB. This is calculated as Sb*, Bi*, and As* $=(VxCd)^{0.5}$, Ag* and W*$=(CuxGe)^{0.5}$. Average MORB (Jenner and O'Neill, 2012) is represented with an open circle, all measured values in Kilauea samples are in light blue diamonds (basalts) and triangles (segregation veins), primitive Kilauea is a dark blue diamond, primitive Eastern Manus Back-arc basin (Jenner et al., 2012) in a green square, and primitive Northwestern Lau Spreading Center (Jenner et al., 2012) is in a red square.

1.6.6 The Kilauea Mantle Source

The Hawaiian mantle source is heterogeneous, as reflected in many trace element and isotopic studies of lavas from difference volcanic centers (Jackson et al., 2012, and references therein). Multiple mantle sources have been invoked to explain these differences: the EM1 signature in Hawaii may reflect a primitive mantle source, given Sr, Pb, and Nd isotopic signatures (White, 1985), while others consider the mantle source to be a mixture of a more depleted reservoir and recycled oceanic crust (White and Hofmann, 1982). Indeed, Pietruszka et al. (2013) found that the Kilauea source can be explained by the addition of 8-16% hydrothermally altered oceanic crust, while Ireland et al. (2009) concluded that the source is composed of depleted MORB mantle with the addition of 3-20% recycled oceanic crust and terrigeneous sediments. Here we explore both a primitive mantle source and a source influenced by recycled crust to explain the Cu, Ga, Ge, As, Mo, Ag, Cd, In, Sn, Sb, W, Tl, Pb, and Bi abundances in Kilauea Iki.

The enrichment of chalcophile PGEs in KI (Pitcher et al., 2009) suggests that sulfides in the mantle source were exhausted by partial melting. Modeling of Pietruska et al. (1999, 2006) suggest that Kilauea basalts represent 10% partial melt of the mantle source, while Ireland et al. (2009) infer 5-10% partial melting of the mantle. Interestingly, neither of these estimates are high enough for sulfides to be consumed by partial melting, which occurs at 12-16% partial melting of a depleted mantle source (Luguet et al., 2003; Nielsen et al. 2014). Thus, we calculated the Kilauea source abundance for Cu, Ga, Ge, As, Mo, Ag, Cd, In, Sn, Sb, W, Tl, Pb, and Bi using the batch melting equation $C_o = C_l(D + (1 - D) * F)$ and a 12% melt fraction – the minimum melt fraction theorized to exhaust sulfides from the mantle source. Element abundances in the KI primitive magma composition (C_l) were calculated at

15 wt% MgO by fitting a linear regression through MgO variation diagrams of whole rock

data for the drill core picrites and basalts (26 wt% to 7 wt% MgO_{WR}) and olivine, as this is

the fractionating phase on the control line, per Puchtel et al. (2004) (supplementary figures).

Cerium and Er were also added to the model as a check for accuracy, given the predictable

behavior of LREE and HREE during mantle melting. Because Cd and Bi abundances in

volcanic glasses have been shown to be affected by outgassing, the calculated primitive

magma composition may be incorrect for these elements. They are included in the

calculations, but the results should be viewed with caution. Model details including bulk D

values and source modal mineralogy are included in the supplementary figures and tables.
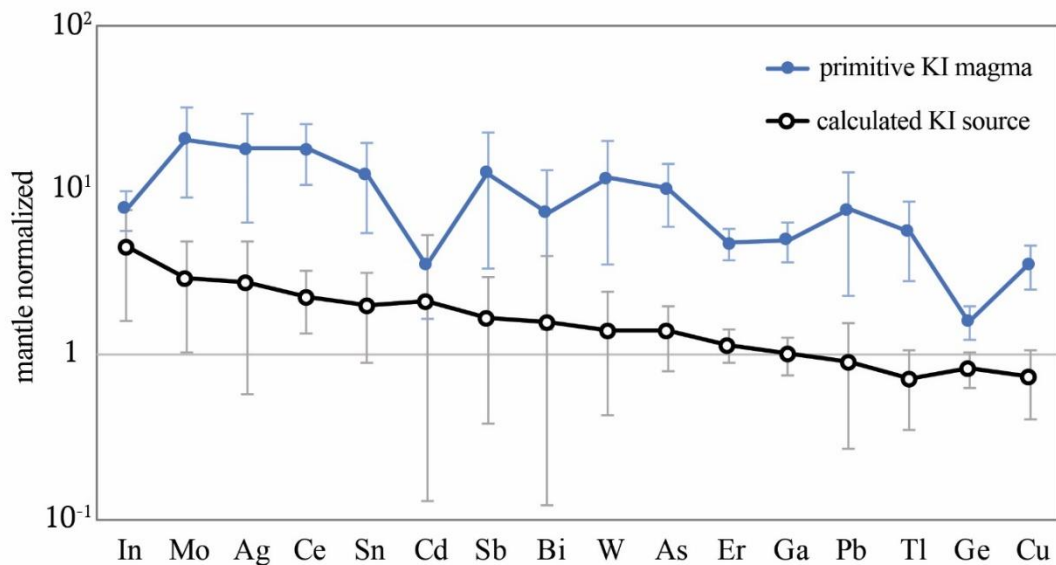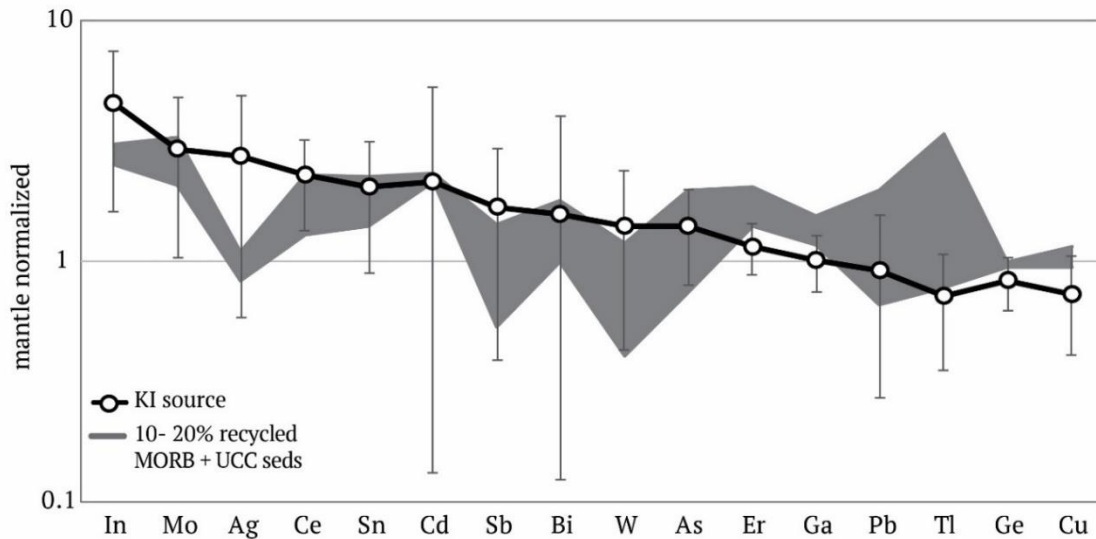

Figure 1.7. Trace element diagram normalized to primitive mantle (McDonough and Sun, 1995) showing the estimated KI primitive magma composition, calculated at 15 wt% MgO given a linear regression through whole rock data in blue. The mantle source results from the batch melting calculations are shown in black, open circles. Error bars represent 2σ calculated from the least squares regression. Cadmium and Bi whole rock data showed virtually no correlation between 25 wt% and 10 wt% MgO (supplementary figures), so their estimated primitive abundance has a large error associated with it. Additionally, Cd and Bi may have been affected by degassing. The elements are ordered by their abundance in the calculated mantle source.

The model results are shown in Figure 7. While the calculated KI mantle source composition is within error of the primitive mantle estimate for some elements, In, Mo, and LREE (as indicated by Ce), are too enriched in the KI source to be derived solely from a primitive mantle source. Incorporation of a UCC component (carried in terrigenous sediment) produces a better fit to the data. When the elements are ordered on a spider diagram by their relative abundance in primitive KI magmas relative to primitive MORB (Jenner and O'Neill, 2012), as calculated by $(X_{KI} - X_{MORB})/X_{MORB}$. With the exception of Ag, the more enriched KI elements that plot at the left side of the diagram correspond quite well with elements that are more enriched in the UCC (Fig. 8). The general trend suggests incorporation of recycled UCC-derived sediments in the mantle source of KI. Therefore, we modelled the KI source as a mixture of depleted MORB mantle (DMM) source and a recycled crust package composed of MORB + UCC sediments per Ireland et al. (2009) to better explain the trace element signature of Kilauea (Fig 9., model details in supplement). We find that the calculated KI source composition matches this DMM + 10 to 20% recycled crust source, within error, for all elements analyzed here (Fig. 9). Specifically, the abundances of the elements In, Mo, Ag, Ce, Sn, Cd, Sb, Bi, W, and As, that are 1.5 to 4 times more enriched in the KI source than in the primitive mantle, are much better explained by the addition of around 20% MORB and UCC-derived sediments to DMM than by a pure primitive mantle source (see the supplement for a discussion of the possible influence of subduction on these elements).
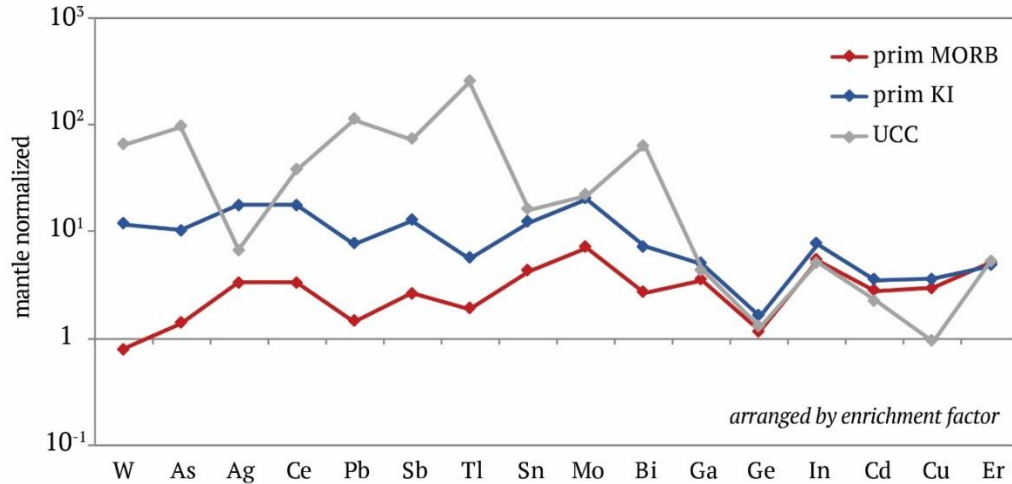
Figure 1.8. Trace element diagram normalized to primitive mantle (McDonough and Sun, 1995) showing the same primitive KI magma as plotted in Fig 7 (blue circles) as well as primitive MORB (Jenner and O'Neill, 2012) in red triangles and UCC (Rudnick and Gao, 2014) abundance in gray diamonds. Elements are ordered by the relative difference between their abundance in the primitive KI and primitive MORB calculated as (X_{KI} – X_{MORB})/X_{MORB}. Note that, with the exception of Ag, the elements that are more enriched in KI are also quite abundant in the UCC.

We conclude that the enrichments observed in the Kilauea Iki magmas (Fig. 6) and the calculated KI mantle source trace element signature can be explained by mixing of 10-20% recycled crust composed of 95 to 99% is MORB and 1 to 5% is UCC-derived sediments. These calculations agree with the results of other studies: Ireland et al. (2009) found the Hawaiian mantle source may contain 3 to 20% recycled material, Sobolev et al. (2005) – 12% recycled material; and Pietruszka et al. (2013) – 9 to 16% recycled material.

Figure 1.9. Trace element diagram, normalized to primitive mantle (McDonough and Sun, 1995) showing the results of the mantle mixing calculations (gray region) and Kilauea mantle source calculation (black line). The gray region represents a range of materials mixed into a DMM source from 10% recycled material of which 99% is MORB and 1% are sediments derived from the UCC (low end) to 20% recycled material of which 95% is MORB and 5% are UCC sediments (high end). All element concentrations agree within error between the modeled KI source and mantle mixture region. Cadmium and Bi may have been affected by degassing, so their mantle abundances may represent minima.

1.7 CONCLUSIONS

In the Kilauea Iki lava lake Ag, Bi, Cd, In, Pb, and Sn are chalcophile, As, Ge, Sb, and Tl are weakly chalcophile to lithophile, and Mo, Ga, and W are lithophile. The mean $D^{sulfide/silicate}$ are: $D_{Ag}= 1252 \pm 1201$ (2σ), $D_{Bi}= 663 \pm 576$, $D_{Cd}= 380 \pm 566$, $D_{In}=40 \pm 34$, $D_{Pb}=34 \pm 18$, $D_{Sn}=5.3 \pm 3.6$, $D_{As} =2.4 \pm 7.6$, $D_{Ge} =1.6 \pm 1.4$, $D_{Sb} =1.3 \pm 1.5$, $D_{Tl} =1.1 \pm 1.7$, $D_{Mo} =0.56 \pm 0.6$, $D_{Ga} =0.10 \pm 0.3$, and $D_W =0.11 \pm 0.1$. The chalcophile elements can be further subdivided into strongly chalcophile elements (Ag, Bi, Cd, and In), whose differentiation behavior is entirely controlled by sulfide saturation, and moderately chalcophile elements (Pb and Sn) that partition into sulfides but do not significantly fractionate from the melt after sulfide saturation given their low $D^{sulfide/silicate}$ values and the

49

low volume of sulfides. These findings are consistent with results from a study of MORB sulfides (Patten et al., 2013), as well as experimental studies run at conditions similar to those that are found in KI (Kiseeva and Wood, 2013; Li and Audétat, 2012). Gallium, Ge, and As may partition into apatite where they could substitute for P, however they likely also partition into aluminosilicate phases where they substitute for Al and Si. Antimony, Tl, and W behave as incompatible elements during differentiation.

Molybdenum generally behaves as a lithophile element; it is not primarily concentrated in the sulfides and is instead found in the glass and Fe-Ti oxides where Mo^{6+} may substitute for Ti^{4+}. This has implications for removal of Mo from the Archean continental crust, in that common igneous sulfides whose breakdown rate is a function of atmospheric oxygen levels, are not a significant host of Mo, whereas glass, which can readily break down in the absence of atmospheric oxygen, is.

The Kilauea mantle source is modeled as a mixture of depleted MORB mantle (DMM) and a recycled package of crust containing MORB and UCC derived sediments. The abundances of the elements studied here are best explained by the addition of 10-20% recycled oceanic crust (of which 1 to 5% is UCC-derived sediments) to DMM. The partial melting of this UCC-influenced source can explain the apparent enrichments in As, Ag, Sb, W, and Bi and other elements observed in Kilauea relative to MORB.

Chapter II. Geochemistry of molybdenum in the continental crust

As published in Geochimica et Cosmochimica Acta in 2018

With co-authors Roberta L. Rudnick[1,2], Richard M. Gaschnig[2,3], Joseph B. Whalen[4], Beatrice Luais[5], John D. Clemens[6]

[1] University of California Santa Barbara, Department of Earth Sciences, Santa Barbara, CA 93106

[2] University of Maryland College Park, Department of Geology, College Park, MD 20742

[3] University of Massachusetts Lowell, Department of Earth Sciences, Lowell, MA 01854

[4] Geological Survey of Canada, Central Canada Division, Ontario, Canada

[5] Centre de Recherches Pétrographiques et Géochimiques, Université de Lorraine, Vandoeuvre-les-Nancy Cedex, France

[6] Stellensbosch University, Department of Earth Sciences, Matieland, South Africa

Author Acknowledgements

ABSTRACT

The use of molybdenum as a quantitative paleo-atmosphere redox sensor is predicated on the assumption that Mo is hosted in sulfides in the upper continental crust (UCC). This assumption is tested here by determining the mineralogical hosts of Mo in typical Archean, Proterozoic, and Phanerozoic upper crustal igneous rocks, spanning a compositional range from basalt to granite. Common igneous sulfides such as pyrite and chalcopyrite contain very little Mo (commonly below detection limits of around 10 ng/g) and are not a significant crustal Mo host. By contrast, volcanic glass and Ti-bearing phases such as titanite, ilmenite, magnetite, and rutile contain significantly higher Mo concentrations (e.g., up to 40 µg/g in titanite), and can account for the whole-rock Mo budget in most rocks. However, mass balance between whole-rock and mineral data is not achieved in 4 out of 10 granites analyzed with in-situ methods, where Mo may be hosted in undetected trace molybdenite. Significant Mo depletion (i.e., UCC-normalized Mo/Ce < 1) occurs in nearly every granitic rock analyzed here, but not in oceanic basalts or their differentiates (Greaney et al., 2017; Jenner and O'Neill, 2012). On average, granites are missing ∼60% of their expected Mo contents. There are two possible reasons for this: (1) Mo partitions into an aqueous magmatic vapor/fluid phase that is expelled from cooling plutons, and/or (2) Mo is partitioned into titaniferous phases during partial melting and fractional crystallization of an evolving magma. The first scenario is likely given the high solubility of oxidized Mo. However, correlations between Mo/Ce and Nb/La in several plutonic suites suggest fractionating phases such as rutile or Fe-Ti oxides may sequester Mo in lower crustal rocks or in subducting slabs in arc settings.

2.1 Introduction

Molybdenum (Mo) geochemistry has emerged as a powerful tool for tracking early atmospheric oxygenation (e.g., Anbar et al., 2007; Wille et al., 2007; Gaschnig et al., 2014), redox conditions in ocean basins (e.g., Siebert et al., 2003; Arnold et al., 2004; Scott et al., 2008; Dahl et al., 2011), and the influence of subducted sediments and fluids on arc magmas (Freymuth et al., 2015; König et al., 2016). The interest in Mo stems from its geochemical properties: Mo is a multi-valent element whose partitioning behavior depends on the redox state of its environment. Despite the rapidly growing literature on the geochemical behavior of Mo at Earth's surface, the behavior of Mo in igneous rocks is less well understood. Yet, such knowledge is crucial for understanding how Mo will behave during crustal weathering and processes that release Mo to sedimentary environments. Additionally, determining the mineralogical hosts of Mo in evolving magmas will lead to a more accurate understanding of Mo behavior during crust formation and differentiation, and the formation of molybdenite deposits in various tectonic settings. This task was first undertaken by Kuroda and Sandell (1954) but, with improved methodology, we aim to expand upon their dataset.

2.1.1 Properties of Mo

Molybdenum is a geochemically versatile element that displays siderophile (iron/metal-loving; Kuroda and Sandell, 1954; Newsom and Palme, 1984; Lodders and Palme, 1991; Walker, 2016), chalcophile (Goldschmidt, 1937; Kuroda and Sandell, 1954), and lithophile behavior (rock/silicate-loving; Newsom and Palme, 1984; Greaney et al., 2017), depending on the composition of the system of interest (including $f\text{O}_2$ and $f\text{S}_2$), the temperature, and the pressure. Molybdenum's redox sensitivity plays a prominent role in its geochemical behavior because its charge, size, and physical properties change depending on

54

its oxidation state. Molybdenum is insoluble in aqueous fluids when reduced to its tetravalent state, but when oxidized to its hexavalent state it becomes soluble. This relationship between charge and solubility is a key factor in determining the behavior of Mo in the crust and on the Earth's surface.

In igneous systems, the transition from Mo^{4+} to Mo^{6+} occurs over a span of ~10 log units fO_2 (O'Neill and Eggins, 2002), with Mo^{4+} being the dominant state at around three log units below the IW buffer (iron-wüstite) and Mo^{6+} being the dominant state at around one log unit below the FMQ buffer (fayalite-magnetite-quartz). Thus, Mo is expected to exist in its oxidized state in mantle and crustal melts, which have oxygen fugacities near the fayalite-magnetite-quartz (FMQ) or Ni-Ni-oxide (NNO) buffers. The work of Fitton (1995), Zack et al (2002), and subsequent experimental studies suggest that Mo partitions into rutile in eclogites (eclogitic rutile: 2-7 ppm Mo; Zack et al., 2002), and can be removed from melts generated in subduction zones, even though Mo is found predominately as 6+ in oxidized experimental melts (Holzheid et al., 1994; O'Neill and Eggins, 2002; Bali et al., 2012; Skora et al. 2017). Bali et al. (2012) show that Mo is compatible in rutile in oxidized systems at the NNO buffer (nickel-nickel oxide). This suggests that Mo may be incorporated into rutile even in its oxidized state. Octahedrally-coordinated Mo^{6+} has a similar ionic radius to octahedrally-coordinated Ti^{4+} (59 and 60.5 pm, respectively; Shannon, 1976), so it can replace Ti in a coupled substitution to maintain electrical neutrality. Alternatively, Mo may be locally reduced to Mo^{4+} (ionic radius = 60.5 pm) before exchanging for Ti^{4+} in an isovalent substitution (Zack et al., 2002; Skora et al. 2017). It has also been proposed that Mo is predominately hosted in biotite and amphibole in igneous rocks (Voegelin et al., 2014; Yang et al., 2017), supporting the idea that it follows similar substitution patterns as

55

Ti. However, Mo can also be reduced and incorporated into molybdenite (MoS_2) during

oxidation-reduction reactions that occur in hydrothermal ore systems (Stein, 1985).

On the surface of Earth and in oceans, 'free' Mo exists in its oxidized, soluble state

given the abundance of atmospheric O_2. Unreactive molybdate (MoO_4^{2-}) is the most

common form of Mo in rivers and oceans today, where Mo has a residence time of around

440,000 years (Miller et al., 2011). However, this was probably not the case on early Earth,

which lacked or contained only trace concentrations of atmospheric oxygen.

2.1.2 Molybdenum as a redox proxy

Throughout the first ~ 2 billion years of Earth's history, the atmosphere was far more

reducing than today, probably containing $< 10^{-5}$ times the present atmospheric level (PAL)

of O_2 (Kasting, 2014 and references therein). Atmospheric oxygen did not accumulate to

significant levels until the Great Oxidation Event (GOE), which occurred between 2.4 Ga

and 2.3 Ga, when it likely rose to somewhere between 10^{-4} and 10^{-2} PAL (Lyons et al, 2014

and references therein).

Many lines of evidence point to the rise of O_2 during the GOE. Arguably the most

important is the disappearance of sulfur-isotope mass-independent fractionation, caused by

the creation of an atmospheric ozone shield (Farquhar et al., 2000). Additionally, several

redox-sensitive metal proxies (Mo, U, Cr, Re) indicate that oxidative weathering of the

continents commenced at or just before the GOE, suggesting that atmospheric O_2 had

become sufficiently abundant to cause oxidative weathering of crustal rocks (Anbar et al,

2007; Wille et al., 2007; Scott et al., 2008). These redox-sensitive metals are assumed to be

concentrated in minerals that will break down in the presence of atmospheric oxygen, *i.e.,* in

sulfides in the case of Mo. Pyrite and molybdenite are commonly invoked as the main Mo

sources that contain reduced, insoluble Mo (Anbar et al., 2007, Miller et al., 2011). When these sulfides break down in the presence of atmospheric O_2, the Mo becomes oxidized (and thereby soluble), and can be transported in solution as molybdate (MoO_4^{2-}) in rivers, and eventually the oceans. Once in the ocean, Mo is slowly removed through uptake by Fe-Mn oxides in oxygenated environments, or deposited in black shales within euxinic (high-S, low-O_2) environments. Archean and Proterozoic black shales have been analyzed for Mo and other redox-sensitive elements to track oxidative continental weathering; enrichments suggest oxidative weathering and/or the development of euxinic ocean basins (Turekian and Bertine, 1971; Helz, 1996; Erickson and Helz, 2000). High sulfur concentrations are required in the water column for Mo to be reduced and incorporated into Fe-Mo-S phases in reduced oceanic sediments (Helz, 1996; Erickson and Helz, 2000). Like Mo, sulfur was probably not abundant in the Archean oceans until atmospheric oxygen caused weathering of continental sulfides during the GOE (Canfield, 2005).

As observed by Gaschnig et al. (2014), Mo enrichments in black shales during and after the GOE are accompanied by contemporaneous Mo depletions in the UCC. The UCC Mo depletion, relative to the light rare earth elements of similar compatibility (Ce and Pr) first appears in the Paleoproterozoic and continues to the present day. These observations support the hypothesis that oxidative weathering of the continents played a role in removing Mo from the weathered continental crust and transporting it into ocean basins after the GOE.

The use of Mo to trace atmospheric O_2 and infer Precambrian oceanic chemistry is widely accepted in the paleo-atmospheric research community. However, using the Mo concentrations in euxinic sediments to quantify the pO_2 is based on the assumption that Mo is primarily concentrated in sulfides in the UCC, and that these sulfides will break down at a

rate that is proportional to $p\mathrm{O_2}$ (Anbar et al., 2007; Williamson and Rimstidt, 1994). While

Mo may behave as a chalcophile element in euxinic sedimentary and low-temperature

hydrothermal environments, its behavior during igneous differentiation and crust formation

is less well understood. Newsom and Palme (1984) suggested that Mo will behave

incompatibly during mantle melting, like Ce and Pr, and this is corroborated by the

observation that Mo is significantly enriched in the UCC (1.1 ppm; Rudnick and Gao, 2003)

relative to the primitive mantle (0.039 to 0.047 ppm; Greber et al., 2015 and Palme and

O'Neill, 2004, respectively). Moreover, Mo is observed to behave incompatibly during

differentiation of intraplate basalt magmas (Yang et al., 2015; Greaney et al., 2017).

Greaney et al. (2017) also showed that while Mo is present in magmatic sulfides (average

2.6 ppm), it is more abundant in basaltic to andesitic volcanic glasses (average 5 ppm) and

Fe-Ti oxides (average 6.4 ppm). However, the partitioning behavior of Mo in typical

continental crustal igneous rocks, such as granites, has not been systematically studied.

Here, we explore the partitioning of Mo in typical UCC granitic rocks, and

incorporate data published on Hawaiian basalts (Greaney et al., 2017), to determine whether

Mo is chalcophile, *i.e.,* concentrated primarily in sulfides in the igneous UCC. We present

in-situ data on Mo concentrations in various minerals as well as whole-rock data on Mo

abundances in granitic and basaltic rocks. Our goals are to determine the main mineralogical

hosts of Mo in the continental crust and to improve our understanding of the behavior of Mo

during crust formation and differentiation.

2.2 SAMPLES

Granitic rocks are considered to be representative of the felsic UCC, so granitic rocks

that span Earth's history form the focus of this study. Since Mo is thought to be generally

incompatible during igneous differentiation (Newsom and Palme, 1984), it is expected to be concentrated in more felsic rocks. Given the bimodal composition of the crust, and the hypothesis that the Archean crust may have been significantly more mafic than present-day UCC (e.g., Taylor and McLennan, 1985; Condie, 1993; Dhuime et al., 2015; Gaschnig et al., 2016; Tang et al., 2016), partitioning data from Hawaiian basalts (Greaney et al., 2017) and MORB (Jenner and O'Neill, 2012; Patten et al., 2013) are also considered. We were particularly interested in sampling Archean crust, because its Mo residence and weathering behavior is directly applicable to the GOE. When possible, we selected granitic rocks that retained igneous textures and mineralogy, with an aim of studying previously well-characterized samples. Archean and Proterozoic samples come from the Superior Province (Whalen et al., 2002; Whalen et al., 2003), Baffin Island (Whalen et al. 2012), the Zimbabwe craton (Luais and Hawkesworth, 1994), and the Barberton greenstone belt (Clemens et al. 2006). The majority of these samples are TTGs (tonalite-trondjhemite-granodiorite rocks) that contain higher sodium contents than the more potassic granites that dominate the Proterozoic and Phanerozoic. Additionally, due to the presence of residual rutile or ilmenite in lower-crustal residues and amphibole in mid-crustal residues (Hoffmann et al. 2011), TTG's are generally characterized by a depletion in the high field-strength elements (HFSE) Ti, Nb, and Ta. Complete sample descriptions and photomicrographs can be found in the supplementary materials.

2.2.1 Barberton TTGs (3.55 – 3.21 Ga)

Powdered samples of TTGs from the Barberton Greenstone Terrane were analyzed here for whole-rock compositions. No thin sections were available for *in-situ* work. Samples from four generations of plutons that represent distinct tectono-magmatic events were

studied: the 3.55-3.49 Ga Steynsdorp pluton; the 3.46-3.42 Ga Stolzburg, Doornhoek, Theespruit, and Erstehoek plutons; the 3.29-3.24 Ga Badplaas pluton; and the 3.24-3.23 Ga Nelshoogte pluton (Clemens et al., 2006; Moyen et al., 2007; Kröner et al., 1991). The Barberton Terrane is one of the most intensively studied suites of Archean TTGs in the world, and several interpretations have been developed to explain the petrogenesis of the TTGs and greenstone belts. A consensus has developed around the hypothesis that these plutons were emplaced during accretion of an exotic terrane and subsequent post-orogenic collapse (Clemens et al., 2006; Moyen et al., 2007).

2.2.2 Superior Province TTGs (3.0 – 2.7 Ga)

The TTGs from the Superior Province come from the North Caribou Terrane plutonic complex (~3.0 Ga; Whalen et al., 2003) and the Central Wabigoon sub-province (~2.7 Ga; Whalen et al., 2002). The North Caribou samples are mainly derived from the English Lake Plutonic Suite and range in composition from felsic tonalites and trondhjemites to amphibolitic and pyroxenitic xenolithic enclaves that may have originated as cumulates. Geochemical modeling suggests a genetic link between the cumulate enclaves and the TTGs, and an overall hydrous source for this suite. The younger Central Wabigoon samples are classified as granite to granodiorite and have a higher K_2O/Na_2O ratios than the North Caribou TTGs. This suite is thought to have formed from the partial melting of over-thickened lower crust during the collision of arcs, such as the one that potentially produced the North Caribou samples. Both whole-rock and *in-situ* data were collected for this suite. Three samples were sectioned for *in-situ* analysis. These are composed of quartz, plagioclase, K-feldspar, biotite, amphibole (primarily hornblende), titanite, Fe-Ti oxides, and minor muscovite and sulfides (Fig. 1), all of which were analyzed for Mo concentration.

2.2.3 Zimbabwe Craton TTGs (2.9 – 2.6 Ga)

The samples from the Zimbabwe craton are mainly tonalites from the 2.9 Ga

Mashaba suite, as well as two samples from the 2.6 Ga Chibi Granite. The Zimbabwe craton

is bounded by three belts that accreted between the Neoarchean Limpopo Belt and the

Neoproterozoic Zambezi and Mozambique Belts. The craton itself is composed of 2.8 – 2.5

Ga greenstone sequences and 3.5 – 2.9 Ga TTGs. Luais and Hawkesworth (1994, 2002)

outline a petrogenetic model that involves partial melting of a garnet-bearing amphibolite

and subsequent fractional crystallization to produce the TTG suites. In this model, the

Mashaba tonalite was formed by direct fusion products of basaltic proto-lower crust leaving

a garnet amphibolite residue. The late Chibi granite is interpreted to have been derived

through partial melting of greenstone mafic volcanic rocks (Hawkesworth et al., 1979).

Partial melting in the deeper part of a thick crust has been invoked to explain the formation

of these units (Hawkesworth et al., 1979; Luais and Hawkesworth, 1994 and 2002). Whole-

rock and *in-situ* data were collected for this suite, and data for major and trace elements

were previously published in Luais and Hawkesworth (1994). The four samples selected for

in-situ analysis are variably foliated and contain alteration products such as chlorite,

cummingtonite, epidote, and sericite. Common phases are quartz, plagioclase, K-feldspar,

biotite, hornblende, muscovite, titanite, Fe-Ti oxides, apatite, and zircon.

2.2.4 Baffin Island (1.88 Ga)

Whole-rock powders from the Qikiqtarjuaq Plutonic Suite (QPS) show the largest

compositional range of all suites studied here, varying from granodiorite/tonalite to gabbro

(Whalen et al., 2012). These intrusive bodies form a portion of the Cumberland batholithic

complex on Baffin Island. The origin of the QPS is uncertain, as it is a relatively newly

discovered and analyzed unit. However, U-Pb ages suggest that it is ~35 Myr older than the Cumberland Batholith (Rayner et al., 2012), which has been interpreted to be a Trans-Hudson Orogeny post-accretionary batholith, possibly resulting from a delamination event from the base of over-thickened crust (Whalen et al., 2010). Thus, it can be inferred that the QPS was emplaced at the initiation of an accretionary event, and may be arc-derived. Data for all major and trace elements were previously published in Whalen et al. (2012), but Mo concentrations were re-analyzed in this study using a more precise standard-addition technique. No thin sections were analyzed.

2.2.5 Phanerozoic Granites

Mesozoic granitic rocks from the Western USA (Gaschnig et al., 2011; 2017) and a Silurian granite from the Eastern US were analyzed as well. These include a garnet-bearing peraluminous granite from the Idaho batholith, a metaluminous tonalite from the Lookout Mountain pluton in the Blue Mountains (Oregon and Idaho, USA), and a Neo-Acadian epidote-bearing granodiorite (Ellicott City Granodiorite, Maryland, USA). These samples consist of common granitic minerals – abundant feldspar, quartz, biotite, and amphibole with accessory muscovite, titanite, epidote, magnetite, ilmenite, apatite, allanite, zircon, and sulfides (Fig. 1, see supplementary sample descriptions). Whole-rock and *in-situ* analyses of thin sections were carried out on these samples.

2.2.6 Kilauea Iki lavas

Data from the Kilauea Iki lava lake, Hawaii, reported in Greaney et al. (2017), are considered here for a more complete assessment of mineralogical hosts of Mo. The lava lake erupted in 1959 and is considered a prime natural laboratory for studying basaltic magma differentiation. Samples ranging through the entire differentiation suite from 43.7 to 57.1

wt% SiO$_2$ were subjected to whole-rock and *in-situ* analysis. The rocks contain olivine,

pyroxene (augite), plagioclase, Fe-Ti oxides, glass, and minor apatite and sulfides (Fig. 1).

Sample	Unit/ Pluton	Age, Ga	Rock type	Analysis	SiO$_2$	Mo (ppm)	2σ
Barberton							
NLG1	Nelshoogte	3.24-3.23	TTG	SA	70.1	0.34	0.01
NLG14	Nelshoogte	3.24-3.23	TTG	SA	NA	0.38	0.01
NLG15	Nelshoogte	3.24-3.23	TTG	SA	63.1	0.48	0.04
NLG25A	Nelshoogte	3.24-3.23	TTG	SA	71.1	0.32	0.02
BDP5A	Badplaas	3.29-3.24	TTG	SA	70.5	<0.16	-
BDP5C	Badplaas	3.29-3.24	tonalite dyke	SA	72.8	0.17	0.01
BDP8A	Badplaas	3.29-3.24	TTG	SA	74	0.18	0.01
EHK1	Eerstehoek	3.46-3.42	TTG	SA	72.4	<0.16	-
TH4A	Theespruit	3.46-3.42	TTG	SA	70.3	0.20	0.01
DNK1	Doornhoek	3.46-3.42	TTG	SA	74	0.23	0.01
STZ1	Stolzburg	3.46-3.42	TTG	SA	70.7	0.48	0.09
STZ17	Stolzburg	3.46-3.42	TTG	SA	71.6	0.34	0.09
STY1	Steynsdorp	3.55-3.49	TTG	SA	65.7	0.16	0.04
STY1 rep						0.14	0.01
STY3A	Steynsdorp	3.55-3.49	TTG	SA	72.9	0.16	0.05
STY4B	Steynsdorp	3.55-3.49	TTG	SA	75.1	<0.16	-
Zimbabwe							
Zb89-53	Chibi	2.7-2.6	granite	SA, LA	72	0.84	0.04
Zb89-57	Chibi	2.7-2.6	granite	SA	74.8	0.26	0.01
ZB89-10	Mashaba I	2.9	tonalite	SA, LA	71	0.25	0.02
ZB89-10 rep						0.13	0.01
ZB89-11	Mashaba I	2.9	tonalite	SA	67.3	0.07	0.02
Zb89-12	Mashaba I	2.9	tonalite	SA	69.4	0.14	0.01
Zb89-13	Mashaba I	2.9	tonalite	SA, LA	68.5	0.20	0.03
Zb89-15	Mashaba I	2.9	tonalite	SA, LA	70.5	0.13	0.02
Zb89-46	Mashaba I	2.9	tonalite	SA	70.1	0.07	0.02
Rh75-Mt7	Mashaba I	2.9	tonalite	SA	71.2	0.05	0.01
Superior							
WXP99-119	N. Caribou	2.999	tonalite	SA	63.7	0.16	0.01
WXP99-123	N. Caribou	2.999	tonalite	SA, LA	62.6	0.14	0.01
WXP99-138	N. Caribou	2.999	quartz diorite	SA	61.7	0.21	0.01
WXP99-176	N. Caribou	3.006	trondhjemite	SA, LA	72.1	0.32	0.02
WXP99-129	N. Caribou	2.999	tonalite	SA	62.5	nd	-
WXP 99-139	N. Caribou	NA	quartz diorite	SA	63.8	<0.10	-
WXP 99-143	N. Caribou	NA	quartz diorite	SA	60.7	<0.10	-
WXP 99-143 rep						0.11	0.01
WXP 99-145	N. Caribou	2.992	gabbro enclave	SA	49.3	0.90	0.05
PBA99-2064c	N. Caribou	NA	gabbro enclave	SA	46.1	<0.10	-

PBA99-2072c	N. Caribou	NA	amph-lite encl.	SA	50.1	0.13	0.02
PBA99-2072e	N. Caribou	NA	pyx-ite encl.	SA	45.2	0.17	0.02
PBA97-23	C. Wabigoon	2.722-2.709	granite	SA, LA	71.3	0.32	0.02
PBA97-319	C. Wabigoon	2.722-2.709	granodiorite	SA	69.6	0.17	0.01
Baffin Island							
10SRB-Y199B-01	QPS	1.88	quartz gabbro	SA	50.3	2.91	0.49
10SRB-Y201A-02	QPS	1.88	granodiorite	SA	64.2	2.27	0.38
10SRB-Y202A-01	QPS	1.88	syenogranite	SA	70.6	0.53	0.09
10SRB-Y204A-02	QPS	1.88	monzogranite	SA	67.3	0.60	0.10
10SRB-M295A-01	QPS	1.88	monzogranite	SA	72.3	0.11	0.02
10SRB-R301A-01	QPS	1.88	granodiorite	SA	65.1	2.10	0.35
Phanerozoic							
AG1401	Ellicott City Gd.	460 Ma	granodiorite	SA, LA	61.6	0.17	0.02
07RMG52	Idaho Bath.	80 Ma	granite	SA, LA	74.5	0.45	0.02
10RMG005	Lookout Mtn	124 Ma	tonalite	SA, LA	65.7	0.19	0.02
Kilauea Iki							
Iki 58	Hawaii OIB	50 yr	pumice	SA	49.9	1.13	0.27
Iki 22	Hawaii OIB	50 yr	pumice	SA	46.7	0.94	0.22
Iki3	Hawaii OIB	50 yr	pumice	SA	47.2	2.19	0.52
67-2-85.7	Hawaii OIB	50 yr	basalt-andesite	SA	56.2	4.55	1.07
67-3-6.8	Hawaii OIB	50 yr	basalt	SA	44.6	0.71	0.17
67-3-27.5	Hawaii OIB	50 yr	basalt	SA	48.6	1.14	0.27
67-3-75.2	Hawaii OIB	50 yr	basalt	SA	50.1	2.04	0.48
67-3-76.2	Hawaii OIB	50 yr	basalt-andesite	LA	50.8	nd	-
75-1-38.9	Hawaii OIB	50 yr	basalt	SA	48.4	1.03	0.24
75-1-121.5	Hawaii OIB	50 yr	basalt-andesite	SA	50.0	1.33	0.31
75-1-130.5	Hawaii OIB	50 yr	basalt	LA	49.7	nd	-
75-1-134.4/133.4	Hawaii OIB	50 yr	olivine basalt	SA, LA	48.9	1.42	0.34
79-1R1-170.9	Hawaii OIB	50 yr	basalt-andesite	SA, LA	54.6	3.61	0.85
79-3-150.4	Hawaii OIB	50 yr	olivine basalt	SA, LA	48.4	1.03	0.24
79-3-158.0	Hawaii OIB	50 yr	basalt-andesite	SA, LA	52.4	2.30	0.54
79-3-160.6/160.3	Hawaii OIB	50 yr	olivine basalt	SA, LA	47.4	0.91	0.21
79-3-171.9/172.8	Hawaii OIB	50 yr	olivine basalt	SA, LA	46.6	0.85	0.20

81-2-88.6	Hawaii OIB	50 yr	basalt-andesite	SA, LA	57.1	4.70	1.11
81-1-119.2	Hawaii OIB	50 yr	basalt-andesite	SA	50.6	1.00	0.24
81-1-169.9	Hawaii OIB	50 yr	olivine basalt	SA	43.7	0.95	0.22
81-1-210.0/209.8	Hawaii OIB	50 yr	olivine basalt	SA, LA	44.9	0.57	0.14
81-1-239.9	Hawaii OIB	50 yr	olivine basalt	SA	44.2	0.56	0.13
81-1-294.7	Hawaii OIB	50 yr	olivine basalt	SA, LA	48.1	0.72	0.17

Table 2.1 Sample descriptions and Mo abundances for the samples studied here.

secondary standard	analysis	Mo (reported)	Mo 95 measured	2s	Mo 97 measured	2s	Mo 98 measured	2s	n
BHVO-2g	LA	3.8	4.09	0.86	4.07	1.15	4.03	1.16	89
NIST 612	LA	37.4	43.6	16.2	40.4	14.0	44.1	7.89	8
JB sulfide	LA	2.55	2.44	0.30	2.45	0.69	2.44	0.20	8
BHVO-1	SA	1.1*	1.17	0.34	1.19	0.33	1.17	0.34	8
AGV-2	SA	1.93*	1.94	0.13	1.93	0.1	1.92	0.07	5

values from Gaschnig et al., 2015

Table 2.2 Secondary standard in-situ and solution data
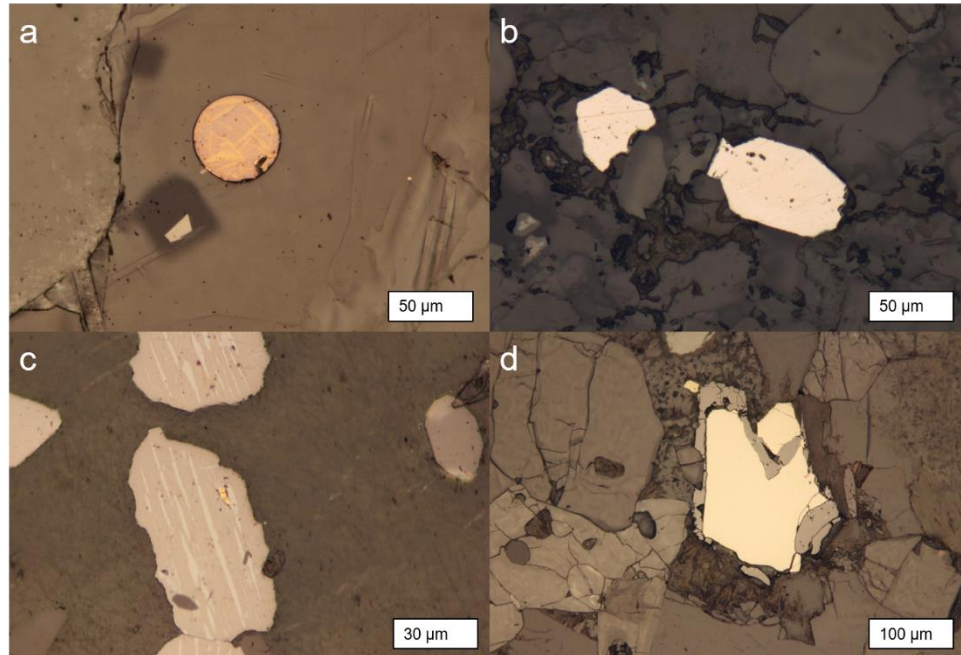
Figure 2.1. Photomicrographs of sulfides targeted for laser ablation analysis. A) Immiscible sulfide bleb from the Kilauea Iki lava lake (KI67-3-76.2) showing needle-like exsolution textures. A second minute (≤1 µm diameter) sulfide is visible on the right. B) Pyrite from the Archean Superior province tonalite (WXP99-119). C) Small chalcopyrite inclusion (yellow) hosted in magnetite having ilmenite exsolution from a Mesozoic granite (10RMG005). D) Pyrite rimmed by magnetite from the Paleozoic Ellicott City Granodiorite (AG1401).

2.3 METHODS

The methods follow those of Greaney et al. (2017) and Gaschnig et al. (2015), and are reproduced here in detail in the supplementary material. Whole-rock trace element analyses were carried out by standard-addition solution inductively coupled plasma mass spectrometry (ICP-MS). Samples were dissolved in high pressure PTFE bombs using HF/HNO3, then three aliquots were spiked with variable known amounts of Mo using spikes created by Gaschnig et al. (2015). This method produces a calibration curve from the sample itself, instead of having to extrapolate a calibration curve from external standards, which could induce errors associated with the extrapolation and improperly calibrated standards. The sample aliquots were analyzed on an Element2 HR-ICP-MS at the University of

67

Maryland in MR and LR mode for three isotopes of Mo (95, 97, and 98). The limit of detection (LOD) ranged from 0.03 ppm to 0.10 ppm for most analytical sessions. However, it was as high as 0.16 ppm during analyses of the Barberton suite TTGs. The variable LOD is reflected in Table 1. The reported Mo abundances for the three isotopes never varied by more than the reported RSD calculated from the counting statistics. USGS standard reference rock powders AGV-2 and BHVO-1 were dissolved alongside each batch of samples and run as secondary standards (Table 2). AGV-2's external reproducibility results in a 2RSD of 7%. BHVO-1 (2RSD ~ 25%) is notoriously difficult to reproduce (Willbold et al., 2016; Gaschnig et al. 2015), possibly due to heterogeneities in the sample powder.

In addition, to demonstrate the robustness of measuring low-Mo abundances with the standard addition method, three low-[Mo] TTGs from different suites were re-dissolved and analyzed by isotope dilution at the Arizona State University Keck Biogeochemistry Lab. Two of the three samples show excellent reproducibility, while the isotope-dilution data gave even lower Mo abundances for the third sample, ZB89-10 (0.13 ppm by ID vs. 0.25 ppm by standard addition). This discrepancy may reflect a slightly heterogeneous powder due to nuggets of a Mo-rich phase, given that mass balance was not achieved for this sample (see section 4.1.3 and Table S4), and a Mo-rich phase was observed within magnetite of another sample from this same TTG suite (see section 4.1.1). These replicate data are reported in the online supplement. Additionally, for most plutonic suites, a full suite of trace elements were analyzed, including Ga, Ge, Cd, In, Sn, Sb, W, Tl, and Bi. These data are provided in the supplementary materials.

In-situ mineral data were collected using electron probe microanalysis (EPMA) followed by laser ablation ICP-MS using a New Wave UP-213 nm laser attached to an

Element2 HR-ICP-MS at the University of Maryland and a Photon Machines 193 nm laser attached to an Agilent 7700x Quadropole ICP-MS at the University of California Santa Barbara. NIST-610 was the external standard, and the glasses BHVO-2g and NIST-612, as well as a synthetic Mo-bearing sulfide produced by James Brenan (formerly at the University of Toronto, now at Dalhousie University) were analyzed as secondary standards (Table 2). Spot-sizes ranged from 25 µm (for smaller sulfides) to 80 µm (for silicates and larger sulfides). Three isotopes of Mo were measured (95, 97, and 98), with all returning values that fell within the error calculated by counting statistics, except when an obvious interference was present (e.g., $^{55}Mn^{40}Ar$ on ^{95}Mo in garnet). Abundances of ^{98}Mo are therefore reported for the *in-situ* data. The LOD for *in-situ* Mo analyses ranges were typically ~0.01 ppm, however they occasionally ranged as high as 0.1 ppm, depending on the analyte/background ratio of the instrument that day. The LA-ICP-MS data were processed using Iolite (Paton et al. 2011).

2.4 RESULTS

2.4.1   In-situ data

2.4.1.1 Sulfides

A total of 78 sulfide grains were analyzed from the Phanerozoic granites, TTGs, and several evolved samples from the Kilauea Iki lava lake, Hawaii. Pyrite, chalcopyrite, and pyrrhotite are present in the granitic samples while the sulfide blebs in the Kilauea Iki lavas form solid solutions between isocubanite and bornite (see Greaney et al., 2017 for analyses). The sulfides are volumetrically insignificant (<1 vol. %) in all of the analyzed samples, and, for most samples, did not register in mineral modes determined by point counting (see the mass balance table in the supplement).

Molybdenum concentrations (designated as [Mo]) in accessory sulfides vary by approximately three orders of magnitude (0.01 ppm to 9.2 ppm). The maximum [Mo] is found in the Kilauea Iki lava-hosted sulfides (mean [Mo]$_{\text{Kilauea sulfides}}$ = 2.7 ppm, max = 9.2 ppm) while the granite-hosted sulfides contain significantly less Mo than those from Kilauea Iki (mean [Mo]$_{\text{granite sulfides}}$ = 0.72 ppm, max = 8.0 ppm, Fig. 2), but have similar concentrations to MORB-hosted sulfides (Patten et al., 2013). Molybdenite was not found as an accessory phase in any sample, but one grain of magnetite in a TTG from the Zimbabwe craton (ZB89-53) contains significant Mo (~1300 ppm), along with Pb and other chalcophile elements. This suggests that a small nugget of MoS_2, or similar phase, may have been embedded within or beneath the magnetite grain, but was not visible on the surface. This analysis was excluded from the magnetite data presented in Fig. 2 and Table 3.

2.4.1.2 Silicates and Oxides

In addition to sulfides, quartz, K-feldspar, plagioclase, biotite, muscovite, hornblende, titanite, garnet, allanite, zircon, epidote, chlorite, olivine, clinopyroxene (augite), volcanic glass, magnetite, ilmenite, rutile, and the rare accessory phase columbite (also called niobite) were all analyzed for their Mo abundances (Table 3). The mean data presented in this table also include analyses that were below the LOD in plagioclase, K-feldspar, biotite, amphibole, muscovite, sulfides, epidote, and quartz. In these cases, the lower LOD commonly calculated for these analyses (0.01 ppm) was used to calculate the mean [Mo] value. Thus, the average concentrations for these phases should be considered maxima. Collectively, these data encompass nearly every major mineral found in common igneous rocks. Most phases were analyzed repeatedly across several rock types and localities except

for columbite/niobite, which is confined to a single crystal in a Phanerozoic granite (07RMG52).

Molybdenum concentrations are presented in box and whisker plots in Figure 2 with the phases arranged from highest to lowest [Mo], as established by the median [Mo] value. Molybdenum concentrations are considered to be significant if they are greater than 1 ppm (average UCC [Mo] = 1.1 ppm; Rudnick and Gao, 2014). Titanite consistently contains significant Mo, except for one sample from the Superior Province (WXP99-176), in which titanite contained between 0.01 and 0.5 ppm. Metamorphic rutile replaced part of the titanite in that sample and may have preferentially incorporated Mo into its lattice, removing it from the titanite. Excluding this sample, [Mo] in titanite is commonly >30 ppm. Ilmenite and magnetite are the other two common phases that routinely contained ≥ 1 ppm Mo in both granitic and basaltic samples. Rutile and columbite/niobite are less common upper crustal minerals, but they were found as primary igneous and secondary metamorphic assemblages in some samples and contain significant Mo. Volcanic glass was also found to be a significant host of Mo in the Kilauea samples where the average Mo_{glass} concentration is 4.8 ppm. Glass data from ~600 MORB samples (Jenner and O'Neill, 2012) are shown for comparison, and have an average [Mo] of 0.62 ppm, which is significantly lower than KI glass because MORB has lower whole-rock [Mo], and many of the KI lavas are more evolved than MORB. Most of the minerals analyzed do not contain abundant (>1 ppm) Mo, including the most common minerals in granitic and basaltic rocks: quartz, feldspars, biotite, amphibole, olivine, and pyroxenes. Sulfides are found near the middle or right-hand side of each plot in Fig. 2, reflecting their generally low [Mo], relative to other minerals. Sulfide

data from MORB (Patten et al., 2013) are shown for comparison to OIB sulfides on the plot

of basaltic minerals.
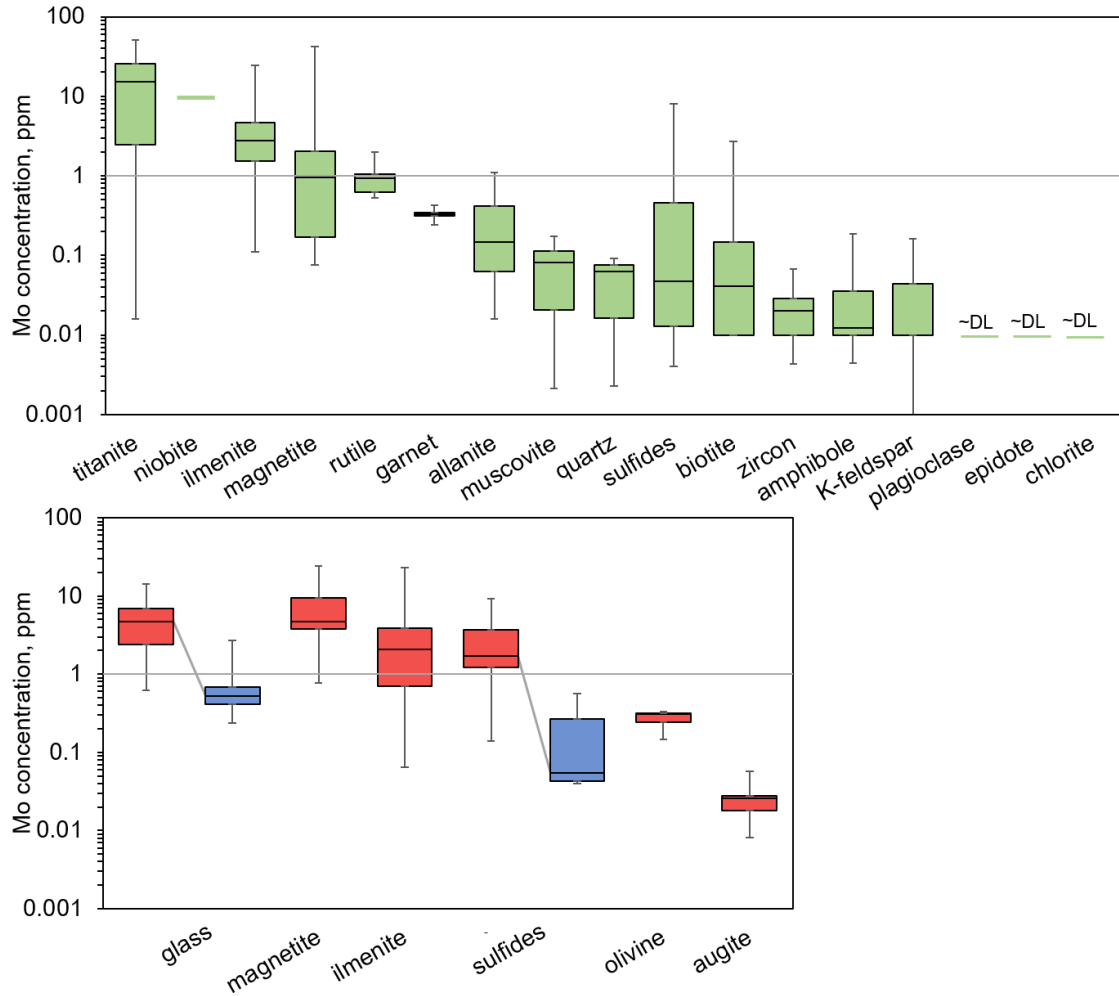
Figure 2.2. Box and whisker plots of Mo abundances in all the minerals analyzed. Minerals are arranged by their median [Mo], with the boxes representing 1st and 3rd quartiles and whiskers representing min and max values measured. Upper plot: Granitic minerals from the Zimbabwe craton, Superior Province, and Phanerozoic granitic rocks. Plagioclase, epidote, and chlorite analyses were often below the detection limits. Lower plot: Minerals in basaltic to intermediate lavas from Kilauea Iki (red; data from Greaney et al., 2017) and MORB (blue; glass data from Jenner and O'Neill, 2012, sulfide data from Patten et al., 2013).

2.4.2   Mass Balance

   Mineral modes were determined for the samples using a least-squares regression program, MINSQ (Herrmann and Berry, 2002). Select samples were also point counted to ensure accuracy of the MINSQ program (supplementary materials). The modal abundances are used together with the measured Mo concentrations to calculate the primary location of Mo (Fig. 3; mass balance provided in supplementary materials). Given their scarcity, sulfides were not registered in point counting exercises, so they were assigned modal abundances of 0.01% to 0.1%, which are likely to be overestimates in most samples. Nevertheless, in most samples the sulfide [Mo] contributes less than 3% of the whole-rock [Mo]. The maximum sulfide Mo contribution occurs in the Kilauea Iki volcanic rocks, where sulfides contain up to 6% of the total whole-rock [Mo]. By contrast, titaniferous phases are the dominant hosts of Mo in granitic rocks. Silicates can also contribute a significant portion of the total Mo budget (e.g., ~25% in one sample, Fig 3), given their volumetric significance in granites. The calculated Mo distribution results in $[Mo]_{whole\ rock, calculated}$ that can be compared to measured whole rock data and $[Mo]_{whole\ rock, measured}$, to see if a mass balance is attained.

   Given analytical uncertainties on the standard addition, laser ablation, and modal mineralogy measurements, we consider that mass balance is achieved if the calculated whole-rock abundance is within 20% of the measured whole-rock value. Of the ten granitic samples evaluated, mass balance is attained in only six. The remaining four are missing anywhere between 60 and 80% of the expected Mo abundance, based-on the whole-rock [Mo] measured by standard addition ICP-MS. All thin sections were carefully examined to

73

ensure that no phase was missing from *in-situ* analysis. The incomplete mass balance is

probably a real phenomenon, and is discussed further below.

	Titanite	Niobite	Magnetite	OIB Glass	Ilmenite	Sulfides	Rutile
Mo (ppm)	15.9	9.83	5.83	4.83	4.09	1.44	0.95
2σ	27.2	n/a	17.5	5.58	11.2	4.09	0.86
n	59	1	36	101	53	78	10
	Garnet	**Allanite**	**Biotite**	**Olivine**	**Muscovite**	**Quartz**	**Hornblende**
Mo (ppm)	0.33	0.32	0.15	0.10	0.08	0.05	0.04
2σ	0.09	0.66	0.85	0.15	0.13	0.06	0.10
n	12	23	41	5	9	25	36
	K-spar	**Augite**	**Zircon**	**Plagioclase**	**Epidote**	**Chlorite**	
Mo (ppm)	0.03	0.02	0.02	≤0.01	≤0.01	≤0.01	
2σ	0.08	0.02	0.03	0.03	0.01	n/a	
n	24	5	21	37	19	1	

Table 2.3 Mean Mo abundances in minerals
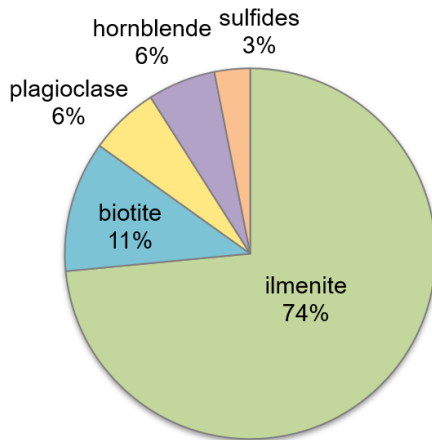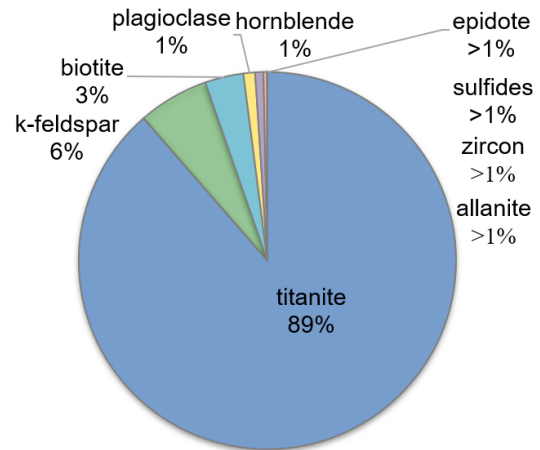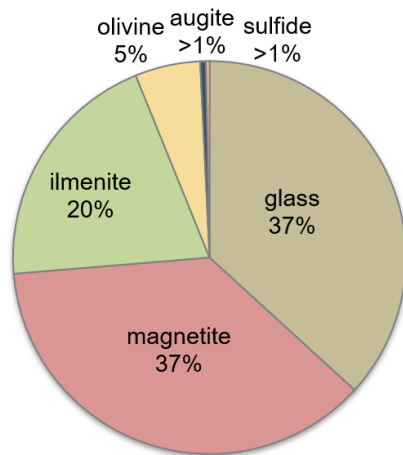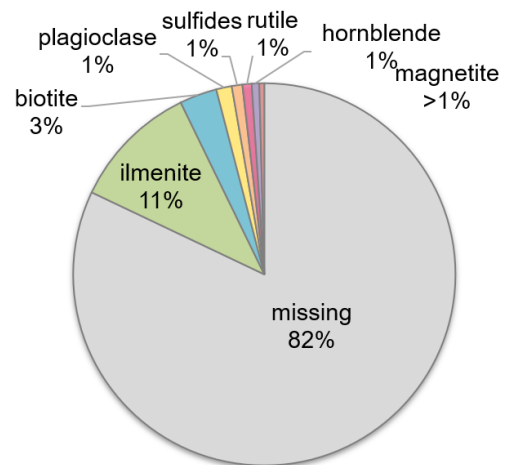
Figure 2.3. Pie charts depicting the total Mo distribution in four samples selected to show variation in major host minerals. Mass balance is achieved in three of the samples depicted (a,b,c), but 82% of the whole-rock [Mo] is missing from sample d. Sample numbers: A) WXP99-123 B) AG1401 C) KI67-3-76.2 D) 10RMG005.

2.4.3   Whole-rock data

Whole-rock [Mo] data are presented in Table 1 and a complete dataset, including major and trace elements (including Ga, Ge, Cd, In, Sn, Sb, W, Tl, and Bi), is presented in the online supplement. Almost all granitic rocks analyzed contain less than 1 ppm Mo, except for three samples from Baffin Island. Several Kilauea Iki samples (data presented in Greaney et al., 2017) contain more than 1 ppm because they are derived from an enriched

mantle source and evolved further than most MORB, without Mo fractionation on a whole-rock scale.

2.4.4 Data representation

During mantle melting and igneous differentiation, Mo is expected to have similar partitioning behavior to the LREE, specifically Ce and Pr given their comparable ionic radii (Newsom and Palme, 1984). Therefore, Mo concentrations are plotted between these two elements on modified multi-element plots (Fig. 4) that have been normalized to the upper continental crust values of Rudnick and Gao (2014). In addition to LREE, Nb is included to indicate whether a sample has a Nb depletion (UCC normalized Nb/La < 1) that may be induced by Ti-oxide fractionation in the subducting slab or during differentiation. The majority of analyzed granitic rocks analyzed are depleted in Mo, relative to Ce and Pr. Only nine of the 45 samples show either a smooth LREE-Mo profile with no depletion, or are enriched in Mo. Given the normalized values for Ce and Pr, an expected Mo value (Mo*) can be calculated as $([Ce]_n \times [Pr]_n)^{0.5}$ where "n" means normalized to the UCC value of Rudnick and Gao (2015). The percentage of Mo "missing" from a given sample can then be calculated as $100 \times (Mo^* - Mo_{meas})/Mo^*$. Between 20 and 90% (with a mean of 60%) of Mo is missing from the 36 samples that show Mo depletion, which equates to between 0.04 and 2.0 ppm, depending on the sample. Details regarding the Mo* calculation can be found in the supplement.

2.5   DISCUSSION

2.5.1 Mineralogical Hosts of Mo

In igneous rocks, Mo is not primarily hosted in accessory sulfide minerals such as pyrite, pyrrhotite, and chalcopyrite. This is most probably due to the relatively oxidized nature of

77

magmas, in which Mo exists in its hexavalent state (O'Neill and Eggins, 2012), making the formation of MoS_2 rare. We conclude that Mo does not behave as a chalcophile element in primary magmatic settings, because it is not sufficiently reduced to be incorporated into a sulfide phase without the presence of abundant reduced sulfur. This contrasts with the behavior of Mo in the low-T epithermal systems that are commonly associated with pluton cooling, in which Mo^{6+} is reduced by H_2S in the exsolving fluids to form molybdenite (Hannah et al., 2007).

The most important Mo-bearing phases in the igneous rocks analyzed here are titanite ($[Mo]_{mean} = 15.9$ ppm), magnetite ($[Mo]_{mean} = 5.83$ ppm), ilmenite ($[Mo]_{mean} = 4.09$ ppm), and glass ($[Mo]_{mean} = 4.83$ ppm) (Fig. 2). Columbite ($FeNb_2O_6$) is also a significant Mo host in one sample from the Idaho batholith, but this is an uncommon mineral. As pointed out above, octahedrally coordinated Mo^{6+} has a similar ionic radius to octahedrally coordinated Ti^{4+} (73 and 74.5 pm, respectively; Shannon, 1976), which occurs in ilmenite, titanite, and rutile. Likewise, the ionic radius of tetrahedral Mo^{6+} is similar to tetrahedral Ti^{4+} (55 and 56 pm, respectively), which occurs in pseudobrookite (a common oxide mineral in the KI lavas) and other titaniferous spinel-group minerals. A coupled substitution with a divalent cation is needed to maintain electrical neutrality when hexavalent Mo replaces tetravalent Ti. This could be achieved by substitution of Fe^{2+} (ionic radius of 75 pm) into octahedrally coordinated sites. In pseudobrookite, for example, an additional mole PFU of Fe^{2+} replacing Fe^{3+} for each mole of Mo replacing Ti would satisfy charge balance.

Other minor Mo hosts include silicates such as garnet ($[Mo]_{mean} = 0.33$ ppm) and biotite ($[Mo]_{mean} = 0.15$ ppm). These results generally agree with those of Voegelin et al. (2014) who found that biotite has the highest Mo abundance of any silicate analyzed in their

78

study, which also included analyses of feldspars, hornblende, olivine, and pyroxenes ([Mo]$_{biotite,Voegelin}$=0.67 ppm), while feldspars contained less than 0.1 ppm. Although these silicates have low Mo concentrations, their high volumetric abundances may contribute significantly to total crustal Mo abundances, as up to 25% of the total whole-rock Mo is attributed to silicates in one tonalite from the Superior Province (Fig. 3). Moreover, these phases are relatively easily altered, compared to the titaniferous phases, and will act as a source of Mo during continental weathering.

Molybdenite (MoS$_2$) was not observed in any of the samples analyzed here, but we propose that very small grains of MoS$_2$ could complete the mass balance in some samples. While it is relatively rare for it to occur as an accessory phase in granites, molybdenite, which contains 60% Mo by weight, is a highly-concentrated source of Mo in the crust, and occurs as a fairly common ore mineral that forms during epithermal processes associated with the emplacement of granitic plutons. Since it is so Mo-rich, an exceedingly small 'nugget' of MoS$_2$ (e.g., <0.0004 vol. % of a thin section) could complete the mass balance in samples that show deficits between calculated and measured whole-rock [Mo]. While uncommon, MoS$_2$ inclusions in quartz have been documented in felsic igneous rocks (Audétat et al., 2011).

2.5.2   *Mo behavior during magmatic differentiation*

2.5.2.1 <u>Mo depletion in granites</u>

Depletion of Mo relative to Ce and Pr is observed in every granitic suite analyzed here, with most of the samples (36 out of 45) exhibiting Mo depletion. The depletion is evident whether the data are normalized to primitive mantle (McDonough and Sun, 1995) or UCC values (Rudnick and Gao, 2014), and is especially stark when compared to MORB and

Kilauea Iki data, in which Mo has a similar or higher normalized abundance to the LREE

(Fig. 4), as predicted by Newsom and Palme (1984). Additionally, recently published Mo

data for granites from the Lachlan Fold Belt also show an UCC-normalized Mo depletion in

the majority of samples for which published Ce data could be located (Yang et al., 2017, and

references therein). The widespread depletion of Mo in granitic rocks may be due to the

following two processes, which are not mutually exclusive: a) Mo could be lost from an

evolving magma to a fractionating titaniferous phase such as rutile or Fe-Ti oxides (Kuroda

and Sandell, 1954; Fitton, 1995; Audétat et al., 2011), or b) Mo could be lost to a magmatic

vapor phase (MVP) exsolved from a cooling pluton (Candela and Holland, 1984; Audétat,

2010; Audétat et al., 2011). We also propose that S-type granites may show Mo depletion

because their source (detrital sediments from oxidatively weathered sources) are depleted in

Mo (per Gaschnig et al., 2014). However, with the exception of sample 07RMG52, the

granitic rocks analyzed here are not proper S-type granites as determined by mineralogy and

Aluminum Saturation Index, so this hypothesis does not apply to our data. The hypothesis

that Mo is removed during crystal fractionation/accumulation in residual phases is evaluated

by determining whether Mo depletion correlates with Nb depletion in the pluton suites,

while MVP exsolution is evaluated by examining correlations between Mo and other fluid-

soluble elements.
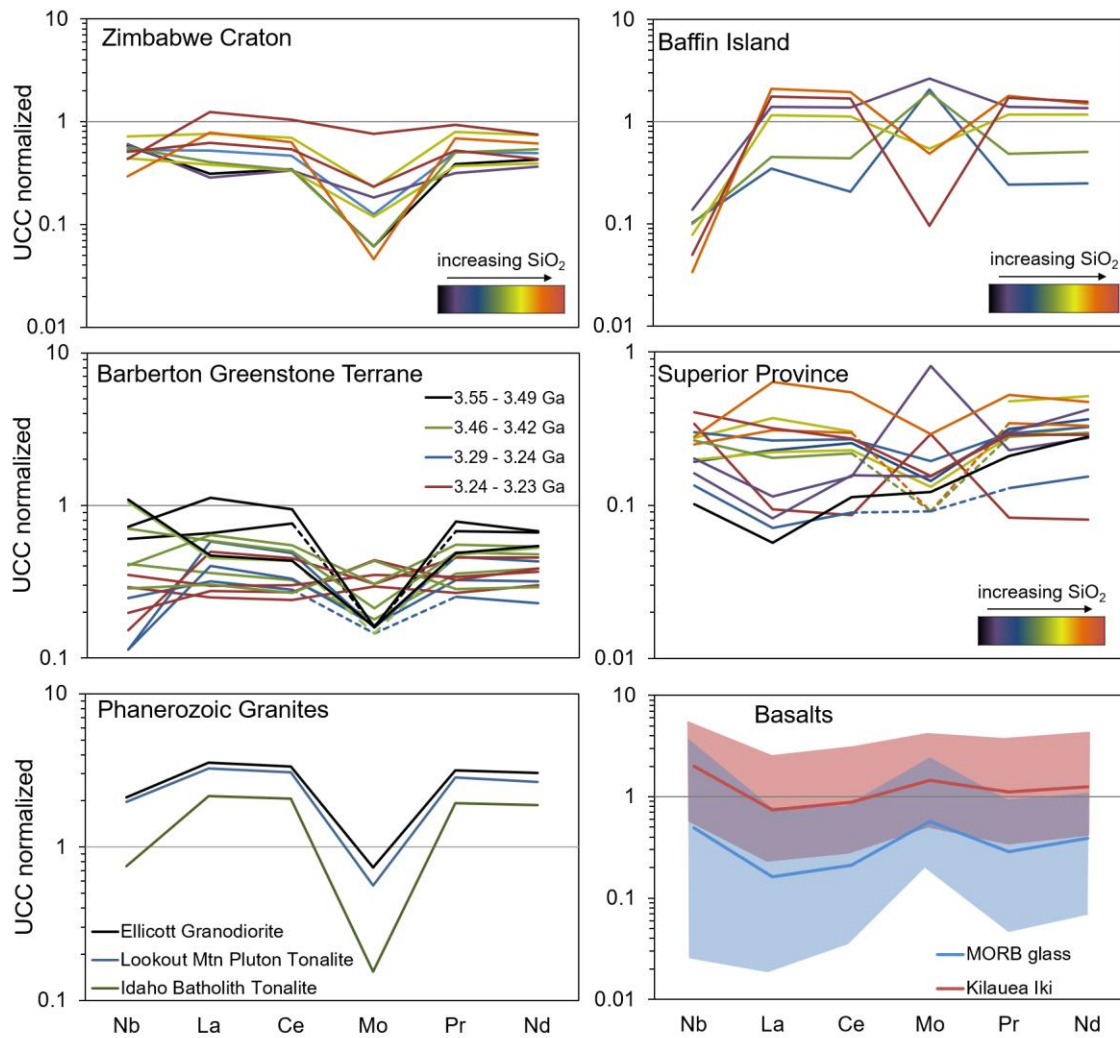
Figure 2.4. UCC normalized spider plots showing Mo behavior relative to LREE in granitic suites (and their associated mafic enclaves/gabbros in the Superior and Baffin Island samples), and modern basalts. The differentiation suites from Zimbabwe, Baffin Island, and Superior Province are defined with a gradient color scale (note the SiO_2 range varies for each suite with black and purple representing mafic or intermediate samples). Dashed lines indicate that Mo was below the detection limit in that sample, so the detection limit is used as the [Mo] value (see Table 1). All data are normalized to the UCC (Rudnick and Gao, 2014). Baffin Island data, except for Mo abundances, come from Whalen et al. (2012). The Kilauea Iki field represents twenty samples (Greaney et al., 2017) and the MORB field represents ~600 glass samples from Jenner and O'Neill (2012), with the mean values for both datasets shown with a line.

81

2.5.2.2 <u>Hypothesis 1: Loss of Mo due to partitioning into titaniferous phases</u>

Within this first hypothesis, we propose two processes that may inhibit Mo from reaching the upper crust: 1) Mo-loss could be due to fractionation of titaniferous phases (e.g., ilmenite, magnetite, rutile, titanite) during igneous differentiation, and/or, 2) In arc settings, Mo could be retained in residual rutile in a subducting slab, like Nb. These are both likely explanations for the Mo depletion given the observed affinity that Mo has for rutile (Fitton, 1995; Zack et al., 2002) and other Ti-bearing phases like ilmenite and magnetite (Arnorsson and Oskarsson, 2006; Audétat, 2010; Greaney et al., 2017; this study), and they are not mutually exclusive. Titanite, a major host of Mo in most of the titanite-bearing samples analyzed here, could also potentially play a role in removing Mo and Nb as well (Marks et al., 2008), although it crystallizes relatively late in a cooling magma. A correlation between Mo/Ce and Nb/La is observed in several of the plutonic suites analyzed here (Fig. 5), suggesting that fractionation into Fe-Ti oxides during differentiation may remove these elements from an evolving magma. This process may sequester Mo and Nb in lower- or mid-crustal cumulates.

The Baffin Island Qikiqtarjuaq Plutonic Suite is an excellent example of differentiation from gabbro to granite. It exhibits a strong correlation between Mo/Ce and Nb/La ($R^2 =$ 0.92, Fig 5) suggesting that Mo and Nb share the same geochemical behavior as the magma evolved. All Baffin Island samples have an UCC-normalized Nb/La ratio <1, suggesting that Nb was initially sequestered in rutile during subduction and mantle melting. The differentiation suite also displays a negative correlation between Nb and SiO_2 ($R^2 = 0.81$) and a negative correlation between Mo/Ce and SiO_2 ($R^2 = 0.75$) over a range from 50.3 to 72.3 wt% SiO_2, suggesting that both elements were removed by crystal fractionation, instead

of behaving incompatibly (Fig. S2). In this plutonic suite, Nb was most likely held in residual rutile, and was then further sequestered in fractionating Fe-Ti oxides, along with Mo, during differentiation (Figs. 4 and 5). The Mo enrichments in the more mafic to intermediate samples may reflect an overabundance of these Mo-bearing minerals relative to the more evolved rocks. This decrease in Mo with differentiation contrasts with observations of Mo increase during differentiation at Hekla volcano, Iceland (Yang et al., 2015) and at Kilauea Iki, Hawaii (Greaney et al., 2017). There appears to be a correlation between Mo/Ce and Nb/La in the Superior Province samples as well (Fig. 5, R^2=0.89), although this strong correlation is achieved by ignoring an apparent outlier in the data. The Mashaba tonalities from the Zimbabwe Craton show a much weaker correlation between Nb/La and Mo/Ce (R^2=0.34) and Ti/Gd and Mo/Ce (R^2=0.42). However, it should be noted that the degree of differentiation in the Zimbabwe tonalites is much less than that observed in other samples and that these samples have been interpreted to represent nearly pure partial melts of a basaltic source without significant fractional crystallization (Luais and Hawkesworth, 1994). Nevertheless, there is a strong correlation between Nb/Ta and SiO_2 in the Zimbabwe data, suggesting that a Ti-bearing phase (e.g., titanite) is being removed from this system during differentiation, but either is not taking Mo with it, or the fractionation signature is overprinted by another process (Fig. S3). We have insufficient data on Phanerozoic granites to draw conclusions about magmatic differentiation for those samples.

Molybdenum isotope studies also support the hypothesis that Mo is partitioned into fractionating Ti-bearing phases. Based on the data in Voegelin et al. (2014), Yang et al. (2017) propose that sequestration of Mo-bearing phases (they suggest biotite and hornblende) in the lower crust may explain the heavy δ^{98}Mo isotope signature observed in

UCC rocks relative to basalts. Additionally, Wille et al. (2018) suggest that Mo isotopes may be fractionated during crystallization of amphibole or clinopyroxene in arc settings. Overall, a net isotope fractionation is observed between average UCC felsic rocks (~ +0.15‰; Willbold and Elliott, 2017) and MORB (~ 0.0‰; Liang et al., 2017; Bezard et al., 2016) and OIB (~ -0.14‰; Liang et al., 2017), suggesting that not only [Mo] but also Mo isotopes may be fractionated during igneous differentiation (Voegelin et al., 2014; Yang et al., 2017; Liang et al., 2017; Greber et al., 2015; Wille et al., 2018). By contrast, other studies show that Mo abundances and isotopes are not significantly fractionated by differentiation processes in intraplate and arc settings (Yang et al. 2015; Gaschnig et al., 2017).

Alternatively, many researchers have proposed that Mo abundances (Fitton, 1995) and isotopes may be fractionated during dehydration and partial melting of the subducting slab in arc settings (Willbold and Elliott, 2017; König et al., 2008). Specifically, Fitton (1995) observed that a coupled Mo and Nb depletion in arc magmas may represent sequestration of these elements in rutile in the subducting slab. Experimental work of Bali et al. (2012) found that at the Ni-NiO buffer, Mo is retained in rutile relative to slab fluids, adding credence to this hypothesis. While sulfides are not found to be major hosts of Mo in granites, Skora et al. (2017) demonstrated experimentally that sulfides and rutile can fractionate Mo during sediment/slab melting in a subduction zone, given sufficiently reducing conditions. This study did not measure Mo abundances in the sulfides or rutile, so partition coefficients are unknown. However, Zack et al. (2002) found that Mo is significantly enriched in rutile relative to sulfide minerals in eclogites and therefore conclude that sulfides contribute less than 5% of the total eclogite Mo budget. Audétat (2010) suggested that Mo may be

84

sequestered in monosulfide solid solution (MSS) during partial melting (e.g., of slab/sediment) and igneous differentiation, given the measured $D^{MSS/melt} \sim 80$. However, a recent study of sulfide-saturated arc lavas found no Mo depletion after the onset of sulfide saturation during differentiation (Jenner, 2017). Instead, Mo is seemingly enriched in the resulting sulfide-depleted magmas. Further studies of Mo in magmatic differentiation suites and in subduction zones are needed to determine which exact phase/s, if any, is/are responsible for elemental and isotopic fractionation.

2.5.2.3 Hypothesis 2: Mo loss during fluid exsolution

As outlined by Audétat (2010) and Audétat et al. (2011), it is likely that Mo is lost from granites due to exsolution of aqueous magmatic fluids or vapor phases, because experimental studies show that Mo is partitioned into these phases (Candela and Holland, 1984; Zajacz et al., 2017). Partition coefficients ($D^{fluid/melt}$) vary due to the nature of different ligands (e.g., Cl, F) and salinity, but typically range from $D = 1$ to $D = 20$ (Zajacz et al., 2008). Molybdenum loss during aqueous fluid exsolution would probably lead to the saturation of molybdenite (MoS_2) in epithermal veins surrounding the plutons and, on larger scales, formation of economically viable Mo porphyry deposits.

Some TTG suites show only a weak (e.g., Zimbabwe, Fig. 5) or no correlation (e.g., Barberton) between Mo and Nb or Mo and Ti, which suggests that fractionation of Mo by Ti- or Nb-bearing phases did not play a dominant role in the evolution of the Mo budgets of these magmas. Alternatively, fractionation may not be captured by the limited differentiation range in these TTGs. Nevertheless, these plutonic suites (except for one set of Barberton TTGs) still show significant Mo depletion. In the Zimbabwe suite, Mo is variably correlated with Cs ($R^2 = 0.84$), Sb ($R^2 = 0.73$), Pb ($R^2 = 0.56$), and As ($R^2 = 0.46$) (Fig. S4) all of which

are moderately compatible in a low-salinity fluid phases (Zajacz et al., 2008), and these

elements are known to be expelled from granitic plutons. However, several of these

correlations hinge on a single data point (Fig. S4). There is no correlation between these

fluid-mobile elements and incompatible, less-fluid mobile elements such as the LREE,

implying that the fluid-mobile element concentrations are dominated by processes other than

crystal-melt differentiation. Indeed, Mo is more strongly depleted relative to Ce in this suite

of TTGs relative to other locales (lower Mo/Ce ratio in Fig. 5), so a vapor phase may have

preferentially removed Mo from the Zimbabwe TTGs. In contrast to the Zimbabwe samples,

no individual pluton suite displays convincing ($R^2 > 0.4$) multi-element correlations in the

Barberton TTGs. Correlations between Mo and fluid-soluble elements are also not found for

the Superior Province or Baffin Island samples. Thus, we suggest that different processes of

Mo-loss from plutons (fluid exsolution v. crystal fractionation) may be acting on different

plutonic suites, and these processes are not mutually exclusive.
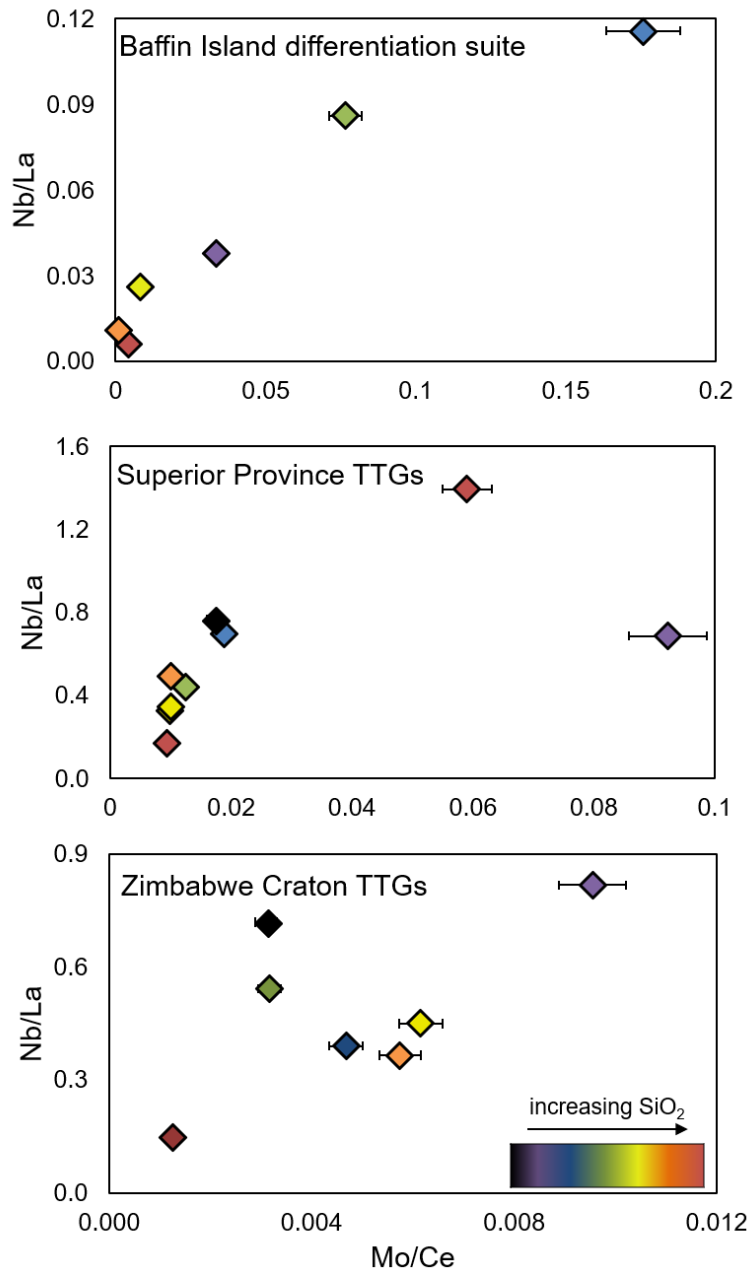
Figure 2.5. Correlations between Mo/Ce and Nb/La in Archean and Proterozoic pluton suites. Samples are color coded based on SiO$_2$ content with red being the most felsic and purple/black being the least. The SiO$_2$ range varies between suites (see Table 1 and supplementary figures). The Zimbabwe data include only the Mashaba tonalite suite. Error bars represent 2σ external reproducibility, as determined by AGV measurements.

If we explore the hypothetical end-member case in which the effects of crystal

fractionation are assumed to be negligible, and Mo behaves as an incompatible element in

all systems, then loss through fluid exsolution to form MoS_2 could account for all calculated Mo depletions. In this scenario, it can be inferred that approximately 60% (average Mo lost from a pluton – see supplement information on Mo* calculation) of the Mo in un-weathered UCC granites is hosted in MoS_2. This is a maximum estimate, because it is likely that Mo loss from the magma during partial melting or crystal fractionation also occurs.

A simple calculation can be used to estimate the maximum amount of Mo released from plutons to form molybdenite. We start with the following parameters and assumptions: the continental crust covers 210×10^6 km^2 of the Earth's surface (Cawood et al., 2013) and, to a depth of 10 km, 40% of that area is granitic rock that initially contains 0.5 ppm Mo (the average interpolated Mo abundance, Mo*, of this study). Mean Mo loss from the granites in this study is 60%, and we initially assume that all Mo 'lost' is due to vapor-phase partitioning. With these assumptions, a maximum 10^{14} kg of Mo would have been released from UCC granitic plutons to form MoS_2. If we instead assume that granite only composes 20% of the upper 10 km of the crust, and only 10% of the Mo missing from a pluton is a result of MoS_2 formation, then approximately 10^{13} kg of Mo would have been released from UCC granitic rocks to form MoS_2. Thus, we conclude that a maximum of 10^{13} kg to 10^{14} kg of Mo may be hosted in MoS_2 in the upper 10 km of the continental crust. The USGS has identified $\sim 10^{10}$ kg of Mo resources available for mining (rounding to the nearest order of magnitude) (USGS, 2009). This suggests that up to three to four orders of magnitude more Mo may lie inaccessible beneath the surface of the continental crust.

In summary, a combination of fractionation during differentiation and loss via vapor phase exsolution probably contributes to the total Mo loss recorded in granites. This would explain discrepancies between plutonic suites – among which some show strong Ti-mineral

fractionation signatures and others do not – yet, nearly all of the samples studied here show depletions in total [Mo]. Further studies of magmatic suites formed by partial melting with Fe-Ti oxides in the residue, or differentiation involving fractionation of Fe-Ti oxides are needed to test these hypotheses.

2.5.3 Release of Mo during oxidative weathering of the UCC

Mo enrichments in black shales that form in euxinic (S-rich) ocean basins are first observed in the rock record at around 2.5 Ga and persist through the Phanerozoic, with a second period of increased Mo abundances beginning at the end of the Proterozoic (Anbar et al. 2007; Scott et al., 2008; Wille et al., 2007). These enrichments are interpreted to reflect changing atmospheric and oceanic oxidation states due to the GOE and the Neoproterozoic Oxidation Event. However, before Mo concentrations in black shales can be calibrated as a paleo-atmospheric oxybarometer, one must first know which O_2 sensitive mineral phases host Mo in the continental crust (Anbar et al., 2007). We have shown here that molybdenite, specifically, is the predominant sulfide host of Mo in the UCC, while other common magmatic sulfides and their subsolidus exsolution products (pyrite, chalcopyrite, etc.) do not contain significant Mo. Based on our findings, it is likely that Mo released from MoS_2 during oxidative weathering is the source of Mo enrichment observed in oceanic sediments since the GOE. Thus, experimentally-determined oxidation rates of MoS_2 at low pO_2 are needed to derive the pO_2 of the atmosphere during the GOE (e.g., Greber et al., 2015). While authigenic pyrite may host some Mo in sedimentary rocks (e.g., Gregory et al., 2017), Mo must first be removed from the primary igneous crust before it can be concentrated in these phases. If Mo was not released significantly from the igneous UCC prior to the GOE – which is likely given the lack of Mo depletion in pre-GOE diamictites (Gaschnig et al.,

2014) – then authigenic sulfides were probably not a weatherable source of Mo from the continental crust at the time of the GOE.

Given the strength of the Ti-O bond, titaniferous phases are fairly resistant to weathering, so Mo will not be easily released from them, irrespective of pO_2. It is very likely that Mo remains in these minerals as the source rocks are weathered and the titaniferous minerals are incorporated into sediments as detrital minerals. However, Mo is also highly enriched in volcanic glass – a phase that is susceptible to weathering in anoxic and oxic environments. Therefore, we propose that weathering of volcanic glass may have released Mo from the crust before the rise of atmospheric oxygen. As no Mo depletion is observed in the UCC before the GOE (Gaschnig et al., 2014), this process was probably not widespread on the continents. However, soluble Mo^{6+} may have been released into the pre-GOE oceans from submarine weathering of glassy basalt. This Mo might have been immediately reduced and sequestered if sufficient S, or another reductant, existed in the water column. Alternatively, if there was insufficient S in the water column to reduce Mo prior to the GOE (as suggested by Canfield, 2005), Mo might have remained in solution in pre-GOE oceans and is therefore not recorded in the marine rock record. This hypothesis has implications for the timing of the evolution of Mo-co-factored enzymes that fix nitrogen, as sufficient Mo must be present in the water column for it to be incorporated into these enzymes (Stüeken et al., 2015). However, this assumes that Mo is not immediately reduced once it is weathered out of volcanic glass, and that Mo is not hosted in secondary alteration phases. Both of these assumptions need to be tested with weathering models and analyses of Mo in altered basalts.

2.5.4 *Molybdenum enrichments in rift-related magmas*

The Barberton Terrane is composed of TTGs, greenstones (metamorphosed Archean basaltic rocks), and sedimentary units that were formed between 3.5 and 3.2 Ga. The samples studied here span 300 Myr in age and were formed during three to four distinct tectono-magmatic events at 3.5 Ga, 3.46 Ga, 3.29 Ga and 3.24 Ga (Clemens et al., 2006, Kröner et al., 1991). On the basis of field relationships and pluton geochemistry, Moyen et al. (2006) interpreted the terrane to have formed during collision of exotic blocks (3.55 – 3.42 Ga plutons) followed by a main orogenic event (3.25 – 3.21 Ga) during which the Badplaas pluton was emplaced. This was followed by post-orogenic collapse at 3.22 – 3.21 Ga, contemporaneous with emplacement of the Nelshoogte pluton in an extensional setting. The plutonic suites emplaced during accretion and the main orogenic stage exhibit Mo depletions relative to LREE (with the exception of one sample from the Stolzburg pluton, STZ), while the Nelshoogte (NLG) pluton, which is associated with post-orogenic collapse, is not depleted in Mo (Fig. 6). The concentrations of REE do not change significantly between the different suites, but the NLG plutonic suite is less enriched in LREE relative to HREE, and is slightly more magnesian. This observation that Mo is enriched in ~3.2 Ga rift-related magmas is similar to Mo-enrichments observed in rift-related magmas today.
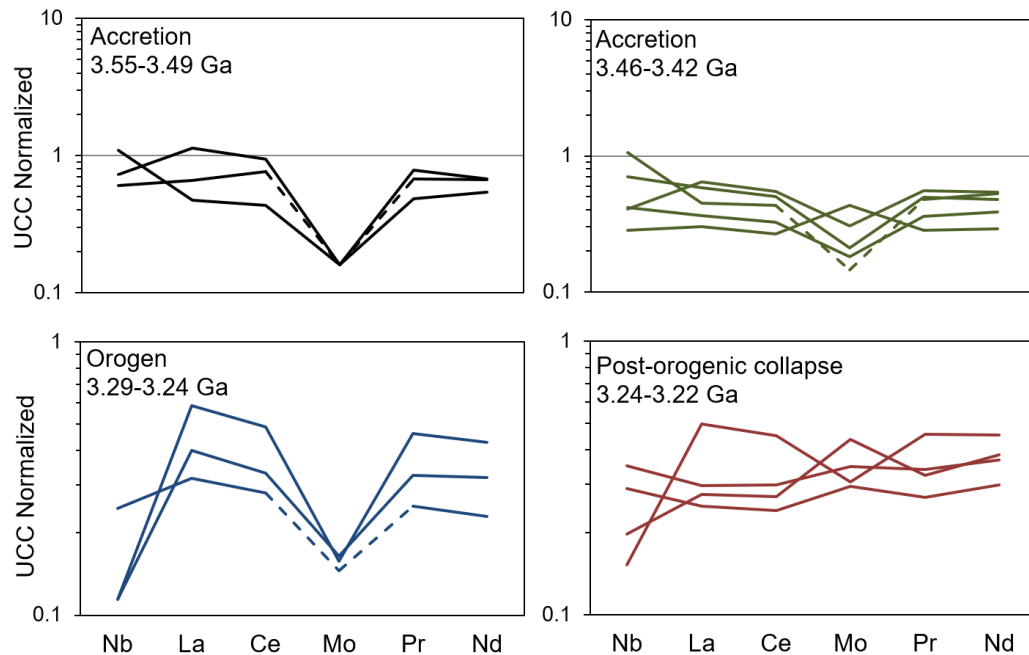
Figure 2.6. UCC normalized spider plots for individual pluton suites in the Barberton Greenstone Belt representing different stages of accretion and post-orogenic collapse. Dashed lines indicate Mo was below the DL in the sample, so the DL is used instead of Mo concentration. Black = Steynsdorp; Green = Eerstehoek, Theespruit, Doornhoek, Stolzburg; Blue = Badplaas; Red = Nelshoogte.

Similarly, while many economic Mo deposits are associated with arc-derived, calc-alkaline magmas (Westra and Keith, 1981; Whalen et al., 2001), the highest-grade Mo-porphyry deposits are associated with rift settings (e.g., Climax-type deposits; Ludington and Plumlee, 2009), and alkaline magmas from continental rifts show significant Mo enrichments (Audétat, 2010; Audétat et al., 2011). The source of Mo in these rift-related magmas is unclear; both the lithospheric mantle and the continental crust have been suggested as sources. Sun et al. (2016) propose that assimilation of sedimentary rocks enriched in Mo (e.g., black shales) may be the source of Mo. Other researchers have suggested that the Mo may ultimately be sourced from Mo-enriched mantle melts that undergo fractional crystallization (Audétat, 2010; Pettke et al., 2010). Pettke et al. (2010) proposed that the lithospheric mantle may be re-enriched in Mo through subduction-related

metasomatism, and that alkaline magmas may be generated from this Mo-rich reservoir during rifting events.

The observation that Mo is enriched in the ~3.2 Ga rift-related NLG pluton can be used to test these hypotheses. Significant Mo enrichments in black shales only occur after the onset of widespread oxidative weathering at ~2.4 Ga (Scott et al., 2008; Anbar et al., 2007). Thus, the hypothesis that rift magmas assimilate Mo-rich sediments, proposed by Sun et al. (2016) does not hold for these Archean magmas. There is evidence for subduction-related magmatism in the Barberton suite (Moyen et al., 2006; Furnes et al., 2012), which adds credence to the hypothesis that a subducting slab may have enriched the lithospheric mantle in Mo (Pettke et al., 2010). However, this hypothesis remains contentious because many authors argue that subduction zones mainly arose after 3.2 Ga (e.g., Condie and Kröner, 2008; Tang et al., 2016, and references therein).
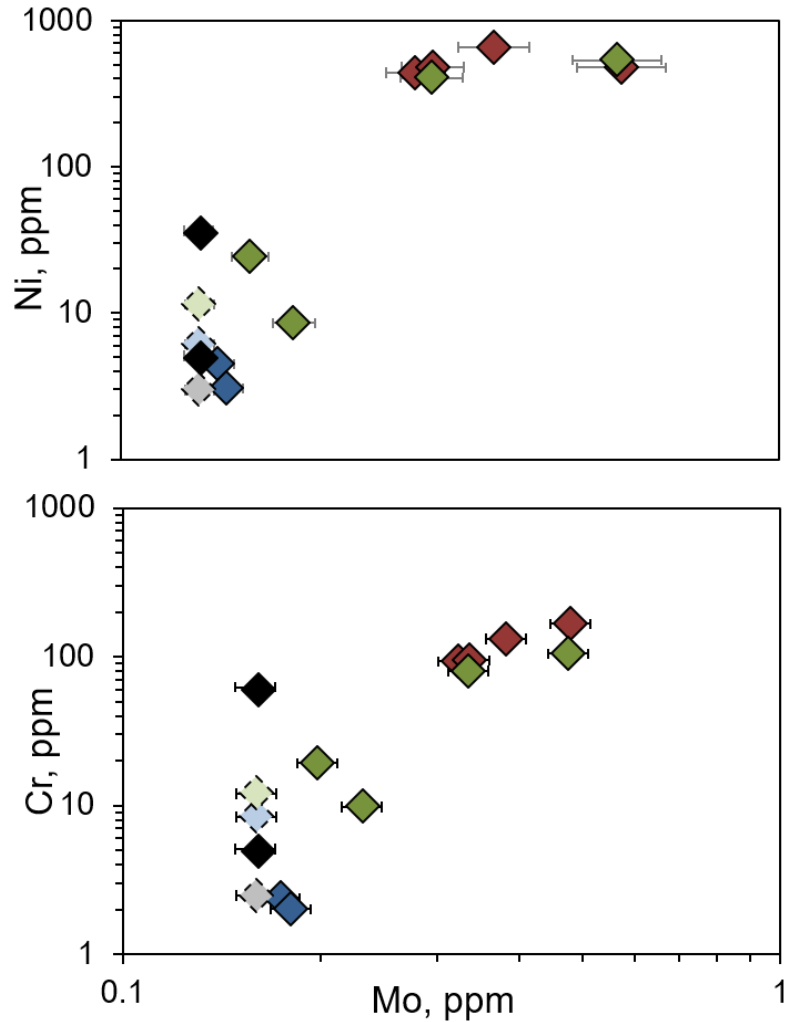
Figure 2.7. Correlations between (A) Mo and Ni and (B) Mo and Cr in the Barberton TTGs. Color scheme is the same as in figure 6; dashed symbols represent samples that contain less Mo than the detection limit (0.16 ppm). Error bars represent 2σ.

In the Barberton samples, Mo correlates with Ni (Fig. 7a) and Cr (Fig. 7b). Additionally,

the overall Mo enrichment of the NLG pluton relative to LREE resembles that of MORB

and Hawaiian lavas (Fig. 4), suggesting a mafic, *i.e.,* mantle, origin for the Mo. Lithospheric

mantle-derived Mo is a something of a paradox because the lithospheric mantle is refractory

and should be depleted in incompatible Mo. This paradox could be resolved if the

lithospheric mantle were metasomatized with fluids derived from a subducting slab, and

then partially melted during a subsequent rifting event (Pettke et al., 2010). Alternatively, it

is possible that the Mo enrichments may be derived from partial melting of Mo-rich cumulates (e.g., Fe-Ti oxides and rutile bearing rocks such as amphibolites and eclogites) during continental rifting. In this scenario, lower crustal rocks may contain the missing Mo recorded in granitic suites and explain the origin of the Mo enrichment in various rift-related magmatic suites. This hypothesis implies that sequestration of Mo in Fe-Ti oxides in lower crustal cumulates must be significant, and further analyses of Mo abundances in such rocks are needed to evaluate this idea.

CONCLUSIONS

In 'common' UCC granitic rocks, Mo is hosted primarily in weathering-resistant, titaniferous phases such as titanite, ilmenite, and magnetite, while in basaltic to andesitic volcanic rocks, Mo is predominately hosted in ilmenite, magnetite, and interstitial glass. Molybdenum mass balance based on in situ analyses of Mo in silicates and oxides cannot be completed in a few granitic samples, suggesting nuggets of MoS_2 may be a significant Mo host in some felsic plutonic rocks.

Silicates (e.g., quartz, biotite, and amphibole) generally contain less than 0.2 ppm Mo, but may be volumetrically significant hosts, contributing up to 25% of the whole-rock Mo in one granitic rock analyzed here.

Common accessory phase sulfides (e.g., pyrite, chalcopyrite, immiscible sulfide blebs) are not significant hosts of Mo in granitic or basaltic rocks.

Nearly all analyzed granitic rocks are depleted in Mo (by 20 – 90%, mean = 60%), relative to Ce and Pr. This may reflect MoS_2 precipitation from fugitive magmatic vapor phases or loss of Mo to fractionating Ti- and Nb-bearing phases during slab melting or magmatic differentiation. Some plutonic suites show correlations between Mo and Nb,

suggesting loss of Mo due to fractionation of Fe-Ti oxides or other titaniferous phases. Other plutonic suites show correlations between Mo and fluid-soluble elements (e.g., Cs, Pb, As, etc), potentially pointing to Mo loss in an aqueous magmatic vapor phase.

If all Mo lost from granitic rocks is attributed to aqueous fluid exsolution and subsequent MoS_2 precipitation, then, on average, 60% of the Mo budget in a pluton would have to be concentrated in distal, epithermal veins that crystallized MoS_2. This is most likely an overestimate as it represents the endmember scenario where all Mo is lost through vapor-phase fractionation.

The ~3.2 Ga rift-related Nelshoogte pluton from the Barberton Greenstone Belt is the only group of samples studied here that do not show a systematic Mo depletion. This is similar to observations of Mo-enrichments in modern rift-related magmas. These data can be used to rule out the hypothesis that Mo enrichments in rift-related magmas are derived from melting of Mo-rich sediments like black shales, because Mo was not enriched in black shales prior to the GOE at ~2.4 Ga. If subduction was occurring at this time, subduction-related metasomatism of the lithospheric mantle could be the source of the enrichment in Mo in these rift-related magmas (Pettke et al., 2010). Alternatively, mantle melts generated during rifting may have assimilated Mo-rich residues in the lower crust or upper mantle to create these Mo enrichments in rift-related magmas. This would imply that significant Mo is removed from evolving magmas in Fe-Ti oxides. Further analyses of Mo in differentiated suites and lower crustal cumulates are needed to test this hypothesis.

The processes of Mo-loss through fluid/vapor-phase partitioning or fractionation of titaniferous phases are likely not mutually exclusive. Here we present arguments for the two

96

end-member scenarios but emphasize that further research is needed to determine the proportion of Mo-loss by these two processes.

Chapter III. Completing the Molybdenum Isotope Mass Balance in Subduction Zones

To be submitted to Earth and Planetary Science Letters

With co-authors: Roberta L. Rudnick[1,2], Stephan J. Romaniello[3], and Ariel D. Anbar[3,4]

[1] University of California Santa Barbara, Department of Earth Science, Santa Barbara, CA 93106

[2] University of Maryland College Park, Department of Geology, College Park, MD 20742

[3] Arizona State University, School of Earth and Space Exploration, Tempe, AZ 85281

[4] Arizona State University, School of Molecular Sciences, Tempe, AZ 85281

Author Contributions

A.T. Greaney conceived the study, carried out the analyses and data interpretation, and wrote the manuscript.

R.L. Rudnick helped conceive the study, provided samples, aided in data interpretation, and provided edits on the manuscript.

S.M. Romaniello provided analytical assistance, aided in data interpretation, and provided edits on the manuscript.

A.D. Anbar aided in data interpretation and provided edits on the manuscript.

ABSTRACT

Molybdenum isotope data suggests that intermediate to felsic rocks of the upper continental crust are generally isotopically heavier than peridotites and basalts that comprise the lithospheric mantle and oceanic crust. Some researchers have looked to igneous differentiation to explain this difference, but we instead explore the hypothesis that Mo isotope fractionation occurs in the subduction zone as Mo is partitioned between a fluid or melt phase and residual slab minerals. We analyzed eclogite xenoliths from the Koidu kimberlite pipe from Sierra Leone that are thought to represent subducted Archean oceanic crust that was partially melted. Using laser ablation ICP-MS we find that on average 90% of the Mo is hosted in rutile in the eclogites and reconstructed bulk-rock values show that Mo falls in line with Le and Ce on primitive-mantle normalized spider diagrams. When compared to LREE data for Archean greenstone basalts, this implies that between 60 and 80% of the LREE, and therefore Mo, were removed from the slab during dehydration and partial melting. Isotope dilution MC-ICP-MS analyses of rutile separates shows that rutile is very isotopically light (mean of $-0.65‰ \pm 0.08$ 2σ), and mass balance dictates that the whole-rock is also isotopically light (mean of $-0.60‰$). We use these data to model isotope fractionation in subduction zones which results in isotopically heavy arc magmas that form the upper crust (between -0.07 to $+0.01‰$). While many arc magmas are isotopically heavier than this, the fractionation that occurs in subduction zones may partially explain the overall fractionation observed. Additionally, we hypothesize that ocean island basalts that are thought to contain recycled eclogite (e.g., HIMU OIB) may contain isotopically light Mo relative to other OIB sources.

3.1 INTRODUCTION

Molybdenum (Mo) isotope geochemistry has been used to trace a range of geologic processes, from using mass dependent isotope fractionation to track the changing chemistry of ancient ocean basins (e.g., Anbar et al. 2007 and many other works) to studying chemical processing of the solar nebula and accretion of the Earth with mass independent isotope fractionation (e.g., Bermingham et al., 2018). Mass-dependent fractionation of Mo isotopes on Earth likely occurs either by oxidation/reduction of Mo between its tetravalent and hexavalent states, and/or by changing coordination state within the mineral or species it is bonded to (Tossel, 2005). There exist seven stable Mo isotopes, making analyses of mass-dependent Mo isotope fractionation relatively straight forward (see review of Kendall et al., 2017). While Mo isotope fractionation is much greater at lower temperatures and has therefore historically been used to trace low-temperature geologic processes, the "high-temperature" geochemistry community has recently turned to Mo isotopes to better understand igneous and metamorphic processes.

With the recent publication of molybdenum isotope data in the Earth's crust and mantle, an overall trend has emerged: the continental crust is seemingly isotopically heavier than the mantle. The bulk earth Mo isotope signature is estimated to have a Mo isotope signature of δ^{98}Mo = -0.16 ± 0.02 (Burkhardt et al., 2014), as established by chondrites. Since Mo is a siderophile element at low fO$_2$ (Newsome and Palme, 1984), significant Mo is expected to have partitioned into the core, likely resulting in isotope fractionation that left the mantle with a sub-chondritic δ^{98}Mo value of -0.21‰ ± 0.06 (Burkhard et al., 2014; Greber et al., 2015; Willbold and Elliott, 2017). Further Mo isotope fractionation likely occurs during partial melting of the mantle to form Mid-Ocean Ridge Basalts (MORB) and

during igneous differentiation processes that form the Upper Continental Crust (UCC). MORB range from -0.24 to +0.15‰ with an average of -0.09‰ (Bezard et al., 2016; Liang et al., 2017). While much variation in crustal rocks exists, the continental crust is generally isotopically heavier with an estimated average δ^{98}Mo value between +0.03 (Greaney et al., in prep – Chapter 4; Wille et al., 2018) and +0.15 (Voegelin et al., 2014; Yang et al., 2017; König et al., 2016). Ocean Island Basalts (OIB) show large variations in δ^{98}Mo space (-0.59 to +0.25‰) with some OIB having δ^{98}Mo values even lighter than the primitive mantle.

The cause for the fractionation of Mo isotopes between the various silicate earth reservoirs is still uncertain. The offset between MORB and the primitive mantle suggests that Mo isotopes are slightly fractionated during partial melting. Further offset between the UCC and MORB and primitive mantle also suggests that fractionation occurs in the subduction zone or during igneous differentiation. Fractionation of a phase like biotite or amphibole has been suggested to cause fractionation during differentiation of arc magmas (Voegelin et al., 2014, Wille et al., 2018). However, Greaney et al. (2017, 2018) found that Mo is generally more enriched in Ti-phases like ilmenite, Ti-magnetite, rutile, and titanite than in silicates. Interestingly, Wille et al. (2018) did not observe overall [Mo] fractionation from the evolving magmatic suite and instead found that it behaves incompatibly, which is corroborated by the results of Toc et al. (in prep – see Appendix G). Isotope fractionation is not observed in non-arc tholeiitic magma differentiation suites like that of Hekla Volcano, Iceland (Yang et al. 2015) and Kilauea Iki, Hawaii. Other researchers suggest that fractionation may occur in the subduction zone during slab dehydration and/or partial melting which implies that a residual slab phase may sequester light Mo isotopes (Freymuth et al. 2015; König et al. 2016).

The aim of this study is to determine whether Mo is sequestered in the slab during subduction and if Mo isotopes are fractionated during this process. We do so by analyzing Mo partitioning behavior and isotopes in xenolithic eclogites from the Koidu kimberlite complex in Sierra Leone.

3.2 SAMPLES

The eclogites studied here were initially collected and characterized by Hills and Haggerty (1989) and Fung and Haggerty (1995). These studies provided modal mineralogy of the major phases, mineral chemistry, and characterized the full suite of eclogites into a high-MgO and low-MgO endmember with different petrogenetic histories. In this study, we focus on the low-MgO endmembers because these eclogites are interpreted to be melt-depleted residues of subducted Archean oceanic crust (Barth et al., 2001). The low-MgO eclogites contain elevated $\delta^{18}O$ signatures and show complimentary trace element signatures to Archean TTGs, suggesting that they interacted with ocean water and that melts derived from them formed the Archean UCC (Barth et al., 2001). Additionally, the low-MgO eclogites record $\delta^{26}Mg$ signatures in omphacite and garnet that exceed mantle values, which also indicates interaction with seawater (Wang et al., 2015). These eclogites contain a high Nb/La ratio that is attributed to the presence of residual rutile, a low Th/U ratio that suggests the "slab" had been partially melted in addition to dehydrated, and a Zr depletion that also suggests the samples were partially melted, as Zr is more compatible in melt than fluid. Geochronological constraints for the eclogites (Re-Os) and inferred complimentary TTGs (U-Pb zircon) overlap, permissive of a genetic connection, with TTG formation at ~2.9 Ga (Barth et al 2002).

Thirteen eclogites were selected for trace element analysis. The samples are composed primarily of garnet and omphacite, with proportions of these two main phases ranging from 26:72 to 63:36 garnet:omphacite. Rutile modes range between 0.5% to 1.6%. These abundances have been normalized to 100 from the reported modes of Hills and Haggerty (1989) and Barth et al. (2001) to remove the dilution effects of altered kimberlite material. Sulfide is also present in these samples but is extremely altered due to kimberlite contamination or supergene weathering (see photos in the supplementary materials). Additionally, pyrite is a major constituent despite the fact that pyrite is not an expected primary mantle phase, given the high S activity needed to form pyrite (Lorand and Luguet, 2016). Therefore, these sulfides are highly altered and were perhaps even deposited by the entraining kimberlite material.

3.3 METHODS

The eclogites are significantly contaminated with kimberlite material (Barth et al., 2001), therefore whole rock analyses would be significantly compromised. Thus, in-situ and mineral separation methods were necessary to determine trace element abundances and Mo isotope signatures. Given the kimberlite contamination, whole-rock data must be reconstructed from mineral data using major element and modal mineralogy data determined by Fung and Haggerty (1995) and Hills and Haggerty (1989). The rutile modes were calculated by Barth et al. (2001) and Rudnick et al. (2000) from the whole-rock Ti concentration.

Laser Ablation ICP-MS was used to determine Mo and other trace element abundances in the major minerals garnet, omphacite, and rutile in thin sections at UC Santa Barbara. A spot size of 65 μm was used and the laser was operated at 10 Hz, 100% output,

with a shot count of 250 with 60 s washout time in between analyses. The data were reduced

using Iolite with Ti as an internal standard for rutile and Si as an internal standard for the

pyroxene and garnet. NIST-612 was used as the calibration standard and BHVO-2g was run

as a secondary standard which reproduced very well, giving a value of 3.95 ($\pm$0.26) with the

reported GeoRem value of 3.8 ppm (precision within 7%, accuracy within 4%). Detection

limits of Mo were generally near 0.01 ppm. A complete set of elements analyzed by LA-

ICP-MS in BHVO-2g can be found in the supplementary data.

Rutile was hand-picked from coarse crushed eclogite for isotope analyses in the

Keck Lab for Biogeochemistry at Arizona State University. The rutile grains were dissolved

in HF + HNO_3 in high pressure Parr bombs at 180°C for three days and dried down

repeatedly in concentrated HCl to remove fluorides before being brought up in 1 mL of 6M

HCl for column chemistry. The samples were taken through anion columns twice using

Biorad AG1X-8 anion exchange resin to remove Zr. Then the Mo was eluted and taken

through cation columns using Biorad AG50WX-8 cation exchange resin to remove Fe. The

eluted Mo from the columns was dissolved in H_2O_2 repeatedly to remove any organic

material, and finally taken up in 0.32M HNO_3 for mass spectrometry. The samples were

analyzed in three aliquots of 25 ng Mo each on a Thermo Fisher Neptune MC-ICP-MS.

Details on the column chemistry and mass spectrometry can be found in Greaney et al. (in

prep – Chapter 4). Isotope ratios are presented as δ^{98}Mo and are normalized to the NIST

3134 standard where $\delta^{98/95}$Mo $=1000*\left(\frac{{}^{98}\text{Mo}^{/95}\text{Mo}_{\text{sample}}}{{}^{98}\text{Mo}^{/95}\text{Mo}_{\text{NIST3134}}}-1\right)$. SDO-1, a Devonian shale USGS

standard, was run as a secondary standard with excellent reproducibility, giving a value of

0.79 ± 0.03‰ (published value = 0.80‰; Goldberg et al., 2013). Long term reproducibility

on the ASU Neptune is ±0.04‰.

3.4 RESULTS

3.4.1 Mo abundances

Sulfides were analyzed by EPMA and were found to be almost entirely overgrown with secondary pyrite that likely formed in equilibrium with the kimberlite material or during supergene alteration. Therefore, their Mo abundances are excluded from the re-calculated whole-rock values. In garnet and omphacite, Mo abundances were routinely below or at the detection limit (0.01 ppm), so the detection limit is used in the re-calculated whole-rock values. In rutile, Mo concentrations vary between 4 and 35 ppm with a mean of 12 ppm. Some rutile also contained regions of ilmenite exsolution with significantly less Mo (mean of 2.6 ppm). Although rutile is the dominant phase, the average of all oxide data for a sample was used as the "rutile" value for the mass balance. Therefore, ilmenite may be oversampled, shifting the average "rutile" Mo concentration to slightly lower values. The reconstructed whole rock trace element data are presented in **Table 3.1** and the data for individual phases is reported in the supplement.

Sample	Th	U	Nb	La	Ce	Mo	Pr	Nd	W
80-A2	0.02	0.04	18.9	0.33	1.71	0.06	0.44	2.72	0.06
81-3	0.04	0.06	8.31	0.97	4.10	0.09	0.74	4.35	0.10
81-8	0.03	0.08	4.40	0.62	2.58	0.38	0.47	2.91	0.24
81-18	0.02	0.04	2.98	0.75	3.20	0.11	0.60	3.18	0.06
86-6	0.005	0.007	0.35	0.57	2.03	0.05	0.44	3.21	0.01
86-12	0.003	0.004	0.56	0.48	2.48	0.08	0.54	3.57	0.26
91-58	0.02	0.01	30.4	0.38	1.44	0.04	0.27	2.05	0.02
91-13	nd	nd	9.77	2.19	6.35	0.17	0.90	4.47	0.10
91-20	nd	nd	29.7	1.47	6.04	0.10	1.02	5.51	0.15
80-B1	nd	nd	0.88	2.66	8.15	0.16	1.30	6.41	0.02
91-4	0.001	0.01	1.95	0.56	2.51	0.08	0.54	3.11	0.03
86-56	0.01	0.02	0.79	0.12	1.00	0.04	0.35	2.77	0.04
91-2	nd	nd	18.4	0.50	2.17	0.18	0.43	2.90	0.07
91-37	nd	nd	nd	nd	nd	0.13	nd	nd	nd
91-49	nd	nd	nd	nd	nd	0.38	nd	nd	nd

Table 3.1 Calculated whole-rock eclogite data for select trace elements in ppm. "nd" stands for "not determined" in that sample. Th and U data taken from Barth et al. (2001).

	Rutile Separates		Calculated Eclogite	
Sample	δ^{98}Mo	2s	δ^{98}Mo	2s
91-13	-0.69	0.02	-0.66	0.11
91-2	-0.61	0.09	-0.57	0.23
91-4	-0.64	0.03	-0.57	0.14

Table 3.2. Measured δ^{98}Mo value of the rutile separates and the associated δ^{98}Mo value of the reconstructed eclogites.

Whole-rock trace element abundances were calculated using the modal mineralogy (Fung and Haggerty; Hills and Haggerty; Barth et al., 2001) and *in-situ* abundances obtained here. On average, reconstructed eclogites contain 0.14 ppm Mo (± ppm) and rutile contains 89% of the bulk-rock Mo. When normalized to primitive mantle values, Mo has similar abundances as LREE (**Fig. 3.1**). Molybdenum also falls in line with LREE on primitive mantle-normalized diagrams in OIB (Newsome and Palme, 1984; Greaney et al., 2107) and MORB (Jenner and O'Neill, 2012). The eclogites are also enriched in Nb relative to La. Trace element data for Archean greenstone basalts were compiled from GeoRoc from the Kaapvaal and Superior Cratons. Relative to these basalts, LREE in the eclogites are depleted by 65% (Nd) to 88% (La). Reliable [Mo] data does not exist for these Archean greenstones, however a value can be estimated by interpolating between the Ce and Pr data under the assumption that Mo partitioning in greenstone basalts is similar to modern MORB and OIB.
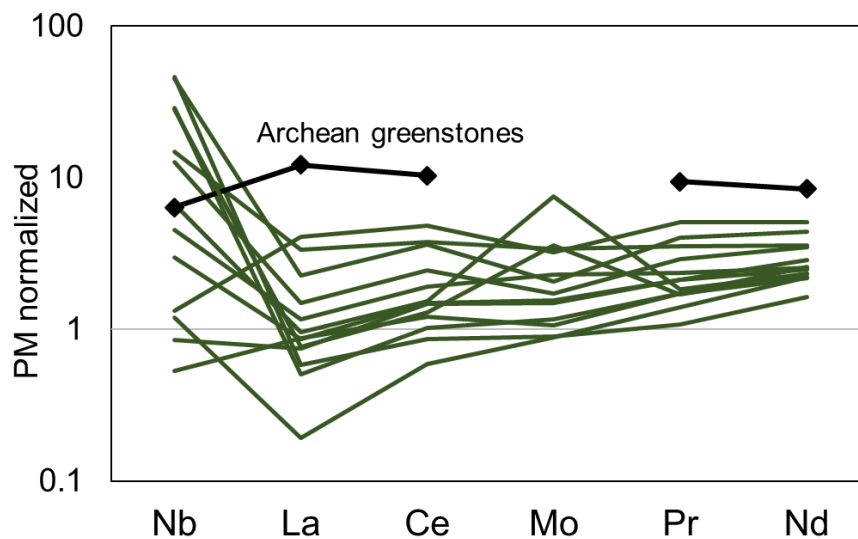
Figure 3.1. Primitive mantle-normalized trace element diagram showing reconstructed whole-rock eclogite data in black. Archean greenstone basalt data were compiled from GeoRoc and are assumed to represent a possible eclogite protolith. Primitive mantle values are from McDonough and Sun (1995).

3.4.2 Mo isotopes

The Mo isotope signature of rutile is consistently isotopically light, with a mean of –0.65‰ (±0.08 2σ) (**Table 3.2**). An isotope mass balance was also calculated for the bulk eclogite using the modal proportions of rutile, pyroxene, and garnet and the δ^{98}Mo values of the rutile. The pyroxene and garnet were not analyzed for Mo isotopes, given their extremely low Mo abundances, therefore they contribute little to the whole rock Mo isotope budget. For the purpose of mass balance calculations, they are assumed to have an average δ^{98}Mo equivalent to that of MORB (–0.09‰). The calculated bulk δ^{98}Mo$_{eclogite}$ ranges from –0.57‰ (±0.23) to –0.66‰ (±0.11). The large error takes into account the unknown δ^{98}Mo signature of the silicate phases, allowing for 0.10‰ variation in the chosen δ^{98}Mo$_{silicate}$ value of –0.09‰.

3.5 DISCUSSION

*3.5.1 Mo Partitioning in Eclogites*

The mass balance shows that, although rutile is volumetrically insignificant, it contributes between 78% and 98% of the Mo mass balance (average of 89%). Molybdenum partitioning into rutile is expected based on prior natural observations and experimental data. Fitton et al. (1995) first proposed that Mo follows Nb in subduction zones and is likely retained in residual rutile. Bali et al. (2012) followed up this work with experiments conducted at subduction zone temperatures (1000°C), pressures (2.61 GPa), and oxygen fugacities (at the Co-CoO, Ni-NiO, and Re-ReO$_2$ buffer). In both saline and non-saline fluids, Mo is compatible in rutile below the Re-ReO$_2$ buffer (D$^{fluid/rutile}$ = 0.01 to 0.21) and in saline fluids, Mo is slightly incompatible in rutile at the Re-ReO$_2$ buffer in one experiment (D$^{fluid/rutile}$ = 2.05). This suggests that fO$_2$ strongly controls Mo behavior in arc settings.

Additionally, these experiments found that Mo is strongly incompatible in pyroxene and garnet ($D^{fluid/silicate}$ = 150 to 2600). Experimental bulk D values imply that Mo is an overall incompatible element in subduction zones, but some Mo may be retained in rutile.

These experiments are corroborated by the findings of this study. The calculated eclogite whole rock Mo concentrations fall in line between LREE on a primitive mantle normalized diagram (Fig. 3.1), suggesting Mo has a similar bulk D to the LREE, even though they are hosted in different phases. Overall, Mo is depleted relative to the interpolated greenstone basalt value by 75%, i.e, ~75% of Mo was lost from the slab during subduction. Therefore, we conclude that overall Mo behaves incompatibly in subduction zones, and the ~25% of Mo that is retained in the slab is found almost entirely in rutile.

It is unclear whether the rutile is the primary Mo host in the eclogites, or if Mo and Nb were initially retained during partial melting by another phase like amphibole that transitioned into rutile during metamorphism. Experimental studies suggest rutile $D^{Nb/Ta}$ should be <1 while amphibole is known to record $D^{Nb/Ta}$ of >1 (Foley et al., 2002, Tiepolo et al., 2007). Because the rutile in this study contain high Nb/Ta (**Figure 3.2**), it is possible that amphibole was the initial retainer of Nb and Mo during dehydration and partial melting, and that rutile formed later as a product of high P metamorphism of the slab. We observe a correlation between Mo and Nb/Ta in the rutile (**Figure 3.2**), but not between Mo and Nb, suggesting that whatever process enriches Nb over Ta also enriches Mo. Amphibole is known to favor Nb over Ta, given their slight differences in radii (Foley et al., 2002), so we propose that Mo may have followed Nb into the M1 site in amphibole. Then, during dehydration melting, the amphiboles lost Mo and Nb at a similar rate, but to varying degrees in different samples, perhaps depending on the degree of dehydration of the sample. It has

been shown experimentally that fluid-rich partial melting should enrich the melt in Nb more

so than Ta (Xiong et al., 2011), and it is known that Mo is very fluid mobile when oxidized.

Therefore, we propose that the amphibole-bearing eclogite precursors that were initially

more fluid saturated lost more Nb relative to Ta as well as lost more Mo than their less-fluid

rich counterparts. This may result in the correlation between Mo and Nb/Ta observed in the

rutile. On Figure 3.2, this means that samples with a high Nb/Ta and high Mo (upper right

corner) likely did not experience significant dehydration, while samples that plot in the

lower left corner (low Nb/Ta and low Mo) experienced more dehydration-melting and lost

more Nb and Mo.
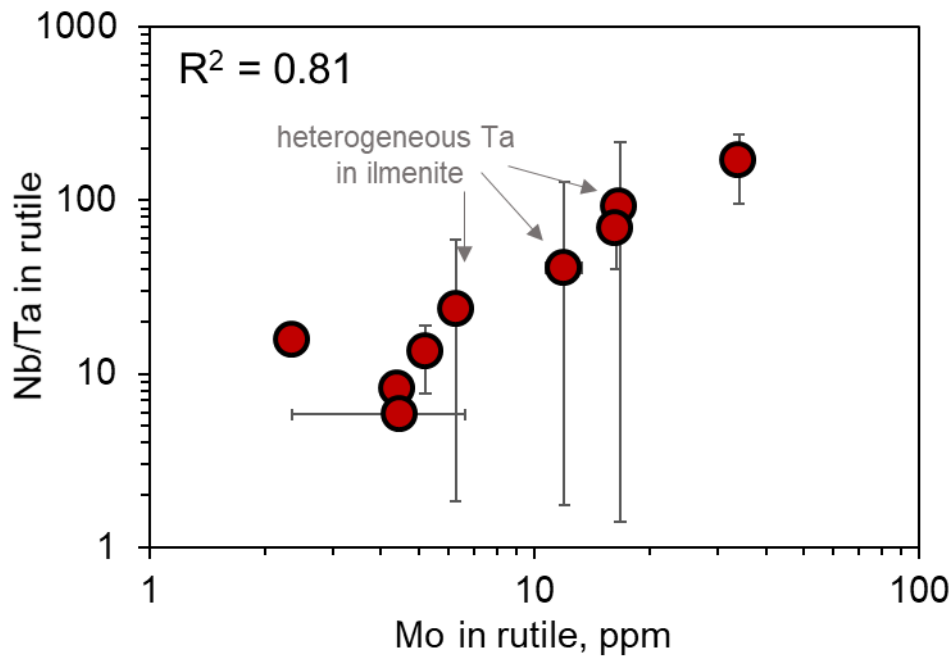
Figure 3.2. Correlation between the Nb/Ta ratio and Mo concentration in rutile. Each point represents one eclogite sample. Error bars represent 2σ of the mean as calculated by repeated analyses of rutile in a sample. The samples with large errors bars on the Nb/Ta ratio contain ilmenite exsolution with heterogenous Ta values.

Finally, we acknowledge the possibility of a metasomatic origin of the high Nb/Ta and

high Mo in the rutile, as proposed by Aulbach et al. (2008). This hypothesis has been put

forward to explain the high Nb/Ta ratio in xenolithic eclogitic rutile, which is otherwise

expected to contain low Nb/Ta (Aulbach et al., 2008), however we are uncertain of where a

metasomatic fluid or melt with exceptionally high Mo and Nb would originate. If all the Mo

was added to the rutile via metasomatic fluid, that would imply that 1) Mo is more

incompatible than the LREE in a subduction zone and would be nearly entirely stripped

from the slab during dehydration/partial melting, since rutile contains nearly all of the Mo in

the samples, and 2) metasomatic fluids or melt in the lithospheric mantle are exceptionally

isotopically light relative to mantle peridotites (Liang et al., 2017) and average crustal rocks

(Yang et al., 2017, Willbold and Elliott, 2017). If further evidence for a metasomatic origin

of the rutile is produced, then these implications should be further explored. However, our

discussion will continue under the assumption that Mo and Nb/Ta enrichments in the rutile

are a primary signature that resulted from the compatibility of Mo and Nb during partial

melting of amphibolite and/or eclogite.
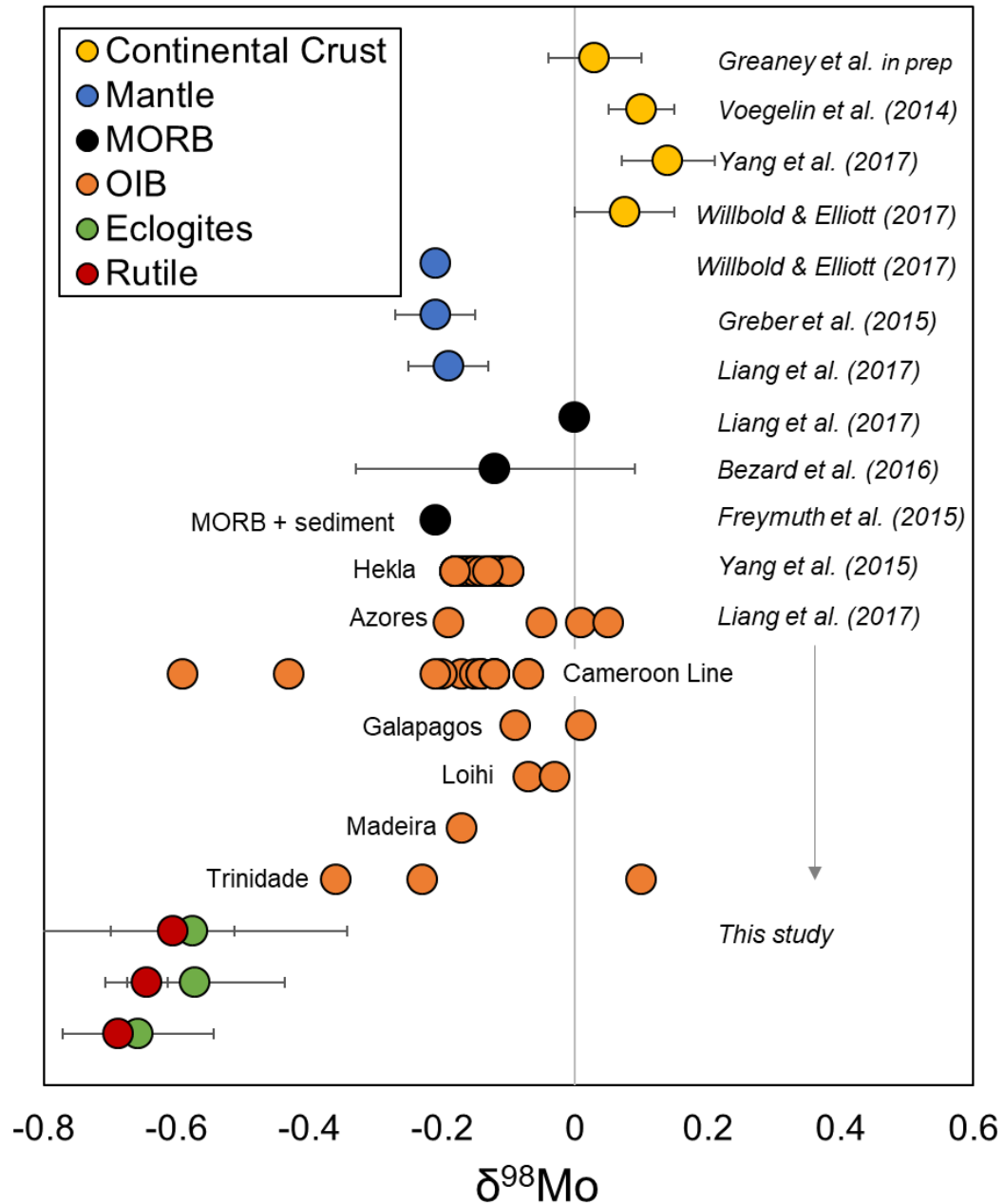
Figure 3.3. Mo isotope signature of various BSE reservoirs. The measured rutile and recalculated eclogite are included.

Another limitation to this study is that primary sulfides were not observed in these

samples. There is ongoing debate as to whether sulfide would be important for the Mo mass

balance in subduction zones. Previous studies of sulfides in basalts, granites, and peridotites

(Patten et al., 2013; Greaney et al. 2017 and 2018; Wang et al., 2018; Greaney et al. *in prep*)

found that sulfides are not major hosts of Mo. Additionally, a study of Mo behavior during tholeiitic differentiation could not resolve [Mo] fractionation after sulfide saturation (Yang et al., 2015). Experimental studies also find that Mo does not strongly partition into sulfides at crustal conditions (Li and Audétat, 2012). Contrary to these results, Skora et al. (2017) propose that Mo may partition into sulfide in subduction zones. Their experiments show that experimental glass is depleted in Mo if sulfide is saturated, however other phases that may incorporate Mo like crystalline SiO_2, titanite, and Fe-Ti oxides are also present in several of their experiments. As Skora et al. (2017) did not measure Mo directly in sulfides in their experiments, we consider the question unresolved. In our study, sulfides, which are likely secondary or altered by kimberlite material, are excluded from the eclogite mass balance. Eclogite that contains primary sulfide should be studied, to help resolve this question, if suitable samples can be identified.

*3.5.2 Mo Isotope Fractionation in Subduction Zones*

The continental crust is isotopically heavier than the primitive mantle and MORB (Willbold and Elliott, 2017), therefore fractionation must occur during igneous differentiation and/or in the subduction zone as Mo is removed from the subducting slab. Freymuth et al. (2015) first noted that arc magmas are generally isotopically heavier than the mantle, therefore they proposed that isotopically light Mo may be retained in the slab. Their mass balance calculations suggest that 35% of Mo is removed from the slab, leaving the residual slab rock isotopically light, with an estimated δ^{98}Mo signature of –0.27‰ to –0.35‰.

The measured rutile and calculated whole-rock eclogite δ^{98}Mo signatures reported here are isotopically lighter than most igneous rocks analyzed, to date (**Figure 3.3**). If these

eclogites truly represent subducted, partially melted oceanic crust, then these results confirm the hypothesis that fractionation occurs in the subduction zone. Light Mo isotopes are incorporated into rutile during slab dehydration and partial melting, and heavy Mo isotopes are removed from the slab and transferred into the sub-arc mantle. The δ^{98}Mo of the reconstructed eclogite is even heavier than predicted by Freymuth et al. (2015), however this heavy signature can still be reconciled with the δ^{98}Mo value of arc magmas and the overall continental crust. If Mo is expected to behave like Ce during igneous differentiation, then approximately 75% of "MORB" Mo is removed from the slab during subduction (as determined by Ce loss in the eclogites relative to greenstone belts). If the starting MORB has a composition of –0.09‰ and the subducted, partially melted eclogite has a composition of –0.60‰, then mass balance dictates that Mo in the partial melt/fluid that is moved into the sub-arc mantle has a δ^{98}Mo value of +0.08‰. Further mixing calculations suggest that if a "typical" arc magma sources 50% of its Mo from the existing sub-arc mantle (-0.21‰) and the other 50% from the slab-derived melt/fluid (+0.08‰), then the resulting magma δ^{98}Mo value should be -0.07 ‰. Alternatively, if 75% of the magmatic Mo is sourced from the slab-derived melt/fluid and only 25% is sourced from the sub-arc mantle, then the magma's δ^{98}Mo value should be +0.01‰ (**Figure 3.4**). These simple mixing calculations suggest that the Mo isotope fractionation that occurs in the subduction zone is significant, and can generate magmas that are isotopically heavier than the primitive mantle and MORB. This result does not preclude Mo isotope fractionation during igneous differentiation, however these data provide evidence for the important role that rutile may play in generating the δ^{98}Mo signature of arc magmas and the continental crust, in general.
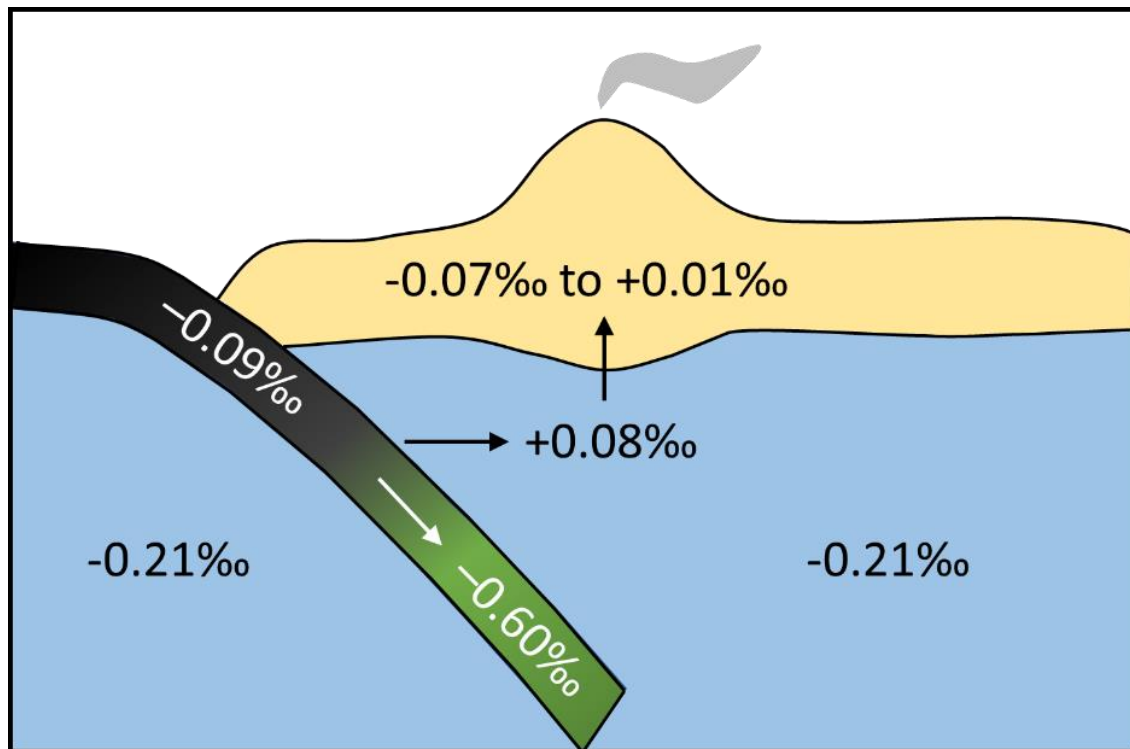
Figure 3.4. Calculated composition of subducted slab (–0.60‰) and Mo that is removed into the sub-arc mantle (+0.32‰). Mixing calculations between the slab-derived Mo and the depleted mantle (–0.21‰) can generate typical UCC values (+0.03 to +0.15‰).
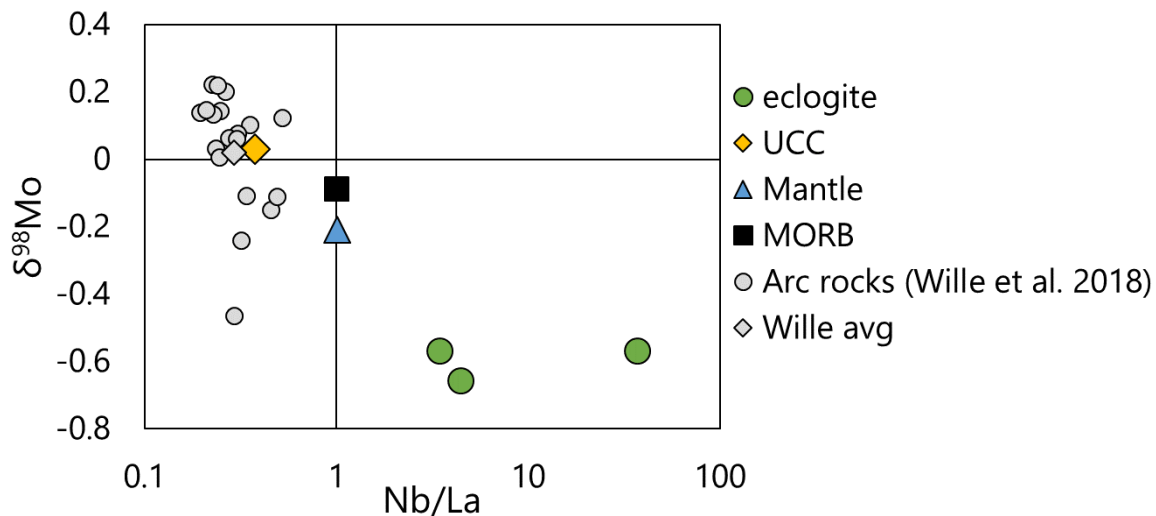
Figure 3.5. Correlation between δ^{98}Mo and Nb/La in various BSE reservoirs. The arc magmas from Wille et al. (2018) are presented because their average closely matches that of the bulk UCC, and these magmas do not reflect a significant sediment contribution which may shift δ^{98}Mo to significantly lighter or heavier values.

116

3.5.3 Recycling of Isotopically Light Mo

Like Nb, the Mo budget of an eclogite is almost entirely controlled by rutile. While Mo is not as enriched in the bulk eclogites as Nb (**Fig 3.1**), these two elements still share similar partitioning behavior in the subduction zone. Indeed, when the δ^{98}Mo signatures of overall Bulk Silicate Earth (BSE) reservoirs (e.g., the UCC, Primitive Mantle, MORB, and eclogite) are plotted against Nb/La ratio, a trend becomes apparent (**Fig 3.5**). The UCC is "missing" Nb relative to La and is enriched in the heavy Mo isotopes while the complementary eclogite reservoir is enriched in Nb relative to La and contains a lighter Mo isotope signature.

The fate of the subducted eclogite slab is debated, however many geochemists believe the chemical signature observed in certain OIB has been suggested to reflect eclogite in the melting source (White and Hofmann, 1980; Willbold and Stracke, 2006). Specifically, HIMU OIB are suggested to be sourced from a mixture of subducted altered oceanic crust (eclogite) and ambient mantle as reflected by the extremely radiogenic Pb signature (due to U-enrichment during sea floor alteration) and elevated Nb/La of these basalts (White and Hofmann, 1980). Given the trend observed between δ^{98}Mo and Nb/La (**Fig 3.5**), we hypothesize that the extremely light δ^{98}Mo signature observed in eclogites may be detectable in HIMU OIB.

A simple mixing calculation allows an estimate of the δ^{98}Mo value of an OIB that was sourced from a mixture of eclogite and depleted mantle (DMM). The mixing parameters for the depleted mantle are [Mo] = 0.025 ppm (Salters and Stracke, 2006) and δ^{98}Mo = − 0.21 (Bezard et al., 2016) while eclogite contains, on average, [Mo] = 0.14 ppm and δ^{98}Mo = –0.60. If one assumes a mixture of 10% eclogite and 90% depleted mantle, then the

resulting OIB source would have δ^{98}Mo = –0.36. Increasing the eclogite proportion to 20% results in an OIB source mantle with δ^{98}Mo = –0.43. This results in a source that is, on average, 0.19‰ lighter than the DMM, from which MORB are sourced.

There are currently no published studies on δ^{98}Mo signatures of the archetype HIMU OIB like the Cook-Australs and St. Helena. The Goldschmidt abstract of Willbold et al. (2012) shows that samples from La Palma (Canary Islands – HIMU source) fall within the calculated range with δ^{98}Mo between –0.48‰ and –0.23‰. However, this same abstract includes samples from the Cook-Australs (Tubuaii and Mangaia) that are not as isotopically light as expected, with a range between –0.25‰ and –0.16‰. It should be noted that this is still isotopically lighter than δ^{98}Mo established for the depleted mantle and chondrites. Liang et al. (2017) published Mo isotope data from the Cameroon Line, which trends towards the HIMU mantle endmember (Hofmann, 2003). These samples have δ^{98}Mo that ranges from –0.59 to –0.07‰, which are the lightest intraplate basalts measured to date. Overall, a comprehensive study of Mo isotopes in various OIB sources is needed to assess whether this light signature is pervasive in HIMU OIB and if it is statistically significant different from other OIB sources. Because Mo is soluble and therefore mobile during oxidative weathering (see Chapters 4 and 5), care should be taken to examine fresh, glassy basalts for Mo isotopes.

CONCLUSIONS

Reconstructed geochemical data for eclogites that are thought to represent subducted Archean oceanic crust allow insights into the behavior of Mo in subduction zones. Rutile contains, on average 89% of the bulk-rock Mo, with garnet and pyroxene containing < 0.01 ppm Mo, on average. On a whole-rock scale, Mo has a similar bulk D to the LRE because it

is apparently depleted from the slab to the same degree as Ce and Pr. On average the eclogites have "lost" 75% of their Mo budget, relative to Archean greenstone basalts (a possible protolith). Rutile separates from these eclogites contain isotopically light Mo with an average δ^{98}Mo of –0.65‰. The δ^{98}Mo value of the reconstructed whole-rock eclogites isotopically light eclogites (average –0.60‰). Isotope fractionation that occurs in the subduction zone may be enough to account for the light isotopic signatures seen in the upper continental crust, however isotope fractionation during intra-crustal differentiation should still be investigated as it likely also contributes to the heavy CC signature. Between different Earth reservoirs, δ^{98}Mo correlates with Nb/La, with the UCC representing one endmember and eclogites representing the other endmember. Isotopically light eclogites may be recycled into the deep mantle where they may be incorporated into the source of certain OIB, such as HIM, which also contain elevated Nb/La.

Chapter IV. Molybdenum isotope fractionation in glacial diamictites tracks the onset of oxidative weathering of the contintenal crust

To be submitted to Earth and Planetary Science Letters

With co-authors: Roberta L. Rudnick[1,2], Stephan J. Romaniello[3], Aleisha C. Johnson[3], Richard M. Gaschnig[4], Ariel D. Anbar[3,5]

[1]University of California Santa Barbara, Department of Earth Science, Santa Barbara, CA 93106

[2]University of Maryland College Park, Department of Geology, College Park, MD 20742

[3]Arizona State University, School of Earth and Space Exploration, Tempe AZ 85281

[4]University of Massachusetts Lowell, Department of Earth Sciences, Lowell, MA 01854

[5]Arizona State University, School of Molecular Sciences, Tempe, AZ 85281

Author Contributions

A.T. Greaney carried out the analyses and data interpretation and wrote the manuscript.

R.L. Rudnick conceived the study, provided samples, aided in data interpretation, and provided edits on the manuscript.

S.M. Romaniello provided analytical assistance, aided in data interpretation, and provided edits on the manuscript.

A.C. Johnson aided in data interpretation and provided edits on the manuscript.

A.D. Anbar aided in data interpretation and provided edits on the manuscript.

ABSTRACT

Glacial diamictites record geochemical averages of the upper continental crust that is exposed to the atmosphere, making them tools that can be used to study paleo-atmospheres. Molybdenum isotopes in twenty-four composites of glacial diamictites spanning depositional ages of 2900 to 300 Ma show a systematic shift to lighter compositions and a decrease in Mo concentrations over time. The diamictites fall into three age groups relative to the Great Oxidation Event (GOE): pre-GOE (2.43 – 2.90 Ga), syn-GOE (2.20 – 2.39 Ga), and post-GOE (0.33 – 0.75 Ga). Pre-GOE composites have an average $\delta^{98}Mo_{NIST3134}$ of +0.03‰, syn-GOE composites average -0.29‰, and post-GOE composites average -0.45‰; these groups are statistically different at p=0.01. We use the pre-GOE data to estimate the average Archean UCC $\delta^{98}Mo$ signature as +0.03 ± 0.18‰ (ext. 2σ), which falls within the range of previous estimates of modern UCC. As the diamictites represent weathered crust, this shift to lighter Mo values over time indicates greater retention of light Mo isotopes in weathered regolith and soils. We hypothesize that this fractionation is due to the mobilization of Mo and preferential adsorption of light Mo onto Fe-Mn oxides and/or organic matter. Rayleigh fractionation of Mo onto these phases and mixing models of soils and regolith reproduce the observed $\delta^{98}Mo$ values. Therefore, these data show that the modern weathered regolith is isotopically lighter than "primary" igneous rocks, and that Mo isotope fractionation in ancient weathered regolith records the rise of atmospheric oxygen and onset of oxidative weathering. This places an independent Mo isotope constraint on the GOE, relative to previous studies of Mo isotope fractionation observed in marine sediments. Mass balance dictates that Mo isotope fractionation during continental weathering results in isotopically heavy groundwater that feeds isotopically heavy rivers.

4.1 INTRODUCTION

Molybdenum concentrations and isotope compositions in sedimentary rocks are powerful proxies used to infer the oxidation state of the ancient atmosphere and oceans, due to the redox sensitivity of Mo (Anbar et al., 2007; Barling et al., 2001; Siebert et al., 2003). While Mo is generally hosted in weathering-resistant, titaniferous silicate and oxide phases in igneous rocks of the upper continental crust (UCC) (Greaney et al. 2018; Kuroda and Sandell, 1954), up to 60% of the Mo delivered to the UCC in felsic plutons may reside in hydrothermal molybdenite (MoS_2) (Greaney et al., 2018). Therefore, a significant fraction of UCC Mo is hosted in a mineral that is susceptible to oxidative weathering following the Great Oxidation Event (GOE) (Anbar et al., 2007; Greber et al., 2015). Once oxidized, Mo is removed from the UCC and transported by groundwater into rivers and, eventually, oceans.

Molybdenum and its redox sensitive host phase, molybdenite, are unique redox proxies because they are not only sensitive to the presence of O_2, but also to the presence of Fe-Mn oxides and organic matter in the weathering environment. There are presently few redox proxies capable of detecting the oxygenation of Earth's atmosphere, and even fewer which record the oxidation and colonization of Earth's earliest land masses. Sedimentary records of molybdenum isotopes can therefore elucidate the nature and magnitude of the GOE, as well as its impact in reshaping the terrestrial biosphere preceding the evolution of eukaryotes and animals.

4.1.1 Mo Isotope Fractionation during Continental Weathering

Modern rivers are isotopically heavy relative to the UCC, with a range of $\delta^{98}Mo$ between +0.2 and +2.3‰ (Archer and Vance, 2008). Some researchers suggest this offset

from crustal values results from adsorption of light Mo isotopes onto oxides in soils and river sediments during continental weathering (Archer and Vance, 2008; Pearce et al., 2010). Others propose that there is no net fractionation during weathering, and that average riverine values reflect weathering of a source that's heavier than average continental crust (Dahl et al., 2011; Neubert et al., 2011).

Recent case studies have addressed Mo isotope fractionation during weathering to determine the magnitude of fractionation and the species responsible for inducing fractionation. Wang et al. (2018) analyzed a saprolite weathering profile that formed on granite and found that Mo isotopes are generally lighter than the bedrock. The majority of light Mo in the soils is associated with Fe-(hyr)-oxides, as opposed to clays and organic matter, which were also present. This study concluded that Fe-Mn oxides in soils retain light Mo values, thereby leaving the complementary ground- and river-water isotopically heavy. Molybdenum isotope fractionation during adsorption onto Fe-Mn oxides has been well established in natural settings (Barling et al., 2001; Barling and Anbar, 2004) and laboratory environments (Goldberg et al., 2009; Wasylenki et al., 2008).

Recent work has also shown that Mo isotopes can be fractionated during adsorption onto organic matter in the same direction and to the same degree as Fe-Mn oxides, in that it adsorbs the lighter isotopes with similar fractionation factors as calculated as α = fluid/oxide (e.g., humic acid (organic matter): α =1.0017 per King et al., 2017; Fe-Mn oxides $1.0004 < \alpha < 1.0027$ per Goldberg et al., 2009 and Wasylenki et al., 2008). In a study of basaltic weathering profiles from Hawaii, Iceland, and Costa Rica, Siebert et al. (2015) conclude that factors other than Mo adsorption onto Fe-Mn oxides (e.g., organic matter, local redox conditions) may disrupt the expected fractionation due to adsorption onto oxides.

Additionally, King et al. (2016) found that while Hawaiian soils are typically lighter than the parent bedrock, there is no correlation between δ^{98}Mo and oxide content of the soil. These authors propose that atmospheric inputs and Mo complexion with organic matter may have a more significant fractionation effect than Mo adsorption onto oxides. Indeed, a mass balance of Mo in forest soils shows that organic matter can retain 40 times more Mo than Fe-Mn oxides (Marks et al., 2015). Finally, pH is known to play a significant role in Mo isotope fractionation during adsorption, because pH controls the protonation of the surface of the adsorbing phase and the protonation of soluble MoO_4^{2-} to MoO_3 or $MoO_3(H_2O)_3$ (the species that will adsorb to the surface of oxides or organic matter; Goldberg et al., 1998; Tossell, 2005; Oyerinde et al., 2008; Goldberg et al., 2008; King et al., 2018).

4.1.2 Glacial Diamictites Record Continental Weathering

To assess if Mo isotopes are fractionated during continental weathering we turn to glacial diamictites. Goldschmidt first proposed the use of glacial deposits as a means of obtaining a geochemical average of the UCC (Goldschmidt, 1933). As glaciers traverse over the exposed crust, they erode the uppermost weathered regolith and un-weathered crust beneath it, effectively averaging out large surface areas of continental crust. These sediments are then deposited as "diamictites" on continental margins or in glacial till deposits. Assuming the diamictites are not greatly weathered or altered after deposition, they record the chemical weathering signature of the UCC at the time of glaciation. These signatures provides a unique window into studying past interactions between the atmosphere and upper crust.

Gaschnig et al. (2014) presented data on glacial diamictites that span the last 2.9 billion years of Earth's history. They found that diamictites do show a UCC weathering

signature, recorded by Sr loss from nearly all samples as exhibited by a low Sr/Sr*

(Sr/Sr*=Sr/(Ce*Pr)$^{0.5}$) and an elevated chemical index of alteration (CIA). The weathering

signature of the diamictites was determined to have been inherited from their provenance, as

there is little to no evidence of post-depositional weathering or alteration (e.g., paleosols or

weathering profiles that formed on top of the deposits) and Li isotopes do not show

systematic changes downward in the diamictite units (Li et al., 2016). Molybdenum and

other redox sensitive metals (e.g., V) were discovered to be notably depleted from the

diamictites that formed after the GOE, suggesting Mo was removed due to oxidative

weathering and that these diamictites may record changes in atmospheric chemistry.

Twenty-four glacial diamictite composites were created by combining multiple

diamictite samples from the same place in space and time as analyzed in Gaschnig et al.

(2014). These composites were subsequently analyzed for major and trace elements and

oxygen isotopes (Gaschnig et al., 2016), Li isotopes (Li et al., 2016), platinum group

elements and Os isotopes (Chen et al., 2016), and Ba isotopes (Nan et al., 2018) and are

analyzed here for Mo isotopes and total organic carbon (TOC). The samples span four

modern continents and range in age from 300 to 2900 Ma. As these deposits record the

weathering signature at the time of glaciation, it can be inferred that the diamictites that

formed before the GOE (>2.4 Ga) record the weathering signatures of an extremely low

oxygen atmosphere (<10^{-5} present atmospheric level pO$_2$), while the diamictites that formed

during and after the GOE record the weathering signature of a relatively oxidized

atmosphere. In this study, we aim to use these diamictites to provide new, independent

constraints on Mo fractionation during continental weathering and determine if Mo isotopes

in the weathered crust record changes in atmospheric chemistry and soil redox.

4.2 METHODS

Molybdenum isotope data were collected at the W.M. Keck Laboratory for Environmental Biogeochemistry at Arizona State University. Sample aliquots containing 75 ng of Mo (between 30 and 300 mg of powder) were ashed at 550°C in a furnace overnight to remove organics. Powders were transferred to Savillex beakers and dissolved on a hotplate using a micture of 5 mL of concentrated HNO_3 and between 1 and 2 mL of concentrated HF, depending on the silica content of the samples. Immediately prior to dissolution, a ^{97}Mo-^{100}Mo double spike was added to the powders to produce a constant 2:1 ratio between the double-spike and sample derived Mo. After two days of hot plate dissolution, the solutions were evaporated to near-dryness and re-fluxed twice overnight in 1 mL of concentrated HCl to produce a clear solution free of precipitates. Finally, the samples were dried down and brought up in 1mL of 6M HCl for column chemistry.

Mo was purified from the sample matrix using a combination of anion and cation exchange chromatography following Romaniello et al. (2016). For anion chemistry, 2 mL of cleaned Biorad AG1X-8 anion exchange resin was loaded into the columns and rinsed with 10 mL of 1 M HCl. Twenty mL of 6 M HCl was then run through the columns for equilibration before the samples (in 6M HCl) were loaded. Sample elution was achieved using repeated volumes of 1M HCl from 0.5 mL up to 10 mL. The elution was dried down and brought in 6M HCl and anion column chemistry was repeated a second time. After the second round, samples were brought up in 0.5 M HCl. Biorad AG50WX-8 cation exchange resin was used for cation column chemistry. Two mLs of resin were loaded into the column then cleaned and equilibrated overnight in 10 mL of 0.5 M HCl. Afterwards, 10 mL of 0.5 M HCl + 0.01% H_2O_2 were added to the columns in order to keep Mo oxidized. The samples

127

hosted in 0.5 M HCl were added to the columns and Mo was eluted with repeated volumes of 0.5 M HCl + 0.01% H_2O_2 from 0.5 mL up to 10 mL. The final elution was dried down and brought up in 1 mL of concentrated HNO_3 + 200 µL of H_2O_2 twice to dissolve any remaining organic compounds. Finally, the samples were dried down and brought up in 3 mL of 2% HNO_3.

The isotopes ^{91}Zr, ^{92}Mo, ^{95}Mo, ^{96}Mo, ^{97}Mo, ^{98}Mo, ^{99}Ru, and ^{100}Mo were measured on the Thermo-Neptune Multi-collector ICP-MS on three samples aliquots of ~25 ng Mo. Ruthenium-99 was monitored to check for high organic content that could interfere with Mo measurements. A double spike inversion was performed using an in-house MATLAB script at ASU which uses non-linear optimization to simultaneously solve for the spike-sample ratio, instrument mass bias, and isotopic fractionation of the samples. Mo isotope data are reported as: $\delta^{98}Mo = 1000*[(^{98}Mo/^{95}Mo_{sample})/(^{98}Mo/^{95}Mo_{standard})-1]$ relative to the isotopic composition of NIST 3134 Mo standard (**Table 1).** The USGS shale SDO-1 was analyzed as a secondary standard and yielded a value of 0.79‰ (±0.03 2σ), in excellent agreement with published values (Goldberg et al., 2013). Additionally, the RGM-1, a rhyolite, was run as a secondary standard and produced a value of +0.03‰ (±0.01 2σ). Internal run precision and long-term precision are both ~ 0.04‰ (2σ). Organic C measurements were made at the University of Maryland. The samples were repeatedly washed in HCl and then Millipore 18Ω water to remove carbonate C and bring the sample up to near neutral pH, respectively. Aliquots of between 5 and 15 mg of sample were loaded in tin cups, then combusted and analyzed using an Eurovector element analyzer.

4.3 RESULTS

The diamictite samples are divided into three age periods: samples that formed before the GOE ("pre-GOE", 2430 – 2900 Ma), those that formed during or just after the GOE ("syn-GOE", 2200 – 2380 Ma), and those that formed significantly after the GOE in the Neoproterozoic/Phanerozoic (labelled "post-GOE", 300 – 755 Ma), based on stratigraphic age constraints (see references in Table 1). The pre-GOE samples are isotopically heavy (average +0.03‰) relative to the syn-GOE samples (average -0.29‰) and the post-GOE samples (average -0.45‰) (**Fig. 1**). The Ce/Mo ratio can be used to track the behavior of Mo during weathering relative to Ce, as the two behave similarly during igneous processes and Ce is relatively immobile during weathering. Therefore a change in Ce/Mo suggests that Mo is decoupled from Ce during weathering. As the δ^{98}Mo of the diamictites decreases over time, the Ce/Mo ratio increases from an average of 34 (pre-GOE) to 72 (syn-GOE) and finally to an average of 148 in the post-GOE samples (**Fig. 2**). The increasing Ce/Mo ratio results from a decreasing average [Mo] over time (pre-GOE = 1.4 ppm, syn-GOE = 1.1 ppm, post-GOE = 0.75 ppm) as well as an increase in Ce over time. While these absolute values may be diluted by the presence of quartz in the diamictite matrix, an increase in Ce/Mo ratios can be used to infer Mo loss. Using this ratio, the syn-GOE diamictites have lost 19% of their "expected" Mo budget relative to pre-GOE samples, and the post-GOE diamictites have lost 47% of their Mo budget. An ANOVA test reveals that there is a statistically significant difference between the δ^{98}Mo and the Ce/Mo ratio of the three populations at p=0.01. The Mo/Ce ratio is inversely related to the δ^{98}Mo value of the diamictites in that the isotopically light diamictites show a Mo depletion relative to modern UCC (Ce/Mo = 57, Rudnick and Gao, 2014).
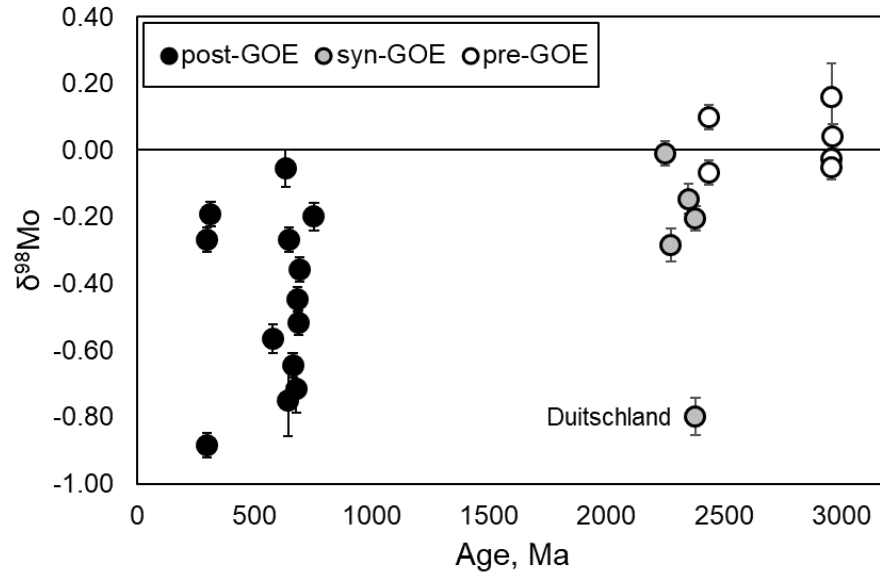
Figure 4.1. δ^{98}Mo data for the glacial diamictites plotted as a function of depositional age. Error bars represent in-run precision (2σ).

4.4 DISCUSSION

We present the first temporally constrained δ^{98}Mo values of the UCC, which record the onset of oxidative weathering and potentially the growth of biomass on land. The glacial diamictites contain two main geochemical signals. The first signal is a primary crustal evolution signature that records the transition of the continental crust from predominately mafic to felsic lithologies (Taylor and McLennan, 1985; Condie, 1993; Gaschnig et al., 2016; Tang et al., 2016).. Overprinted on this primary signature is a secondary chemical weathering signature, which is evidenced by Sr loss and elevated chemical index of alteration. Therefore, the temporal δ^{98}Mo trend observed in the diamictites could be driven by two processes: 1) isotope fractionation induced during crustal differentiation as the UCC evolves from mafic to felsic, or 2) isotope fractionation induced during weathering/removal of Mo from the UCC.
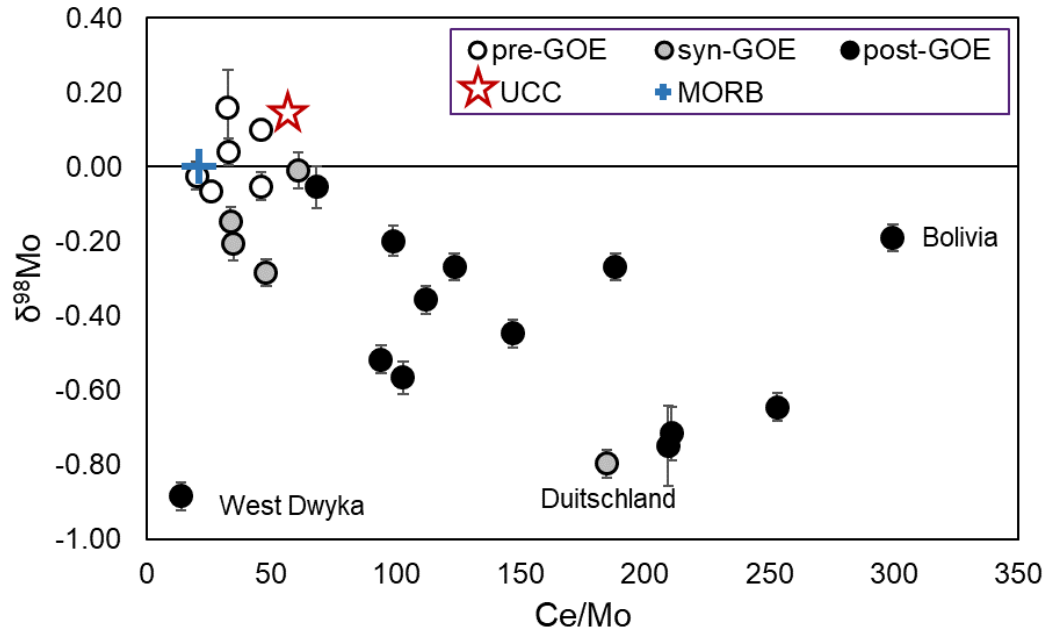
Figure 4.2. Correlation of δ^{98}Mo with Ce/Mo ratio. Average MORB [Mo]: Jenner and O'Neill (2012); δ^{98}Mo: Bezard et al. (2016); Liang et al. (2017) and modern UCC [Mo]: Rudnick and Gao (2014); δ^{98}Mo: Willbold and Elliot (2017) are shown for comparison.

Sample	Country	Age (Ma*)	Rel. GOE	δ⁹⁸Mo (‰)	2SD	TOC (wt%)	Mo† (ppm)
Mozaan Group	S. Africa	2965	pre	0.04	0.04	0.06	0.884
Afrikander Frm	S. Africa	2960	pre	0.16	0.10	0.03	0.471
Coronation Frm	S. Africa	2960	pre	-0.02	0.04	0.08	2.97
Promise Frm	S. Africa	2960	pre	-0.05	0.04	0.08	0.774
Ramsay Lake Frm	Canada (Ontario)	2436	pre	-0.07	0.04	0.07	2.29
Makganyene Frm	S. Africa	2436	pre	0.10	0.04	0.15	1.04
Bruce Frm	Canada (Ontario)	2380	syn	-0.21	0.04	0.05	1.46
Duitschland Frm	S. Africa	2380	syn	-0.80	0.06	0.12	0.547
Gowganda Frm	Canada (Ontario)	2350	syn	-0.15	0.05	0.06	1.78
Bottle Creek Frm	USA (Wyoming)	2275	syn	-0.28	0.05	0.05	0.578
Timeball Hill Frm	S. Africa	2250	syn	-0.01	0.04	0.15	1.3
Kaigas Frm	Namibia	755	syn	-0.20	0.04	0.08	1.01
Konnarock Frm	USA (Virginia)	665	post	-0.65	0.04	0.05	0.478
Gaskiers Frm	Canada (Newfoundland)	580	post	-0.57	0.04	0.06	0.559
Pocatello Frm	USA (Idaho)	685	post	-0.45	0.04	0.07	1.17
Nantuo Frm	China (Hubei)	645	post	-0.75	0.11	0.09	0.317
Gucheng Frm	China (Hubei)	680	post	-0.72	0.07	0.19	0.332
Blaubeker Frm	Namibia	693	post	-0.36	0.04	0.05	0.49
Chuos Frm	Namibia	690	post	-0.52	0.04	0.11	0.614
Numees Frm	Namibia	650	post	-0.27	0.04	0.10	0.425
Ghaub Frm	Namibia	635	post	-0.05	0.06	0.11	0.463
Bolivia Group	Bolivia	315	post	-0.19	0.04	0.26	0.239
Dwyka East	S. Africa & Namibia	300	post	-0.27	0.04	0.15	0.73
Dwyka West	S. Africa & Namibia	300	post	-0.89	0.04	0.31	2.88

*Age dates are averages of min and max dates provided by references, therefore should not be considered exact. Syn-GOE ages are estimated based on published ages and stratigraphic constraints relative to oxidatve weathering signature (see Gumsley et al., 2017).
†From Gaschnig et al. (2016)

Table 4.1. Mo isotope and select major and trace element data for the diamictite composites. All major and trace element data can be found in Gaschnig et al. (2016). See supplementary table S1 for references on the age and geologic setting on the diamictites.

4.4.1 Fractionation during crustal differentiation and evolution

The "pre-GOE" samples are isotopically heavier than the syn-GOE and post-GOE samples. Pre-GOE samples also contain more Mo and a higher average Ce/Mo ratio than the modern average UCC. While these observations could reflect a shift in the geochemistry of the "primary" igneous crust as it evolved from a more mafic to a more felsic endmember, we explain below that this is likely not the case.

The δ^{98}Mo signature of the modern un-weathered UCC is surprisingly difficult to pin down. Upper crustal igneous rocks and molybdenite grains display a wide range of δ^{98}Mo values, encompassing almost the entire range of fractionation seen in river and marine environments (Breillat et al., 2016). Archean komatiites (average -0.21 ± 0.28‰ 2σ; Greber et al., 2015) overlap with peridotites (-0.22 ± 0.06‰ 2σ; Liang et al., 2017) and both are slightly lighter than chondrites (average -0.16 ± 0.02‰ 2σ; Burkhardt et al., 2014), although these reservoirs overlap within error. Felsic igneous rocks vary from -0.35‰ to $+0.59$‰ (Freymuth et al., 2016; Voegelin et al., 2014; Yang et al., 2017, 2015), excluding samples affected by hydrothermal activity, while MORB (average -0.09 ± 0.02‰ 2σ) and OIB (average -0.14 ± 0.06‰ 2σ) tend to be relatively lighter than most felsic igneous rocks (Bezard et al., 2016; Liang et al., 2017). While no Mo isotope fractionation is observed by Yang et al. (2015) in an anhydrous intraplate setting, fractionation is proposed to occur in subduction zones, which leaves arc magmas – therefore the UCC – isotopically heavier than mafic and ultramafic rocks (Voegelin et al., 2014; Freymuth et al., 2015; König et al., 2016; Wille et al., 2018). Average estimates for the modern igneous UCC range between $+0.05$‰ and $+0.15$‰ (Voegelin et al., 2015; Yang et al., 2017; Willbold and Elliott, 2017).

Because arc magmas can be significantly isotopically heavier than the mantle and MORB (Freymuth et al., 2015; König et al., 2016; Wille et al., 2018), we would expect the evolution from a more mafic to more felsic continental crust to shift the UCC to heavier values with time. However, the secular trend recorded in the diamictites shows the opposite trend. The pre-GOE diamictites fall within the range of average modern continental igneous rocks, while the younger samples are isotopically lighter. Therefore, we conclude that the trend to lighter isotope values over time as recorded in the diamictites is not a product of igneous differentiation and the compositional evolution of the UCC.

4.4.2 Fractionation due to oxidative weathering

The decrease in the δ^{98}Mo values of the UCC with time is best explained by increased fractionation during oxidative weathering and Mo transport. On the modern Earth, molybdenum is removed from the exposed upper crust during the oxidative weathering of molybdenite, and transported in solution to rivers and eventually oceans, as evidenced by authigenic Mo enrichments in marine sediments (McManus et al., 2002; Miller et al., 2011). These marine enrichments above UCC values (~1.1 ppm: Rudnick and Gao, 2014) first appear in the rock record at the time of the GOE, suggesting there was limited oxidative weathering and Mo removal from the UCC before the GOE (Anbar et al., 2007; Scott et al., 2008; Wille et al., 2013). Complementary to the marine record, the diamictites record Mo loss from the UCC just after the GOE (Gaschnig et al., 2014), providing independent evidence for the hypothesis that Mo is transported from the UCC to oceans during oxidative weathering. As oxidative weathering increased with the increasing pO_2 of Earth's atmosphere, more oxidized Mo was available for fractionation in the weathering environment, consistent with the secular δ^{98}Mo trend of the diamictites. Thus, we propose

that the increased Mo isotope fractionation observed in the diamictites after the GOE is the result of an increased Mo reservoir from oxidative weathering. Because Mo is not depleted from the UCC relative to Ce before the GOE, we can conclude that the δ^{98}Mo value of the "primary" igneous crust in the Archean is +0.03‰ (±0.18). This is within error of modern estimates of the UCC (see previous section).
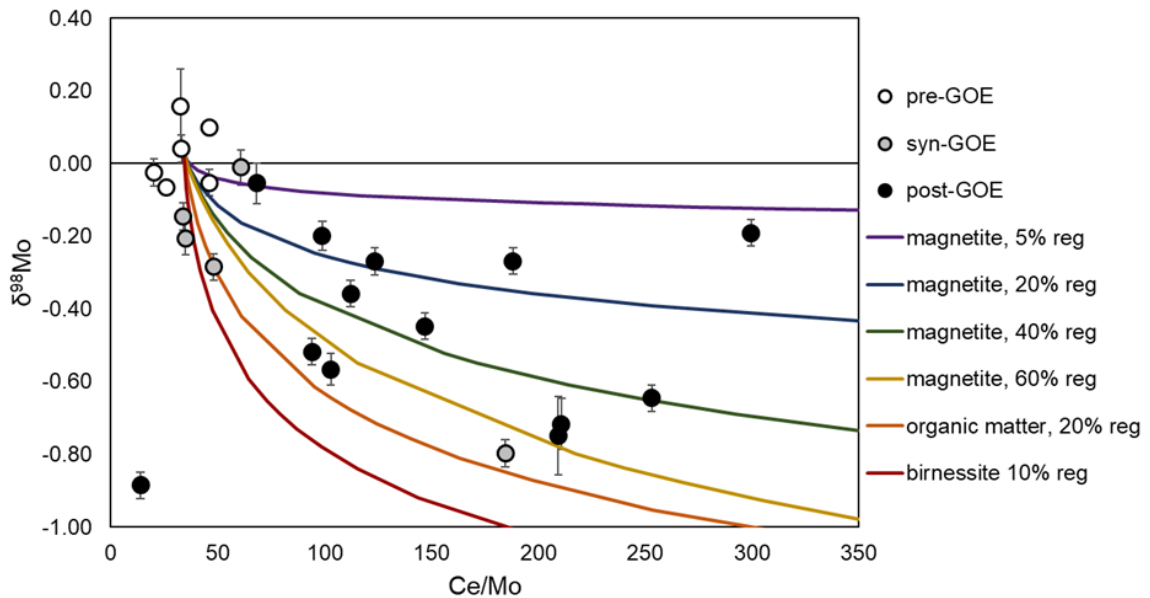
Figure 4.3. Results of the Rayleigh fractionation and mixing models. Endmember fractionation factors from Goldberg et al. (2009) are used, representing Mo adsorption to magnetite (solid lines) and hematite (dashed lines). A range of regolith:bedrock proportions are denoted as % reg (% regolith).

In-situ fractionation of Mo isotopes in soils has been proposed to explain the heavy riverine and seawater δ^{98}Mo signature (Siebert et al., 2003; Archer and Vance, 2008), and we show here that this *in-situ* fractionation is observed in the weathered-rock record beginning at the time of the GOE as well. Molybdenum isotope fractionation during weathering likely occurs during selective Mo adsorption onto Fe-Mn oxides or organic matter (OM) in the weathering profile. Fractionation between oxides and organic matter has been empirically determined and reported in multiple laboratory studies where isotopically

135

light Mo is adsorbed to the oxide or organic matter, while the Mo that remains in solution is relatively heavy (Barling et al., 2001; Barling and Anbar, 2004; Wasylenki et al., 2008; Goldberg et al., 2009; King et al. 2017). Experimental fractionation factors have been derived for the Mn-oxide birnessite (Wasylenki et al., 2008), the Fe-oxides hematite, magnetite, ferrihydrite, and goethite (Goldberg et al., 2009), and humic acid (King et al., 2018). We use these experimentally-derived fractionation factors to model the observed isotope fractionation in the diamictites.

4.4.2.1 Modeling the data

Rayleigh fractionation modelling supports the hypothesis that Fe-Mn oxides and/or organic matter incorporate light Mo isotopes into weathered regolith during weathering (**Fig. 4.3**). To build the mode, we assume that all initial Mo is derived from the igneous bedrock and fractionation occurs as Mo partitions between fluid that removes Mo from the system (e.g., groundwater) and oxides and/or organic matter that form in the weathered regolith. Dissociation and protonation of MoO_4^{2-} to MoO_3 or $MoO_3(H_2O)_3$ and subsequent adsorption to regolith-bound oxides or organic matter incorporates light Mo (Tossel et al. 2005; Oyerinde et al., 2008; Wasylenki et al. 2008), resulting in the removal of isotopically heavy Mo in groundwater. Here the oxides/organic matter are named "regolith" as we assume that all Mo retained in the weathered regolith is adsorbed to these phases. Isotope fractionation is modeled as equation (1) where α is the experimentally determined fractionation factor and F represents the fraction of Mo retained by the oxides:

$$\delta^{98}Mo_{regolith} = \delta^{98}Mo_{bedrock} - 1000 * F^{(\alpha-1)} - 1000 \qquad \textbf{(1)}$$

Fractionation factors (α = oxide/fluid) are derived from experimental work range from 0.9994 (magnetite – fluid fractionation) to 0.9973 (birnessite – fluid fractionation). We use a starting igneous bedrock value of 0.03‰ and a starting Ce/Mo ratio of 34, which are the pre-GOE averages of diamictites that have not lost and fractionated Mo. This calculation gives the δ^{98}Mo signature of the weathered regolith that contains oxides/regolith, but the diamictites are likely a mixture of weathered regolith in addition to un-weathered bedrock. Therefore, the fractionation signal imposed on the regolith during oxidative weathering may be diluted in the sampled diamictite, resulting in a poor fit to the data (**Fig. S4**). Therefore, to generate a model that more accurately mimics the diamictites, the resulting regolith is mixed with unfractionated igneous bedrock (δ^{98}Mo = 0.03, Ce/Mo=34) with equation (2) where F indicates the proportion of regolith and bedrock:

$$\delta^{98}Mo_{diamictite} = \left(\delta^{98}Mo_{regolith}\right) * F_{regolith} + (0.03‰) * F_{bedrock} \qquad \textbf{(2)}$$

The results of this model fit the syn- and post-GOE data well if the different diamictite deposits are composed of variable proportions of Mo derived from weathered regolith to Mo derived from un-weathered bedrock (**Figures 4.3, S5**). We can use the chemical index of alteration (CIA) to estimate the proportion of bedrock to regolith that compose the diamictites. If we assume that igneous bedrock has a CIA of 52 and highly weathered regolith has a CIA of 90, we can build the following mixing model (**eqn 3**), where X = proportion of bedrock.

$$CIA = X(52) + (1 - X)(90) \qquad \textbf{(3)}$$

The results of this model can be found in **Table 4.2** and the appendix and show that the syn- and post-GOE samples contain highly variable proportions of bedrock to regolith (between 5 and 79% weathered regolith). These variable mixtures of bedrock to regolith

137

partially explain the spread observed in the δ^{98}Mo and Ce/Mo, data as well as explain apparent outliers like the Duitschland sample (e.g., **Figure 4.4**). We can take this modelling exercise further and use the calculated proportion of bedrock:regolith to estimate the δ^{98}Mo and Ce/Mo values of the regolith that these diamictites sampled. Again, assuming that igneous bedrock has a δ^{98}Mo of 0.03‰ and a Ce/Mo of 34, we can plug in the calculated proportion of regolith and bedrock in the samples to the following equations:

$$\delta^{98}Mo_{diamictite,measured} = (1-X)(\delta^{98}Mo_{regolith}) + X(0.03) \quad \textbf{(4)}$$

$$Ce/Mo_{diamictite,measured} = (1-X)(Ce/Mo_{regolith}) + X(34) \quad \textbf{(5)}$$

These calculations result in regolith that is very isotopically light (Table 2, Figure 4) and matches the results of the Rayleigh modelling well. Again, these data support the hypothesis that oxides and/or organic matter form in the regolith during weathering and incorporate light Mo isotopes.
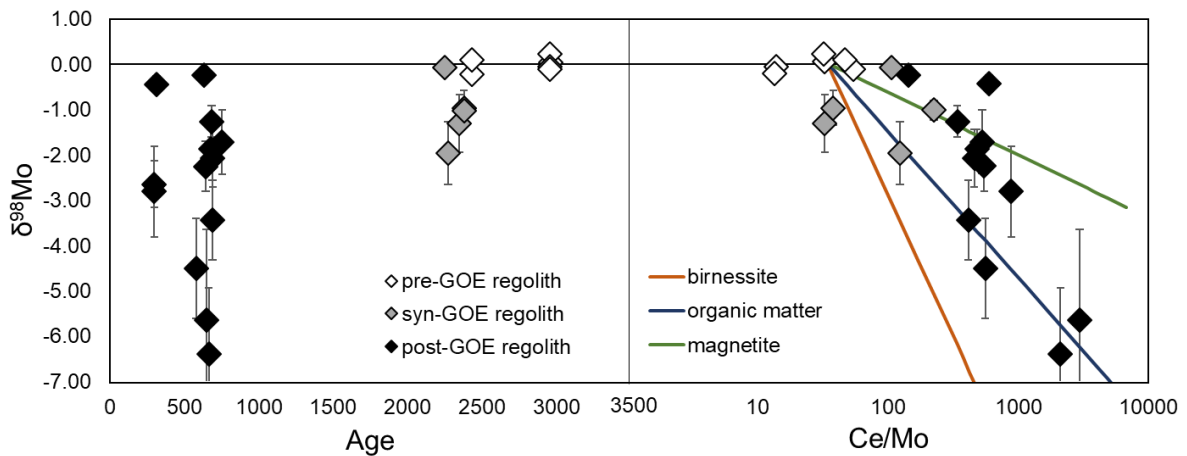
Figure 4.4. Calculated composition of the regolith that was incorporated into the diamictites. The Rayleigh model results of equation 1 without the additional mixing model fit these data well.

	age	proportion		calculated regolith		
Sample	Rel-GOE	% bedrock	% regolith	δ^{98}Mo	2s	Ce/Mo
Mozaan	pre	42	58	0.0	0.0	32
Afrkiander	pre	34	66	0.2	0.1	32
Coronation	pre	32	68	0.0	0.1	14
Promise	pre	39	61	-0.1	0.1	54
Ramsay Lake	pre	61	39	-0.2	0.2	13
Makganyene	pre	3	97	0.1	0.1	46
Gowganda	syn	87	13	-1.3	0.6	33
Bottle Creek	syn	84	16	-2.0	0.7	123
Bruce	syn	76	24	-1.0	0.4	38
Timeball	syn	63	37	-0.1	0.1	107
Duitschland	syn	21	79	-1.0	0.2	225
Konnarock	syn	89	11	-6.4	1.5	2116
Gaskiers	post	87	13	-4.5	1.1	559
Pocatello	post	63	37	-1.3	0.3	341
Nantuo	post	66	34	-2.2	0.5	547
Gucheng	post	61	39	-1.9	0.4	482
Blaubeker	post	82	18	-2.1	0.6	459
Kaigas	post	87	13	-1.7	0.7	528
Chuos	post	84	16	-3.4	0.9	415
Numees	post	95	5	-5.6	2.0	2964
Ghaub	post	68	32	-0.2	0.2	142
Bolivia	post	53	47	-0.4	0.2	595
Dwyka East	post	89	11	-2.8	1.0	885
Dwyka West	post	66	34	-2.6	0.5	NA

Table 4.2. Calculated proportion of bedrock and regolith contained in each diamictite composite along with the calculated δ^{98}Mo value and Ce/Mo ratio of the regolith. The Ce/Mo ratio of the regolith for Dwyka West could not be calculated because the original diamictite sample contained a lower Ce/Mo ratio than the Archean diamictites from which the "bedrock" Ce/Mo ratio was estimated.

4.4.2.2 Addressing outliers

The West Dwyka sample is as an outlier on a plot of δ^{98}Mo vs. Ce/Mo. While this diamictite was deposited at 300 Ma, much of the bedrock sampled by these glaciers was Archean to Proterozoic in age (Visser, 1982) which may contribute to the mixed signal reported here, in that the West Dwyka sample has not lost Mo relative to the pre-GOE samples. Additionally, the West Dwyka sample contains the highest TOC fraction of the diamictites (0.31 wt%, Table 1), suggesting that organic matter may influence the Mo isotope signature of this relatively modern sample that formed at the end of the Carboniferous Period when land-plants flourished.

The Duitschland diamictite, an outlier from the other syn-GOE samples, seemingly displays a very strong oxidative weathering signature (Fig. 1). Not only does the Duitschland show a Mo depletion with a low δ^{98}Mo, but it is also the only Paleoproterozoic diamictite to be depleted in U (as observed in a high Th/U ratio of 6.4 while the average of all diamictites is 4.3, **Figure 5**), which is a feature found in some Neoproterozoic diamictites, but not observed at other time periods (Gaschnig et al., 2014; 2016). It is also strongly depleted in V, consistent with a strong oxidative weathering signature (Gaschnig et al., 2014). This apparently different sample can be explained by the fact that the Duitschland diamictite has a higher proportion of regolith to bedrock than the other syn-GOE samples, therefore it more faithfully records the weathering conditions at the time of the GOE. When the samples are corrected for the bedrock input (**Figure 4**), Duitschland is no longer an outlier and all of the syn-GOE samples contain regolith with similar δ^{98}Mo values. These "bedrock-corrected" regolith values may be used in future modeling studies to place constraints on the amount of atmospheric O2 needed to mobilize and fractionate Mo

isotopes enough to generate the signatures seen between the syn-GOE and post-GOE samples.

4.4.2.3 Other oxidative weathering signatures

Of the entire trace element suite measured in Gaschnig et al. (2016), negative correlations are observed between δ^{98}Mo and [Ba] and Mo and Th/U (R^2=0.75, excluding Duitschland and West Dywka as outliers and R^2=0.63, excluding West Dwyka, respectively) in the diamictites (**Fig. 5**). While these correlations may reflect changing UCC composition, we suggest instead that they further reflect changing atmospheric conditions. Detrital uraninite is found in sediments >2.4 Ga, indicating that uraninite was a stable mineral on the Earth's surface prior to the GOE (Johnson et al., 2014 and references therein). Diamictites that incorporated these uraninite-bearing sediments may have low Th/U (<3.8) due to the increased abundance of U compared to post GOE sediments. An increase in Th/U with time therefore suggests U is being removed from the continents as soluble U^{6+}, similar to Mo. This is supported by U enrichments in black shales over time (Partin et al., 2013).
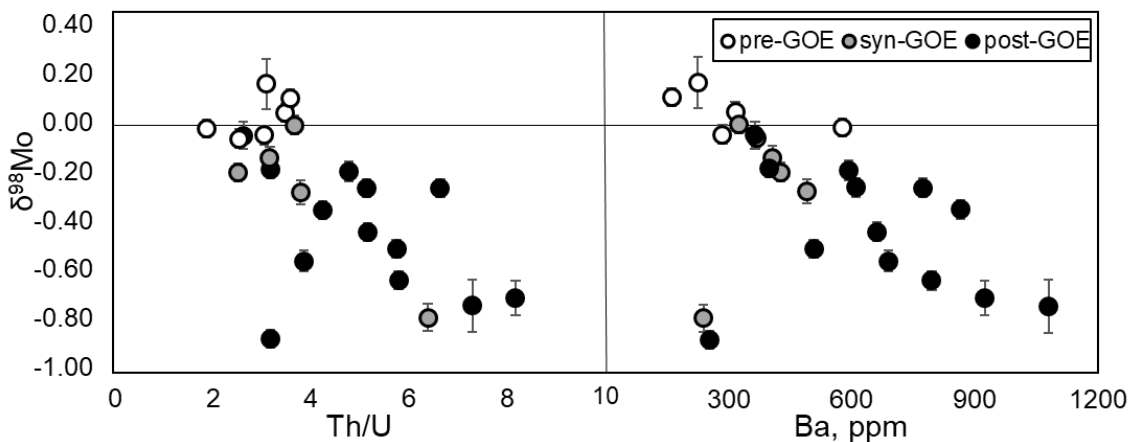

Figure 4.5. Correlations between δ^{98}Mo and Th/U and Ba.

The negative correlation observed between δ^{98}Mo and Ba may also be explained by a change in atmosphere composition, rather than a changing UCC. Widespread stabilization of barite (BaSO$_4^{2-}$) in sediments may have caused an increase in the Ba concentration of weathered regolith sampled by diamictites over time, due to the increase abundance of oxidized sulfur in the form of sulfate (Canfield, 2005). We conclude that inverse correlations of U and Ba concentrations with δ^{98}Mo are a result of increased O$_2$ levels, which preferentially removed U^{6+} from UCC, and retained Ba in sulfate deposits following the GOE.

4.4.2.4 The role of Fe-Mn oxides and organic matter

Given these data and results of Rayleigh fractionation modeling, we conclude that Mo isotopes in the diamictites record the onset of oxidative weathering at the time of the GOE, as oxygen is needed to liberate Mo from molybdenite in the crust. While we cannot confidentially determine whether Fe-Mn oxides or organic matter are the dominant phase that incorporates light Mo isotopes in the regolith, it is clear that oxidative continental weathering results in Mo isotope fractionation due to one or both of these phases. There is a slightly more robust correlation between δ^{98}Mo and Fe$_2$O$_3$ and MnO than between δ^{98}Mo and organic matter (supplementary figures 1 and 2), suggesting that Fe-Mn oxides may play a stronger role in long-term retention of light Mo in weathered regolith. The presence of Fe-Mn oxides in soils is, in itself, an oxidative weathering signature, as these phases are not expected to be stable under an anoxic atmosphere (Murakami et al., 2011). Therefore, the correlation between the stabilization of oxides in soils after the GOE and the onset of Mo isotope fractionation during weathering is expected. If organic matter is the primary

142

fractionating mechanism, then the diamictites may also record an increase in continental

biomass in addition to oxidative mobilization of Mo.
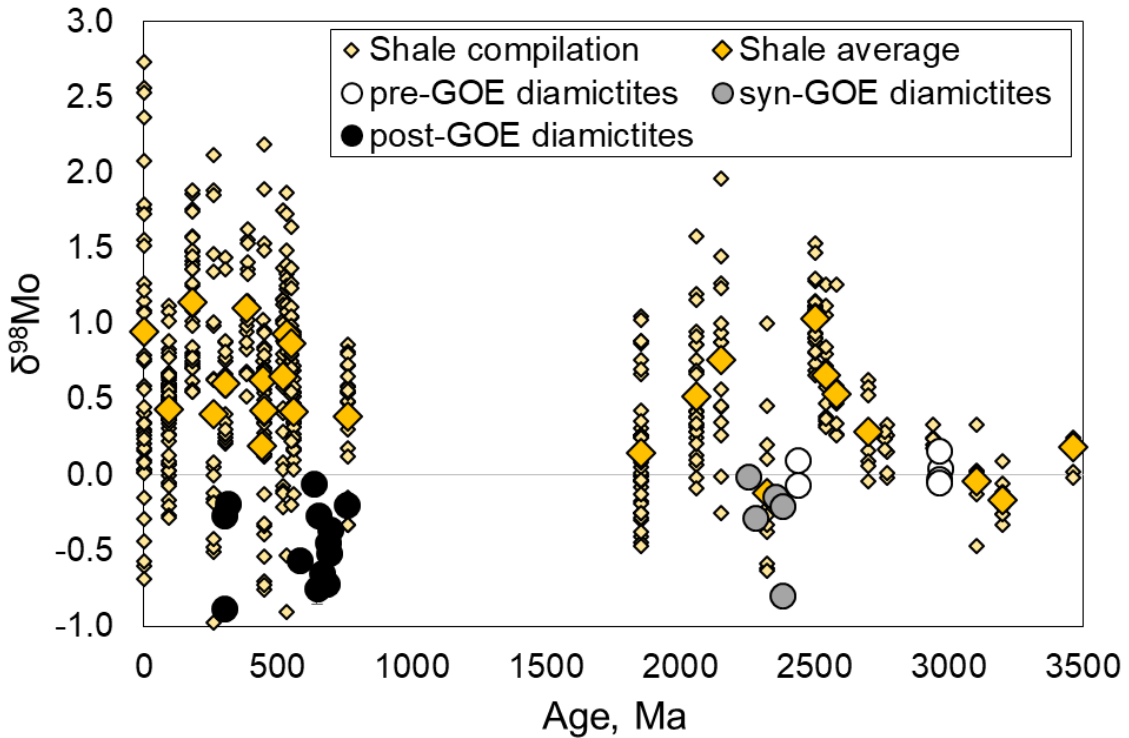
Figure 4.6. Marine shales and sediments in yellow diamonds show the complementary signature to the weathered upper crust as represented by the diamictites. The average δ^{98}Mo value for each shale group is presented in the larger diamond. Shale data are taken from Goldberg et al. (2016), Lu et al. (2017), Yin et al. (2018), Cheng et al. (2016), Kurzweil et al. (2015; 2015b), Siebert et al. (2005), Pearce et al. (2010), Wille et al. (2013), Wille et al. (2008), Duan et al. (2010), Gordon et al. (2009), Scheiderich et al. (2011), Dahl et al. (2011), Kendall et al. (2011), Hermann et al. (2012), Zhou et al. (2012), Asael et al. (2010). The data are recalculated to be normalized to NIST 3134.

4.4.3 Implications for δ^{98}Mo of river water through time

We show here that modern weathered continental crust is isotopically light and

provides a complementary reservoir for modern rivers that are isotopically heavy relative to

the UCC (Archer and Vance, 2008). Some researchers attribute this to adsorption of light

Mo isotopes onto oxides in regolith during continental weathering (Archer and Vance, 2008;

Pearce et al., 2010), while others propose that that heavy riverine values instead reflect

weathering of a source that's heavier than average continental crust, such as molybdenite (Dahl et al., 2011; Neubert et al., 2011). The temporal trend of the upper continental crust, as recorded by diamictites, mirrors that of marine shales suggesting that mass balance is maintained over time (Figure 6). We can infer that the Mo isotope signature of Archean rivers was likely indistinguishable from Archean crust. These rivers were likely nearly devoid of Mo without oxidative weathering to liberate Mo from molybdenite in the crust. However, Mo may have been released from weathering of basaltic glass (Greaney et al., 2017) or other weathering-susceptible Mo-bearing phases, and the lack of Fe,Mn - oxides in pre-GOE soils (Murakami et al., 2011) would have resulted in an Archean riverine Mo isotopic signature identical to that of the Archean crust (~0.03‰). Because rivers produce supply 90% of Mo to oceans (McManus et al., 2002; Miller et al., 2011), this likely means that any Mo in pre-GOE oceans would have also been isotopically similar to the UCC. This is evidenced by pre-GOE marine shales that show a similar Mo isotopic signature (average δ^{98}Mo = +0.18‰ ± 0.22) to the pre-GOE diamictites, within analytical error (Figure 6).

CONCLUSIONS

A secular change in δ^{98}Mo of the weathered UCC is observed in glacial diamictites that were deposited between 2900 and 300 Ma. The δ^{98}Mo signature of the diamictites that formed before the GOE (average 0.03‰) is similar to the range that encompasses continental igneous rocks while the diamictites that formed during and after the GOE (average –0.29‰ and –0.45‰, respectively) are significantly lighter. We use the pre-GOE data to establish that the δ^{98}Mo signature of the "primary" Archean continental crust, before undergoing Mo removal and fractionation via oxidative weathering, is +0.03‰. We conclude that the shift in Mo isotopes to lighter values with time is due to fractionation

144

during weathering, as isotopically light Mo is adsorbed onto authigenic/residual Fe-Mn oxides or organic matter in soils and sediment. This can only occur under an oxidized atmosphere that mobilizes Mo. These data imply that Mo isotope fractionation occurs immediately during weathering, and that the Mo removed from the continents should be isotopically heavy. The isotopically light weathered continental crust is therefore a complementary reservoir to isotopically heavy rivers.

Chapter V. Assessing molybdenum isotope fractionation during the various stages of continental weathering as recorded by saprolites and bauxites

To be submitted to Chemical Geology

With coauthors: Roberta L. Rudnick[1,2], Stephan J. Romaniello[3], Ariel D. Anbar[3,4], Michael Cummings[5]

[1]University of California - Santa Barbara, Department of Earth Science, Santa Barbara, CA 93106

[2]University of Maryland College Park, Department of Geology, College Park, MD, 20742

[3]Arizona State University, School of Earth and Space Exploration, Tempe, AZ 85281

[4]Arizoza State University, School of Molecular Sciences, Tempe, AZ 85281

[5]Portland State University, Department of Geology, Portland, OR 97207

Author Contributions

A.T. Greaney conceived the study, carried out the analyses and data interpretation, and wrote the manuscript.

R.L. Rudnick conceived the study, provided samples, aided in data interpretation, and will provide edits on the manuscript.

S.M. Romaniello provided analytical assistance, aided in data interpretation, and will provide edits on the manuscript.

A.D. Anbar aided in data interpretation and will provide edits on the manuscript.

M. Cummings provided the bauxite samples and will provide edits on the manuscript.

ABSTRACT

In order to investigate the behavior of Mo stable isotopes during continental weathering, we measured Mo isotopes in three deep and well-characterized weathering profiles: a saprolite profile formed on meta-diabase from South Carolina, USA, and two ferruginous bauxites, that formed on the Columbia River Basalts in Oregon, USA. Saprolites show an overall loss of Mo relative to the fresh bedrock and are isotopically lighter (δ^{98}Mo range from –0.89 to –0.05‰, mean = –0.40‰, cf. +0.55‰ for the bedrock). By contrast, the ferruginous bauxites generally show an addition of Mo relative to the fresh bedrock (determined by calculating tau-Mo values relative to immobile Ti), and the bauxites have systematically higher δ^{98}Mo than the parent basalts (δ^{98}Mo bauxites = –0.14 and +0.38‰ compared to +0.02‰ to +0.38‰ for the fresh bedrock. The low δ^{98}Mo values in the saprolites likely reflect partial Mo adsorption onto clays and accessory Fe-oxides during weathering, whereas the high δ^{98}Mo values in the bauxites reflect the addition of isotopically heavy Mo from groundwater or precipitation. When the three profiles are combined, there is a trend between τ_{Mo} and δ^{98}Mo, suggesting that when Mo is lost during continental weathering, the resulting regolith is isotopically light, whereas groundwater addition can shift the regolith to heavier values. Because saprolites are a more ubiquitous weathering product than bauxites, we conclude that, in general, continental weathering fractionates Mo isotopes, resulting in an isotopically light weathered upper crust and causing the groundwater that leaches Mo from the weathered crust to be isotopically heavy. This process likely contributes to the isotopically heavy global riverine signature.

5.1 INTRODUCTION

Molybdenum geochemistry has emerged at the forefront of paleo-redox proxies given that it is hosted in molybdenite in the crust – a mineral whose weathering rate is a function of oxygen content in the atmosphere – and that Mo is soluble when oxidized to its hexavalent state. Generally, paleo-redox studies involve the interpretation of marine Mo isotope data to determine the chemical state of the oceans or atmosphere at the time of deposition (e.g., Duan et al., 2010; Wille et al., 2013; Kendall et al., 2017; and references therein). These studies rarely address possible Mo isotope fractionation produced during continental weathering, which may be an important step in generating the Mo isotope signatures of marine sediments. For example, seawater (+2.3‰; Siebert et al., 2003) and river water (+0.7; Archer and Vance, 2008) are isotopically heavier than the igneous continental crust (average between +0.05 and +0.20‰; Voegelin et al., 2014; Willbold and Elliott, 2017; Yang et al., 2017), and this fractionation is often attributed to fractionation that occurs within seawater or river water, like absorption onto Fe-Mn oxides and nodules (Siebert et al., 2003; Barling et al., 2001). However, continental weathering may also induce isotope fractionation that contributes to the difference between water and the continental crust (Archer and Vance, 2008; Pearce et al., 2010; Greaney et al., in prep – Chapter 4).

5.1.1 Mo isotope fractionation in weathering profiles

Iron-manganese (hydr)-oxides are known to preferentially adsorb light Mo isotopes, leaving heavier isotopes in solution. This was first observed naturally in oxic pelagic sediments (Siebert et al., 2003; Barling et al., 2003) and has since been demonstrated experimentally through adsorption of Mo onto goethite, magnetite, hematite, ferrihydrite, and birnessite (Barling and Anbar, 2004; Goldberg et al., 2008; Waslynski et al., 2009). This

149

adsorption in oxic marine settings has been suggested to be the cause of the heavy seawater signature. However, in a recent study of Mo isotope fractionation in a saprolite profile found that adsorption onto Fe-Mn oxides induces Mo isotope fractionation, suggesting that continental weathering may have similar effects (Wang et al., 2018).

Molybdenum concentration correlates with organic carbon in black shales (Anbar et al. 2007; Chappaz et al., 2014; Dahl et al., 2017), suggesting that organic matter may serve as an important scavenger of Mo and may also lead to isotopic fractionation. In studies of forest soils, Wichard et al. (2009) found that ~25% of Mo is complexed by organic matter in the organic-rich topsoil, while Marks et al. (2015) found that, on average, 33% of bulk soil Mo is complexed to organic matter. When molybdate (MoO_4^{2-}, the dominant Mo compound in oxidized waters) complexes with leaf litter, for example, it changes coordination state from tetrahedral to octahedral (Wichard et al. 2009), and one might presume that an isotope fractionation would accompany such change. In Hawaiian soils, a positive correlation exists between δ^{98}Mo and organic carbon abundance (King et al., 2016). This suggests that organic matter incorporates heavy Mo isotopes, thus inducing the opposite fractionation as Fe,Mn-oxides. By contrast, King et al. (2018) showed experimentally that lighter Mo isotopes are adsorbed onto humic acid, the lighter Mo isotopes are retained by organic matter, much like what is observed during Fe-Mn oxide adsorption. This is the opposite of what is observed in natural weathering profiles of King et al. (2016) and (2018), where δ^{98}Mo is positively correlated with organic matter. King et al. (2018) attribute Mo isotope signature of the soil profiles to late addition of isotopically heavy atmospheric inputs coming from precipitation and volcanic fog. These studies that highlight the potential importance of organic matter were performed in shallow soil settings (< 100 cm).

A comprehensive study on the behavior of Mo isotopes in three weathering profiles from Hawaii, Puerto Rico, and Iceland found that redox conditions, organic matter, Fe,Mn-hydroxides, degree of weathering, pH, atmospheric inputs, climate, and parent rock type can all influence Mo isotope fractionation during continental weathering (Siebert et al. 2015), again suggesting that continental weathering may have a significant influence on the global Mo isotope cycle. Soils that show a net Mo loss retain light Mo isotopes, relative to the parent rock, while soils with a net Mo gain are offset to heavier isotopic values than the parent material. Molybdenum is correlated with organic matter in soils that show a net Mo gain. Again, this study mostly sampled shallow soils (< 130 cm) with the exception of one deeper saprolite from Puerto Rico.

Finally, aluminum oxides (e.g., gibbsite) and some clays (e.g., montmorillonite) are capable of adsorbing Mo at low pH and may also play a role in Mo isotope fractionation during continental weathering (Goldberg et al., 1996). The pH of the soil will play a strong role in overall Mo adsorption, no matter the adsorbing phase. Goldberg et al. (1996) show that nearly 100% of Mo is retained in acidic soils at a pH < 4, with about 0% retention occurring at pH > 8. Overall, Fe-Mn oxides, organic matter, pH of the soil, and atmospheric inputs may also play a large role in generating Mo isotope fractionation during continental weathering.

5.1.2 Reconciling temporal trends with weathering patterns

A global shift in the geochemical behavior of Mo is observed across the Archean-Proterozoic boundary, coinciding with the GOE at ~2.4 Ga. Net Mo enrichment and isotope fractionation towards heavier values are observed in black shales that formed in euxinic ocean basins at the time of the GOE (Anbar et al., 2007; Scott et al., 2008; Duan et al., 2010;

Wille et al., 2013), and simultaneous Mo depletion and isotopic fractionation towards lighter

values in glacial diamictites that sample weathered upper continental crust from ~2.4 Ga

onwards (Gaschnig et al., 2014; Greaney et al., in prep). It is hypothesized that the rise of O_2

resulted in the weathering of molybdenite and release of soluble Mo from the crust, and

deposition of this Mo in euxinic ocean basins. While it has been proposed that the

continental crust evolved from more mafic to felsic over time (Condie 1993; Tang et al.

2016; Gaschnig et al. 2016), the observed shift in the δ^{98}Mo signature of weathered UCC

over time is unlikely to reflect changing bulk composition because felsic igneous rocks have

higher δ^{98}Mo (Willbold and Elliot, 2017; Yang et al., 2017) than mafic rocks (average ~

–0.09‰ Bezard et al., 2016; Liang et al. 2017; Greber et al. 2015). Thus, the igneous UCC

should have evolved to isotopically heavier values as it shifted from mafic to felsic.

In this paper, we attempt to synthesize previously published data on Mo isotopic

fractionation during weathering and contribute new data on Mo isotopic fractionation in

saprolite and bauxite weathering profiles. We use these data to determine whether

continental weathering can explain the temporal Mo isotope shift of the weathered upper

continental crust recorded by glacial diamictites.

5.2 SAMPLES

To assess the influence of chemical weathering on Mo isotopes we analyzed weathering

profiles through a saprolite and two bauxites that represent different weathering end

members. Saprolites form under relatively moderate weathering conditions where clays are

the stable and dominant mineral species, whereas bauxites form under intense leaching

conditions in the presence of added rainwater or groundwater where Si is removed

152

(Schellman 1994). The saprolite and bauxite samples studied here were originally collected and characterized by Gardner et al. (1981) and Fassio (1990), respectively.

Seventeen samples from a saprolite profile that formed on a meta-diabase in South Carolina were selected for analyses. The samples span 11 m depth and formed in the Tertiary in a subtropical climate; the current MAP is 1200 mm/yr with a current MAT of 18°C (Gardner et al., 1981; Rudnick et al., 2004). The saprolites are formed on a diabase dike that experienced greenschist facies metamorphism as determined by the significant abundance of talc and chlorite (Rudnick et al. 2004). It is unknown exactly when these saprolites formed, but similar saprolites in the Piedmont of Virginia have been estimated to have formed in the Miocene (Pavich and Obermeier, 1985). The saprolites are primarily composed of kaolinite and smectite, as determined by XRD (Gardner et al., 1981). A redox discontinuity is observed at ~2 m depth, above which Fe-rich smectite and Fe-hydroxides formed in a relatively oxidizing environment, and below which kaolinite is the dominant assemblage reflecting more reducing conditions (**Figure 5.1**). Siderite veins are found just below the 2 m discontinuity suggesting that reducing conditions allowed Fe to become soluble. These saprolites have been previously studied for Li, Mg, Cu, and Fe isotopes (**Figure 5.1**; Rudnick et al., 2004; Teng et al., 2010; and Liu S. et al., 2014). The Cu and Fe isotope data suggest that Fe-oxides formed by the oxidation of siderite in the uppermost 2 m of the profile. This oxide precipitation scavenged light Fe and heavy Cu isotopes (Liu S. et al. 2014).

The bauxites developed on the ~16 Ma Columbia River Basalts on the western and rainy side of the Cascade Mountains in Columbia County, Washington and Cowlitz County, Oregon. All samples come from drill core. The present day Mean Annual Precipitation

(MAP) is ~ 1100 mm/yr and Mean Annual Temperature (MAT) is ~11°C (Liu et al., 2013; Western Regional Climate Center), however it is likely that the bauxites formed in a warmer and more humid environment (e.g., ~20°C and 120 mm/yr MAP; Bogatyrev et al., 2009 and references therein). Eight samples span each bauxite profile, named Columbia and Cowlitz, to ~8 m depth. As the drill cores did not penetrate fresh basalt, the parental basalts were collected elsewhere (see details in Liu et al., 2013). The bauxites are composed of gibbsite, halloysite, ±kaolinite, hematite, goethite, ±maghemite, and the uppermost samples contain quartz, as determined by XRD (Liu et al., 2013, Fassio 1990). The bauxite profiles can be divided into two major zones: an upper zone containing varying proportions of iron pisolites (**Table 5.1;** Supplementary Figures – Appendix E), and a lower zone composed of nodular gibbsite (Fassio 1990). This separation into a ferruginous layer overlying an aluminous layer is a common feature of bauxite deposits (Schellman 1994; Bogatyrev et al., 2009). Both profiles have been previously analyzed for Li, Nd, and Mg isotopes (Liu et al., 2013; Liu et al., 2014). Lithium fractionation was observed in all profiles, resulting in offset to lighter δ^7Li values. Net Mg fractionation was also observed in all profiles, resulting in offsets to heavier $\delta^{26}Mg$. However, Liu et al. (2013) also determined that aeolian dust was added to the bauxite samples in the upper 3 m of the weathering profile, given the presence of quartz and less radiogenic Nd isotope values. The dust did not significantly affect the δ^7Li signature, but did add lighter Mg to the top 3 m of the bauxites.

Here we measure $\delta^{98}Mo$ in the above described saprolite and bauxite weathering profiles to improve our understanding of the behavior of Mo isotope fractionation during these different stages of continental weathering. With these data we an aim to establish whether Mo is systematically fractionated during continental weathering and thereby better interpret

154

the temporal trend of the weathered UCC towards lighter Mo values, as recorded by the glacial diamictites in Greaney et al. (in prep – chapter 4).

5.3 METHODS

Mo isotope and trace element analyses were carried out in the W.M. Keck Foundation Laboratory for Environmental Biogeochemistry at Arizona State University. Molybdenum and other trace element concentrations were measured on an iCAP Quadropole ICP-MS with data reduction done by calibrating counts per second (CPS) relative to synthetic standard solutions. Precision on Mo is generally better than 8%. Molybdenum isotopes were analyzed using a Mo double spike method and a Neptune MC-ICP-MS. Methods follow that of Greaney et al. (in prep – chapter 4) and are replicated in the supplementary information.in Appendix E. Molybdenum isotope data are reported as $\delta^{98}Mo = 1000*[(^{98}Mo^{/95}Mo_{sample})/(^{98}Mo^{/95}Mo_{standard})-1]$, using the NIST 3134 standard. The USGS standard SDO-1, a Devonian shale, was dissolved and run alongside the samples to assess data quality. SDO-1 shows excellent reproducibility of literature values, with an average composition of $+0.79 \pm 0.03$‰ (**Table 5.1**). All uncertainties are reported as 2σ. Additionally, the USGS standard RGM-1, a rhyolite, was analyzed and yielded a $\delta^{98}Mo$ value of $+0.03 \pm 0.04$‰, in excellent agreement with previous analyses (Greaney et al. in prep – chapter 4). Long term reproducibility is 0.04‰.

	Depth (m)	δ^{98}Mo	2s	Mo (ppm)	2s	τMo - Ti	Δ^{98}Mo$_{BR-WP}$
SDO-1		0.79	0.03	154	11.7		
RGM-1		0.03	0.04	2.41	0.18		
Saprolites							
M1	0.10	-0.56	0.05	0.21	0.02	-0.63	1.10
M3	0.50	-0.05	0.06	0.41	0.03	-0.44	0.60
M4	1.00	-0.06	0.08	0.38	0.03	-0.18	0.61
M5	1.50	-0.57	0.14	0.68	0.05	0.31	1.12
M6	2.00	-0.34	0.05	0.75	0.06	0.25	0.88
M7	3.00	-0.05	0.05	1.69	0.13	0.99	0.59
M8	4.00	-0.51	0.06	0.51	0.04	-0.39	1.06
M9	5.00	-0.89	0.05	0.28	0.02	-0.65	1.44
M10	6.00	-0.58	0.06	0.38	0.03	-0.51	1.13
M11	7.00	-0.23	0.01	0.27	0.02	-0.58	0.78
M12	8.00	-0.16	0.04	0.29	0.02	-0.57	0.71
M13	9.00	-0.35	0.03	0.28	0.02	-0.64	0.90
M14	10.00	-0.63	0.04	0.32	0.02	-0.60	1.17
L14-8	10.00	-0.16	0.02	0.42	0.03	-0.34	0.70
L14-9	10.00	ND	ND	0.25	0.02	-0.59	0.55
M15	11.00	-0.83	0.07	0.27	0.02	-0.65	1.38
M20- BR		0.55	0.01	0.60	0.05		
Columbia							
514	2.74	0.19	0.01	5.57	0.42	3.76	0.52
516	3.96	0.19	0.00	6.09	0.46	3.44	0.52
518	4.57	0.14	0.03	7.83	0.59	2.74	0.47
5110	5.49	0.26	0.04	16.53	1.26	3.57	0.59
5112	6.71	0.34	0.02	12.03	0.91	3.56	0.67
5114	7.32	-0.09	0.04	3.49	0.27	0.07	0.24
5115	7.92	-0.14	0.04	3.03	0.23	0.04	0.20
POM - BR		-0.33	0.11	0.73	0.06		
Cowlitz							
931	2.13	0.28	0.05	4.66	0.35	1.67	0.27
933	2.74	0.38	0.05	8.03	0.61	2.75	0.37
9310	5.79	-0.13	0.06	1.76	0.13	-0.11	0.14
9319	6.25	-0.10	0.07	1.51	0.12	-0.11	0.12
9321	7.62	-0.07	0.02	1.44	0.11	-0.23	0.08
9322	8.23	0.00	0.06	1.97	0.15	0.03	0.01
9323	9.14	-0.16	0.06	1.23	0.09	-0.30	0.18
SB1- BR		0.02	0.02	0.90	0.07		

Table 5.1. Molybdenum concentration and isotope data for the three profiles studied here. BR stands for bedrock.

5.4 RESULTS

5.4.1 Saprolites

The saprolites contain between 0.21 and 1.69 ppm Mo, with an average of 0.46 ppm. Mo isotope values range between –0.89 and –0.05‰, with an average of –0.40‰ (**Table 5.1**). Sample M20 is estimated to be the best representation of the metamorphosed diabase bedrock and contains 0.60 (±0.05) ppm Mo with an isotopic signature of +0.55‰. There is no systematic variation in Mo concentration or isotope fractionation with depth in the profile, with the exception of the samples that lie at or above the 2m redox discontinuity (**Figure 5.1**). In **Figure 5.1** and subsequent figures, the top five samples are shaded darker to represent the different redox environment that they formed in. These samples are more oxidized and have a kaolinite/smectite (K:S) ratio of <1 while the samples below this boundary are more reducing with a higher kaolinite/smectite ratio. Molybdenum mobility during weathering is calculated as tau (τ) relative to the immobile element Ti, where WP = weathering profile and BR = bedrock in the following calculation:

$$\tau_{Ti}^{Mo} = \left(\frac{Mo_{WP} * Ti_{BR}}{Ti_{WP} * Mo_{BR}}\right) - 1 \qquad \textbf{(1)}$$

Positive tau values indicate that Mo was gained relative to immobile elements, while negative tau values indicate that Mo was lost. All saprolite samples, save three, have lost Mo (**Figure 5.2**). The three samples that have gained Mo sit at the redox-interface at between 2 and 3 meters depth.
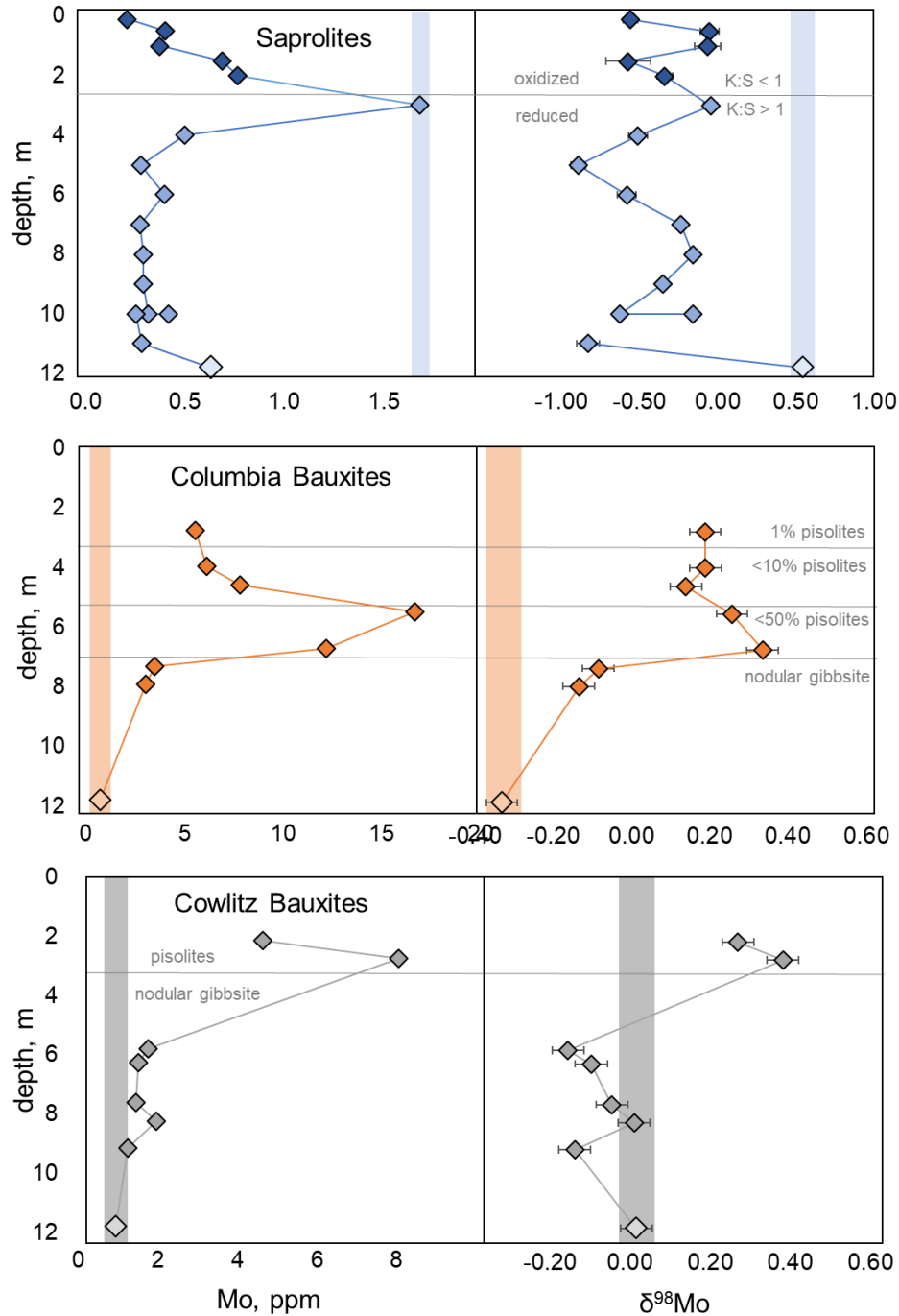
Figure 5.1. Variations in Mo concentration and isotope fractionation with depth. The highlighted bar represents the bedrock in the figures, and the bedrock value is also plotted at 12 m depth. In the case of the bauxites, fresh bedrock was not encountered in the drill hole, so fresh basalts of the same member were sampled elsewhere. In the saprolite profile, the kaolinite:smectite ratio change is denoted by K:S and the samples that formed above this redox discontinuity are colored dark blue. The iron pisolite and gibbsite layers are delineated in the bauxite profiles.

5.4.2 Bauxites

The bauxites contain between 1.23 and 16.5 ppm Mo, with an average of 5.37 ppm.

Molybdenum isotope values range between –0.14 and +0.38‰, with an average of +0.08‰

(**Table 5.1**). POM and SB-1 are the parent basalts for the two bauxite profiles and contain

0.73 (±0.06) and 0.90 (±0.07) ppm Mo with isotopic signatures of –0.33‰ and +0.02‰,

respectively. In the Columbia samples (**orange, Figure 5.1**), there is an excursion in

compositions to higher and heavier values above 7 m depth. Similarly, the Cowlitz profile

(**gray, Figure 5.1**), the uppermost two samples show higher Mo concentrations and heavier

Mo isotopes. The tau calculations show that the lower gibbsite layers of the two profiles

have not gained or lost Mo, however the samples from the overlying iron-pisolite layers

have gained Mo (**Figure 5.2**).
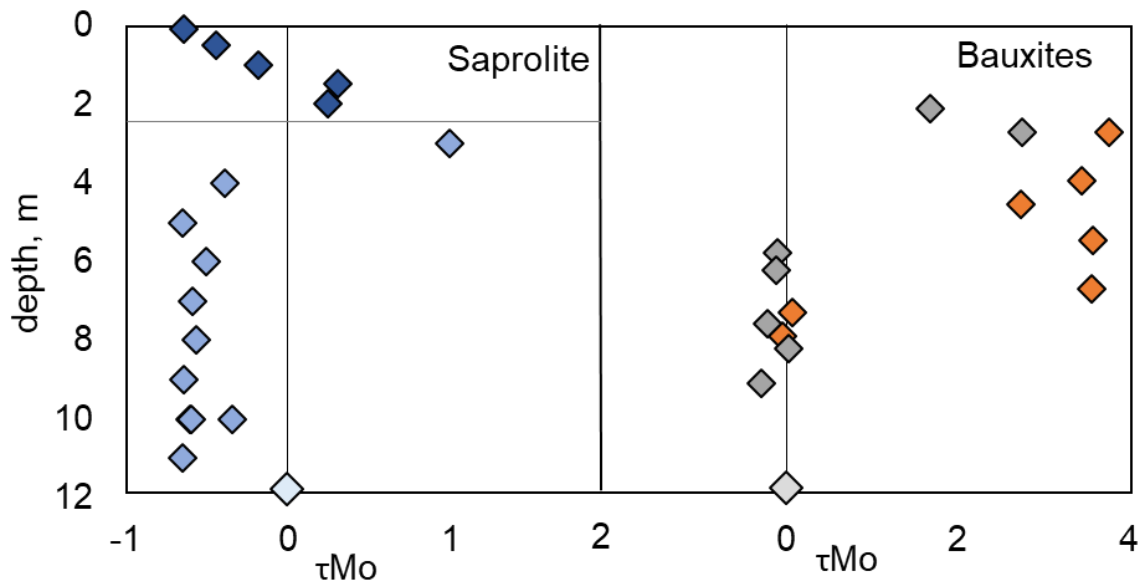
Figure 5.2. Calculated tau values as a function of depth in the saprolite profile (left) and bauxite drill cores (right). These show that Mo was gained in both profiles at certain horizons. The horizontal line in the saprolite profile at ~ 2 m denotes a redox discontinuity and a change in kaolinite:smectite, and the dark blue symbols represent those that formed above the discontinuity as in Figure 5.1. The bedrock is plotted at 12 m.

5.5 DISCUSSION

5.5.1 Saprolites

The saprolites formed on a "diabase" dike that has experienced greenschist facies metamorphism prior to weathering. While there are no outstanding systematic trends within either [Mo] or δ^{98}Mo, there are several interesting features in the dataset. First off, Mo shows varying behavior on either side of the redox discontinuity at ~2 m depth. Above this discontinuity, where Fe-rich smectite is the dominant clay species and the environmental is likely more oxidizing, [Mo] forms a continuous trend of decreasing concentration towards the top of the profile (**Figure 5.1, 5.2**). In the smectite zone, there is a weak correlation between [Mo] and P_2O_5 (supplementary figures – Appendix E), which has been shown to compete with Mo for adsorption sites on the surfaces of minerals (Goldberg et al., 1996; Gustaffson, 2003). Because adsorption of both elements has been shown experimentally to be strongly pH-dependent, we speculate that pH of saprolites controls Mo behavior in the oxidized smectite zone.
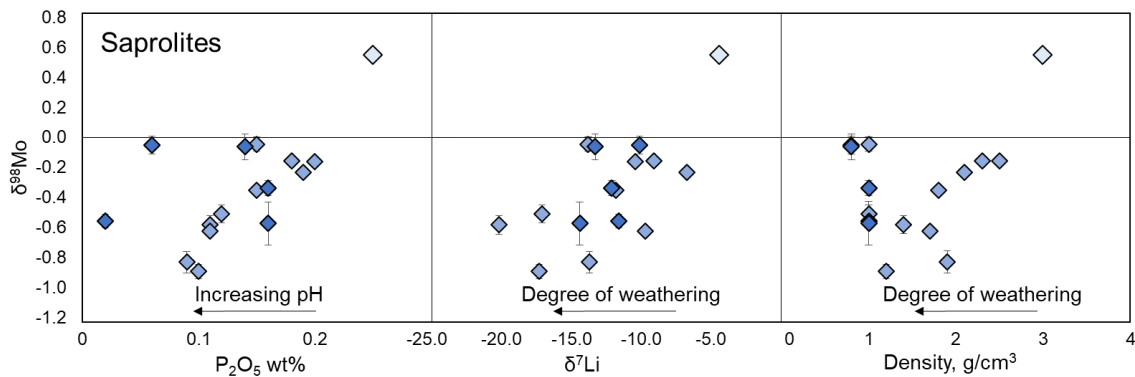
Figure 5.3. The lightest blue diamond with highest δ^{98}Mo represents the bedrock diabase, the medium shaded blue represents samples in the kaolinite-dominated region below the redox discontinuity, and samples in the darkest blue are samples taken from above the redox discontinuity. The P2O5, δ^7Li, and density data came from Gardner et al. (1981) and Rudnick et al (2004).

Below the redox discontinuity, kaolinite is the dominant clay species and the saprolites are cut by siderite veins. With the exception of the sample that borders the redox discontinuity, Mo concentrations are quite constant in this region and there is no obvious trend in δ^{98}Mo values (**Figure 5.1**). However, comparing δ^{98}Mo to other chemical indexes helps to elucidate fractionation behavior. The δ^{98}Mo value of the samples below the redox discontinuity (**light blue in Figure 5.3**) is weakly correlated with P_2O_5. While we do not have pH data for these samples, the fact that P_2O_5 and Mo sorption are both pH dependent suggests that pH controls Mo sorption and isotope fractionation in the kaolinite region. P_2O_5 is more strongly adsorbed at low pH (Gustaffson 2003), so one can infer that samples with a lower P_2O_5 concentration formed at higher pH. Therefore, our data show that at higher pH, phosphate is less retained in the profile, and Mo isotopes are more strongly fractionated (e.g., lighter) from the bedrock value (**Figure 5.3**). This latter observation that Mo is more strongly fractionated at higher pH is consistent with the results of King et al. (2017) and an overall compilation of literature data that shows an anticorrelation between pH and δ^{98}Mo (**Figure 5.4**).

Additionally, in the lower, kaolinite-dominated region of the saprolite profile, δ^{98}Mo is weakly correlated with δ^7Li and density (which are also correlated). Both of these indexes measure the degree of weathering, so this implies that the most weathered samples contain the lightest δ^{98}Mo values. The saprolites do contain some oxides, which may be the fractionating species here since experimental studies show that Mo is much more strongly adsorbed to oxides than clays (Goldberg et al., 1996), and leaching studies of Wang et al. (2018) suggest oxides control Mo behavior more so than clays in saprolites.
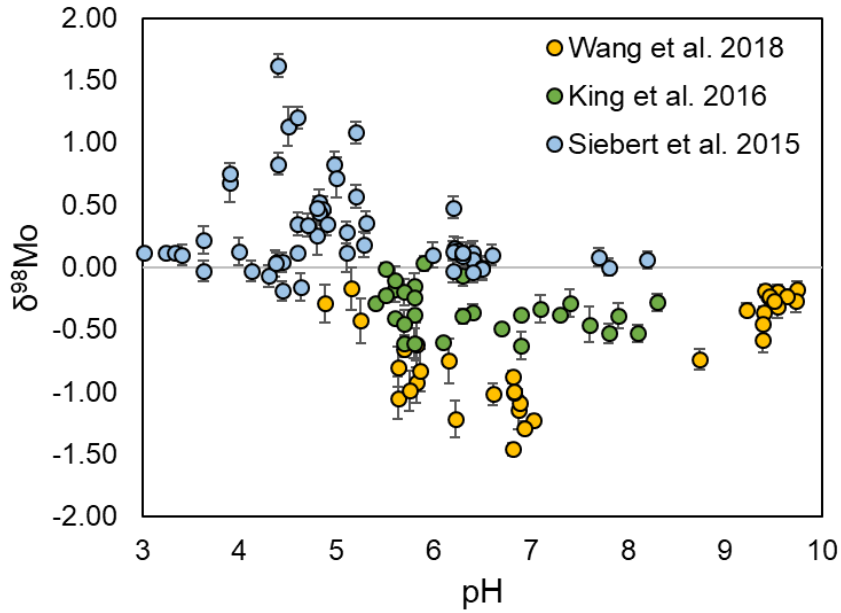
Figure 5.4. Relationship between pH and δ^{98}Mo from published studies of soils. Data compiled from Siebert et al. (2015), King et al. (2016), and Wang et al. (2018).

The observed isotope fractionation can be modeled by Rayleigh distillation equations to determine the fractionation factor of Mo onto phases like kaolinite and the minor oxides observed in the profile. These data suggest that isotopically light Mo is adsorbed to minerals that make up the saprolite, which is consistent with experimental results for other adsorbing phases like Fe,Mn-oxides and organic matter (Waslynski et al., 2008; Goldberg et al., 2009; King et al., 2017). Simple Rayleigh fractionation calculations can be used to model the saprolite data using experimentally determined fractionation factors of magnetite (1.0006; Goldberg at al., 2009) and humic acid/organic matter (King et al., 2017) and the following the equation: $\delta^{98}Mo_{saprolite} = (\delta^{98}Mo_{parent\,rock} + 1000) * f^{(\alpha-1)} - 1000$ where α is the fractionation factor and f is the proportion of Mo in the saprolite relative to the un-weathered bedrock (**Figure 5.5**). Most of the saprolite samples fall within the model curves in **Figure 5.5**, suggesting that organic matter, oxides, or a phase with a similar fractionation factor is

adsorbing Mo in the saprolites. While we cannot determine which phase is the dominant

fractionating vehicle in these saprolites, we can conclude that during saprolite-producing

weathering, isotopically heavy Mo is removed from the weathering profile.
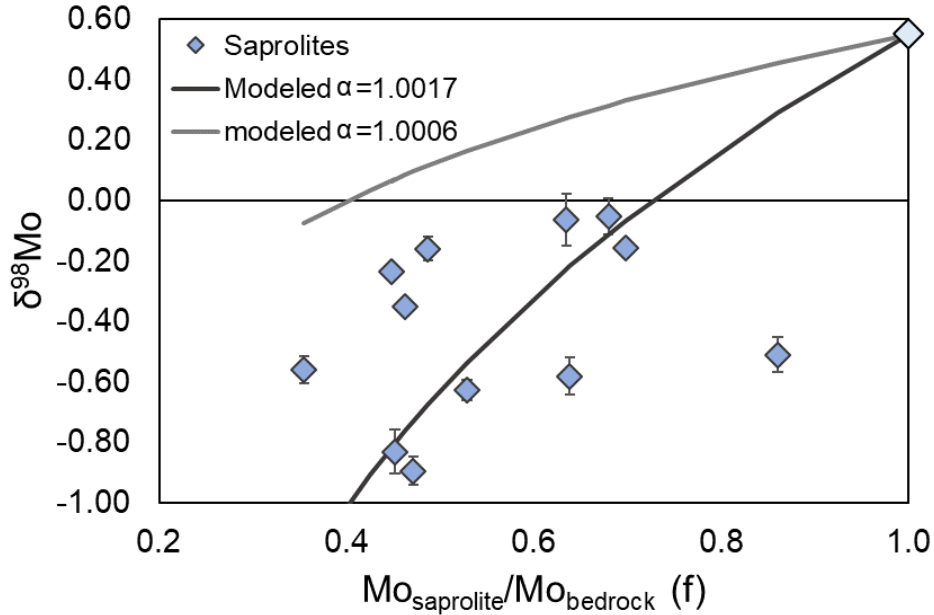
Figure 5.5. Results of the Rayleigh fractionation calculations using a range of experimentally determined fractionation factors. α=1.0006 was experimentally derived for magnetite (Goldberg et al., 2009) and α=1.0017 for organic matter (King et al., 2017). Note that three samples that appeared to show relative Mo addition to the profile (i.e., f value >1) were not included in this figure.

5.5.2 Bauxites

The bauxites tell a more complex story than the saprolites, which can be explained by a

single stage of weathering where Mo is removed from the weathering profile and

fractionated in the process, regions of the bauxite profiles contain significantly more Mo

than the bedrock. By contrast, portions of the bauxite profiles show a range of Mo

concentrations and δ^{98}Mo values that follow the major mineralogy of the profile: the upper

pisolite portion contains more Mo and higher (e.g., heavier) δ^{98}Mo values than the lower

gibbsite region and the parent basalts. Indeed, even within the pisolite layers of the

Columbia profile, [Mo] and δ^{98}Mo correlate with the proportion of pisolites determined by Fassio, 1990 (**Figure 5.1**). The pisolites are thought to have nucleated onto quartz crystals and are primarily composed of hematite, goethite, and minor maghemite (Fassio, 1990). It is unsurprising that these regions of the bauxite profile are enriched in Mo, given Mo's propensity to adsorb onto Fe-oxides (Goldberg et al. 1996). However, Mo has been experimentally shown to fractionate in the *opposite* direction due to adsorption onto Fe-oxides, *i.e.,* the oxides are expected to attract isotopically light Mo, leaving isotopically heavy Mo in solution (Goldberg et al., 2009). In the bauxite profiles, samples that lie within the pisolite zone have δ^{98}Mo values ranging from +0.14 to +0.38‰, which yields a Δ^{98}Mo between +0.25‰ and +0.67‰ relative to bedrock values. A similar phenomenon has been observed for Mo fractionation during adsorption onto organic matter. Although experiments suggest that organic matter should attract isotopically light Mo, studies of topsoil show that increasing proportions of organic matter in soils retain correlates with increasingly heavier Mo isotopes (King et al., 2016; 2017). King et al. (2016; 2017) suggested that the infiltration of isotopically heavy precipitation added isotopically heavy Mo that was retained by organic matter. Here, we propose that the addition of isotopically heayy precipitation or groundwater added Mo to the bauxites which was retained by the Fe-pisolite regions of the profiles. This interpretation follows the proposed stages of bauxite formation (Schellman, 1994): 1) moderate weathering of basalt leads to saprolite formation, 2) prolonged percolation of precipitation or groundwater results in intense leaching of Si from the weathering profile, 3) residual Fe and Al form layers of gibbsite and Fe-oxides. Precipitation is known to be isotopically heavy (average value of +1.11‰ in Hawaii; King et al., 2016), as is groundwater (estimates range between +0.14 and +0.34‰; King et al., 2016; Neely et al.,

2018), so percolation of either of these fluids through the weathering profile could deposit isotopically heavy Mo onto the growing Fe-oxide pisolites.

If rainwater with a δ^{98}Mo value of +1.11‰ is the percolating fluid, and we use the experimentally determined fractionation factor between fluid and hematite of Δ^{98}Mo = 1.4‰ (Goldberg et al. 2009), then approximately 50% of the Mo from the percolating fluid needs to be adsorbed onto the Fe-oxides in the pisolite layer to generate enrichments up to +0.38‰. Only 30% of the precipitation-derived Mo percolating through the bauxite would need to adsorb to the pisolites if the fractionation factor determined for goethite is used (Δ^{98}Mo = 1.11; Goldberg et al., 2009). Alternatively, groundwater could be the infiltrating fluid that deposited Mo. Because the measured range of groundwater overlaps that observed in the pisolite layer (δ^{98}Mo from +0.14 to +0.38‰), quantitative removal of Mo from groundwater would be needed to generate equally heavy Mo enrichments in the bauxites. This could be possible given the nature of the goethite and hematite pisolites, as continual concentric growth of the pisolites provides a constant increase in "fresh" surface area for molybdate (or another Mo compound) to adhere to. Because groundwater contains two to three orders of magnitude more Mo than precipitation (King et al., 2016; Neely et al., 2018), groundwater is more likely to generate the large Mo enrichments observed in the pisolite layers.

While the Fe-pisolite layers are enriched in Mo and contain heavy Mo isotopes, the lower gibbsite layers are more geochemically similar to the saprolites. The gibbsite layers have neither gained nor lost Mo, relative to Ti, and their compositions vary from the bedrock by Δ^{98}Mo = +0.01‰ to +0.25‰. This isotopic fractionation from bedrock values suggests that adsorption onto gibbsite is an effective fractionation mechanism for Mo isotopes,

although it does not fractionate Mo as strongly as Fe-oxides. The Cowlitz profile gibbsites contain τMo values slightly below zero – indicating slight loss of Mo from the profile – which corresponds well with δ^{98}Mo values that are lighter than the bedrock. As in the saprolite profile, this implies that Mo is fractionated during weathering, leaving isotopically light Mo in the sediment residue while isotopically heavy Mo is leached from the profile by groundwater. Likewise, the Columbia gibbsites contain higher tau values than the Cowlitz profile, implying that Mo is slightly more retained in this profile, and thus they have slightly heavier δ^{98}Mo values.

Liu et al. (2013) concluded that the addition of 20-60 wt% dust to the top of the bauxite profiles added quartz and non-radiogenic Nd to the upper layers of the bauxite profiles. The addition of dust is likely not the source of the heavy δ^{98}Mo observed in the upper portion of the profile because loess analyzed to-date has an average δ^{98}Mo identical to estimates of the "primary" igneous continental crust (+0.06 ±0.17‰; Wang et al., 2018). These loess samples were derived from China, though, and loess from western North America may have a different isotopic composition. This does not preclude dust from being added to these profiles, but another, heavier source of Mo (groundwater or rainwater) is also a necessary addition.

5.5.3 Mo behavior during continental weathering

When we combine these two datasets, the overall Mo isotope behavior during weathering becomes clear. Plotting δ^{98}Mo against both [Mo] and τ_{Mo} reveals a general trend where regolith has lost Mo during weathering (e.g, saprolites and some gibbsite samples from the bauxites) are isotopically lighter than the bedrock and general estimates of "primary" igneous UCC (**Figure 5.6**). On the other hand, sediments that have gained Mo –

due to great abundances of Fe-oxides that captured Mo from percolating groundwater or precipitation – are isotopically heavier than the bedrock and average UCC.

When we compare these data to a similar study of saprolites by Wang et al. (2018), we see the same general trend: Mo has been lost from the saprolites relative to the bedrock, as determined by the tau value, and nearly all of the saprolites are isotopically lighter than the bedrock (a granite). Interestingly, their data show a negative relationship between τMo and δ^{98}Mo, however the weathered samples that lost Mo are still lighter than the granite bedrock, so the overall trend holds. This trend is not as evident in studies of topsoil (King et al., 2016 and Siebert et al., 2015), however these soils are much younger and shallower and still under the influence of decaying organic matter and atmospheric inputs. Therefore, we find that while such studies generate useful information about Mo behavior during weathering, they do not record trends on longer timescales of continental weathering like these saprolites and bauxites that formed in the Miocene.

Additionally, while the bauxites studied here are actually enriched in Mo and heavy Mo isotopes, bauxites are a relatively rare weathering product, and only form under extreme weathering conditions. Usually these sediments are confined to tropical latitudes and form on more mafic rocks under intense leaching conditions (Schellman 1994; Bogatyrev et al., 2009), whereas saprolites are more ubiquitous and found on mafic to felsic rocks (e.g, Wang et al., 2018 and this study). Thus, we consider saprolites to be more representative of widespread continental weathering. From these data, we conclude that during continental weathering, there is a net loss of Mo which leaves the weathered regolith isotopically light and contributes to the isotopically heavy signature observed in rivers (Archer and Vance, 2008; Wang et al., 2018).

Finally, these data corroborate the findings of Greaney et al. (in prep – chapter 4) who show that the weathered UCC, as recorded by glacial diamictites, has evolved to isotopically lighter values over time due to the increase in oxygen levels present in the atmosphere. Increasing oxidative weathering breaks-down Mo-bearing phases like MoS_2 (Greber et al., 2015), mobilizes Mo, and results in a net Mo loss and fractionation of Mo from the upper crust.
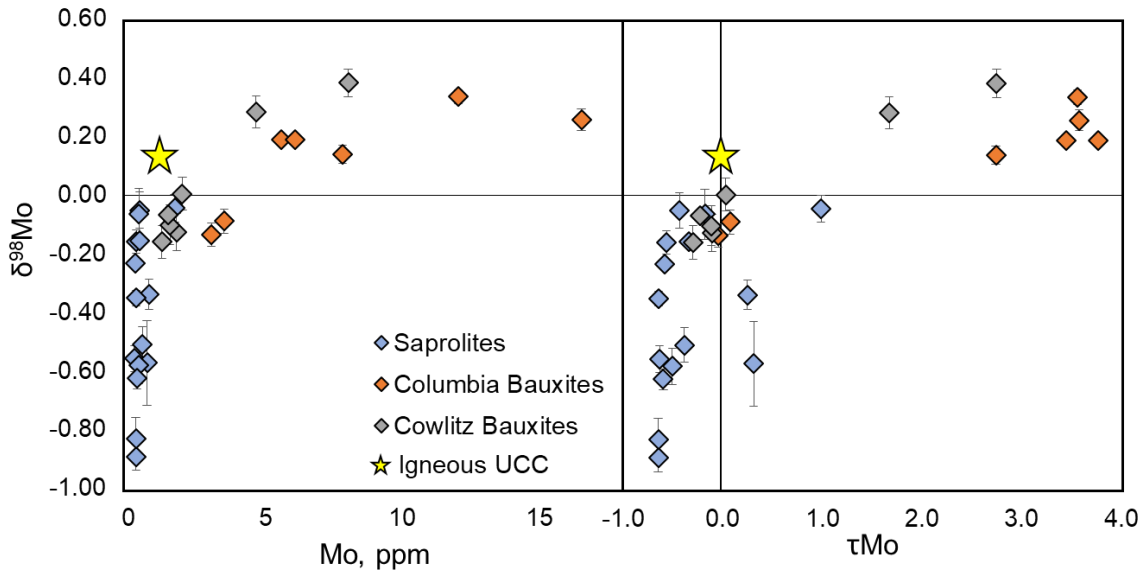
Figure 5.6. Trend between d98Mo and [Mo] and tau Mo. Estimates for the igneous upper crust are shown as a star (UCC [Mo] from Rudnick and Gao 2014; $\delta^{98}Mo$ estimated from Willbold and Elliott, 2017; Voegelin et al., 2014; Yang et al., 2017).

CONCLUSIONS

An investigation of Mo isotopes in a saprolite and two bauxite profile highlights the "long term" behavior of Mo during different types of continental weathering. The saprolites, which we consider to represent typical weathering conditions of bedrock given their widespread abundance, show an overall Mo loss with preferential retention of light Mo isotopes. By contrast, the bauxites – which represent extreme weathering that is typically

restricted to tropical regions with high rainfall and significant leaching of the profile – show a net Mo gain with preferential retention of heavy Mo isotopes. From these data we conclude that moderate continental weathering results in a loss of Mo from weathering profiles accompanied by fractionation as light Mo isotopes are retained onto minor Fe-Mn oxides and clays in the weathering profile. The Mo that is leached from the profile is therefore isotopically heavy, which partially explains why ground and river water is known to be isotopically heavy (Archer and Vance, 2008; King et al., 2016; Neely et al, 2017). Bauxites form by significant leaching by groundwater and/or rain water and these profiles precipitate significant Fe-oxides (up to 50% of the modal mineralogy). While heavy Mo isotopes may initially be stripped from the bauxite profile during the early stages of formation, continual leaching by isotopically heavy groundwater or rainwater causes the adsorption of isotopically heavy Mo onto the abundant Fe-oxides that form in the profile.

ACKNOWLEDGEMENTS

Chapter VI. The distribution of V, Ga, Ge, Mo, Cd, In, Sn, Sb, W, Tl, and Bi in the lithospheric mantle

To be submitted to Contributions to Mineralogy and Petrology

With co-authors: Roberta L. Rudnick[1,2], Jean-Pierre Lorand[3]

[1]University of California Santa Barbara, Department of Earth Science, Santa Barbara, CA 93106

[2]University of Maryland College Park, Department of Geology, College Park, MD 20742

[3]Laboratoire de Planétologie et Géodynamique de Nantes, Université de Nantes, 44035 Nantes, France

Author Contributions

A.T. Greaney conceived the study, carried out the analyses and data interpretation, and wrote the manuscript.

R.L. Rudnick conceived the study, provided samples, aided in data interpretation, and provided edits on the manuscript.

J.P Lorand provided samples, aided in data interpretation, and will provide edits on the manuscript.

ABSTRACT

We investigate the partitioning behavior of the variably chalcophile elements V, Ga, Ge, Mo, Cd, In, Sn, Sb, W, Tl, and Bi in xenolithic and massif peridotites from the North China Craton (Hannuoba basalts) and Pyrenees Massif, respectively. Using solution ICP-MS we present whole-rock abundances of these elements as well as their concentrations in mantle minerals using laser ablation ICP-MS, with a focus on their concentration in sulfides. We find that V, Ga, Ge, Cd, and In form coherent whole rock trends relative to MgO that we can use to estimate primitive mantle abundances of V = 71.2 ppm, Ga = 3.35 ppm, Ge = 1.02 ppm, Cd = 0.035 ppm, and In = 0.012 ppm, which are consistent with previous estimates. The whole rock abundances of the other elements have been altered by metasomatism which has deposited Mo, W, Sn, Tl, and Bi along grain boundaries of the Hannuoba xenolithic peridotites, and deposited Mo and W along some grain boundaries of the Pyrenees massif peridotites. When a mass balance is completed, we find that only Bi and Tl are consistently hosted in sulfide across multiple samples and in both types of peridotites. However, silicates are needed to obtain mass balance for these two elements, and mass balance is not obtained in many samples. The other elements are predominatly lithophile in that mass balance can be obtained with silicates and spinel (V, Ga, Ge, Cd, In, and Sb), or their mass balance is rarely obtained (Sn, Mo, W) which may be explained by metasomatic addition to grain boundaries that were not included in the mass balance, thereby implying extremely incompatible behavior of these elements. Additionally, Mo and W partitioning into sulfide is dependent on temperature, causing Mo and W to become more chalcophile at higher T. Ga and Ge show simliar, but weaker, temperature dependencies during sulfide partitioning.

172

6.1 INTRODUCTION

The elements V, Ga, Ge, Mo, Cd, In, Sn, Sb, W, Tl, and Bi show variable geochemical behavior between Earth's different reservoirs. While many of these elements are important ore-forming elements, processes that lead to their enrichment in the crust are not well constrained, nor is their overall partitioning behavior in the mantle. All of these elements have been shown (experimentally or empirically) to partition into sulfides to varying degrees (Li and Audetat, 2012; Kiseeva and Wood, 2015). However, these elements can also exhibit siderophile (V, Ga, Ge, Mo, Sn, Sb, W) and lithophile (V, Ga, Ge, Mo, Cd, In, Sn, Sb, W, Tl) behavior based on studies of mantle peridotites (Witt-Eickschen et al., 2009), and mantle-derived magmas (Greaney et al., 2017; Patten et al., 2013; Yi et al., 1995; Jochum et al., 1993; Jochum and Hofmann, 1997; McDonough and Sun, 1995). Many previous studies have inferred the geochemical behavior of these elements based on element ratios in the whole rock or glass and do not directly measure the abundance of these variably chalcophile elements in sulfides and other phases. By measuring the abundances of variably chalcophile elements *in-situ*, their mineralogical hosts and partitioning behavior can be directly determined. These data serve as a comparison to experimental data and will allow for greater accuracy in determining the behavior of these elements during partial melting and fractional crystallization. For example, the comprehensive experimental partitioning study of Adam and Green (2006) found that the partitioning behavior of Sn, Bi, Cd, and Tl in mantle silicate minerals is inconsistent with lattice strain models. With this investigation of partitioning in natural samples, we hope to place further constraints on the partitioning of these elements. Additionally, we aim to determine more direct bulk silicate Earth (BSE) abundances for the highly volatile (e.g., Cd and In) and moderately volatile elements (Ga, Ge) than those

173

calculated by element ratios in mantle melts like basalts and komatiites from McDonough and Sun (1995).

Studies on the partitioning behavior of subsets of these elements in mantle peridotites have appeared recently. For example, Wang et al. (2018) showed that Mo in serpentinized peridotites from the Ivrea Zone in the Alps is not generally retained in sulfides, although *in-situ* Mo abundances were not obtained by this study. Liu et al. (2018) showed that W is hosted in secondary Ti-phases or along grain boundaries in xenolithic peridotites. Witt-Eickschen et al. (2009) performed a mass balance for Ga, Cd, In, and Sn in peridotite xenoliths combining whole rock data with in-situ data for minerals analyzed by laser ablation ICP-MS to determine their BSE abundances. Sulfides in these samples were too small to be analyzed by LA-ICP-MS, and the study found that Cd, In, and Sn are primarily hosted in clinopyroxene while Ga is hosted in Al-rich phases like olivine and spinel.

Here we present a mass-balance approach employing standard addition ICP-MS methods for whole rocks, and LA-ICP-MS for minerals to determine the partitioning behavior of V, Ga, Ge, Mo, Cd, In, Sn, Sb, W, Tl, and Bi in xenolithic and orogenic peridotites. The peridotite suites were chosen because they retain sulfide, which can be uncommon for xenolithic samples, and because they show coherent trends between S and MgO (**Figure 6.1**).

6.2 SAMPLES

Xenolithic spinel-peridotite from the North China Craton and orogenic spinel-peridotites from the Pyrenees were selected for whole-rock and *in-situ* analyses.

6.2.1 Hannuoba Xenolithic Peridotites

The Hannuoba peridotite xenoliths are contained within 10-22 Ma alkali basalts [reference here for the age of basalts] from the Damaping locality and vary from relatively un-depleted lherzolites (Mg# 89.5) to moderately melt depleted harzburgites (Mg# 91.1) (**Table 6.1**). A Re-Os 'errorchron' age of 1.9 Ga suggests that this section of lithospheric mantle underwent melting/cratonization during the Trans-North China orogen (Gao et al., 2002; Rudnick et al., 2004; Zhao et al., 2000). The Hannuoba xenoliths are unusual among xenolithic peridotites in that they contain well-preserved sulfides that have not undergone significant alteration or removal prior to or during ascent from the mantle, nor during supergene weathering (cf. Lorand, 1990). Sulfur shows a good correlation with MgO, suggesting that the xenoliths may accurately record S behavior during melt depletion of the lithospheric mantle (**Figure 6.1**). These samples investigated here were previously characterized for major elements, sulfur, and Re-Os isotopes (Gao et al., 2002), mineral chemistry, trace elements, and Sr-Nd isotopes (Rudnick et al., 2004), and HSE and re-analysis of Re-Os isotopes (Becker et al., 2006; Liu et al., 2010). Eight samples were selected for whole-rock analyses and seven were sectioned for *in-situ* analyses to determine the distribution of the moderately chalcophile and lithophile elements, targeting olivine, clinopyroxene, orthopyroxene, spinel, and sulfide. One sample, DMP-23a, was analyzed using LA-ICP-MS but not with whole-rock methods, so mass balance is not determined in this sample. Line scans were also run across grain boundaries to complete the mass balance for select elements.

6.2.2 Pyrenees Massif Orogenic Peridotites

Orogenic-type spinel peridotites from the Pyrenees were selected for this study from the Lherz, Porteteny, Pic de Géral, and Freychinède localities found along the North Pyrenean

Fault that defines the contact between the Iberian and European plate. The peridotite massifs were tectonically emplaced into sediments during compression during the Cretaceous that followed extension and thinning of the lithosphere (Vielzeuf and Kornprobst, 1984). The North Pyrenean Fault is part of an extensive metamorphic regime known as the North Pyrenean Metamorphic Zone, therefore the peridotite massifs are foliated to varying degrees and are interlayered with pyroxenite and cut by pyroxenite and hornblendite dikes (Bodinier et al., 1988; Lorand, 1989; Lorand, 1999). The pyroxenite veins are interpreted to have formed during interaction with alkali basalt melts (Bodinier et al., 1988), but are not considered here in this study.

The samples selected for this study are weakly foliated with textures ranging from primary protogranular to recrystallized porphyroclastic. We chose well-characterized samples that span a range of MgO (lherzolites: Mg# 89.2 to harzburgites: Mg# 91.5) and S content (**Table 6.1**) and display relatively unaltered mineralogies. Like the xenolithic samples, the massif peridotites show a clear correlation between S and MgO, suggesting they record the incompatible behavior of S during mantle melting (**Figure 6.1**). The samples were originally collected and analyzed for major element data by Conquere (1978). Trace element abundances (Bodinier et al. 1988), S, Cu, and HSE abundances (Lorand, 1989; Luguet et al., 2007), and PGE and Au abundances (Lorand et al., 1999) have also been determined for these samples. Of the eleven samples selected for whole-rock analyses, four were also sectioned for *in-situ* analyses of olivine, clinopyroxene, orthopyroxene, spinel, and sulfide. Line scans were run across grain boundaries to complete the mass balance for select elements. Some samples contained minor secondary amphibole (<1%) that was not analyzed

176

given that it is not a primary mantle mineral and likely formed during interaction with a metasomatic agent (Bodinier et al., 1988).
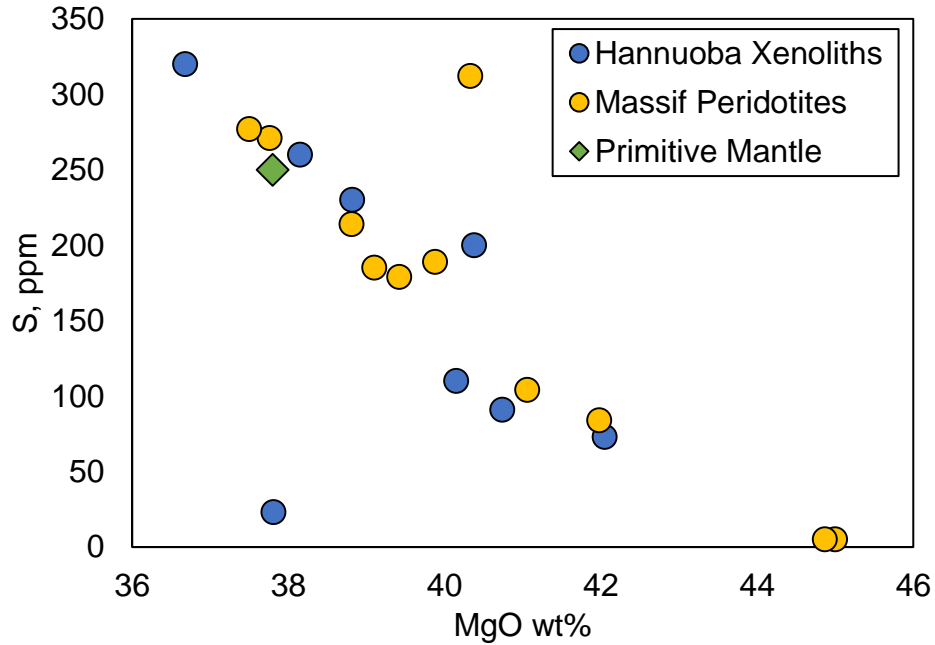
Figure 6.1. Whole-rock sulfur data for both peridotite suites displaying S depletion with melt depletion. Primitive mantle from McDonough and Sun (1995).

6.3 METHODS

6.3.1 Whole rock data

Whole rock major element data were determined by XRF and neutron activation (Gao et al., 2002; Rudnick et al., 2004; Bodinier et al., 1988), and are reported in **Table 6.1**. Whole-rock trace element abundances were measured by standard addition solution ICP-MS (Ga, Ge, Mo, Cd, In, Sn, Sb, W, Tl, and Bi) and externally calibrated ICP-MS (all other trace elements) at the University of Maryland. For the standard addition method, 50 mg of powder were dissolved in HF-HNO$_3$ using high-pressure Parr Bombs in an oven at 180°C for 72 hours, dried down on a hotplate multiple times and brought up in concentrated HNO$_3$, and then placed back into the oven overnight. Samples were then dissolved into two aliquots

for standard addition and trace element analysis: one aliquot was spiked with a Rh drift

monitor and synthetic solutions of Ga, Ge, Mo, Cd, In, Sn, Sb, W, Tl, and Bi using the

standard addition technique of Gaschnig et al. (2015). Arsenic was also included in the

standard addition solution, but none of the samples had As concentrations above detection

limits (0.4 ppm), so it is not reported here. In was added to the other aliquot to use as a drift

corrector for general trace element analysis using USGS standards to externally calibrate the

data. The samples were analyzed on a Thermo-Finnigan Element2 single-collector

Inductively Coupled Plasma Mass Spectrometer (ICP-MS) using an ESI Apex desolvating

nebulizer. The instrument was tuned to keep oxide production under 1.2% and the following

isotopes were run in low (LR) and medium (MR) resolution mode: (LR) ^{51}V, ^{95}Mo, ^{97}Mo,

^{98}Mo, ^{111}Cd, ^{115}In, ^{117}Sn, ^{118}Sn, ^{119}Sn, ^{121}Sb, ^{182}W, ^{183}W, ^{205}Tl, ^{209}Bi; (MR) ^{69}Ga, ^{71}Ga, ^{73}Ge,

^{74}Ge, ^{95}Mo, ^{97}Mo, ^{98}Mo, ^{111}Cd, ^{115}In, ^{117}Sn, ^{118}Sn, ^{119}Sn, ^{121}Sb, ^{183}W. Tin-117 was used to

correct for Sn interferences on ^{115}In. The following isotopes/resolution modes are reported

here in **Table 6.2**: ^{96}Ga (MR), ^{74}Ge (MR), ^{95}Mo (MR), ^{111}Cd (MR), ^{115}In (MR), ^{118}Sn (MR),

^{121}Sb (MR), ^{183}W (MR), ^{205}Tl (LR), ^{209}Bi (LR). The limits of detection, as calculated by a

total analytical blank analyzed after each sample, were: Ga = 0.04 ppm, Ge = 0.03 ppm, Mo

= 0.05 ppm, Cd = 0.008 ppm, In = 0.003 ppm, Sn =0.10 ppm, Sb = 0.006 ppm, W = 0.02

ppm, Tl = 0.002 ppm, Bi = 0.002 ppm. General trace element data is presented in

supplementary information (**Appendix F**) and the secondary standard BHVO-1 was

measured and presented in the supplementary information (**Appendix F**).

6.3.2 In-situ data

Major element data for the minerals targeted in this study (olivine, orthopyroxene,

clinopyroxene, spinel, sulfides) were measured on an electron probe microanalyzer (EPMA)

at the University of California-Santa Barbara, or data were taken from previous studies (e.g.,

Rudnick et al., 2004). Between one and four points were measured by EPMA on sulfides,

depending on the diameter of the grain, as many sulfides showed exsolution of multiple

phases (e.g., chalcopyrite (ccp)-pentlandite (pn)-pyrrhotite (po)-mono sulfide solid solution

(MSS): **Figure 6.2**).

wt%	Locale	SiO_2	TiO_2	Al_2O_3	Cr_2O_3	Fe_2O_3	MnO	NiO	MgO	CaO	Na_2O	K_2O	P_2O_5	Total	Mg#	*In-situ*
Hannuoba Xenoliths, North China Craton																
DMP 60		46.34	0.11	3.67	0.38	7.48	0.13	0.25	36.68	3.47	0.38	0.006	0.009	98.9	89.7	yes
DMP 56		44.79	0.13	3.49	0.35	7.97	0.14	0.26	38.15	3.21	0.36	0.007	0.006	98.9	89.5	yes
DMP 41		44.75	0.06	2.76	0.40	7.74	0.13	0.26	40.15	2.12	0.27	0.004	0.011	98.7	90.2	yes
DMP 19		44.83	0.03	1.91	0.34	7.07	0.12	0.31	40.74	1.8	0.19	0.025	0.01	97.4	91.1	yes
DMP 04		44.40	0.06	2.29	NA	7.33	0.13	0.31	42.05	1.94	0.28	0.015	0.01	98.8	91.1	yes
DMP 58		44.87	0.08	3.16	0.34	7.92	0.13	0.27	38.82	2.76	0.34	0.012	0.005	98.7	89.7	
DMP 59		43.90	0.06	2.58	0.40	7.99	0.13	0.29	40.38	2.43	0.27	0.007	0.019	98.5	90.0	yes
DMP 67c		44.00	0.2	3.78	0.42	8.39	0.14	0.26	37.81	2.88	0.3	0.26	0.02	98.5	88.9	
DMP 23a		44.22	0.1	2.32	0.42	7.77	0.13	0.31	41.25	1.64	0.24	0.1	0.03	98.53	90.4	yes
Pyrenees Massif, France																
POR-1	Porteteny	44.87	0.08	2.85	0.32	8.65	0.13	0.29	39.88	2.6	0.01	0.19	NA	99.9	90.1	yes
POR-2	Porteteny	46.08	0.13	3.24	0.35	8.43	0.03	0.27	37.76	3.13	0.01	0.22	NA	99.7	89.9	yes
POR-3	Porteteny	45.08	0.12	3.07	0.36	8.65	0.13	0.28	38.81	2.92	0.01	0.2	NA	99.6	89.8	yes
16-4	Lherz	45.00	0.35	3.65	0.26		0.13	0.27	37.50	3.1	n.d.	0.27	NA	90.5	90.0	
PGER-2	Pic de Géral	43.70	0.06	2.30	0.38	8.22	0.12	0.3	41.06	1.77	0.01	0.11	NA	98.0	90.6	
PGER-3	Pic de Géral	44.28	0.07	2.00	0.38	8.10	0.12	0.31	41.98	1.37	0.01	0.1	NA	98.7	91.0	
71-336	Frechinede	44.46	0.14	3.47	0.41	8.42	0.14	0.29	39.42	2.78	0.04	0.36	NA	99.9	90.0	yes
71-335	Frechinede	45.01	0.18	2.72	0.24	8.74	0.14	0.28	40.33	2.28	0.04	0.29	NA	100.3	89.9	
64-3	Lherz	40.84	0.04	0.30	0.21		0.06	0.5	45.00	1.1	0.01	0.06	NA	88.1	91.5	
71-323	Lherz	44.20	0.06	0.76	n.d.		0.12	n.d.	44.87	0.38	0.04	0.08	NA	90.5	91.3	
73-273	Lherz	43.00	0.26	3.11	0.33		0.13	0.32	39.10	2.8	n.d.	0.24	NA	89.3	89.2	

Table 6.1 Major element data for the selected samples. Hannuoba Xenolith data taken from Rudnick et al. (2004) and Gao et al. (2002); Pyrenees Massif data taken from Conquere (1978), Bodinier et al. (1988), Lorand (1989), Luguet et al. (2007).

ppm	MgO	S*	V	Ga	Ge	Mo	Cd	In	Sn	Sb	W	Tl	Bi
Hannuoba Xenoliths, North China Craton													
DMP 60	36.68	320	72.5	3.01	NA	0.23	0.035	0.012	0.38	0.17	0.08	0.003	BDL
DMP 56	38.15	260	65.1	3.26	NA	0.11	0.030	0.013	0.54	0.07	0.02	0.005	0.022
DMP 41	40.15	110	51.7	8.62	NA	0.16	0.022	0.009	0.21	0.05	0.02	0.005	0.013
DMP 19	40.74	91	32.2	2.67	NA	0.17	0.017	0.005	0.85	0.05	0.02	0.013	0.020
DMP 04	42.05	73	45.1	2.08	NA	0.35	0.020	0.007	0.25	0.06	0.07	BDL	0.008
DMP 58	38.82	230	59.0	3.17	NA	0.11	0.025	0.010	0.23	0.00	0.02	0.003	0.006
DMP 59	40.38	200	44.0	NA	NA	NA	0.023	0.007	NA	0.04	NA	BDL	0.003
DMP 67c	37.81	23	64.8	NA	NA	NA	0.041	0.013	NA	0.13	NA	BDL	0.017
DMP 23a	41.25	NA	NA	NA	NA	NA	NA	NA	NA	NA	NA	NA	NA
Pyrenees Massif, France													
POR-1	39.88	189	76.3	2.38	0.96	0.10	0.048	0.015	0.28	0.10	0.06	0.007	0.019
POR-2	37.76	271	71.1	2.92	1.01	0.09	0.032	0.012	0.35	0.07	0.05	BDL	BDL
POR-3	38.81	214	72.2	2.80	1.05	0.06	0.035	0.016	0.29	0.06	0.03	0.009	0.009
16-4	37.50	277	85.2	3.08	1.03	0.10	0.041	0.012	0.40	0.08	0.11	0.003	BDL
PGER-2	41.06	104	40.8	1.36	0.82	BDL	0.016	0.005	0.13	0.01	0.02	BDL	0.002
PGER-3	41.98	84	44.8	1.39	0.88	0.14	0.016	0.007	0.25	0.03	0.04	BDL	BDL
71-336	39.42	179	73.4	2.57	3.82	0.15	0.034	0.012	0.17	1.14	0.12	BDL	BDL
71-335	40.33	312	60.9	2.32	0.91	0.16	0.028	0.011	0.19	0.02	0.12	BDL	0.003
64-3	45.00	5	30.0	0.80	0.79	0.24	0.015	0.004	2.14	0.15	0.10	BDL	BDL
71-323	44.87	5	29.0	NA	NA	NA	NA	NA	NA	NA	NA	NA	NA
73-273	39.10	185	65.3	2.41	0.98	0.34	0.027	0.010	0.16	0.03	0.11	0.018	BDL

*S data from Lorand (1989) and Gao et al. (2002)

Table 6.2 Trace element data for the whole-rock samples. BDL = below detection limit and NA = not analyzed. General trace element data is presented in Table 6.5.

	V	Ga	Ge	Mo	Cd	In	Sn	Sb	W	Tl	Bi
Pyrenees Massif Sulfides											
min	0.01	0.01	0.06	0.01	0.002	0.001	0.04	0.03	0.003	0.004	0.004
median	**1.46**	**0.13**	**1.15**	**0.05**	**1.295**	**0.003**	**0.92**	**0.26**	**0.009**	**0.888**	**1.205**
mean	16.7	0.75	2.49	0.35	4.618	0.040	1.76	1.06	0.023	6.798	4.223
max	210	20.6	27.1	7.00	59.0	0.710	23.0	8.90	0.590	103	60.9
# BDL	2	18	23	24	0	30	5	15	32	0	3
Hannuoba Xenolith Sulfides											
min	0.0	0.02	0.06	2.40	0.002	0.001	0.04	0.03	0.009	0.001	0.004
median	**7.1**	**2.20**	**5.53**	**84.0**	**0.970**	**0.130**	**0.44**	**2.50**	**0.179**	**0.300**	**0.484**
mean	88.7	117	25.1	344	5.082	0.717	6.93	18.1	6.725	2.857	1.644
max	1060	2200	560	2200	74.0	16.0	320	600	330	81.0	41.0
# BDL	2	0	6	0	10	20	24	14	15	4	5
All Sulfides											
min	0.01	0.007	0.06	0.01	0.002	0.001	0.04	0.03	0.003	0.001	0.004
median	**3.7**	**0.379**	**4**	**2.85**	**1.250**	**0.023**	**0.61**	**0.66**	**0.021**	**0.360**	**0.660**
mean	52.4	58.4	13.7	171	4.848	0.376	4.33	9.49	3.349	4.842	2.943
max	1060	2200	560	2200	74.0	16.0	320	600	330	103	60.9
# BDL	4	18	29	24	10	50	29	29	47	4	8

Table 6.3. *In-situ* trace element concentrations of sulfides (ppm). A total of 64 Pyrenees Massif sulfide points and 65 Hannuoba xenolithic sulfide points were analyzed. These data include the detection limit in place of analyses that were below the detection limit (BDL). The number of these analyses are denoted as # BDL. Individual analyses are provided in the supplementary data tables and these data also include Co and Mn abundances that were not included in mass balance calculations.

Trace element data were measured by LA-ICP-MS at the University of California-Santa Barbara using a Photon Machines 193 nm excimer laser attached to an Agilent 7700x quadropole ICP-MS. The laser was operated at 10 Hz and using a spot size of 65 µm for the silicates and spinel, and a spot size of 25 – 65 µm for the sulfides, depending on the size of the grains. Silicon was used as an internal standard for the silicates and Al or Ni was used for spinel. Three internal standards were tested on the sulfides by reducing the LA-ICP-MS data for homogeneous sulfides with Ni, Fe, and Co to check that each reduction scheme returned similar values. Many sulfides showed complex heterogeneous exsolution textures on the surface of the thin section, making it infeasible to determine the proportion of each sulfide type that exists beneath the thin section surface (**Figure 6.2).** To address this heterogeneity, the element (Ni or Fe) whose abundance varied the least between the phases present on the surface of the sulfide was used as the internal standard by averaging the abundance: e.g., if MSS2 and pentlandite were present within the diameter of the laser spot, the Ni content for both phases, as determined by EPMA, was averaged and used as the internal standard value. Generally, Ni is preferred as an internal standard over Fe, because it produces more accurate data as determined by comparisons to EPMA data for elements like Co and Mn that were analyzed by both methods. While this method does not completely solve the issue of heterogeneous regions within the sulfides, it provides the best estimate of trace element content given the methods available. Examination of the time resolved spectra suggests that as the laser drilled into the sulfide, the composition of the sulfide did not change significantly, except for in a few cases. For these, the integration period was shortened in order to capture data only for the known phase that was present at the surface. Data were reduced using the Iolite software (Paton et al., 2011), using NIST-612 as the

calibration standard. In addition to the main minerals found in the peridotites, line scans were run across grain boundaries and fractures within silicates to determine if any elements were concentrated in these areas, either due to incompatibility or deposition by a metasomatic agent.

The following isotopes are reported as in-situ averages in **Table 6.3**: ^{69}Ga, ^{74}Ge, ^{95}Mo, ^{111}Cd, ^{115}In, ^{122}Sn, ^{184}W, ^{121}Sb, ^{205}Tl, ^{209}Bi. Their detection limits in ppm are as follows: V = 0.01, Ga = 0.01, Ge = 0.06, Mo = 0.005, Cd = 0.002, In = 0.001, Sn = 0.04, Sb = 0.03, W = 0.009, Tl = 0.004, Bi = 0.004. Data for secondary standards BHVO-2g, Ge-7 (synthetic glass created by James Brenan), and JB-sulfide and NiS-4 (synthetic sulfides created by James Brenan) can be found in the **supplementary data**.
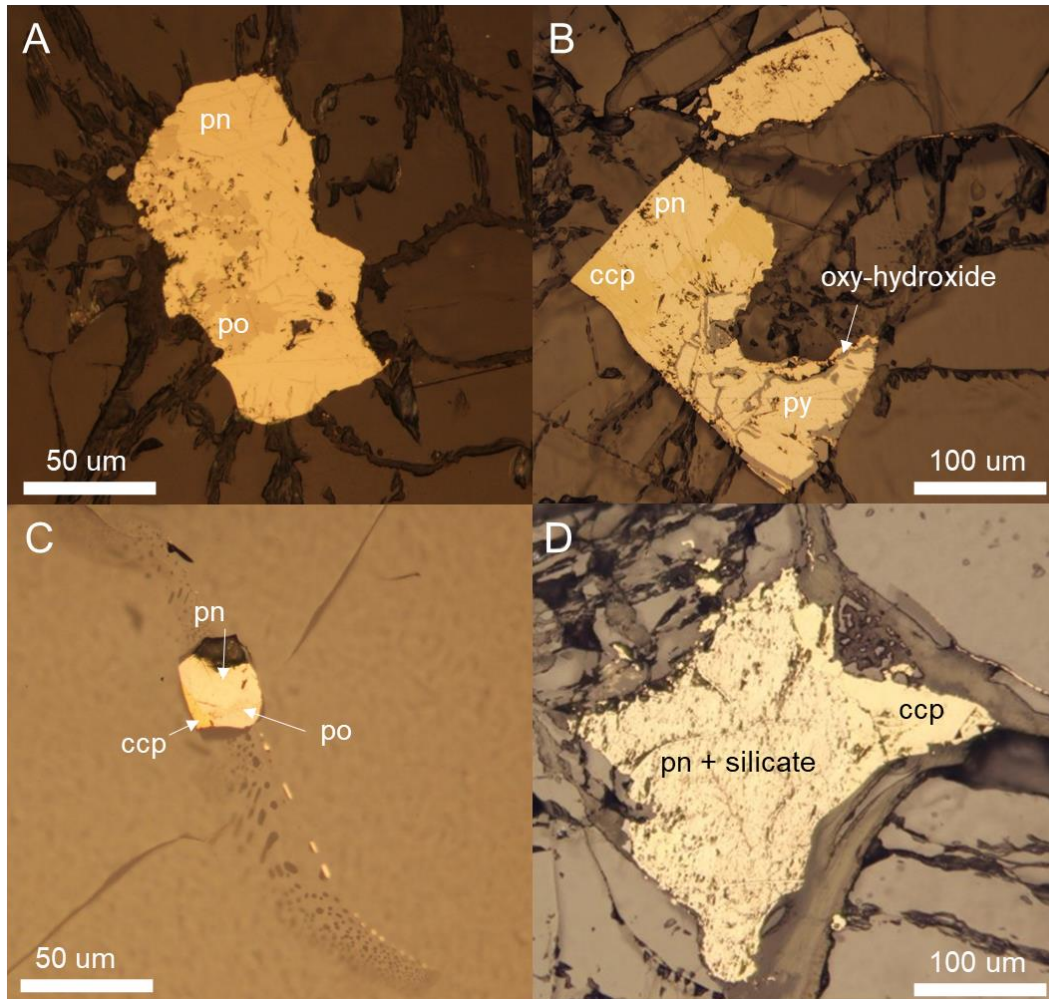
Figure 6.2. Sulfide photomicrographs: A) primary massif peridotite sulfide (POR-1, S06) showing exsolved regions of pentlandite and pyrrhotite, B) altered massif peridotite sulfide (POR-3, S13) showing replacement of the primary sulfide by pyrite and oxides, C) primary xenolith sulfide (DMP-56, S01) enclosed along a healed fracture in an olivine grain, D) secondary xenolith sulfide (DMP-60, S22) affected by metasomatic fluids. po = pyrrhotite, pn = pentlandite, ccp = chalcopyrite, py = pyrite.

6.4 RESULTS

6.4.1 Whole-rock trends

Of the elements analyzed by solution ICP-MS in the whole rock samples, five show coherent trends with MgO (**Figure 6.4**). Plots of other elements that do not show trends with MgO are presented in the supplementary material. In both the Hannuoba and Pyrenees Massif peridotites, In, Cd, V, and Ga show incompatible behavior, as displayed by an inverse correlation with MgO (Figure 6.4). Least squares regressions of the Cd and In data result in "primitive mantle" values of 0.035 ppm (±0.034), 0.012 ppm (±0.011), and respectively, assuming MgO content of the primitive mantle is 38 wt. % (McDonough and Sun, 1995). While the errors on these estimates are large, due to scatter in the data, they are quite similar to previous estimates of 0.040, 0.033 and 0.035 ppm for Cd and 0.011 ppm, 0.016, and 0.018 ppm for In (McDonough and Sun, 1995; Witt-Eickschen et al., 2009; Palme and O'Neill, 2014, respectively) (**Figure 6.4**). Alternatively, we can estimate the primitive mantle using the mean value of the four samples that fall between 37.5 and 38.5 wt% MgO which results Cd = 0.036 ppm (±0.012) and In = 0.012 (±0.01), yielding nearly identical values.

The Ga regression results in a primitive mantle abundance of 3.35 ppm (±1.7), excluding a significant outlier (sample DMP-41, with 8.62 ppm Ga). Taking the mean of the four "primitive" samples gives a primitive mantle value of 3.09 (±0.34). This value is lower than previous estimates by ~35%. However, Ga in BHVO-1 reproduced within 2% of the expected value and the two peridotite suites were analyzed over a year apart, so we are confident that instrument drift or analytical error are not the cause of these differences.

The V regression results in a primitive mantle abundance of 71.2 ppm (±62) and the average of the four primitive samples gives 71.5 ppm (±19). Palme and O'Neill estimate 86 ppm and McDonough and Sun estimate 82 ppm V in the primitive, both from studies of peridotites and komatiites.

Germanium was only analyzed in the Pyrenees Massif samples and does not show significant compatible or incompatible behavior, with one sample plotting as a clear outlier. Using a regression through the Pyrenees Massif data, we estimate a primitive mantle Ge value of 1.02 ppm (±0.30), and the mean of the two primitive samples gives a value of 1.13 (±0.39), which are in excellent agreement with previous estimates of 1.10 and 1.20 ppm (McDonough and Sun, 1995; Palme and O'Neill, 2014).
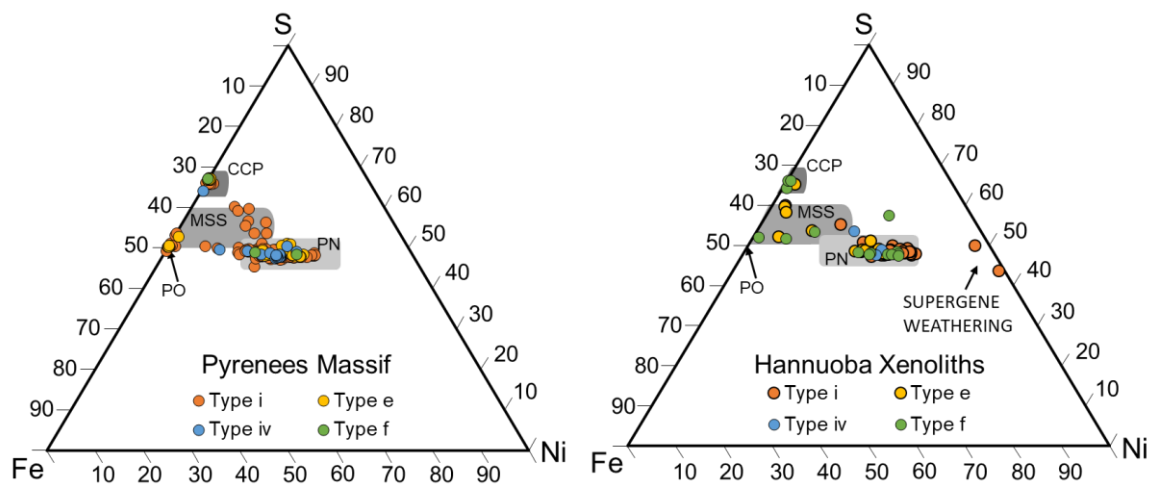
Figure 6.3 Ternary diagrams representing all EPMA sulfide data for both the Hannuoba xenolithic peridotites and Pyrenees Massif peridotites. Some sulfides showed regions of exsolution, so they are plotted as multiple points if multiple EPMA point analyses were measured. Gray fields denote common sulfide assemblages. All data are shown in atomic %.
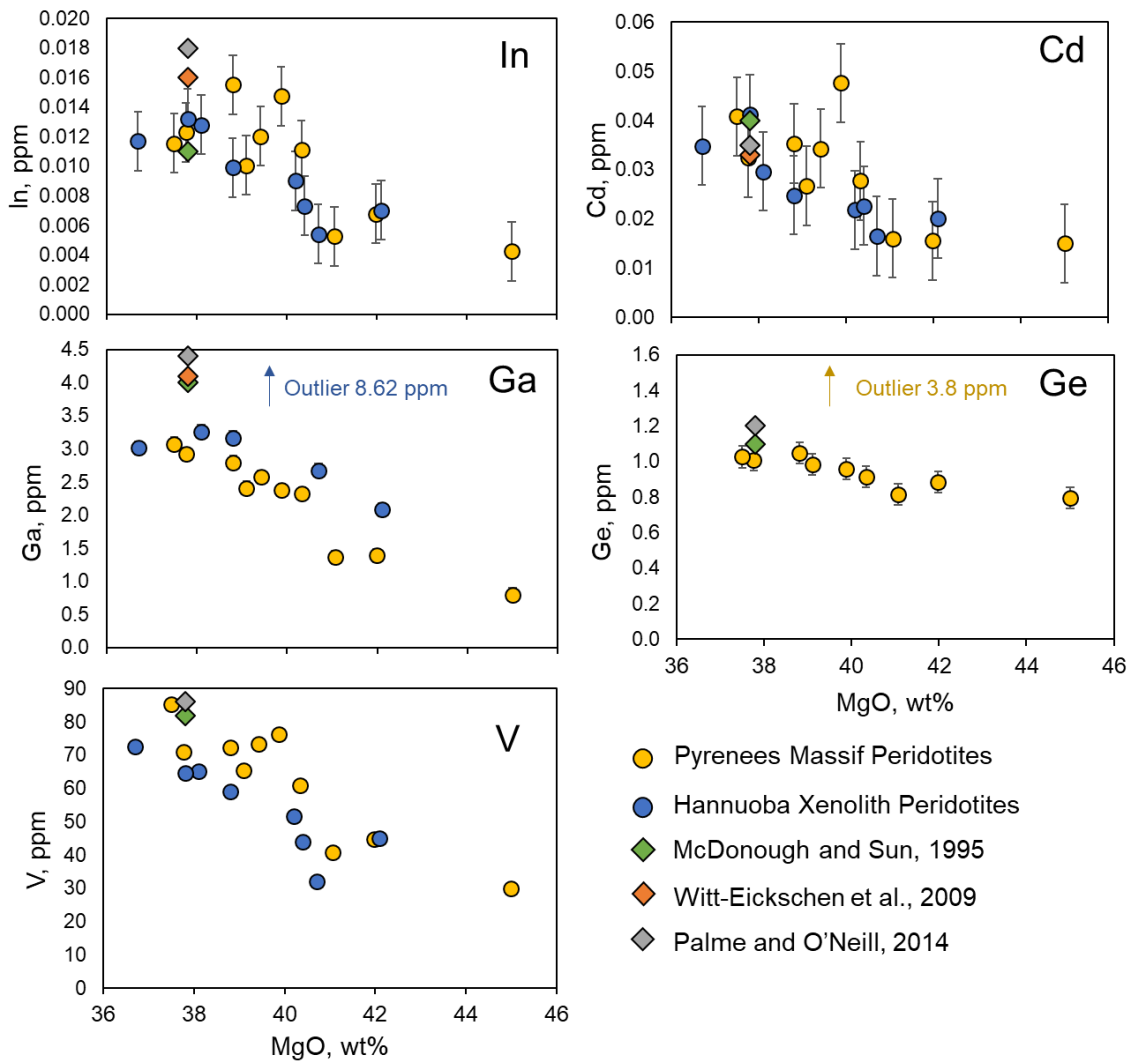
Figure 6.4. Major element variation diagrams showing the behavior of In, Cd, Ga, Ge, and V during melting. Other elements did not form coherent trends. The Ga and Ge figures exclude outliers. Three estimates for the primitive mantle are given from McDonough and Sun (1995), Witt-Eickschen et al. (2009), and Palme and O'Neill (2014). To be conservative, the error on the samples represents 2RSD calculated on the highest concentration sample.

|	V	Ga	Ge	Mo	Cd	In	Sn	Sb	W	Tl	Bi
Pyrenees Massif Peridotites											
olivine	**0.40**	**0.01**	**0.67**	*0.006*	**0.02**	**0.003**	**0.24**	*0.03*	*0.009*	*0.004*	*0.004*
2σ	0.14	0.02	0.14	0.006	0.04	0.004	0.34	0.01	0.000	0.000	0.000
cpx	**223**	**3.13**	**1.17**	**0.010**	**0.14**	**0.046**	**0.42**	*0.03*	*0.010*	*0.004*	*0.004*
2σ	52.2	1.38	0.34	0.041	0.08	0.013	0.37	0.00	0.009	0.002	0.002
opx	**88.0**	**2.37**	**1.38**	**0.008**	**0.05**	**0.014**	**0.31**	*0.03*	*0.009*	*0.005*	*0.004*
2σ	23.6	0.81	0.33	0.012	0.06	0.011	0.44	0.02	0.006	0.008	0.003
spinel	**329**	**59.1**	**0.11**	*0.006*	**0.04**	**0.005**	**0.44**	*0.03*	*0.009*	*0.005*	**0.005**
2σ	154	14.9	0.21	0.007	0.09	0.016	0.89	0.00	0.000	0.005	0.006
Hannuoba Xenolith Peridotites											
olivine	**2.77**	**0.03**	**1.16**	*0.006*	**0.01**	**0.015**	*0.04*	**0.08**	*0.009*	*0.004*	**0.006**
2σ	1.04	0.04	1.22	0.006	0.02	0.029	0.00	0.17	0.002	0.002	0.009
cpx	**252**	**3.20**	**1.72**	*0.006*	**0.08**	**0.043**	**0.06**	**0.09**	**0.011**	**0.005**	**0.008**
2σ	17	1.13	1.00	0.007	0.09	0.037	0.14	0.19	0.011	0.014	0.015
opx	**85**	**2.72**	**1.50**	*0.006*	**0.03**	**0.014**	*0.03*	**0.06**	*0.008*	*0.004*	*0.004*
2σ	9.40	0.77	1.21	0.005	0.06	0.031	0.03	0.14	0.004	0.003	0.004
spinel	**386**	**59.7**	**0.48**	**0.014**	**0.01**	**0.018**	*0.04*	**0.09**	**0.009**	**0.006**	**0.013**
2σ	126	16.6	2.03	0.036	0.06	0.068	0.02	0.54	0.000	0.010	0.046

Table 6.4. *In-situ* trace element concentrations in silicates and spinel. Mo, Sb, W, Tl, and Bi were routinely below detection in the silicates and spinel, as denoted by the italics. In the Hannuoba samples, Sn was routinely below detection limits as well. The detection limit was used in lieu of those analyses, therefore the mean concentration may be skewed to higher values that realistically exist.
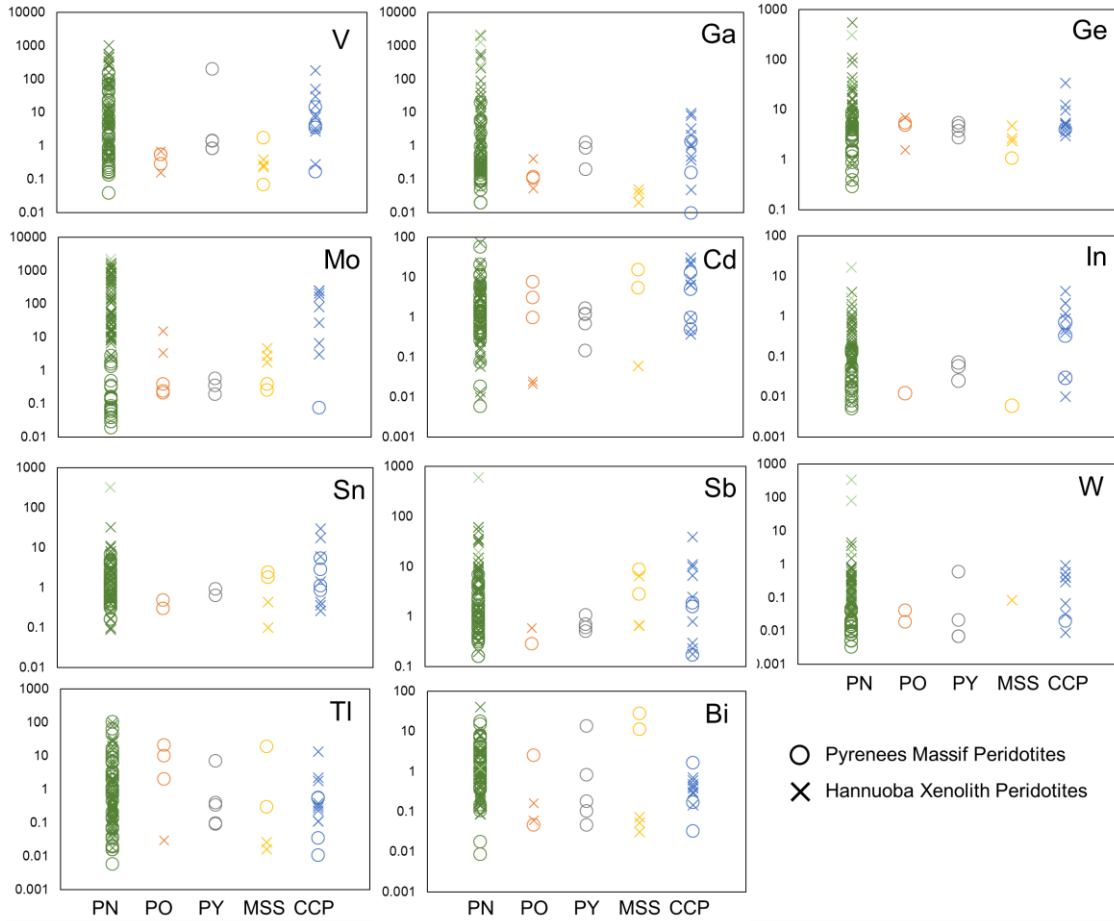
6.4.2 Sulfides

Fifty-five Hannuoba Xenolith sulfides were analyzed by EPMA and 48 of those sulfides were then analyzed by LA-ICP-MS. Ninety-eight Pyrenees Massif sulfides were analyzed by EPMA and 48 of those sulfides were analyzed by LA-ICP-MS. Some of these sulfides were large enough that multiple EPMA or LA-ICP-MS points could be analyzed on one grain. The sulfides are composed of pentlandite, pyrrhotite, chalcopyrite, which are considered to be sub-solidus exsolution products of mono-sulfide solid solution (MSS) (**Figure 6.3**). Pyrite is present as well. Several sulfides in the Pyrenees Massif samples and

few sulfides in the Hannuoba samples are also rimmed by Fe-hydroxides (**e.g., Figure 6.2b**). Sulfides are divided into Type e (enclosed in another mineral), Type i (interstitial), Type iv (interstitial vein), and Type f (fracture filling) on **Figure 6.3,** however no systematic correlation is observed between sulfide type and composition.

There is significant spread in the trace element LA-ICP-MS data within sulfides from the same locality and between localities. Because of this, we present both mean and median element concentrations in the sulfides (**Table 6.3**, data for individual spot analyses are provided in the supplementary files), and we focus on the median value for the discussion given that the distribution is not normal. Box and whisker plots representing all the LA-ICP-MS data collected are presented in **Figure 6.5**. Note that several elements are routinely below the detection limits in the sulfides, so the data presented in **Table 6.3** and **Figure 6.5** include that element's detection limit in place of those BDL analyses. None of the element concentrations in sulfide presented here follow a normal distribution (supplementary figures – **Appendix F**).
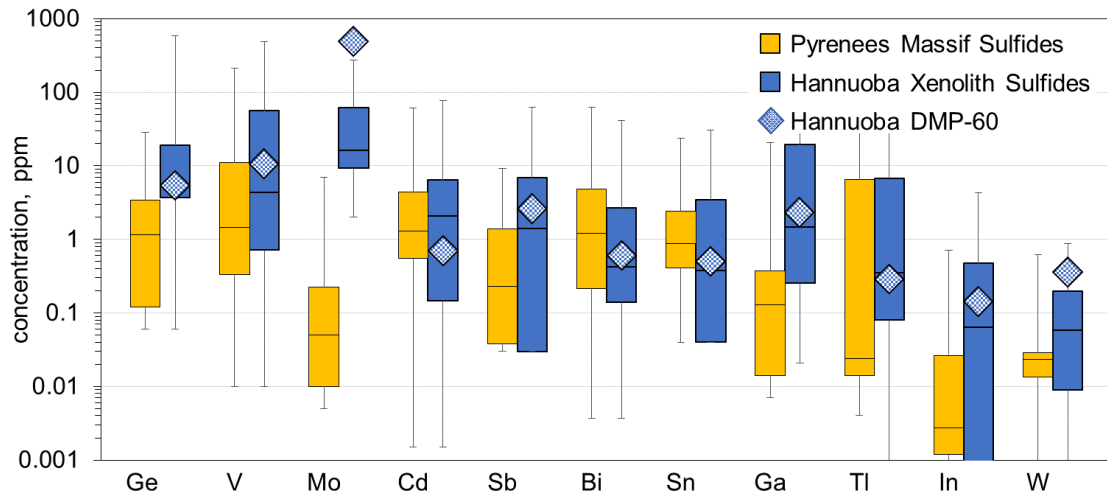
Figure 6.5 Trace element abundances in sulfides, arranged from highest median abundance on the left to lowest on the right. The Hannuoba box and whisker plots do not contain metasomatically altered sulfides from DMP-60. The median concentrations of the elements in sulfides from DMP-60 are plotted as a diamond.

Figure 6.6. Abundances of the elements (ppm) in different sulfide minerals in the Pyrenees Massif samples (open circles) and Hannuoba xenoliths (Xs). Pentlandite (Pn) is in green, pyrrhotite (Po) in orange, pyrite (Py) in gray, monosulfide solid solution (MSS) in yellow, and chalcopyrite (CCP) in blue. Three pentlandite samples are shaded in light green to mark that they show anomalously high abundances of the elements in all samples. These data do not include analyses that were BDL.
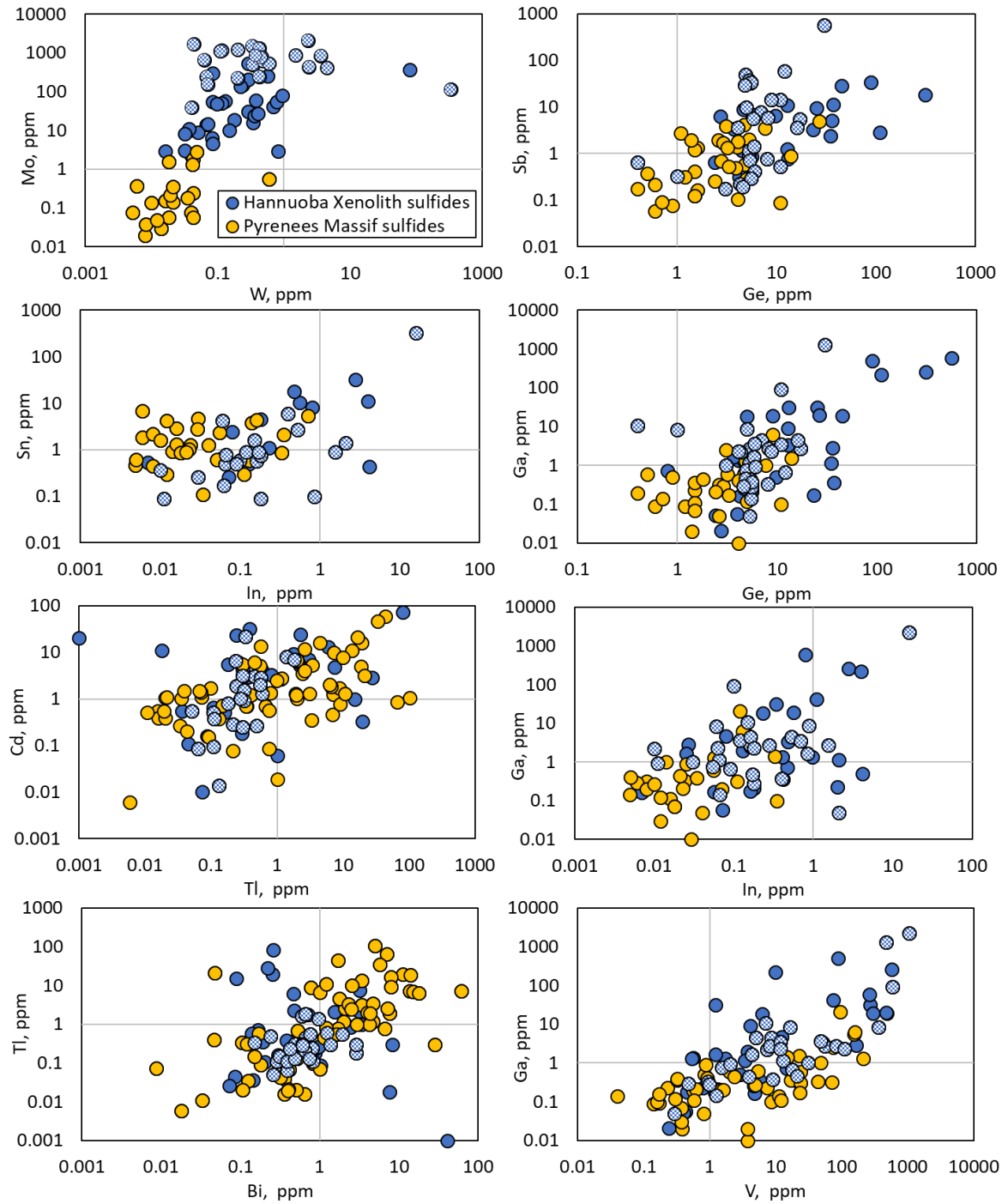
Figure 6.7. Multi element variations in sulfides in the Hannuoba xenolithic peridotites (blue) and Pyrenees Massif (yellow) sulfides. As in Fig. 6.5, the blue hatched pattern highlights sulfides from sample DMP-60 (Hannuoba Xenoliths), which shows evidence for metasomatic sulfide addition (see text).

6.4.3 Pyroxenes, Olivine, Spinel

In addition to sulfides, the major phases orthopyroxene, clinopyroxene, olivine, and spinel were analyzed by LA-ICP-MS for the elements of interest (**Table 6.4, Figure 6.8**). The data presented in **Table 6.4** and **Figure 6.8** include the detection limit in place of analyses where the element abundance was below the detection limit. Therefore, these data may be skewed to slightly higher mean and median values. These mean data are used to complete a mass balance for each element.

*6.4.4 Grain boundaries and fractures*

Line scans were run between mineral grains and across fractures within single minerals in the peridotites to assess whether elements are contained within these areas. In the Hannuoba xenolithic peridotites, Mo and W were found along nearly every grain boundary analyzed, as well as in fractures within single minerals (**Figure 6.9**). Molybdenum and W were also found on some Pyrenees massif grain boundaries, but their enrichment was not as significant as in the xenolithic peridotites. In addition, Ga, Sn, Tl, and Bi were found along several grain boundaries in the Hannuoba peridotites, but these elements are not ubiquitously enriched like Mo and W. While these enrichments could not be accurately quantified, given small surface areas of the interstitial spaces, qualitative estimates can be made by comparing the peaks measured in the time resolved spectra with secondary standards. We estimate that the grain boundaries contain between 0.5 and 1 ppm Mo and W, and in some cases up to several (3 to 4) ppm Mo. The grain boundaries in the Hannuoba peridotites that show enrichment in the other elements (e.g., sample DMP-56; **Figure 6.9**) may contain up to 0.10 ppm Tl and Bi, 1 ppm Sn, and 1.5 ppm Ga.

6.4.5 Mineralogical distribution of elements and mass balance

Mass balance was calculated using modal mineralogy from Rudnick et al. (2004) for the

Hannuoba samples and modes estimated by Lorand et al. (1999). Sulfide proportions in both

peridotite localities were calculated using the total sulfur content and assuming a pentlandite

stoichiometry. The median concentrations of the elements of interest in sulfides for each

sample is used, which can vary significantly, as do the mean concentrations in the silicates

and spinels. The calculated whole-rock concentration of an element was then compared to

the measured whole-rock concentration to determine if any proportion was "missing". To

account for error in the modal mineralogy and concentrations in the minerals, we assume

that any reconstructed whole rock concentration within 20% of the concentration measured

by solution ICP-MS completes the mass balance. In total, a mass balance was completed on

six samples from the Hannuoba Xenolith peridotites and four samples from the Pyrenees

Massif peridotites (**Figure 6.9**). Mass balanced is obtained for V and In in 90% of the

samples, for Cd in 80% of the samples, for Ge in 75% of the Pyrenees samples, for Ga, Sb,

and Tl in 70% of the samples, for Bi in 40% of the samples, for Sn in 30% of the samples,

for Mo in 10% of the samples, and mass balance was never obtained for W (**Figure 6.10**).
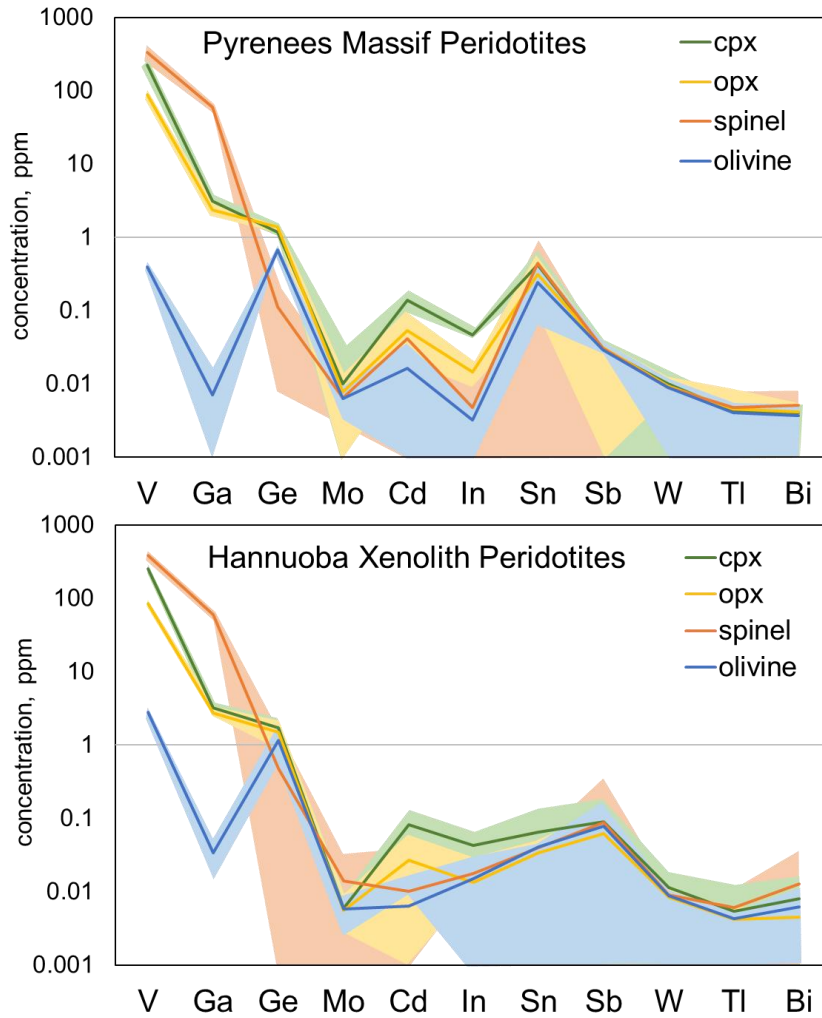
Figure 6.8 Element concentrations in the silicate minerals and spinel. The line represents the mean concentration and colored envelopes represent 1σ standard deviation of the mean of multiple analyses. Note that Sb, W, Tl, and Bi were routinely below detection limits in the minerals so the mean concentration here may be skewed towards higher values.
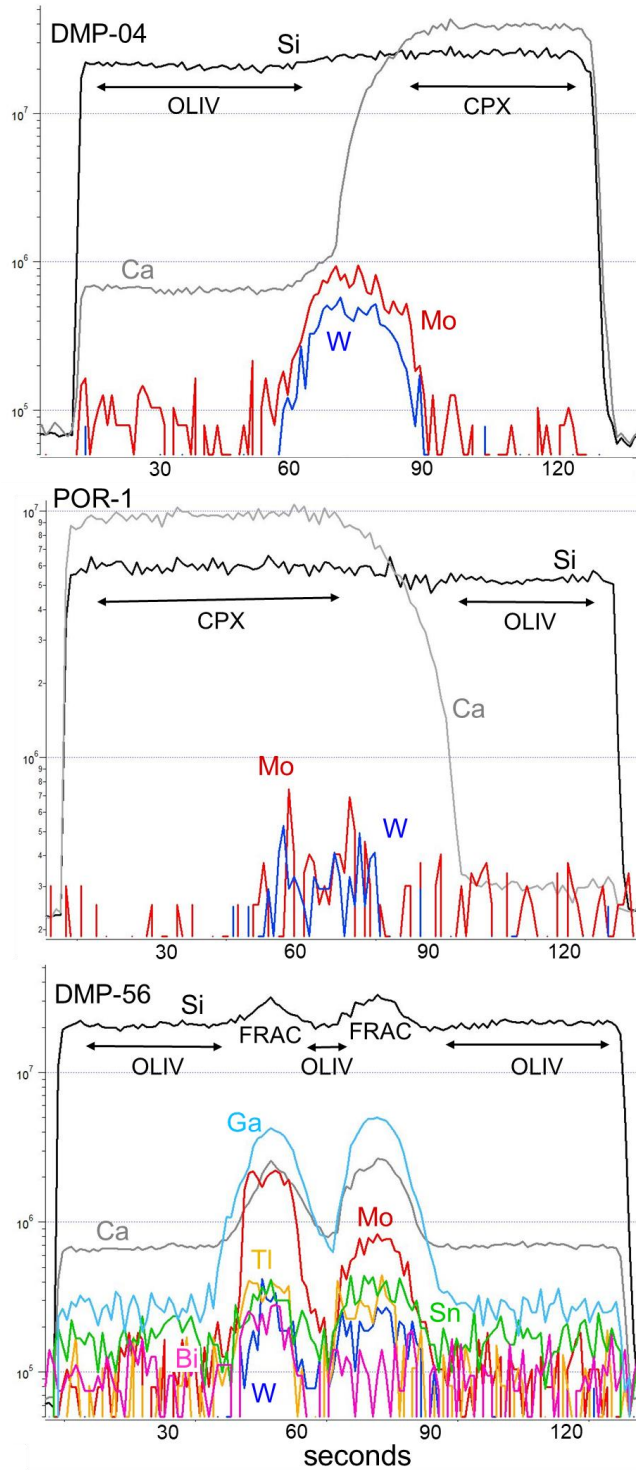
Figure 6.9 Laser ablation time resolved spectra showing enrichments of Mo in interstitial spaces between silicate mineral grains or in fractures (FRAC) within mineral grains in the peridotites. Samples DMP-04 and DMP-56 are from the Hannuoba xenoliths and sample POR-1 is from the Pyrenees Massif.

6.4 DISCUSSION

6.4.1 Deposition on grain boundaries

Several lines of evidence suggest that both suites of peridotites, and especially the Hannuoba xenoliths have been affected by metasomatic agents. Firstly, in the whole-rock data, several elements do not form coherent trends with respect to the degree of melt depletion of the sample (i.e., MgO) for whole rock data. This includes Mo, Sn, Sb, W, Tl, and Bi as well as the LREE and several other fluid-mobile elements like Rb. These are the same elements that typically cannot be mass balanced and are more enriched along grain boundaries than within minerals (except for sulfide in some cases). Therefore, we conclude that a fluid or low degree partial melt infiltrated both peridotite suites to different degrees – the Hannuoba xenoliths record ubiquitous grain boundary enrichments (GBE) for several highly incompatible elements, while the Pyrenees Massif peridotites generally only record Mo and W GBE. The effect of this metasomatic overprinting as well as the overall behavior of each element is explored in detail below.

	Sc	V	Cr	Co	Ni	Cu	Rb	Sr	Y	Zr	Nb	Ba	La	Ce	Pr
Pyrenees Massif Peridotites															
POR-1	13.77	76.3	2691	110	2226	26.6	1.52	16.9	3.28	2.48	0.15	7.87	0.39	1.21	0.20
POR-2	11.92	71.1	2743	103	1921	28.5	0.40	2.97	2.65	1.19	0.05	1.08	0.04	0.21	0.06
POR-3	8.72	72.2	2177	95	1908	30.3	0.51	6.05	3.08	1.17	0.21	6.15	0.14	0.44	0.09
16-4	13.07	85.2	2845	100	2311	39.9	0.35	10.71	3.39	4.91	0.16	0.80	0.17	0.60	0.12
PGER-2	8.21	40.8	2428	107	2168	6.1	0.11	3.18	0.75	0.98	0.15	0.61	0.08	0.26	0.04
PGER-3	9.20	44.8	2477	108	2213	11.3	0.32	4.18	0.92	0.44	0.21	1.20	0.08	0.30	0.05
71-336	10.13	73.4	2398	100	2655	27.3	0.18	10.38	3.26	2.98	0.02	1.32	0.09	0.37	0.08
71-335	10.37	60.9	2169	100	2601	21.2	0.15	11.30	2.56	2.30	0.03	3.38	0.08	0.30	0.07
64-3	6.72	30.0	2100	106	2226	1.7	BDL	0.56	0.54	BDL	0.13	0.38	0.02	0.06	0.01
71-323	6.59	29.0	2335	106	2189	2.2	BDL	3.69	0.04	BDL	0.08	0.18	0.01	0.03	0.00
73-273	9.94	65.3	2599	101	2270	23.2	0.02	8.89	2.71	2.52	0.07	0.80	0.19	0.61	0.11
Hannuoba Xenolith Peridotites															
DMP 60	17.2	72.5	2960	101	2007	24.7	0.33	19.09	3.71	4.66	0.08	5.51	3.47	1.21	0.10
DMP 56	15.7	65.1	2468	101	1900	26.9	0.21	11.28	3.37	6.00	0.26	1.07	0.21	0.61	0.11
DMP 41	12.9	51.7	3032	111	2067	15.0	0.27	7.32	1.92	2.47	0.06	0.32	0.88	1.45	0.16
DMP 19	9.3	32.2	2576	107	2174	9.2	0.18	19.59	0.67	2.75	0.50	0.33	0.19	0.39	0.05
DMP 04	12.9	45.1	3040	116	2289	18.1	0.21	5.40	1.55	1.80	BDL	0.43	0.18	0.37	0.06
DMP 58	14.7	59.0	2651	113	2102	23.4	0.67	5.80	2.77	2.39	0.21	0.47	0.12	0.25	0.04
DMP 59	12.3	44.0	2677	114	2157	24.9	0.58	9.64	1.79	4.02	0.36	5.48	1.43	2.06	0.21
DMP 67c	16.6	64.8	2857	110	1927	12.7	5.87	38.83	4.22	15.38	1.19	16.93	1.45	3.46	0.51

Table 6.5. Whole rock trace element data measured by solution ICP-MS (continued on next page)

	Nd	Sm	Eu	Gd	Tb	Dy	Ho	Er	Tm	Yb	Lu	Hf	Ta	Pb	Th	U
Pyrenees Massif Peridotites																
POR-1	1.02	0.32	0.12	0.39	0.08	0.51	0.12	0.33	0.06	0.34	0.05	0.08	0.01	1.88	0.08	0.02
POR-2	0.37	0.19	0.08	0.30	0.06	0.45	0.10	0.29	0.05	0.31	0.05	0.05	BDL	0.27	0.02	0.02
POR-3	0.50	0.22	0.09	0.33	0.07	0.48	0.11	0.33	0.06	0.34	0.05	0.04	BDL	1.10	0.01	0.02
16-4	0.67	0.27	0.11	0.39	0.08	0.57	0.13	0.37	0.06	0.38	0.08	0.13	0.01	5.12	0.01	0.01
PGER-2	0.18	0.06	0.03	0.09	0.02	0.12	0.03	0.09	0.02	0.10	0.02	0.00	0.01	0.30	0.01	BDL
PGER-3	0.23	0.08	0.03	0.11	0.02	0.14	0.03	0.10	0.02	0.12	0.02	BDL	0.01	0.39	0.07	0.02
71-336	0.45	0.22	0.09	0.33	0.07	0.51	0.12	0.34	0.07	0.36	0.05	0.08	BDL	0.91	BDL	BDL
71-335	0.37	0.16	0.07	0.25	0.05	0.41	0.09	0.27	0.05	0.29	0.04	0.05	BDL	0.51	BDL	0.03
64-3	0.04	0.02	0.01	0.05	0.01	0.08	0.02	0.06	0.01	0.08	0.01	BDL	BDL	0.13	BDL	0.01
71-323	0.00	0.00	0.00	0.01	0.00	0.01	0.00	0.01	0.00	0.01	0.00	BDL	BDL	0.08	BDL	BDL
73-273	0.59	0.22	0.09	0.29	0.06	0.45	0.10	0.29	0.05	0.30	0.05	0.06	BDL	0.35	0.02	BDL
Hannuoba Xenolith Peridotites																
DMP 60	0.53	0.24	0.10	0.37	0.08	0.54	0.12	0.38	0.06	0.38	0.06	0.14	BDL	*1.10*	0.43	0.06
DMP 56	0.66	0.26	0.11	0.38	0.08	0.53	0.12	0.35	0.05	0.35	0.06	0.17	BDL	*1.56*	BDL	0.01
DMP 41	0.66	0.16	0.06	0.21	0.04	0.28	0.06	0.20	0.03	0.21	0.03	0.07	BDL	*0.17*	BDL	0.03
DMP 19	0.25	0.06	0.03	0.07	0.01	0.10	0.02	0.07	0.01	0.09	0.01	0.03	0.01	*0.23*	BDL	0.05
DMP 04	0.29	0.09	0.04	0.15	0.03	0.22	0.05	0.16	0.02	0.17	0.03	0.05	BDL	*0.50*	BDL	BDL
DMP 58	0.26	0.14	0.06	0.24	0.05	0.38	0.09	0.27	0.04	0.28	0.04	0.07	BDL	*0.04*	BDL	0.03
DMP 59	0.83	0.18	0.06	0.21	0.04	0.26	0.06	0.19	0.03	0.19	0.06	0.08	0.01	*0.36*	BDL	0.02
DMP 67c	2.48	0.68	0.23	0.73	0.12	0.73	0.15	0.41	0.06	0.35	0.05	0.35	0.06	*1.93*	BDL	0.04

Table 6.5. Whole rock trace element data measured by solution ICP-MS. Pb data in the Hannuoba samples from Rudnick 2004

6.4.2 Sulfide origin

Most of the sulfides analyzed in both suites are "primary" base metal sulfides composed of pentlandite and pyrrhotite with regions of chalcopyrite exsolution (Lorand and Luguet, 2016). Several sulfides in the Pyrenees massif samples also contain secondary pyrite and Fe-hydroxides (**e.g. Figure 6.2b**). Pyrite is generally not considered a primary mantle phase (Lorand and Alard, 2011), therefore both phases are interpreted to be the result of low-temperature alteration as sulfur was added into the rocks from surrounding country rock. This sulfur may have been introduced via fluids that also caused the precipitation of hydrated Fe-oxide phases from Fe sourced from pre-existing sulfides or silicate phases. Interestingly, this alteration does not seem to have affected trace element abundances in the sulfides, as there is no systematic enrichment or depletion of any element in pyrite relative to "primary" phases from either the Pyrenees massif samples or Hannuoba xenolith samples (**Figure 6.6**). Therefore, we conclude that although pyrite may be a secondary phase, these sulfides may still record primary trace element characteristics.

Additionally, we propose that one of the Hannuoba xenolith samples studied here contains a different type of secondary sulfide. Sample DMP-60 has been suggested to have experienced significant metasomatic overprinting based on a lack of Sr mass balance and zoned LREE profiles in clinopyroxene (Rudnick et al., 2004). This sample also contains a higher proportion of Cu-rich sulfides and higher S content than the primitive mantle (Liu et al. 2010). We corroborate this suggestion with our textural observations, trace element data, and the fact that sample DMP-60 contains an order of magnitude more sulfide grains than any other Hannuoba sample analyzed. Several sulfides in DMP-60 show complex reaction textures that suggests interaction with some form of silicate melt (**e.g. Figure 6.2d**).

Additionally, several trace elements like Mo and W show extreme enrichments in the DMP-60 sulfides. The sulfides from this sample are highlighted in a patched pattern in **Figure 6.7**. As Mo and W are enriched on nearly every grain boundary analyzed, we conclude that sulfides in the DMP-60 sample were deposited by a metasomatic agent enriched in S, Mo, and W.

Except for the sulfur addition to sample DMP-60 and alteration to pyrite in some of the Pyrenees samples, we conclude that the majority of the sulfides present in the peridotites are primary, given the strong correlation between whole-rock S and MgO. Nevertheless, as explored below, the trace element signatures of some of these sulfides may have been overprinted during metasomatic addition of some elements, namely Ga, Mo, and W.

6.4.3 Vanadium

Vanadium partitioning between silicate minerals and spinel is very well documented in experimental studies (e.g., Canil 2002; Righter et al., 2006), however its partitioning into sulfides is less well-studied. Vanadium mass balance can be completed in nine out of ten samples analyzed here based on clinopyroxene, orthopyroxene, and spinel alone, reflecting its lithophile behavior. In several samples, nearly half of the total V is hosted in clinopyroxene, consistent with V incompatibility during mantle melting. There is a positive correlation between the percentage of V hosted in spinel and the degree of melt depletion of a sample (**Figure 6.11**) indicating that V partitions into spinel during partial melting of the mantle. These data confirm thermodynamic calculations of V partitioning during partial melting of Canil and Fedortchuk (2000). Prytulak et al. (2013) found that there is a positive correlation between $\delta^{51}V$ and Al_2O_3 in peridotites, suggesting that V isotopes are fractionated during mantle melting. Prytulak et al. rule out V isotope fractionation due to

partitioning between clinopyroxene and orthopyroxene. Because V partitioning into spinel is temperature and $f\mathrm{O}_2$ dependent (Righter et al., 2006), we propose that increased partitioning into spinel during partial melting, as demonstrated here, may induce isotope fractionation and warrants further study.

Of all the elements analyzed here, vanadium is one of the most abundant element in sulfides (**Figure 6.5**). However, its median concentration of 3.7 ppm in sulfide is negligible compared to several hundred ppm in the silicate phases, making V a definitively lithophile element in the mantle. These data are consistent with the experimentally determined $D^{\mathrm{sulfide/silicate\ melt}}$ for V of 0.01 and 0.1 (Li and Audetat, 2012). Vanadium concentration in the sulfides is correlated with Ga (**Figure 6.7**) and Mn (supplementary figures – Appendix F), both lithophile elements. Like V, Mn has been experimentally determined to be incompatible in sulfide (Li and Audetat, 2012), and their partitioning into sulfide is likely due to increased oxygen content of the sulfide with increasing $f\mathrm{O}2$ (Kiseeva and Wood, 2013; Gaetani and Grove, 1997).

6.4.4 Gallium

Like V, Ga is predominately hosted in clinopyroxene, orthopyroxene, and spinel. The similarities between the two elements is unsurprising given their expected 3+ valence states and likely substitution for Al in these minerals. However, unlike V, Ga is expected to remain in the 3+ valence state regardless of the $f\mathrm{O}_2$ of the sample. Spinel alone accounts for around 50% of the total Ga budget in half of the samples. The one sample (DMP 41) that could not be mass balanced plots as an extreme outlier in the whole rock data and is excluded from the discussion. While the percentage of Ga hosted in spinel is relatively constant relative to the degree of melt depletion in the samples, the percentage of Ga hosted

in orthopyroxene appears to decline with increasing melt depletion (**Figure 6.10**) suggesting

that orthopyroxene, and likely clinopyroxene, are the predominate hosts of Ga. Additionally,

in the Hannuoba xenoliths, Ga was found along some, but not all, grain boundaries (e.g.,

Figure 6.9). This Ga was likely added by an infiltrating low degree partial melt.

Despite Ga's high abundance in some sulfides (up to several hundreds to thousands

of ppm in the Hannuoba xenoliths), sulfide is not a major host of Ga in peridotites.

However, as predicted by the experimental studies of Kiseeva and Wood (2015), we observe

a positive relationship between temperature of the sample (as calculated by the pyroxene

thermometer of Brey and Kohler, 1990; Liu et al., 2010) and the median concentration of Ga

in the sulfides of the sample (**Figure 6.12**). While this correlation is not statistically

rigorous, it suggests that temperature does indeed influence trace element partitioning into

sulfides, which may partially explain why the Hannuoba Xenolith sulfides contain

significantly more Ga than the Pyrenees Massif sulfides (**Figure 6.5)** The addition of Ga to

the Hannuoba xenolith samples from a metasomatic agent may also have added Ga to the

sulfides in those samples. Indeed, the Ga content of the Pyrenees Massif sulfides is much

more similar to that measured in sulfides from the Kilauea Iki lava lake in Hawaii (Greaney

et al., 2017; supplementary figures).

6.4.5 Germanium

Germanium is predominately hosted in the silicate phases olivine, orthopyroxene,

and clinopyroxene. This is to be expected given the likely substitution of Ge for Si in these

crystal lattices. The one sample for which mass balance was not obtained (71-336) plots as

an outlier in the whole rock data set and it not included in the discussion. Given its

preference for olivine and orthopyroxene, Ge does not behave as a strongly incompatible

element and its concentration is relatively constant in all samples, with a slightly negative slope (**Figure 6.4**). The presence of Ge in sulfide and clinopyroxene, two phases that are unstable during partial melting, may result in a lower bulk D value for Ge during melting which might account for the slightly negative slope of the whole-rock Ge trend relative to MgO. Interestingly, Ge has the highest median concentration in sulfide of all elements analyzed (overall median of 4.1 ppm), however sulfide is not a significant host of Ge in any sample due to the low modal proportion of sulfide relative to silicates. Like Ga, Ge also shows a slight temperature dependence (**Figure 6.12**) where Ge is more chalcophile in peridotites that equilibrated at higher temperatures. Unlike Ga, there is no evidence for the addition of Ge to the samples by metasomatism.

6.4.6 Molybdenum

Molybdenum behaves like a highly incompatible element in these peridotites, as expected given its enrichment in basalts over peridotites (Newsome and Palme, 1984; McDonough and Sun, 1995). In the whole-rock data, Mo appears to be positively correlated with MgO wt%, implying that it behaves compatibly (Supplementary Figure F2). However we instead propose that Mo is displaying a phenomenon observed by Frey and Green (1974) where the most melt-depleted peridotites are most enriched in incompatible elements. Molybdenum was likely stripped from these samples during mantle melting and then re-deposited by the influx a metasomatic agent (possibly a low degree partial melt) that coated the grain boundaries (**Figure 6.9**). This suggests that every sample has been slightly metasomatically overprinted with Mo.

With the exception of sample DMP-60 where Mo is enriched in the metasomatically deposited sulfides, Mo is not compatible in any mineral analyzed here. It is routinely below

detection limits in several silicates and spinel and is found along nearly all grain boundaries analyzed. As shown in **Figures 6.5, 6.6, and 6.7**, Mo is significantly more enriched the Hannuoba sulfides (median 84.0 ppm) relative to the Pyrenees Massif sulfides (median = 0.05 ppm) which is similar to the behavior of Ga and W. As these elements also enrich grain boundaries, we suggest that the same metasomatic fluid that deposited these elements in the interstitial space also altered the sulfides in the Hannuoba xenolith samples. There is a strong temperature dependence on Mo partitioning (**Figure 6.12**), where the sulfides in the Hannuoba samples that equilibrated at higher T (between ~960°C and ~1380°C) contain orders of magnitude more Mo than the Pyrenees sulfides that equilibrated between ~740°C and ~860°C. This may be because the Hannuoba samples are closer to and even overlap Fe-Ni-Cu-S sulfide solidus (calculated at 1145°C using the experiments of Zhang and Hirschmann, 2016). Therefore, we suggest that although Mo may have been added to both the Hannuoba and Pyrenees samples by a metasomatic agent, Mo was only incorporated into sulfide in the Hannnuoba samples that equilibrated at higher temperature, perhaps because the sulfides were above the solidus. Therefore, the Pyrenees massif samples that record relatively low Mo as well as low Ga and W are likely more representative of "primary" mantle sulfides that are not overprinted by a metasomatic agent. Indeed, the median Mo abundance in the Pyrenees sulfides is similar to previous concentrations of Mo estimated in peridotite sulfides (Wang and Becker, 2018), and measured in basalt-hosted sulfides (Greaney et al., 2017; Patton et al., 2015) and granitic sulfides (Greaney et al., 2018) (see supplementary figure F6).
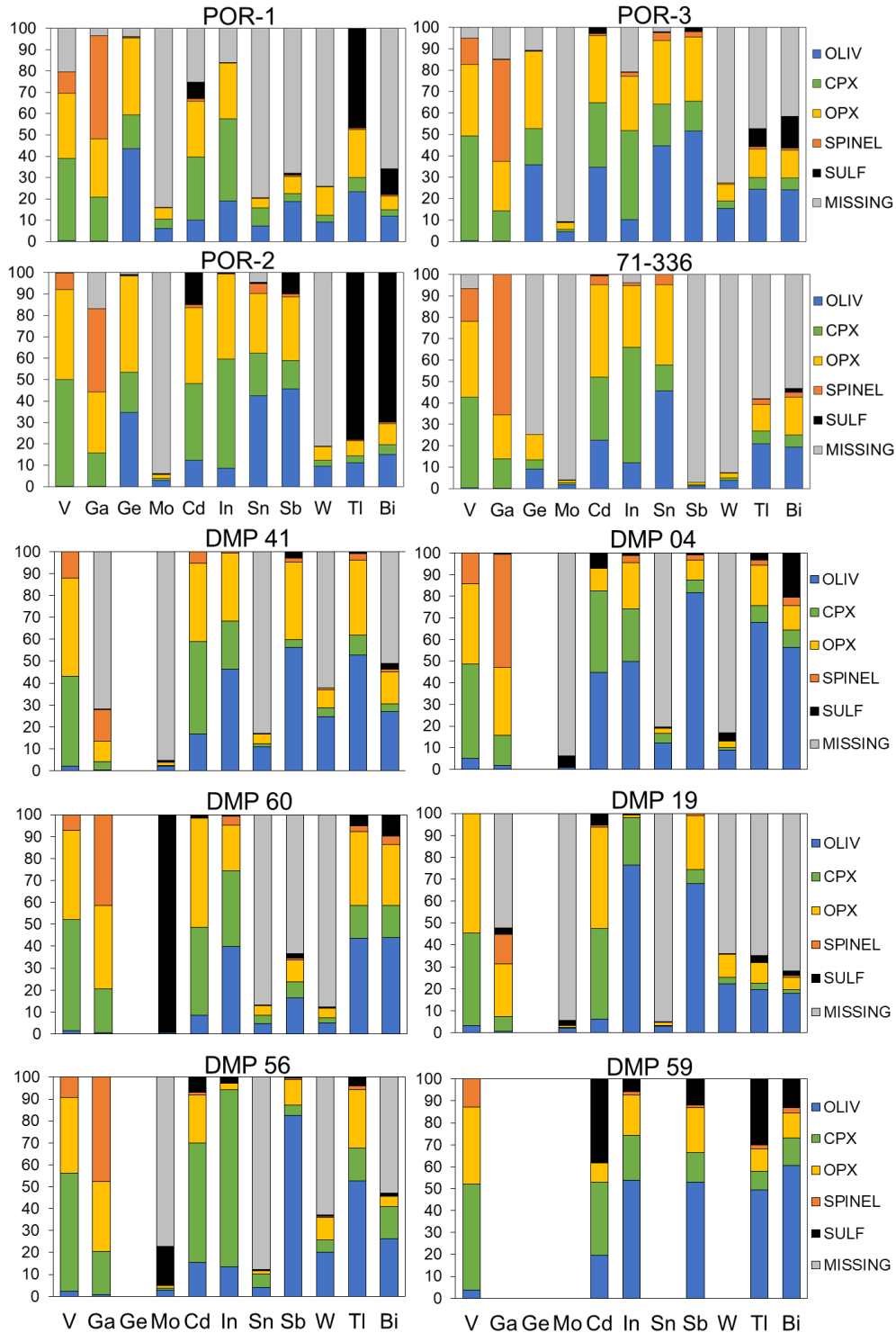
Figure 6.10 Mass balance results showing the mineralogical distribution of the elements. Whole rock data was not collected for the elements Ga, Mo, Sn, and W in DMP-59 so a mass balance relative to the whole-rock concentration could not be completed. Additionally, whole rock data was not collected for Ge in the Hannuoba samples. The mass balance has been normalized to 100%.

6.4.7 Cadmium

Mass balance for Cd is achieved in all but one sample (POR-1). The distribution of Cd varies slightly between samples, with some samples achieving mass balance entirely within the silicates, while other samples have up to 38% of their Cd within sulfides. In each sample locale, there is a slight negative trend between percentage of Cd hosted by clinopyroxene and whole rock MgO wt% (**Figure 6.11**), but it is not statistically significant. There is no other systematic variation between Cd hosts and degree of melt depletion of the sample. The experimental data of Adam and Green (2006) and study of Witt Eickshen et al. (2009) on natural xenolithic peridotites suggest that Cd substitutes for Ca in the M2 site in clinopyroxene given their similar atomic radii, and our data support this. However, we also observe sub-equal partitioning of Cd into orthopyroxene and, to a lesser extent, olivine. The ionic radius of both octahedrally coordinated and 8-fold coordinated Cd sits just outside the 15% envelope of the radius of 6-fold and 8-fold coordinated Mg (Shannon, 1969). Therefore, we also propose that Cd may also substitute into the M1 and M2 sites in orthopyroxene and olivine, where it replaces Mg. On a whole-rock scale, Cd correlates strongly with the MREE to HREE (e.g., see Cd – Ho plots in the supplementary figures), confirming its generally incompatible behavior during mantle melting (**Figure 6.4**). The weaker correlation with the LREE than the MREE/HREE is likely due to the fact that LREE were added into several samples by a metasomatic agent.

Given that Cd is hosted in clinopyroxene and, in some samples, sulfide, Cd is both a lithophile and chalcophile element in the lithospheric mantle. When compared to data from the Kilauea Iki lava lake basaltic differentiation suite (Greaney et al. 2017; supplementary figure S6), we find that Cd is significantly more enriched in basalt-hosted sulfides than

peridotite-hosted sulfides. This may be because Cd is more compatible in the Cu-rich sulfides (ISS) found in the basaltic system as opposed to the Ni-Fe-sulfides (MSS) found in the peridotites.

6.4.8 Indium

Like Cd, In mass balance is achieved in all samples. Despite its trivalent state, In does not follow Al like V and Ga do, and instead behaves similarly to Cd and the REE that are hosted in pyroxenes (see In-Ho correlation supplementary figure S5). However, unlike Cd, sulfide is not a significant host for In, and In is one of the lowest abundance elements in the sulfides analyzed here. This makes In a strictly lithophile element in the lithospheric mantle, as shown by Witt-Eickshen et al. (2009). Indium's explicitly lithophile behavior diverges from studies of In partitioning into sulfides in the Kilauea Iki lava lake basaltic differentiation suite, where In is more chalcophile (Greaney et al. 2017; supplementary figure F6). Like Cd, this may be due to the fact that the basalt-hosted sulfides are much more Cu-rich than those found in the peridotites.

With increasing degrees of melt depletion, olivine becomes a more significant host of In (**Figure 6.11**), suggesting that clinopyroxene and orthopyroxene are the primary hosts of In before partial melting occurs. Clinopyroxene has the highest mean In content, signifying that In substitutes for Ca in the M2 site, in addition to partitioning into the M1 pyroxene site where other +3 cations are often found (Morimoto, 1988; Hill et al., 2001). The fact that olivine is also a significant host for In suggests that In can also substitute for Mg in the M1 site in these minerals.

6.4.9 Tin

None of the Hannuoba samples, and three of the Pyrenees samples achieve mass balance for Sn (**Figure 6.10**). In the Hannuoba peridotites, Sn is found along grain boundaries (**Figure 6.9**). It is therefore possible that the "missing" Sn in the Hannuoba xenolith mass balance resides on grain boundaries. While it is not possible to obtain quantitative concentrations of Sn on the grain boundaries, we estimate that the interstitial space in the Hannuoba samples could contain ~ 1 ppm Sn, which is significantly more than any mineral analyzed, save sulfide. Tin is not present along grain boundaries in the Lherz Massif, therefore we suggest that Sn may be present in trace amphibole that was not analyzed in this study. Despite Sn's enrichment in sulfides over silicate minerals, sulfide is not a significant host, making Sn a lithophile element in the mantle.

Despite their similar WR concentrations, Sn abundances in the minerals in the Hannuoba xenolithic peridotites are lower than those in the Pyrenees Massif samples (**Table 6.4, Figure 6.8**). In the Pyrenees Massif samples that attain mass balance, the olivine and orthopyroxene, and to a lesser extent clinopyroxene are the main hosts for Sn. Nevertheless, clinopyroxene contains the highest Sn concentration Tin partitioning is likely redox depending, and both divalent and tetravalent Sn have been shown to be stable in melts at and above the FMQ redox buffer, depending on melt composition (Farges et al., 2006). Therefore, both species may be present in the lithospheric mantle. Given their nearly identical radii, Sn^{+2} could easily substitute for Ca in the M2 site in clinopyroxene and similarly, Sn^{+4} has a nearly identical radius to Mg^{+2}, and may thus substitute into the M1 or M2 site through a coupled substitution. Adam and Green (2006) note that Sn deviates from its expected placement on a Onuma diagram with other +4 cations in an experimental study

210

of clinopyroxene. This could be due to redox effects. Badullovich et al. (2018) calculate that Sn^{+2} would be more compatible in silicate minerals, but they propose that Sn^{+4} is the dominant species in terrestrial magmatic environments. Here we propose that tetravalent Sn present in the mantle likely substitutes for Mg into the M1 site in pyroxene and olivine.

6.4.10 Antimony

Antimony was unfortunately below detection limits in almost every silicate point analyzed in the Pyrenees massif samples, *e.g.,* only 9 of the 170 laser ablation analyses on silicates and spinel returned values above the detection limit of 0.03 ppm. Therefore, the values used for the mass balance may be skewed to higher values as the detection limit was used in lieu of the BDL analyses to calculate average concentrations in each mineral. However, we were able to obtain *in-situ* Sb data in the Hannuoba xenolith samples that suggest that Sb partitions relatively equally between olivine, pyroxene, and spinel (**Figure 6.10**). Thus, Sb deviates from the behavior of other trivalent cations like In that generally favors clinopyroxene. We suggest that the smaller radius of Sb^{+3}, relative to In^{+3}, allows it to preferentially substitute for Mg in the M1 site in pyroxene and olivine. Redox may also affect Sb partitioning, like Sn, because Sb may exist in the pentavalent state in addition to the trivalent state, however we cannot place constraints on the oxidation state of Sb from these data.

Sulfide contains a median of 1 ppm Sb which is significantly more than any of the silicates or spinel. The presence of sulfide is necessary for the mass balance of two samples, DMP-59 and POR-2, making Sb moderately chalcophile in the mantle.
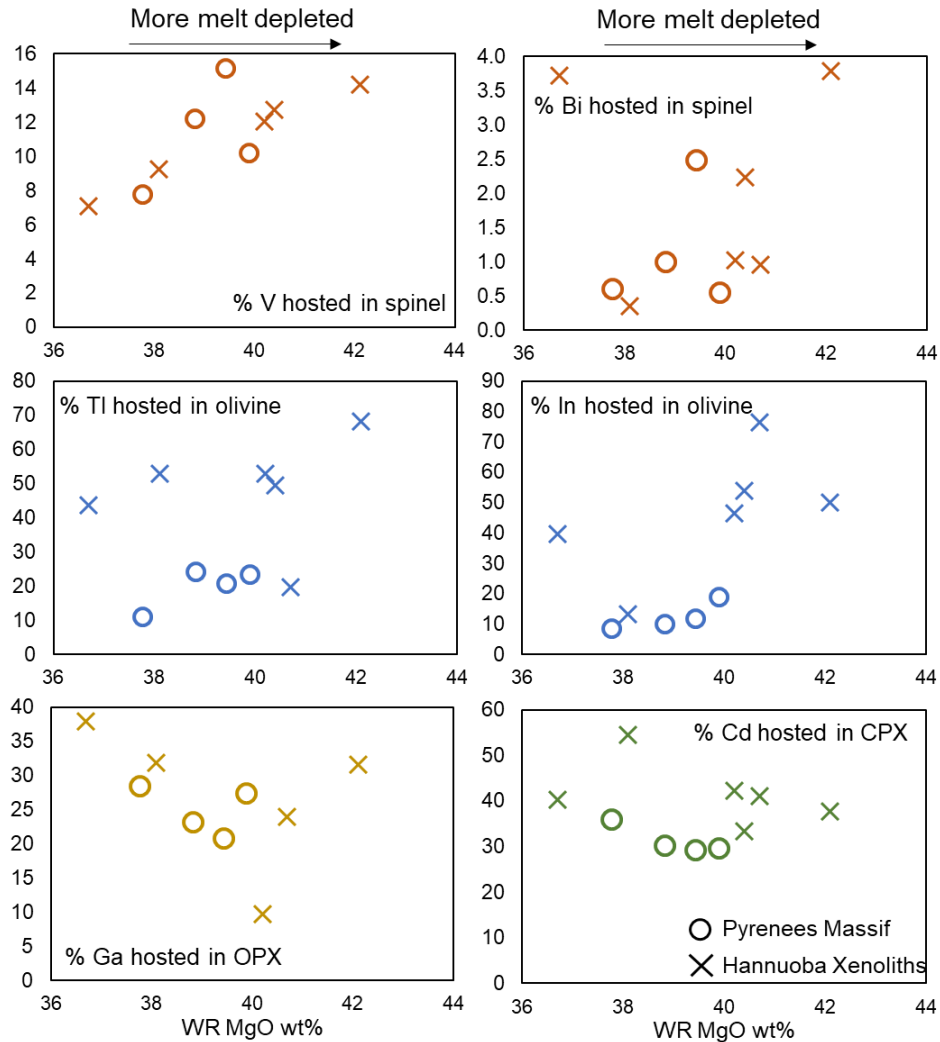
Figure 6.11 Correlations between the degree of melt depletion in a sample and the proportion of an element that hosted in a particular phase. Circles are the Pyrenees massif samples, X's are the Hannuoba xenolith samples. WR = whole rock.

6.4.11 Tungsten

Tungsten proved difficult to measure with *in-situ* methods, with the majority of the analyses of the Pyrenees Massif silicates and several analyses in the Hannuoba silicates returning values below the detection limit. Therefore, the W concentrations used in the mass balance likely overestimate the actual amount of W held in the silicate minerals, but even these data can be useful. Mass balance is not completed for W in any sample analyzed here, however – like its geochemical twin, Mo – W is found on nearly every grain boundary that

212

was analyzed (**Figure 6.11**). These findings agree with those of Liu et al. (2018) who found that W was either predominately hosted in Ti-phases that are not present in our samples, along grain boundaries, or in "cryptic W-bearing trace phases".

Tungsten is the least abundant element analyzed in the sulfide minerals, but it is still more enriched in sulfide than the silicates or spinel. Additionally, its concentration is correlated with Mo – a mildly chalcophile element – between the sulfides in the two peridotite groups (**Figure 6.7**). This may have to do with redox effects, as both elements can be found in their tetravalent and hexavalent states at terrestrial mantle oxygen fugacities (e.g., experiments of Bali et al., 2012). While we don't know the redox state of W and Mo present in the samples, more reducing conditions likely favor substitution of tetravalent Mo and W into sulfide. Another possibility is that metasomatism of the high temperature Hannuoba samples introduced significant Mo and W into the system that were incorporated into sulfides, because, like Mo, W partitioning is temperature dependent (**Figure 6.12**). The temperature dependence for W and Mo s in line with the experiments of Kiseeva and Wood (2015) who – although they did not study W – found that lithophile elements in general become more chalcophile at higher temperatures.

6.4.12 Thallium

Thallium was below the detection limit (0.004 ppm) in most silicate and spinels, but could be measured in almost all sulfides. Thallium is enriched by two orders of magnitude in sulfides (median 0.38 ppm) relative to the silicates and spinel (<0.004 to 0.006 ppm), making it a chalcophile element in the mantle, however silicates are still needed to achieve mass balance. If the detection limit is used for the silicates (almost assuredly an overestimate), then mass balance can be obtained in most samples (**Figure 6.10**). The

presence of Tl along several grain boundaries analyzed may account for the incomplete mass balance in some samples.
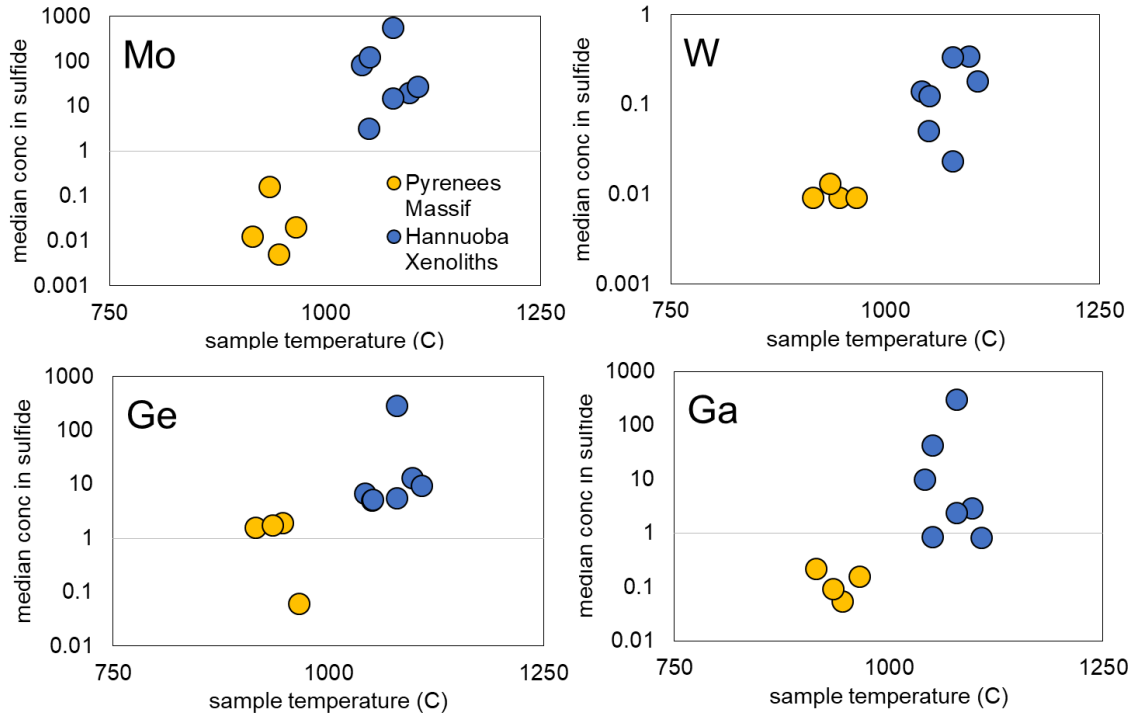
Figure 6.12 Trends between the median concentration of an element in sulfides of a sample and the equilibration temperature of that sample. Temperature was calculated from the pyroxene thermometer of Brey and Kohler (1990) and can be found in the supplementary information.

6.4.13 Bismuth

   Bismuth displays many geochemical similarities to Tl: both elements are below detection limits in most silicate analyses (Bi DL = 0.004 ppm) and both elements are enriched in sulfides by two orders of magnitude relative to the silicates minerals (median Bi concentration in sulfides = 0.655 ppm). Indeed, Bi and Tl concentrations are even correlated in the sulfides (**Figure 6.7**). Unlike other element concentrations in sulfide, the Hannuoba xenolith and Pyrenees massif sulfides are indistinguishable in their Bi and Tl concentrations, indicating that either bulk redox differences, temperature differences, or metasomatic inputs

214

to one peridotite population vs. the other did not affect Bi and Tl partitioning into the sulfides. Like Tl, Bi is a definitively chalcophile element in the mantle.

If the detection limit is used in place of the Bi concentration in the silicate minerals, a mass balance can be completed in four out of 10 samples. Sulfide is a major host of Bi, providing up to 70% of the whole rock Bi concentration. However, mass balance cannot be completed in most samples. Grain boundaries may retain the missing Bi (**Figure 6.8**).

6.4.14 Synthesis

While several of these elements can be quite chalcophile in certain settings in the crust (e.g., hydrothermal or porphyry settings) or under high T and/or low fO$_2$ experimental conditions, we show here that base-metal sulfides are not the sole or even primary host of most of these elements in mantle settings. As predicted by the experiments of Kiseeva and Wood (2015), the predominately lithophile elements Ga, Ge, Mo, and W appear to become more chalcophile at higher temperatures, however their enrichments in higher T sulfides may also be the result of metasomatic addition of the elements to those higher-T peridotites. Their overall low abundances in sulfides are consistent with sulfide-silicate melt partition coefficients calculated in basalts (Greaney et al., 2017; Patten et al., 2015).

As first reported by Witt-Eickschen et al. (2009), In is predominately hosted in silicate minerals in peridotites, and its abundance in sulfides is significantly lower than as observed in Cu-rich basalt-hosted sulfides (Greaney et al., 2017). This is likely due to In's geochemical similarity to Cu, suggesting that it primarily substitutes for Cu in sulfide minerals. The weakly behavior of In seems to diverge from experimental studies (e.g., Kiseeva and Wood, 2015, Kiseeva et al., 2017) that predict In to be chalcophile at mantle conditions (D$^{sulf/sil}$ >10).

Of the elements analyzed here, only Cd, Sb, Tl, and Bi have average modified

$D^{sulfide/wholrock}$ values that are above 1 in both peridotite suites (see Appendix Figure F6),

making them the only moderately chalcophile elements in the mantle. Nevertheless, sulfide

is not the dominant host for any of these elements, so their presence in silicates and on grain

boundaries (e.g., extreme incompatible behavior) should be taken into account when

modeling their behavior during mantle melting.

CONCLUSIONS

Xenolithic peridotites from the Hannuoba basalts (North China Craton) and Massif

peridotites from the Pyrenees mountains (France) contain primary base-metal sulfides

primarily composed of sub-solidus equilibration products of MSS (e.g., pentlandite,

pyrrhotite, and chalcopyrite). While some of the elements investigated here (V, Ga, Ge, Mo,

Cd, In, Sn, Sb, W, Tl, and Bi) can be enriched in sulfides to several hundred to thousand

ppm, none of these elements can be considered definitively chalcophile where sulfide is the

sole or dominant host. Bismuth and Tl are the only two elements that are consistently hosted

in sulfide to some extent across all samples, however silicate minerals and grain boundary

enrichments are still needed to achieve mass balance. Antimony and Cd can be considered

weakly chalcophile in that sulfide is occasionally needed to obtain mass balance. The

majority of the elements analyzed (V, Ga, Ge, In, Sn, and W) are purely lithophile, where

sulfide does not contribute to their mass balance at all. There is a temperature dependence

on element partitioning into sulfide for Mo and W, and to a lesser extent Ga and Ge – these

elements partition into sulfide more strongly at higher T. Mo, Ga, and W are significantly

more enriched in sulfides from the Hannuoba xenoliths that also contain these elements

along the grain boundaries, so we propose that a metasomatic agent introduced these

elements into the Hannuoba peridotites and they overprinted the primary trace element signature within sulfides. Therefore, we suggest that the sulfides from the Pyrenees massif may record more accurate concentrations of these elements in mantle sulfides.

By establishing melt depletion trends from the peridotite whole-rock data, we can provide new estimates of the primitive mantle abundances of V, Ga, Ge, Cd, and In that may be more accurate than previous methods that used element ratios from basalts. We estimate 71.2 ppm V, 3.35 ppm Ga, 1.02 ppm Ge, 0.035 ppm Cd, and 0.012 ppm In in the primitive mantle with an MgO content of 38 wt%.

SUMMARY AND OUTLOOK

Mo distribution in the crust

In Chapter 2, I show that granites and TTGs are "missing" an average of 60% of their expected Mo abundance, relative to the LREE. We presented the following hypotheses to explain this discrepancy: 1) Mo is fractionated into Fe-Ti oxides during differentiation, 2) Mo is retained in Fe-Ti oxides in the subducting slab and never makes it to the crust, or 3) Mo is removed from the pluton in a vapor phase during cooling and deposited in MoS_2 in epithermal veins. Magali Toc's work (Appendix G) shows that Mo is not fractionated during igneous differentiation in a calc-alkaline differentiation suite, therefore we can rule out the first hypothesis. Chapter 3 shows that while Mo is hosted in rutile in eclogitized slab residues, Mo is present in the same abundances as the LREE so approximately 75% of the Mo was likely removed from the slab during subduction. This rules out the second hypothesis, therefore we are left with the third hypothesis that approximately 60% of the Mo transported to the UCC in igneous plutons forms molybdenite, MoS_2. It has long been hypothesized that Mo is released from sulfides like pyrite during oxidative crustal weathering, and the distinction that Mo is hosted specifically in MoS_2 as opposed to pyrite is important as both phases show slightly different behavior during oxidative weathering. My collaborators at Arizona State University have shown that both phases break down at a definable rate in the presence of extremely low levels of atmospheric O_2, however the slopes of these reactions are slightly different and MoS_2 is relatively hydrophobic which may inhibit reaction rates and imply that kinetics likely plays a large role in MoS_2 break-down in the presence of atmospheric O_2. Further experimental and modeling studies are needed to

218

accurately assess the rates of breakdown of MoS_2 in order to transform Mo weathering into a quantitative redox proxy.

Mo weathering from basaltic glass

Between Chapters 1 and 2, I showed that while much Mo is likely hosted in MoS_2 in the upper crust, Mo is also hosted in Fe-Ti oxides and volcanic glass. The presence of Mo in this glass may have interesting implications for the abundance of Mo in Archean oceans. In modern oceans, Mo is found as the molybdate ion (MoO_4^{2-}) and is one of the most abundant trace metals with one of the longest residence times (Miller et al., 2011). This is due to its oxidized, soluble state and general non-reactivity with minerals that may precipitate out of solution in oxidized settings. On the other hand, in euxinic settings MoO_4^{2-} is transformed into tetrathiomolybdate, MoS_4^{2-}, which is known to be effectively shuttled out of solution onto Mo-Fe-S species (Erickson and Helz, 2000). Because Mo can be quite abundant in basaltic glass and Mo is expected to be oxidized in those glasses, we propose that seafloor weathering may supply Mo to ocean water where Mo will remain as long as S is not around to transform molybdate, MoO_4^{2-}, into tetrathiomolybdate, MoS_4^{2-} that can settle out of the water column. Canfield (2005) suggests that S should not be present in pre-GOE oceans because oxidative weathering is needed to oxidized and mobilize S from the continental crust into the oceans. Therefore, assuming an absence of S, Mo may have been present in pre-GOE oceans. Back of the envelope calculations show that removal of Mo from the upper 1 to 10 m of oceanic basalt that contains 3% glass with 0.50 ppm Mo would supply between 0.6 and 1.2 nM Mo to the oceans. While this number may seem insignificant, it could have implications for the evolution of Mo-cofactored enzymes that fix nitrogen. Stueken et al. (2015) find N isotope evidence for Mo-facilitated N-fixation at 3.2 Ga – almost one billion

years before it has been proposed to have evolved if Mo was not supplied to the oceans until after the GOE at ~2.4 Ga. Mo-bearing enzymes that fix N only need about 1 nM [Mo] to survive, so the addition of Mo to pre-GOE oceans from basaltic weathering may have been significant. However, this model relies on several assumptions – the most important being that Mo is not retained in secondary alteration phases during seafloor weathering. Therefore, future work is needed to assess the behavior of Mo during alteration of basaltic glass.

Mo isotope fractionation during partitioning into Fe-Ti oxides

Preliminary results from Chapter 3 suggest that isotopically light Mo is incorporated into Fe-Ti oxide minerals during partitioning between fluid or melt endmembers, which could be one explanation as to why the average felsic upper crust is isotopically heavier (Willbold and Elliott, 2017; Voegelin et al., 2014) than more mafic reservoirs like MORB (Bezard et al., 2016), the mantle (Liang et al., 2017), and komatiites (Greber et al., 2015). More δ^{98}Mo data for rutile and other oxide separates from eclogites and lower crustal cumulates are needed to fully assess this hypothesis, however. For example, although Toc et al. (Appendix G) do not see whole-rock [Mo] fractionation during differentiation of a calc-alkaline suite, neither do Wille et al. (2018), yet they find Mo isotope fractionation. The role that oxides play in determining the Mo isotopic signature of the upper crust is beginning to become clearer, but further studies are needed. The Rindjani differentiation suite studied by Toc et al. (Appendix G) would make an excellent target for Mo isotope fractionation studies where oxides are separated from the matrix and analyzed separately for Mo isotopes.

Recycling of eclogite into HIMU mantle sources

Chapter 3 leaves another hypothesis untested: if eclogites contain isotopically light Mo and those eclogites are recycled into the deep mantle and sampled by certain ocean

island basalts, are those OIB also isotopically light? There is yet to be a systematic study of Mo isotopes in all flavors of ocean island basalts, which I believe would be of great benefit to the community. We predict that OIB that sample recycled eclogite (e.g., HIMU) would show isotopically lighter Mo than other OIB.

Mo isotope fractionation during weathering

Chapters 4 and 5 showed that Mo isotopes are fractionated during continental weathering. We find that Mo is lost from weathering profiles during saprolite formation and the little Mo that is retained is isotopically lighter than the un-weathered bedrock. On the other hand, bauxites that are full of Fe-oxides have had isotopically heavy Mo added to them. Under the assumption that bauxites are less prominent weathering lithologies than saprolites, we conclude that overall continental weathering results in a loss of isotopically heavy Mo, leaving the regolith isotopically light. These results can be applied to the study of glacial diamictites that span the last 2.9 Ga and show a trend towards lighter isotope values with time. We attribute this trend towards the onset of oxidative weathering that allowed Mo to become mobilized out of the regolith and allowed for the formation of Fe-oxides in the regolith that retained light Mo isotopes. However, further work could be done to confirm this hypothesis. More varied studies of deep weathering profiles are needed (e.g., saprolites, laterites, bauxites, etc) to confirm if saprolites are consistently isotopically light and to confirm that saprolites are one of the more wide-spread products of continental weathering. Additionally, Mo isotope studies paleosols that span the GOE boundary – like those studied in Murakami et al. (2016) – would make for great targets for testing the hypothesis that Mo isotopes are fractionated during weathering after the GOE, but not before.

REFERENCES

Adam J. and Green T. (2006) Trace element partitioning between mica- and amphibole-bearing garnet lherzolite and hydrous basanitic melt: Experimental results and the investigation of controls on partitioning behaviour. *Contrib. to Mineral. Petrol.* **152**, 1–17.

Anbar A. D., Duan Y., Lyons T. W., Arnold G. L., Kendall B., Creaser R. A., Kaufman A. J., Gordon G. W., Scott C., Garvin J. and Buick R. (2007) A whiff of oxygen before the great oxidation event? *Science.* **317**, 1903–1906.

Archer C. and Vance D. (2008) The isotopic signature of the global riverine molybdenum flux and anoxia in the ancient oceans. *Nat. Geosci.* **1**, 597–600.

Arevalo R. and McDonough W.F. (2008) Tungsten geochemistry and implications for understanding the Earth's interior, *Earth and Planet. Sci. Lett.* **272**, 656-665

Asael D., Rouxel O., Poulton S.W., Lyons T.W., Bekker A. (2018) Molybdenum record from black shales indicates oscillating atmospheric oxygen levels in the early Paleoproterozoic, *Am. Jour. Sci.* **318**, 275-299

Audétat A. (2010) Source and Evolution of Molybdenum in the Porphyry Mo (-Nb) Deposit at Cave Peak, Texas, *J. Petrol.* **51**, 8, 1739-1760

Audétat A., Dolejs D., Lowenstern J.B. (2011) Molybdenite Saturation in Silicic Magmas: Occurrence and Petrological Implications, *J. Petrol.* **52**, 5, 891-904

Aulbach S., O'Reilly S. Y., Griffin W. L. and Pearson N. J. (2008) Subcontinental lithospheric mantle origin of high niobium/tantalum ratios in eclogites. *Nat. Geosci.* **1**, 468–472.

Badullovich N., Moynier F., Creech J., Teng F.-Z. and Sossi P. A. (2017) Tin isotopic fractionation during igneous differentiation and Earth's mantle composition. *Geochemical Perspect. Lett.*, 24–28. Available at: http://www.geochemicalperspectivesletters.org/article1741.

Barling J. and Anbar A. D. (2004) Molybdenum isotope fractionation during adsorption by manganese oxides. *Earth Planet. Sci. Lett.* **217**, 315–329.

Barling J., Arnold G. L. and Anbar A. D. (2001) Natural mass-dependent variations in the isotopic composition of molybdenum. *Earth Planet. Sci. Lett.* **193**, 447–457.

Barth M. G., Rudnick R. L., Horn I., McDonough W. F., Spicuzza M. J., Valley J. W. and Haggerty S. E. (2002) Geochemistry of xenolithic eclogites from West Africa, part 2: Origins of the high MgO eclogites. *Geochim. Cosmochim. Acta* **66**, 4325–4345.

Barth M. G., Rudnick R. L., Horn I., McDonough W. F., Spicuzza M. J., Valley J. W. and Haggerty S. E. (2001) Geochemistry of xenolithic eclogites from West Africa, part I: A link between low MgO eclogites and archean crust formation. *Geochim. Cosmochim. Acta* **65**, 1499–1527.

Becker H., Horan M. F., Walker R. J., Gao S., Lorand J. P. and Rudnick R. L. (2006) Highly siderophile element composition of the Earth's primitive upper mantle: Constraints from new data on peridotite massifs and xenoliths. *Geochim. Cosmochim. Acta* **70**, 4528–4550.

Bermingham K. R., Worsham E. A. and Walker R. J. (2018) New insights into Mo and Ru isotope variation in the nebula and terrestrial planet accretionary genetics. *Earth Planet. Sci. Lett.* **487**, 221–229. Available at: http://linkinghub.elsevier.com/retrieve/pii/S0012821X18300359.

Bezard R., Fischer-Gödde M., Hamelin C., Brennecka G. A. and Kleine T. (2016) The effects of magmatic processes and crustal recycling on the molybdenum stable isotopic composition of Mid-Ocean Ridge Basalts. *Earth Planet. Sci. Lett.* **453**, 171–181.

Bodinier, J.-L., Dupuy, C., Dostal, J., 1988. Geochemistry of Eastern Pyrenean peridotites. Geochim. Cosmochim. Acta 52, 2893–2907

Bogatyrev B. A., Zhukov V. V and Tsekhovsky Y. G. (2009) Formation Conditions and Regularities of the Distribution of Large and Superlarge Bauxite Deposits. **44**, 135–151.

Boyd E.S., Hamilton T.L., Peters J.W. (2011) An alternative path for the evolution of biological nitrogen fixation, *Front. Microbio.* **2**, 1-11

Burkhardt C., Hin R. C., Kleine T. and Bourdon B. (2014) Evidence for Mo isotope fractionation in the solar nebula and during planetary differentiation. *Earth Planet. Sci. Lett.* **391**, 201–211. Available at: http://dx.doi.org/10.1016/j.epsl.2014.01.037.

Candela P.A. and Holland H.D. (1984) The partitioning of copper and molybdenum between silicate melts and aqueous fluids, *Geochim Cosmochim Acta*, **48**, 373-380

Canfield D. E. (2005) The early history of atmospheric oxygen: Homage to Robert M. Garrels. *Annu. Rev. Earth Planet. Sci.* **33**, 1–36. Available at:

http://www.annualreviews.org/doi/10.1146/annurev.earth.33.092203.122711.

Canil D. (2002) Vanadium in peridotites, mantle redox and tectonic environments: Archean to present. *Earth Planet. Sci. Lett.* **195**, 75–90.

Canil D. and Fedortchouk Y. (2000) Clinopyroxene-liquid partitioning for vanadium and the oxygen fugacity during formation of cratonic and oceanic mantle lithosphere. *J. Geophys. Res. Solid Earth* **105**, 26003–26016. Available at: http://doi.wiley.com/10.1029/2000JB900221.

Cawood P.A., Hawkesworth C.J., Dhuime B. (2013) The continental record and the generation of continental crust, *GSA Bull.* **125**, 14-32

Chappaz A., Lyons T. W., Gregory D. D., Reinhard C. T., Gill B. C., Li C. and Large R. R. (2014) Does pyrite act as an important host for molybdenum in modern and ancient euxinic sediments? *Geochim. Cosmochim. Acta* **126**, 112–122. Available at: http://dx.doi.org/10.1016/j.gca.2013.10.028.

Chen H., Savage P., Teng F.Z., Helz R.T., Moynier, F. (2013) Zinc isotope fractionation during magmatic differentiation and the isotopic composition of the bulk Earth, *Earth and Planet. Sci. Lett.* **369-370**, 34-42

Chen K., Walker R. J., Rudnick R. L., Gao S., Gaschnig R. M., Puchtel I. S., Tang M. and Hu Z. C. (2016) Platinum-group element abundances and Re–Os isotopic systematics of the upper continental crust through time: Evidence from glacial diamictites. *Geochim. Cosmochim. Acta* **191**, 1–16. Available at: http://dx.doi.org/10.1016/j.gca.2016.07.004.

Cheng M., Li C., Zhou L., Algeo T. J., Zhang F., Romaniello S., Jin C., Lei L. and Feng L. (2016) ScienceDirect Marine Mo biogeochemistry in the context of dynamically euxinic mid-depth waters : A case study of the lower Cambrian Niutitang shales , South China. *Geochim. Cosmochim. Acta* **183**, 79–93. Available at: http://dx.doi.org/10.1016/j.gca.2016.03.035.

Clemens J.D., Yearron L.M., Stevens G. (2006) Barberton (South Africa) TTG magmas: Geochemical and experimental constraints on source-rock petrology, pressure of formation and tectonic setting, *Precambrian Res.* 1**51**, 53-78

Condie and Kroner (2008) When did plate tectonics begin? Evidence from the geologic record, GSA Special Paper, **440**, 281-294

Condie K. C. (1993) Chemical Composition and Evolution of the Upper Continental Crust :

Contrasting Results from Surface and Shales. **104**, 1–37.

Conquéré F. (1978) Petrologic des complexes ultramahques de lherzolites a spinelle de l'Ariege (France). These Doct. Etat. Paris, 333p.

Dahl T. W., Canfield D. E., Rosing M. T., Frei R. E., Gordon G. W., Knoll A. H. and Anbar A. D. (2011) Molybdenum evidence for expansive sulfidic water masses in ~750Ma oceans. *Earth Planet. Sci. Lett.* **311**, 264–274.

Dahl T. W., Chappaz A., Hoek J., McKenzie C. J., Svane S. and Canfield D. E. (2017) Evidence of molybdenum association with particulate organic matter under sulfidic conditions. *Geobiology* **15**, 311–323.

Duan Y., Anbar A. D., Arnold G. L., Lyons T. W., Gordon G. W. and Kendall B. (2010) Molybdenum isotope evidence for mild environmental oxygenation before the Great Oxidation Event. *Geochim. Cosmochim. Acta* **74**, 6655–6668. Available at: http://dx.doi.org/10.1016/j.gca.2010.08.035.

Erickson B.E. and Helz G.R. (2000) Molybdenum(VI) speciation in sulfidic waters: Stability and lability of thiomolybdates, *Geochim. Cosmochim. Acta* **64**, 1149-1158

Farges F. and Linnen R. L. (2006) Redox and speciation of tin in hydrous silicate glasses: a comparison with Nb , Ta , Mo and W. **44**, 795–810.

Fassio J. M. (1990) Geochemical evolution of ferrginous bauxite deposits in northwestern Oregon and southwestern Washington. **MS Thesis**, 103.

Fitton J. G. (1995) Coupled molybdenum and niobium depletion in continental basalts. *Earth Planet. Sci. Lett.* **136**, 715–721.

Foley S., Tiepolo M. and Vannucci R. (2002) Growth of early continental crust controlled by melting of amphibolite in subduction zones. **417**, 837–840.

Freymuth H., Elliott T., van Soest M. and Skora S. (2016) Tracing subducted black shales in the Lesser Antilles arc using molybdenum isotope ratios. *Geology* **44**, 987–990.

Freymuth H., Vils F., Willbold M., Taylor R. N. and Elliott T. (2015) Molybdenum mobility and isotopic fractionation during subduction at the Mariana arc. *Earth Planet. Sci. Lett.* **432**, 176–186.

Frey F.A. and Green D.H. (1974) The mineralogy, geochemistry, and origin of spinel lherzolite inclusions in Victorian basanites, *Geochim. Cosmochim. Acta* **38**, 1023-1059

Fung A. T. and Haggerty S. E. (1995) Petrography and mineral compositions of eclogites

from the Koidu kimberlite complex, Sierra-Leone. *J. Geophys. Res. Earth* **100**, 20451–20473.

G. Brey T. K. (1990) Geothermobarometry in Four-phase Lherzolites II . New Thermobarometers , and Practical Assessment of Existing Thermobarometers. **31**, 1353–1378.

Gaetani G. A. and Grove T. L. (1997) Partitioning of moderately siderophile elements among olivine, silicate melt, and sulfide melt: Constraints on core formation in the Earth and Mars. *Geochim. Cosmochim. Acta* **61**, 1829–1846.

Gao S., Rudnick R. L., Carlson R. W., McDonough W. F. and Liu Y. S. (2002) Re-Os evidence for replacement of ancient mantle lithosphere beneath the North China craton. *Earth Planet. Sci. Lett.* **198**, 307–322.

Gardner L. R. (1981) Geochemistry and Mineralogy of an Unusual Diabase Saprolite Near Columbia, South Carolina. *Clays Clay Miner.* **29**, 184–190.

Gaschnig R. M., Rudnick R. L. and Mcdonough W. F. (2015) Determination of Ga, Ge, Mo, Ag, Cd, In, Sn, Sb, W, Tl and Bi in USGS Whole-Rock Reference Materials by Standard Addition ICP-MS. *Geostand. Geoanalytical Res.* **39**, 371–379.

Gaschnig R. M., Rudnick R. L., McDonough W. F., Kaufman A. J., Hu Z. and Gao S. (2014) Onset of oxidative weathering of continents recorded in the geochemistry of ancient glacial diamictites. *Earth Planet. Sci. Lett.* **408**, 87–99. Available at: http://dx.doi.org/10.1016/j.epsl.2014.10.002.

Gaschnig R. M., Rudnick R. L., McDonough W. F., Kaufman A. J., Valley J. W., Hu Z., Gao S. and Beck M. L. (2016a) Compositional evolution of the upper continental crust through time, as constrained by ancient glacial diamictites. *Geochim. Cosmochim. Acta* **186**, 316–343. Available at: http://dx.doi.org/10.1016/j.gca.2016.03.020.

Ghiorso M.S. and Evans B.W. (2008) Thermodynamics of rhombohedral oxide solid solutions and a revision of the Fe-Ti two-oxide geothermometer and oxygen-barometer, *Am. J. Sci.* **208**, 957-1039

Goldberg S., Forster H. S. and Godfrey C. L. (1996) Molybdenum Adsorption on Oxides, Clay Minerals, and Soils. *Soil Sci. Soc. Am. J.* **60**, 425. Available at: https://www.soils.org/publications/sssaj/abstracts/60/2/SS0600020425.

Goldberg T., Archer C., Vance D. and Poulton S. W. (2009) Mo isotope fractionation during

adsorption to Fe (oxyhydr)oxides. *Geochim. Cosmochim. Acta* **73**, 6502–6516.

Goldberg T., Gordon G., Izon G., Archer C., Pearce C. R., McManus J., Anbar A. D. and Rehkämper M. (2013) Resolution of inter-laboratory discrepancies in Mo isotope data: an intercalibration. *J. Anal. At. Spectrom.* **28**, 724. Available at: http://xlink.rsc.org/?DOI=c3ja30375f.

Goldberg T., Poulton S. W., Wagner T., Kolonic S. F. and Rehkämper M. (2016) Molybdenum drawdown during Cretaceous Oceanic Anoxic Event 2. *Earth Planet. Sci. Lett.* **440**, 81–91. Available at: http://dx.doi.org/10.1016/j.epsl.2016.02.006.

Goldschmidt V.M. (1937) The principles of distribution of chemical elements in minerals and rocks, Hugo Müller Lecture, Chemical Society

Goldberg S. and Forster H.S. (1998) Factors affecting molybdenum adsorption by soils and minerals, Soil Science 163, 109-114

Gordon G. W., Lyons T. W., Arnold G. L., Roe J., Sageman B. B. and Anbar A. D. (2009) When do black shales tell molybdenum isotope tales? *Geology* **37**, 535–538.

Greaney A. T., Rudnick R. L., Gaschnig R. M., Whalen J. B., Luais B. and Clemens J. D. (2018) Geochemistry of molybdenum in the continental crust. *Geochim. Cosmochim. Acta* **238**, 36–54.

Greaney A. T., Rudnick R. L., Helz R. T., Gaschnig R. M., Piccoli P. M. and Ash R. D. (2017a) The behavior of chalcophile elements during magmatic differentiation as observed in Kilauea Iki lava lake Hawaii. *Geochim. Cosmochim. Acta* **210**, 71–96. Available at: http://dx.doi.org/10.1016/j.gca.2017.04.033.

Greber N. D., Mader U. and Nagler T. F. (2015a) Experimental dissolution of molybdenum-sulphides at low oxygen concentrations: A first-order approximation of late Archean atmospheric conditions *Earth Sp. Sci.*, 173–180.

Greber N. D., Puchtel I. S., Nägler T. F. and Mezger K. (2015b) Komatiites constrain molybdenum isotope composition of the Earth's mantle. *Earth Planet. Sci. Lett.* **421**, 129–138. Available at: http://dx.doi.org/10.1016/j.epsl.2015.03.051.

Gregory D.D., Large R.L., Halpin J.A., Bauturina E.L., Lyons T.W., Wu S., Danyushevsky L., Sack P.J., Chappaz A., Maslennikov V.V., Bull S.W. (2015) Trace element content of sedimentary pyrite in black shales, *Econ. Geol.* **110**, 1389-1410

Gustafsson J. P. (2003) Modelling molybdate and tungstate adsorption to ferrihydrite. *Chem.*

Geol. **200**, 105–115.

Hannah J.L, Stein H.J., Wieser M.E., de Laeter J.R., Varner M.D. (2007) Molybdenum isotope variations in molybdenite: Vapor transport and Rayleigh fractionation of Mo, *Geology* **35**, 703-706

Hart S.R. and Gaetani G.A. (2006) Mantle Pb paradoxes: the sulfide solution, *Contrib Mineral Petrol* **152**, 295-308

Harvey J., Konig S., Luguet A. (2015) The effects of melt depletion and metasomatism on highly siderophile and strongly chalcophile elements: S-Se-Te-Re-PGE systematics of peridotite xenoliths from Kilbourne Hole, new Mexico, *Geochim. Cosmochim. Acta* **166**, 210-233

Helmy H.M., Ballhaus C. Wohlgemuth-Ueberwasser C., Fonseca R.O.C., Laurenz V. (2010) Partitioning of Se, As, Sb, Te and Bi between monosulfide solid solution and sulfide melt Application to magmatic sulfide deposits, *Geochim. Cosmochim. Acta* **74**, 6174-6179

Helz G. R., Bura-Nakic E., Mikac N., Ciglenecki I. (2011) New model for molybdenum behavior in euxinic waters, *Chem. Geol.* **284**, 323-332

Helz G.R., Miller C.V., Charnock J.M., Mosselmans J.F.W., Pattrick R.A.D, Garner C.D., Vaughan D.J. (1996) Mechanism of molybdenum removal from the sea and its concentration in black shales: EXAFS evidence, *Geochim. Cosmochim. Acta,* **60**, 19, 3631-3642

Helz R.T. (1987) Differentiation behavior of Kilauea Iki lava lake, Kilauea Volcano, Hawaii: an overview of past and current work. In Mysen, B.O., ed., *Magmatic Processes: Physicochemical Principles*. Geochemical Society Special Publication 1, 241-258

Helz R.T. and Thornber C.R. (1987) Geothermometry of Kilauea Iki Lava Lake, Hawaii, *Bull. Volcanol.* **49**, 651-668

Helz, R.T. and Wright, T.L. (1983) Drilling report and core logs for the 1981 drilling of Kilauea Iki lava lake (Kilauea Volcano, Hawaii), with comparative notes on earlier (1967-1979 drilling experiences. *USGS Open-file Report 83-326.*

Helz R.T. and Wright T.L. (1992) Differentiation and magma mixing on Kilauea's east zone. *Bull. Volcanol.* **54**, 361-384.

Helz R.T., Kirschenbaum H., Marinenko J.M., Qian R. (1994) Whole-rock analyses of core samples from the 1967, 1975, 1979 and 1981 drillings of Kilauea Iki lava lake, Hawaii. *USGS Open-file Report 94-684*

Helz R.T. and Taggert J.E. (2010) Whole-Rock Analyses of Core Samples from the 1988 Drilling of Kilauea Iki Lava Lake, Hawaii, *USGS Open File Report 2010-1093*

Helz R.T. (2012) Trace Element Analyses of Core Samples from the 1967-1988 Drillings of Kilauea Iki Lava Lake, Hawaii, *USGS Open-file Report 2012-1050*

Helz, R.T., Cottrell, E., Brounce, M.N., and Kelley, K.A. (2017) Olivine-melt relationships and syneruptive redox variations in the 1959 eruption of Kilauea Volcano as revealed by XANES. *J. Volcanol. Geotherm. Res*., dx.doi.org/10/1016/j.volgeores.2016.12.006

Herrmann, A.D., et al., 2012. Anomalous molybdenum isotope trends in Upper Pennsylvanian euxinic facies: significance for use of $\delta98Mo$ as a global marine redox proxy. *Chem. Geol.* 324–325, 87–98

Herrmann W. and Berry R.F. (2002) MINSQ – a least squares spreadsheet method for calculating mineral proportions from whole rock major element analyses, *Geochemistry: Exploration, Environment, Analysis* **2**, 361-368

Herzberg C. and Rudnick R.L. (2012) Formation of cratonic lithosphere: An integrated thermal and petrological model, *Lithos*, **149**, 4-15

Hills D. V. and Haggerty S. E. (1989) Petrochemistry of eclogites from the Koidu Kimberlite Complex, Sierra Leone. *Contrib. to Mineral. Petrol.* **103**, 397–422.

Hofmann A.W. (1988) Chemical differentiation of the Earth: the relationship between mantle, continental crust, and oceanic crust, *Earth Planet Sci. Lett* **90**, 297-314

Hofmann A.W. (2003) Sampling mantle heterogeneity through oceanic basalts: Isotopes and trace elements, *Treatise on geochemistry* **2.03**, 61-101

Ireland T.J., Arevalo R., Walker R.J., McDonough W.F. (2009) Tungsten in Hawaiian picrites: A compositional model for the sources of Hawaiian lavas, *Geochim. Cosmochim. Acta* **73**, 4517-4530

Jackson M.G., Weis D., Huang S. (2012) Major element variations in Hawaiian shield lavas: Source features and perspectives from global ocean island basalt (OIB) systematics, *Geochem. Geophys. Geosyst.* **13**, 1-24

Jenner F.E., Hauri E.H., Bullock E.S., Koenig S., Arculus R.J., Mavrogenes J.A., Mikkelson N., Goddard C. (2015) The competing effects of sulfide saturation versus degassing on the behavior of the chalcophile elements during the differentiation of hydrous melts, *Geochem. Geophys. Geosyst.* **16**, 1490-1507

Jenner F.E., Arculus R.J., Mavrogenes J.A., Dyriw N.J., Nebel O., Hauri E.H. (2012) Chalcophile element systematics in volcanic glasses from the northwestern Lau Basin, *Geochem. Geophys. Geosyst.* **13**, No. 6, 1-25

Jenner F. E. and O'Neill H. S. C. (2012) Analysis of 60 elements in 616 ocean floor basaltic glasses. *Geochemistry, Geophys. Geosystems* **13**, 1–11.

Jenner F.E., O'Neill H.S.C., Arculus R.J., Mavrogenes J.A. (2010) The Magnetite Crisis in the Evolution of Arc-related Magmas and the Initial Concentration of Au, Ag, and Cu, *J. Petrol* **51**, 2445-2464

Jochum K. P., Hofmann A. W. and Seufert H. M. (1993) Tin in mantle-derived rocks: Constraints on Earth evolution. *Geochim. Cosmochim. Acta* **57**, 3585–3595.

Jochum K.P. and Hofmann A.W. (1997) Constraints on earth evolution from antimony in mantle-derived rocks, *Chem. Geol.* **139**, 39-49

Johnson J. E., Gerpheide A., Lamb M. P. and Fischer W. W. (2014) O2 constraints from Paleoproterozoic detrital pyrite and uraninite. *Bull. Geol. Soc. Am.* **126**, 813–830.

Jugo P. (2009) Sulfur content at sulfide saturation in oxidized magmas, *Geology* **37**, No. 5, 415-418

Kato C., Moynier F., Foriel J., Teng F.Z., Puchtel I.S. (2017) The gallium isotopic composition of the bulk silicate Earth, *Chem. Geol.* **448**, 164-172

Kendall B., Dahl T. W. and Anbar A. D. (2017) the Stable Isotope Geochemistry of Molybdenum. *Rev. Mineral. Geochemistry* **82**, 683–732. Available at: http://rimg.geoscienceworld.org/lookup/doi/10.2138/rmg.2017.82.16.

Kendall B., Gordon G. W., Poulton S. W. and Anbar A. D. (2011) Molybdenum isotope constraints on the extent of late Paleoproterozoic ocean euxinia. *Earth Planet. Sci. Lett.* **307**, 450–460. Available at: http://dx.doi.org/10.1016/j.epsl.2011.05.019.

König S., Wille M., Voegelin A. and Schoenberg R. (2016) Molybdenum isotope systematics in subduction zones. *Earth Planet. Sci. Lett.* **447**, 95–102.

King E. K., Perakis S. S. and Pett-Ridge J. C. (2018) Molybdenum isotope fractionation

during adsorption to organic matter. *Geochim. Cosmochim. Acta* **222**, 584–598. Available at: https://doi.org/10.1016/j.gca.2017.11.014.

King E. K., Thompson A., Chadwick O. A. and Pett-Ridge J. C. (2016) Molybdenum sources and isotopic composition during early stages of pedogenesis along a basaltic climate transect. *Chem. Geol.* **445**, 54–67.

Kiseeva E. S. and Wood B. J. (2013) A simple model for chalcophile element partitioning between sulphide and silicate liquids with geochemical applications. *Earth Planet. Sci. Lett.* **383**, 68–81. Available at: http://dx.doi.org/10.1016/j.epsl.2013.09.034.

Kiseeva E. S. and Wood B. J. (2015) The effects of composition and temperature on chalcophile and lithophile element partitioning into magmatic sulphides. *Earth Planet. Sci. Lett.* **424**, 280–294. Available at: http://dx.doi.org/10.1016/j.epsl.2015.05.012.

Kiseeva E.S., Fonseca R.O.C., Smythe D.J. (2017) Chalcophile Elements and Sulfides in the Upper Mantle, *Elements* **13**, 111-116, doi: 10.2113/gselements.13.2.111

Korzhinsky M.A., Tkachenko S.I., Shmulovich K.I., Taran Y.A., Steinberg G.S. (1994) Discovery of a pure rhenium mineral at Kudriavy volcano, Nature **369**, 51-52

Kroner A., Byerly G.R., Lowe D.R. (1991) Chronology of early Archaean granite-greenstone evolution in the Barberton Mountainland, South Africa, based on precise dating by single zircon evaporation, *Earth Planet. Sci. Lett*, **103**, 41-54

Kuroda P.K. and Sandell E.B. (1954) Geochemistry of Molybdenum, *Geochim. Cosmochim. Acta* **6**, 35-63

Kurzweil F., Wille M., Schoenberg R., Taubald H. and Kranendonk M. J. Van (2015) ScienceDirect Continuously increasing d 98 Mo values in Neoarchean black shales and iron formations from the Hamersley Basin. *Geochim. Cosmochim. Acta* **164**, 523–542. Available at: http://dx.doi.org/10.1016/j.gca.2015.05.009.

Lassiter J.C. (2003) Rhenium volatility in subaerial lavas: constraints from subaerial and submarine portions of the HDSP-2 Mauna Kea drillcore, *Earth and Planet. Sci. Lett.* **214**, 311-325

Lee C.T.A., Luffi P., Chin E.J., Bouchet R., Dasgupta R., Morton D.M., Le Roux V., Yin Q., Jin, D. (2012) Copper Systematics in Arc Magmas and Implications for Crust-Mantle Differentiation, *Science* **336**, 64-68

Li S., Gaschnig R. M. and Rudnick R. L. (2016) Insights into chemical weathering of the

upper continental crust from the geochemistry of ancient glacial diamictites. *Geochim. Cosmochim. Acta* **176**, 96–117.

Li Y. and Audétat A. (2012) Partitioning of V, Mn, Co, Ni, Cu, Zn, As, Mo, Ag, Sn, Sb, W, Au, Pb, and Bi between sulfide phases and hydrous basanite melt at upper mantle conditions, *Earth and Planet. Sci. Lett.* **335-336**, 327-340

Li Y. and Audétat A. (2015) Effects of temperature, silicate melt composition, and oxygen fugacity on the partitioning of V, Mn, Co, Ni, Cu, Zn, As, Mo, Ag, Sn, Sb, W, Au, Pb, and Bi between sulfide phases and silicate melt, *Geochim. Cosmochim. Acta* **162**, 25-45

Liang Y. H., Halliday A. N., Siebert C., Fitton J. G., Burton K. W., Wang K. L. and Harvey J. (2017) Molybdenum isotope fractionation in the mantle. *Geochim. Cosmochim. Acta* **199**, 91–111.

Liu J., Pearson D. G., Chacko T. and Luo Y. (2018) A reconnaissance view of tungsten reservoirs in some crustal and mantle rocks: Implications for interpreting W isotopic compositions and crust-mantle W cycling. *Geochim. Cosmochim. Acta* **223**, 300–318. Available at: https://doi.org/10.1016/j.gca.2017.12.015.

Liu J., Rudnick R. L., Walker R. J., Gao S., Wu F. and Piccoli P. M. (2010) Processes controlling highly siderophile element fractionations in xenolithic peridotites and their influence on Os isotopes. *Earth Planet. Sci. Lett.* **297**, 287–297. Available at: http://dx.doi.org/10.1016/j.epsl.2010.06.030.

Liu S. A., Teng F. Z., Li S., Wei G. J., Ma J. L. and Li D. (2014) Copper and iron isotope fractionation during weathering and pedogenesis: Insights from saprolite profiles. *Geochim. Cosmochim. Acta* **146**, 59–75. Available at: http://dx.doi.org/10.1016/j.gca.2014.09.040.

Liu X. M., Rudnick R. L., McDonough W. F. and Cummings M. L. (2013) Influence of chemical weathering on the composition of the continental crust: Insights from Li and Nd isotopes in bauxite profiles developed on Columbia River Basalts. *Geochim. Cosmochim. Acta* **115**, 73–91. Available at: http://dx.doi.org/10.1016/j.gca.2013.03.043.

Liu X. M., Teng F. Z., Rudnick R. L., McDonough W. F. and Cummings M. L. (2014) Massive magnesium depletion and isotope fractionation in weathered basalts. *Geochim. Cosmochim. Acta* **135**, 336–349.

Lorand J. P. (1989) Abundance and distribution of CuFeNi sulfides, sulfur, copper and platinum-group elements in orogenic-type spinel lherzolite massifs of Ariège (northeastern Pyrenees, France). *Earth Planet. Sci. Lett.* **93**, 50–64.

Lorand J. P. (1990) Are spinel Iherzolite xenoliths representative of the abundance of sulfur in the upper mantle? *Geochim. Cosmochim. Acta* **54**, 1487–1492.

Lorand J. P. and Alard O. (2011) Pyrite tracks assimilation of crustal sulfur in Pyrenean peridotites. *Mineral. Petrol.* **101**, 115–128.

Lorand J. P., Gros M. and Pattou L. (1999) Fractionation of platinum-group elements in the upper mantle: A detailed study in Pyrenean orogenic peridotites. *J. Pet.* **40**, 951–987.

Lorand J.-P. and Luguet A. (2016) Chalcophile and Siderophile Elements in Mantle Rocks: Trace Elements Controlled By Trace Minerals. *Rev. Mineral. Geochemistry* **81**, 441–488. Available at: http://rimg.geoscienceworld.org/lookup/doi/10.2138/rmg.2016.81.08.

Lu X., Kendall B., Stein H. J., Li C., Hannah J. L., Gordon G. W., Ove J. and Ebbestad R. (2017) Marine redox conditions during deposition of Late Ordovician and Early Silurian organic-rich mudrocks in the Siljan ring district , central Sweden. *Chem. Geol.* **457**, 75–94. Available at: http://dx.doi.org/10.1016/j.chemgeo.2017.03.015.

Luais B. and Hawkesworth C.J. (1994) The generation of continental crust: An integrated study of crust-forming processes in the Archaean of Zimbabwe, *J. Petrol*. **35**, 43-93

Lyons T.W., Reinhard C.T., Planavsky N.J. (2014) The rise of oxygen in Earth's early ocean and atmosphere, *Nature*, **506**, 307-215

Luguet A., Shirey S.B., Lorand J.P., Horan M.F., Carlson R.W. (2007) Residual platinum-group minerals from highly depleted harzburgites of the Lherz massif (France) and their role in HSE fractionation of the mantle, *Geochim. Cosmochim. Acta* **71**, 3082-3097

Luguet A., Lorand J.P., Seyler M. (2003) Sulfide petrology and highly siderophile element geochemistry of abyssal peridotites: A coupled study of samples from the Kane Fracture Zone (45°W 23°20N, MARK Area, Atlantic Ocean), *Geochim. Cosmochim. Acta* **67**, 1553-1570

Marks J. A., Perakis S. S., King E. K. and Pett-Ridge J. (2015) Soil organic matter regulates molybdenum storage and mobility in forests. *Biogeochemistry* **125**, 167–183.

Marks M.A., Coulson I.M., Schilling J., Jacob D.E., Schmitt A.K., Markl G. (2008) The effect of titanite and other HFSE-rich mineral (Ti-bearing andradite, zircon, eudialyte) fractionation on the geochemical evolution of silicate melts, *Chem. Geol.* **257**, 153-172

McDonough W.F. and Sun S.s (1995) The composition of the Earth, *Chem. Geol.* **120**, 223-253

McManus J., Nagler T.F., Siebert C., Wheat C.G., Hammond D.E. (2002) Oceanic molybdenum isotope fractionation: Diagenesis and hydrothermal ridge-flank alteration, *Geochem. Geophys. Geosyst.* **3**, 1-9

Miller K.J, Zhu W.L., Montesi L.G.J., Gaetani G.A. (2014) Experimental quantification of permeability of partially molten mantle rock, *Earth and Planet. Sci. Lett.* **388**, 273-282

Miller C. A., Peucker-Ehrenbrink B., Walker B. D. and Marcantonio F. (2011) Re-assessing the surface cycling of molybdenum and rhenium. *Geochim. Cosmochim. Acta* **75**, 7146–7179. Available at: http://dx.doi.org/10.1016/j.gca.2011.09.005.

Morimoto N, Fabries J., Ferguson A.K., Ginzburg I.V., Ross M., Siefert F.A., Zussman J., Aoki K., Gottardi G. (1988) Nomenclature of pyroxenes, *Am. Mineral.* **73**, 1123–1133.

Moyen J.F., Stevens G., Kisters A.F.M., Belcher R.W. (2007) TTG plutons of the Barberton Granitoid-Greenstone Terrain, South Africa, *Precambrian Ophiolites and Related Rocks, Develop. Precamb. Geol*. **15**, 1-62

Mungall J.E. and Brenan J.M. (2014) Partitioning of platinum-group elements and Au between sulfide liquid and basalt and the origins of mantle-crust fractionation of the chalcophile elements, *Geochim. Cosmochim. Acta* **125**, 265-289

Murakami T., Sreenivas B., Sharma S. Das and Sugimori H. (2011) Quantification of atmospheric oxygen levels during the Paleoproterozoic using paleosol compositions and iron oxidation kinetics. *Geochim. Cosmochim. Acta* **75**, 3982–4004.

Murakami T., Matsuura K., Kanzaki Y. (2016) Behaviors of trace elements in Neoarchean and Paleoproterozoic paleosols: Implications for atmospheric oxygen evolution and continental oxidative weathering, *Geochim. Cosmochim. Acta* **192**, 203-219

Nan X., Yo H., Rudnick R.L., Gaschnig R.M., Xu J., Li W., Zhang Q., Jin Z., Li X., Huang F. (2018) Barium isotopic composition of the upper continental crust, *Geochim. Cosmochim. Acta* **233**, 33-49

Neely R. A., Gislason S. R., Ólafsson M., McCoy-West A. J., Pearce C. R. and Burton K.

W. (2018) Molybdenum isotope behaviour in groundwaters and terrestrial hydrothermal systems, Iceland. *Earth Planet. Sci. Lett.* **486**, 108–118. Available at: https://doi.org/10.1016/j.epsl.2017.11.053.

Neubert N., Heri A. R., Voegelin A. R., Nägler T. F., Schlunegger F. and Villa I. M. (2011) The molybdenum isotopic composition in river water: Constraints from small catchments. *Earth Planet. Sci. Lett.* **304**, 180–190. Available at: http://dx.doi.org/10.1016/j.epsl.2011.02.001.

Newsom H. E. and Palme H. (1984) The depletion of siderophile elements in the Earth's mantle: new evidence from molybdenum and tungsten. *Earth Planet. Sci. Lett.* **69**, 354–364.

Nielsen S.G., Shimizu N., Lee C.T.A, Behn M.D. (2014) Chalcophile behavior of thallium during MORB melting and implications for the sulfur content of the mantle *Geochem. Geophys. Geosyst.* **15**, 1-15

Noll P.D., Newsom H.E., Leeman W.P., Ryan J.G. (1996) The role of hydrothermal fluids in the production of subduction zone magmas: Evidence from siderophile and chalcophile trace elements and boron, *Geochim. Cosmochim. Acta* **60**, 587-611

Norman M.D., Garcia M.O., Bennett V.C. (2004) Rhemium and chalcophile elements in basaltic glasses from Ko'olau and Moloka'I volcanoes: Magmatic outgassing and composition of the Hawaiian plume, *Geochim. Cosmochim. Acta* **68**, 3761-3777

O'Neill H.S.C. and Eggins S.M. (2002) The effect of melt composition on trace element partitioning; and experimental investigation of the activity coefficients of FeO, NiO, CoO, MoO_2 and MoO_3 in silicate melts, *Chem. Geol.* **186**, 151-181

Oyerinde O. F., Weeks C. L., Anbar A. D. and Spiro T. G. (2008) Solution structure of molybdic acid from Raman spectroscopy and DFT analysis. *Inorganica Chim. Acta* **361**, 1000–1007.

Palme H. and O'Neill H. (2013) *Cosmochemical Estimates of Mantle Composition*. 2nd ed., Elsevier Ltd. Available at: http://dx.doi.org/10.1016/B978-0-08-095975-7.00201-1.

Partin C. A., Bekker A., Planavsky N. J., Scott C. T., Gill B. C., Li C., Podkovyrov V., Maslov A., Konhauser K. O., Lalonde S. V., Love G. D., Poulton S. W. and Lyons T. W. (2013) Large-scale fluctuations in Precambrian atmospheric and oceanic oxygen levels from the record of U in shales. *Earth Planet. Sci. Lett.* **369-370**, 284–293.

Paton C., Hellstrom J., Paul B., Woodhead J. and Hergt J. (2011) Iolite: Freeware for the visualisation and processing of mass spectrometric data. *J. Anal. At. Spectrom.* **26**, 2508. Available at: http://xlink.rsc.org/?DOI=c1ja10172b.

Patten C., Barnes S. J., Mathez E. A. and Jenner F. E. (2013) Partition coefficients of chalcophile elements between sulfide and silicate melts and the early crystallization history of sulfide liquid: LA-ICP-MS analysis of MORB sulfide droplets. *Chem. Geol.* **358**, 170–188.

Pavich M. and Obermeier S.F. (1985) Saprolite formation beneath Coastal Plain sediments near Washington, D.C January, Geological Society of America Bulletin 96 (7)

Peach C.L., Mathez E.A., Keays R.R. (1990) Sulfide melt-silicate melt distribution coefficients for noble metals and other chalcophile elements as deduced from MORB: Implications for partial melting, *Geochim. Cosmochim. Acta* **54**, 3379-3389

Pearce C. R., Burton K. W., von Strandmann P. A. E. P., James R. H. and Gíslason S. R. (2010) Molybdenum isotope behaviour accompanying weathering and riverine transport in a basaltic terrain. *Earth Planet. Sci. Lett.* **295**, 104–114. Available at: http://dx.doi.org/10.1016/j.epsl.2010.03.032.

Pettke T., Oberli F., Heinrich C.A. (2010) The magma and metal source of giant porphyry-type ore deposits, based on lead isotope microanalysis of individual fluid inclusions, *Earth Planet Sci. Lett*. **296**, 267-277

Pietruszka A.J. and Garcia M.O. (1999) A rapid fluctuation in the mantle source and melting history of Kilauea Volcano inferred from the geochemistry of its historical summit lavas (1790-1982), *J. Petrol.* **40**, 1321-1342

Pietruszka A.J., Hauri E.K., Carlson R.W., Garcia M.O. (2006) Remelting of recently depleted mantle within the Hawaiian plume inferred from the 226Ra-230Th-238U disequilibria of Pu'u 'O'o eruption lavas, *Earth and Planet. Sci. Lett.* **244**, 155-169

Pietruszka A.J., Norman A.D., Garcia M.O., Marske J.P., Burns D.H. (2013) Chemical heterogeneity in the Hawaiian mantle plume from the alteration and dehydration of recycled oceanic crust, *Earth and Planet. Sci. Lett.* **361**, 298-309

Pitcher L., Helz R.T., Walker R.J., Piccoli P.M. (2009) Fractionation of the platinum-group elements and Re during crystallization of basalt in Kilauea Iki Lava Lake, Hawaii, *Chem. Geol.* **260**, 196-210

Prytulak J., Nielsen S. G., Ionov D. A., Halliday A. N., Harvey J., Kelley K. A., Niu Y. L., Peate D. W., Shimizu K. and Sims K. W. W. (2013) The stable vanadium isotope composition of the mantle and mafic lavas. *Earth Planet. Sci. Lett.* **365**, 177–189. Available at: http://dx.doi.org/10.1016/j.epsl.2013.01.010.

Puchtel I.S., Humayun M., Campbell A.J., Sproule R.A., Lesher C.M. (2004) Platinum group element geochemistry of komatiites from the Alexo and Pyke Hill areas, Ontario, Canada, *Geochim. Cosmochim. Acta* **68**, 1361-1383

Rayner N.M., Sanborn-Barrie S., Young M.D., Whalen J.B. (2012) U-Pb ages of Archean basement and Paleoproterozoic plutonic rocks, southern Cumberland Peninsula, eastern Baffin Island, Nunavut, *Geological Survey of Canada, Current Research 2012-8*, 1-24

Richter D.H. and Moore J.G. (1966) Petrology of the Kilauea Iki Lava Lake, Hawaii, *USGS. Professional Paper 537-B*

Righter K., Leeman W. P. and Hervig R. L. (2006) Partitioning of Ni, Co and V between spinel-structured oxides and silicate melts: Importance of spinel composition. *Chem. Geol.* **227**, 1–25.

Rudnick R. L., Barth M., Horn I. and McDonough W. F. (2000) Rutile bearing refractory eclogite: missing link between continents and depleted mantle. *Science (80-.).* **287**, 278–281.

Rudnick R. L. and Gao S. (2013) *Composition of the Continental Crust*. 2nd ed., Elsevier Ltd. Available at: http://dx.doi.org/10.1016/B978-0-08-095975-7.00301-6.

Rudnick R. L., Gao S., Ling W. L., Liu Y. S. and McDonough W. F. (2004a) Petrology and geochemistry of spinel peridotite xenoliths from Hannuoba and Qixia, North China craton. *Lithos* **77**, 609–637.

Rudnick R. L., Tomascak P. B., Njo H. B. and Gardner L. R. (2004b) Extreme lithium isotopic fractionation during continental weathering revealed in saprolites from South Carolina. *Chem. Geol.* **212**, 45–57.

Salters V. J. M. and Stracke A. (2004) Composition of the depleted mantle. *Geochemistry, Geophys. Geosystems* **5**.

Savage P.S., Moynier F., Chen H., Shofner G., Siebert J., Puchtel I.S. (2015) Copper isotope evidence for large-scale sulphide fractionation during Earth's differentiation, *Geochem. Perspect. Lett.* **1**, 53-64

Schellmann W. (1994) Geochemical differentiation in laterite and bauxite formation. **21**, 131–143.

Schoepp-Cothenet B., van Lis R., Philippot P., Magalon A., Russell M.J., Nitschke W. (2012) The ineluctable requirement for the trans-iron elements molybdenum and/or tungsten in the origin of life

Scheiderich, K., Zerkle, A.L.,Helz, G.R., Farquhar, J.,Walker, R.J. (2010) Molybdenum isotope,

multiple sulfur isotope, and redox-sensitive element behavior in early Pleistocene Mediterranean sapropels. Chemical Geology 279 (3–4), 134–144.

Scott C., Lyons T. W., Bekker A., Shen Y., Poulton S. W., Chu X. and Anbar A. D. (2008) Tracing the stepwise oxygenation of the Proterozoic ocean. *Nature* **452**, 456–459.

Shannon R. D. and Prewitt C. T. (1969) Effective ionic radii in oxides and fluorides. *Acta Crystallogr. Sect. B Struct. Crystallogr. Cryst. Chem.* **25**, 925–946. Available at: http://scripts.iucr.org/cgi-bin/paper?S0567740869003220.

Siebert C., Nägler T. F., von Blanckenburg F. and Kramers J. D. (2003) Molybdenum isotope records as a potential new proxy for paleoceanography. *Earth Planet. Sci. Lett.* **211**, 159–171.

Siebert C., Pett-Ridge J. C., Opfergelt S., Guicharnaud R. A., Halliday A. N. and Burton K. W. (2015) Molybdenum isotope fractionation in soils: Influence of redox conditions, organic matter, and atmospheric inputs. *Geochim. Cosmochim. Acta* **162**, 1–24.

Skora S., Freymuth H., Blundy J., Elliott T. and Guillong M. (2017) An experimental study of the behaviour of cerium/molybdenum ratios during subduction: Implications for tracing the slab component in the Lesser Antilles and Mariana Arc. *Geochim. Cosmochim. Acta* **212**, 133–155. Available at: http://dx.doi.org/10.1016/j.gca.2017.05.025.

Sobolev A.V., Hofmann A.W., Sobolev S.V., Kikogosian I.K. (2005) An olivine-free mantle source of Hawaiian shield basalts, *Nature* **434**, 590-597

Stone W.E. and Fleet M.E. (1991) Nickel-copper sulfides from the 1959 eruption of Kilauea Volcano, Hawaii: Contrasting compositions and phase relations in eruption pumice and Kilauea Iki lava lake, *Am. Mineral.* **76,** 1363-1372

Stueken E.E., Buick R., Guy B.M., Koehler M. (2015) Isotopic evidence for biological nitrogen fixation by molybdenum-nitrogenase from 3.2 Gyr, *Nature* **520**, 666-670

Sun W., Bennett V.C., Eggins S.M., Kamenetsky V.S., Arculus J. (2003) Enhanced mantle to crust rhenium transfer in undegassed arc magmas, *Nature* **422**, 294-297

Tang M., Chen K. and Rudnick R. L. (2016) Archean upper crust transition from mafic to felsic marks the onset of plate tectonics. *Science (80-.).* **351**, 372–375.

Tang M., Rudnick R. L., Lee C. A. and Condie K. C. Archean ultra-thick crust reflects mantle overturn in early Earth.

Taylor S.R. and McLennan S.M. (1985) The Continental Crust; Its composition and evolution, Blackwell, Oxford

Teng F.Z., Wadhwa M., Helz R.T. (2007) Investigation of magnesium isotope fractionation during basalt differentiation: Implications for a chondritic composition of the terrestrial mantle, *Earth and Planet. Sci. Lett.* **261**, 84-92

Teng F.Z., Dauphas N., Helz R.T. (2008) Iron Isotope Fractionation During Magmatic Differentiation in Kilauea Iki Lava Lake, *Science* **320**, 1620-1622

Teng F. Z., Li W. Y., Rudnick R. L. and Gardner L. R. (2010) Contrasting lithium and magnesium isotope fractionation during continental weathering. *Earth Planet. Sci. Lett.* **300**, 63–71. Available at: http://dx.doi.org/10.1016/j.epsl.2010.09.036.

Tessalina S.G., Yudovskaya M.A., Chaplygin I.V., Birck J., Capmas F. (2008) Sources of unique rhenium enrichments in fumaroles and sulphides at Kudryavy volcano, *Geochim. Cosmochim. Acta* **72**, 889-909

Tiepolo M., Oberti R., Zanetti A., Vannucci R., Pavia U. and Foley S. F. (2007) Trace-Element Partitioning Between Amphibole and Silicate Melt. **67**, 417–452.

Tomascak P.B., Tera F., Helz R.T., Walker R.J. (1999) The absence of lithium isotope fractionation during basaltic differentiation: New measurements by multicollector sector ICP-MS, *Geochim. Cosmochim. Acta* **63**, No.6, 907-910

Tossell J. A. (2005) Calculating the partitioning of the isotopes of Mo between oxidic and sulfidic species in aqueous solution. *Geochim. Cosmochim. Acta* **69**, 2981–2993.

Turekian K.K. and Bertine K.K (1971) Deposition of molybdenum and uranium along the major ocean ridge systems, *Nature*, **229**, 250-251

Vielzeuf D. and Kornprobst J. (1984) Crustal splitting and the emplacement of Pyrenean lherzolites and granulites, *Earth Planet. Sci. Lett.* **67**, 87-96

Visser J. N. J. (1982) in the north by the Ghaap Plateau , in the west by the Doringberg Range (Fig . l) and in the south and east by inliers of basement . The size of this basin-like structure (henceforth referred to as the " Prieska Basin ") and its location along the nort. **38**.

Voegelin A. R., Pettke T., Greber N. D., von Niederhäusern B. and Nägler T. F. (2014) Magma differentiation fractionates Mo isotope ratios: Evidence from the Kos Plateau Tuff (Aegean Arc). *Lithos* **190-191**, 440–448. Available at: http://dx.doi.org/10.1016/j.lithos.2013.12.016.

Walker R.J. (2016) Siderophile elements in tracing planetary formation and evolution, *Geochem. Perspect.* **5**, No. 1, 1-143

Wang and Becker (2015) Abundances of Ag and Cu in mantle peridotites and the implications for the behavior of chalcophile elements in the mantle, *Geochim. Cosmochim. Acta* **160**, 209-226

Wang S. J., Teng F. Z., Rudnick R. L. and Li S. G. (2015) Magnesium isotope evidence for a recycled origin of cratonic eclogites. *Geology* **43**, 1071–1074.

Wang Z. and Becker H. (2018) Molybdenum partitioning behavior and content in the depleted mantle: Insights from Balmuccia and Baldissero mantle tectonites (Ivrea Zone, Italian Alps). *Chem. Geol.*, 0–1. Available at: https://doi.org/10.1016/j.chemgeo.2018.09.023.

Wang Z., Ma J., Li J., Wei G., Zeng T., Li L., Zhang L., Deng W., Xie L. and Liu Z. (2018) Fe (hydro) oxide controls Mo isotope fractionation during the weathering of granite. *Geochim. Cosmochim. Acta* **226**, 1–17. Available at: https://doi.org/10.1016/j.gca.2018.01.032.

Wasylenki L. E., Rolfe B. A., Weeks C. L., Spiro T. G. and Anbar A. D. (2008) Experimental investigation of the effects of temperature and ionic strength on Mo isotope fractionation during adsorption to manganese oxides. *Geochim. Cosmochim. Acta* **72**, 5997–6005. Available at: http://dx.doi.org/10.1016/j.gca.2008.08.027.

Whalen J.B., Sanborn-Barrie M., Young M. (2012) Geochemical data from Archean and Paleoproterozoic plutonic and volcanic rocks of Cumberland Peninsula, eastern Baffin Island, Nunavut, *Geol. Survey Canada Open File 6933*

Whalen J.B. Wodicka N., Taylor B.E., Jackson G.D. (2010) Cumberland batholith, Trans-Hudson Orogen, Canada: Petrogenesis and Implications for Paleoproterozoic crustal and orogenic processes, *Lithos* **117**, 99-118

Whalen J.B., Percival J.A., McNicoll V.J., Longstaffe F.J. (2003) Intra-oceanic production of continental crust in a Th-depleted ca. 3.0 Ga arc complex, western Superior Province, Canada, *Contrib. Mineral. Petrol.* **146**, 78-99

Whalen J.B., Percival J.A., McNicoll V.J., Longstaffe F.J. (2002) A mainly crustal origin for tonalitic granitoid rocks, Superior Province, Canada: Implications for Late Archean tectonomagmatic processes, *J. Petrol.* **43**, 8, 1551-1570

White W.M. (1985) Sources of oceanic basalts: Radiogenic isotopic evidence, *Geology* **13**, 115-118

White W. and Hofmann A. (1982) Sr and Nd isotope geochemistry of oceanic basalts and mantle evolution. *Nature* **296**, 821–825.

Wichard T., Mishra B., Myneni S. C. B., Bellenger J. P. and Kraepiel A. M. L. (2009) Storage and bioavailability of molybdenum in soils increased by organic matter complexation. *Nat. Geosci.* **2**, 625–630. Available at: http://dx.doi.org/10.1038/ngeo589.

Willbold M. and Elliott T. (2017) Molybdenum isotope variations in magmatic rocks. *Chem. Geol.* **449**, 253–268.

Willbold M., Elliott T., Archer C. (2012) Mass-dependent molybdenum isotope variations in ocean island basalts, *Goldschmidt Conf. Abstract*

Willbold M. and Stracke A. (2006) Trace element composition of mantle end-members: Implications for recycling of oceanic and upper and lower continental crust, *Geochem. Geophys. Geosyst.* **7**, 1-30

Wille M., Kramers J. D., Nägler T. F., Beukes N. J., Schröder S., Meisel T., Lacassie J. P. and Voegelin A. R. (2007) Evidence for a gradual rise of oxygen between 2.6 and 2.5 Ga from Mo isotopes and Re-PGE signatures in shales. *Geochim. Cosmochim. Acta* **71**, 2417–2435.

Wille M., Kurzweil F., Drost K., Pas J., Taubald H., Schoeckle D. and Schoenberg R. (2015) ScienceDirect Coupled sulfur , iron and molybdenum isotope data from ´ -Barrandian unit argue against black shales of the Tepla deep ocean oxygenation during the Ediacaran. **171**, 121–142.

Wille M., Nebel O., Van Kranendonk M. J., Schoenberg R., Kleinhanns I. C. and Ellwood M. J. (2013) Mo-Cr isotope evidence for a reducing Archean atmosphere in 3.46-2.76Ga black shales from the Pilbara, Western Australia. *Chem. Geol.* **340**, 68–76. Available at: http://dx.doi.org/10.1016/j.chemgeo.2012.12.018.

Wille M., Nebel O., Pettke T., Vroon P. Z., König S. and Schoenberg R. (2018) Molybdenum isotope variations in calc-alkaline lavas from the Banda arc, Indonesia: Assessing the effect of crystal fractionation in creating isotopically heavy continental crust. *Chem. Geol.* **485**, 1–13.

Witt-Eickschen G., Palme H., O'Neill H. S. C. and Allen C. M. (2009) The geochemistry of the volatile trace elements As, Cd, Ga, In and Sn in the Earth's mantle: New evidence from in situ analyses of mantle xenoliths. *Geochim. Cosmochim. Acta* **73**, 1755–1778. Available at: http://dx.doi.org/10.1016/j.gca.2008.12.013.

Wright, T. L., 1973. Magma mixing as illustrated by the 1959 eruption, Kilauea Volcano, Hawaii: Geological Society of America Bulletin 84, 849-858.

Xiong X., Keppler H., Audetat A., Ni H., Sun W., Li Y. (2011) Partitioning of Nb and Ta between rutile and felsic melt and the fractionation of Nb/Ta during partial melting of hydrous metabasalt *Geochim. Cosmochim. Acta* **75**, 1673-1692

Yang J., Barling J., Siebert C., Fietzke J., Stephens E. and Halliday A. N. (2017) The molybdenum isotopic compositions of I-, S- and A-type granitic suites. *Geochim. Cosmochim. Acta* **205**, 168–186. Available at: http://dx.doi.org/10.1016/j.gca.2017.01.027.

Yang J., Siebert C., Barling J., Savage P., Liang Y. H. and Halliday A. N. (2015) Absence of molybdenum isotope fractionation during magmatic differentiation at Hekla volcano, Iceland. *Geochim. Cosmochim. Acta* **162**, 126–136. Available at: http://dx.doi.org/10.1016/j.gca.2015.04.011.

Yi W., Halliday A. N., Alt J. C., Lee D.-C., Rehkämper M., Garcia M. O., Langmuir C. H. and Su Y. (2000) Cadmium, indium, tin, tellurium, and sulfur in oceanic basalts:

Implications for chalcophile element fractionation in the Earth. *J. Geophys. Res.* **105**, 18927–18948. Available at: http://dx.doi.org/10.1029/2000JB900152.

Yin L., Li J., Tian H. and Long X. (2018) Rhenium – osmium and molybdenum isotope systematics of black shales from the Lower Cambrian Niutitang Formation , SW China : Evidence of a well oxygenated ocean at ca . 520 Ma. *Chem. Geol.* **499**, 26–42. Available at: https://doi.org/10.1016/j.chemgeo.2018.08.016.

Zajacz Z., Halter W.E., Pettke T., Guillong M. (2008) Determination of fluid/melt partition coefficients by LA-ICPMS analysis of co-existing fluid and silicate melt inclusions: Controls on element partitioning, *Geochim Cosmochim Acta*. **72**, 2169-2197

Zhang W, Hu Z., Liu Y., Chen L., Chen H., Li M., Zhao L., Hu S., Gao S. (2012) Reassessment of HF/HNO3 decomposition capability in the high-pressure digestion of felsic rocks for muti-element determination by ICP-MS, *Geostan. Geoanal. Res.*

Zhang Z. and Hirschmann M. M. (2016) Experimental constraints on mantle sulfide melting up to 8 GPa. *Am. Mineral.* **101**, 181–192.

Zhou, X.H., Sun, M., Zhang, G.H., Chen, S.H. (2002) Continental crust and lithospheric mantle interaction beneath North China: isotopic evidence from granulite xenoliths in Hannuoba, Sino– Korean craton. Lithos 62, 111– 124

Zhou L., Wignall P.B., Su J., Feng Q., Xie S., Zhao L., Huang J. (2012) U/Mo ratios and δ98/95Mo as local and global redox proxies during mass extinction events, Chem. Geol. 324, 99-107

Appendix A.

The behavior of chalcophile elements during magmatic differentiation as observed in

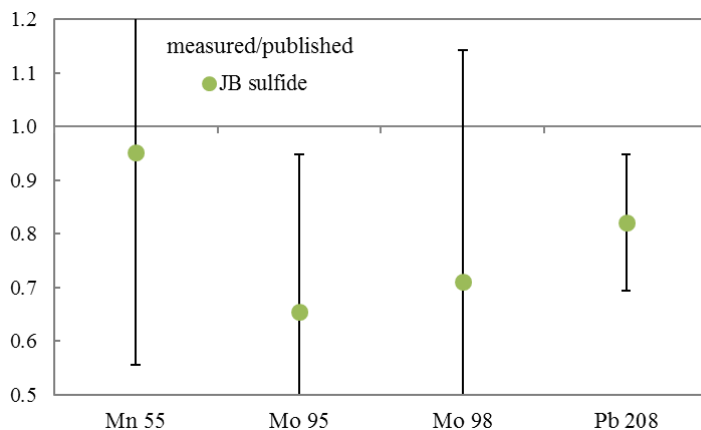## Kilauea Iki lava lake, Hawaii - Supplementary Information
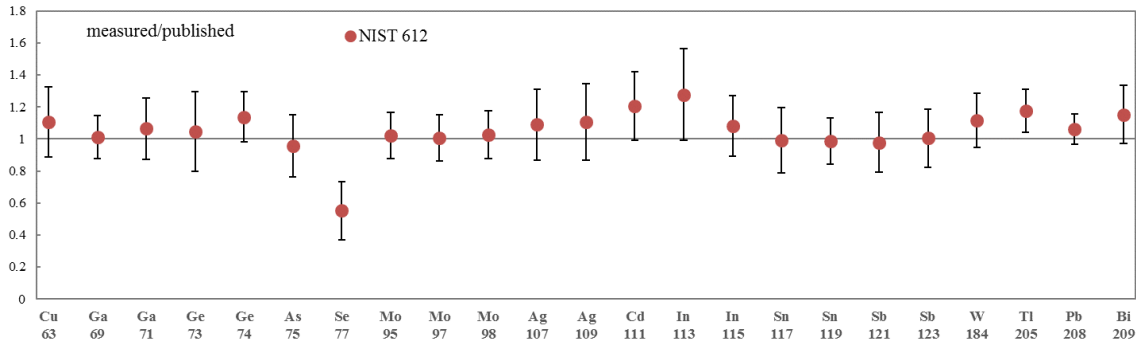
Figure A1. NIST612. Standard reference materials used as external standards for laser ablation ICP-MS. SRMs were run between every 6 to 10 analyses on the laser. Data points show the mean of multiple analyses divided by published values (GeoRem): NIST 612 n=22, BHVO-2g n=17, JB sulfide n=13. JB sulfide was used primarily to determine how well the sulfides were ablating, even though it does not contain all the elements of interest. There are no known published values for As, Se, Ag and Tl for BHVO-2G. Error bars are 2σ from replicate analyses. Isotopes chosen for data analysis were Cu 63, Ga 71, Ge 74, As 75, Mo 95, Ag 109, Cd 111, In 115, Sn 119, Sb 121, Tl205, Pb 208, and Bi 209.
Within the sample data, large uncertainties associated with some sample means can reflect true heterogeneity of the glasses, but may also reflect the difficulty in simultaneously measuring multiple extremely low abundance (10-100 ppb) elements by LA-ICP-MS with a limited spot size. True glass heterogeneity can be recognized if an increase in spot size (i.e., an increase in sensitivity for low abundance elements) does not improve the RSD associated with multiple spot analyses on a thin section.
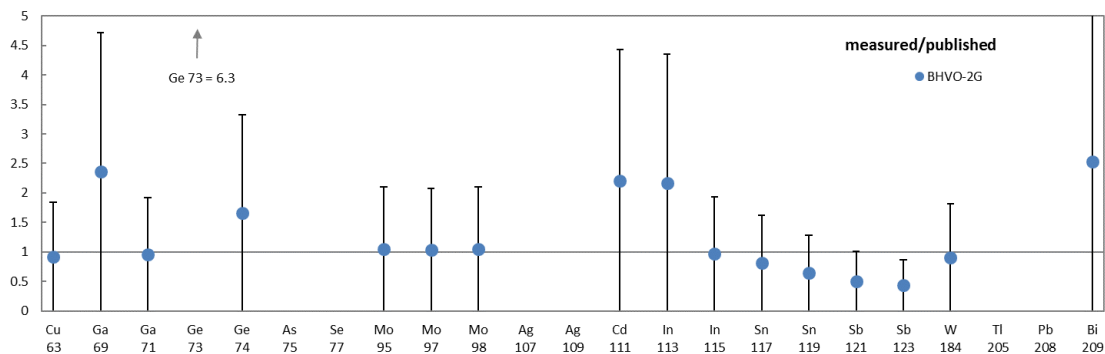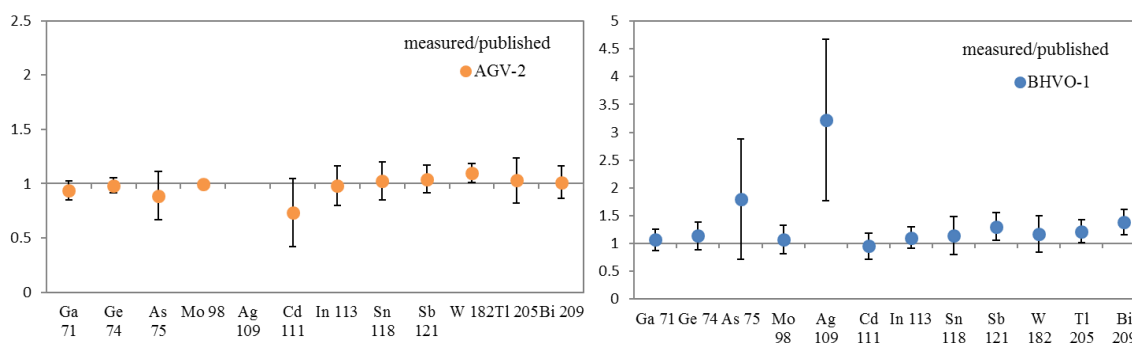

Figure A2. BHVO2g. Standard reference materials used as external standards for laser ablation ICP-MS. SRMs were run between every 6 to 10 analyses on the laser. Data points show the mean of multiple analyses divided by published values (GeoRem): NIST 612

n=22, BHVO-2g n=17, JB sulfide n=13. JB sulfide was used primarily to determine how well the sulfides were ablating, even though it does not contain all the elements of interest. There are no known published values for As, Se, Ag and Tl for BHVO-2G. Error bars are 2σ from replicate analyses. Isotopes chosen for data analysis were Cu 63, Ga 71, Ge 74, As 75, Mo 95, Ag 109, Cd 111, In 115, Sn 119, Sb 121, Tl205, Pb 208, and Bi 209.


Figure A3. JBsulfide. Standard reference materials used as external standards for laser ablation ICP-MS. SRMs were run between every 6 to 10 analyses on the laser. Data points show the mean of multiple analyses divided by published values (GeoRem): NIST 612 n=22, BHVO-2g n=17, JB sulfide n=13. JB sulfide was used primarily to determine how well the sulfides were ablating, even though it does not contain all the elements of interest. There are no known published values for As, Se, Ag and Tl for BHVO-2G. Error bars are 2σ from replicate analyses. Isotopes chosen for data analysis were Cu 63, Ga 71, Ge 74, As 75, Mo 95, Ag 109, Cd 111, In 115, Sn 119, Sb 121, Tl205, Pb 208, and Bi 209.


Figure A4-standard addition. Standard reference materials used as external standards for standard addition solution ICP-MS. Data points represent the mean of multiple analyses (n~6) normalized to published values (Gaschnig et al., 2014). Arsenic and Ag are normalized to USGS values (no published value for Ag in AGV-2). The isotopes chosen for data analysis are displayed. Error bars represent 2σ.
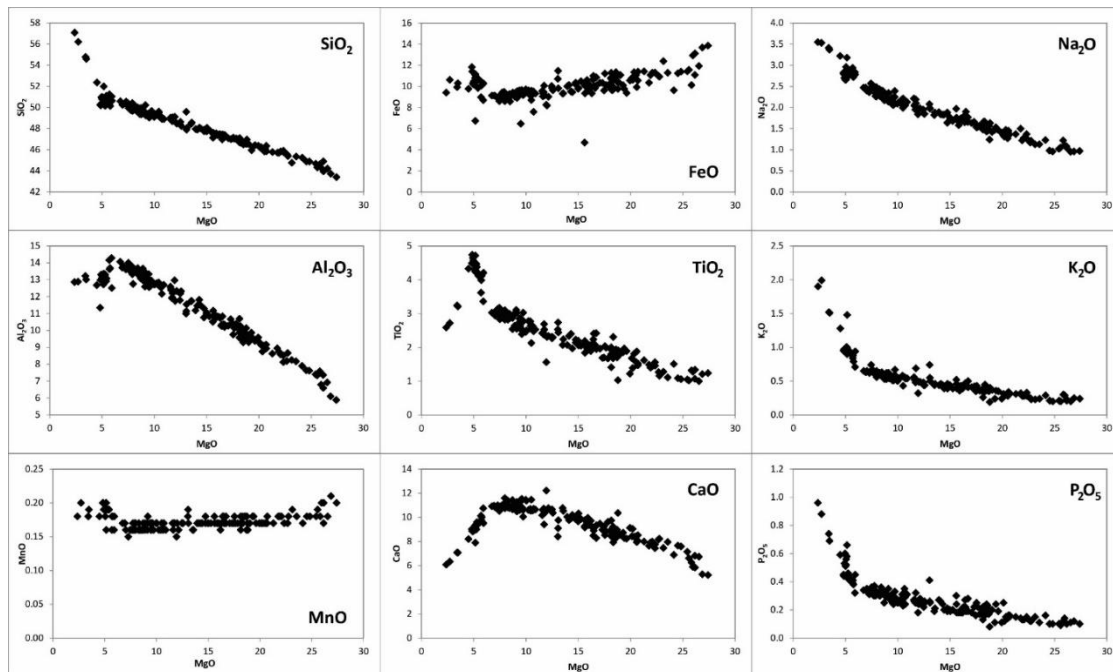
Figure A5. WR. Whole rock variation diagrams of major element differentiation trends, data from Helz and Taggert (2010).
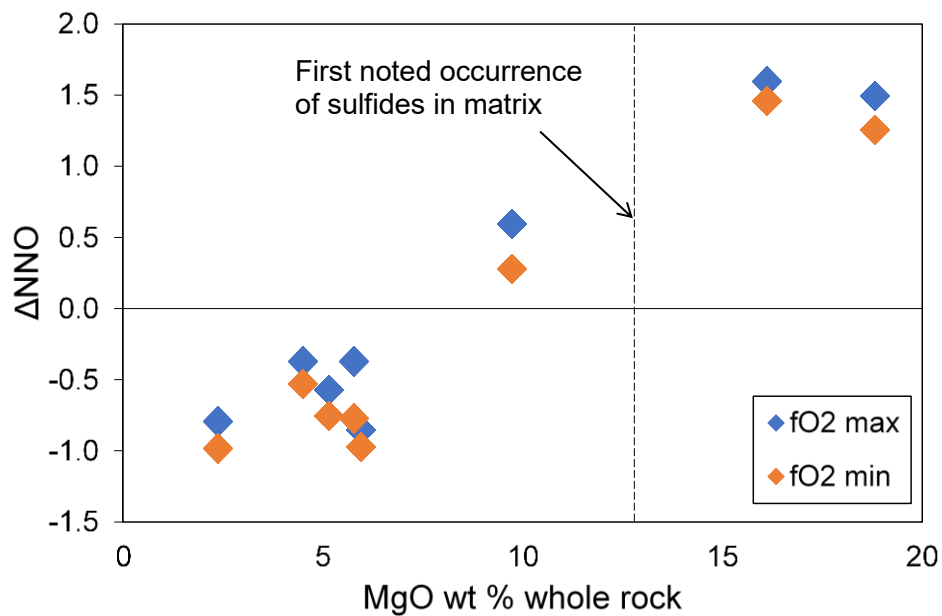
Figure A6. FO2. fO2 of eight samples calculated using the oxide oxy-thermobarometer of Ghiorso and Evans (2008). A min and max value were determined for each sample given the variation in oxide compositions found within the sample.
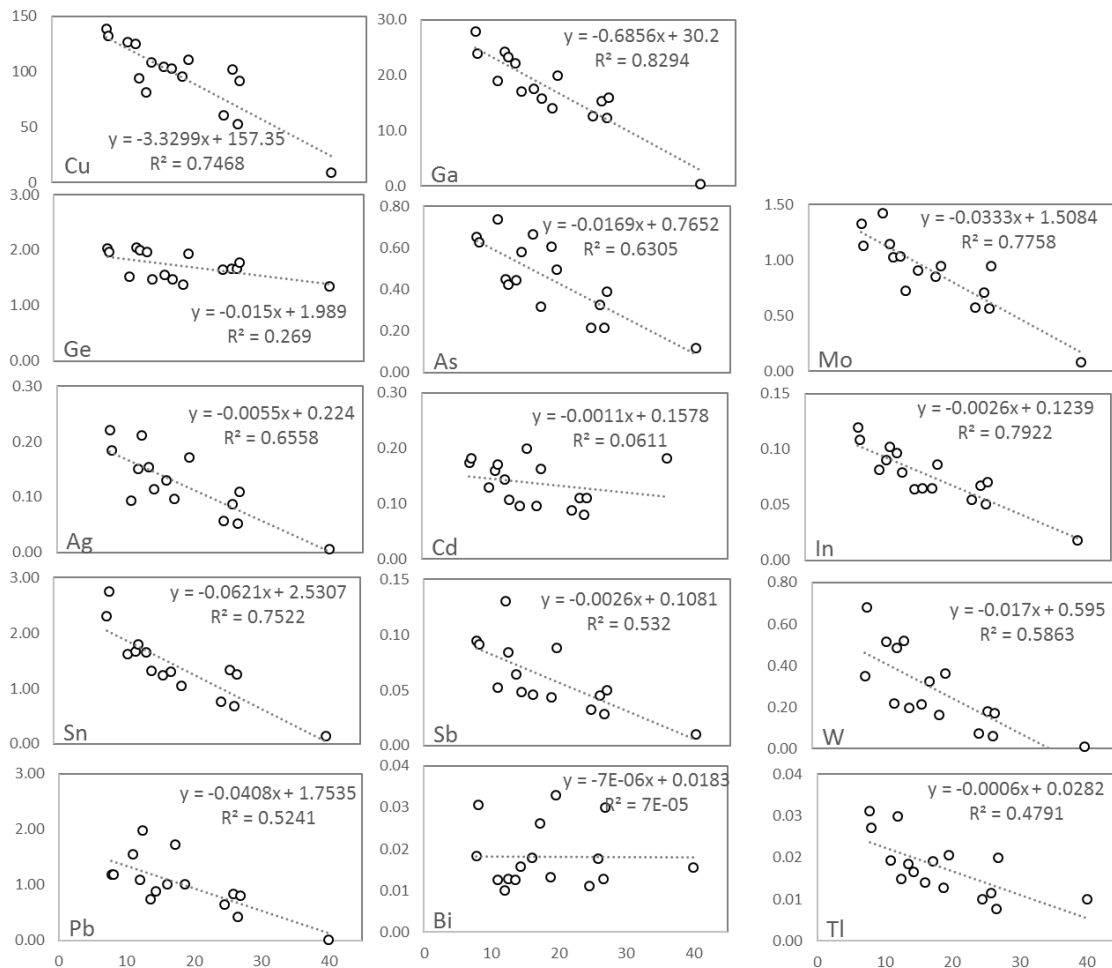
Figure A7. Rgression: Regressions used to calculate the primitive KI composition. Note Cd and Bi R2 are extremely low and caution should be taken when interpreting the Cd and Bi source composition.

Kilauea source composition (batch melting equation)

The regression of Puchtel et al (2004) resulted in an R^2 of >0.5 for all elements except Cd and Bi, so these elements are not well constrained in the Kilauea mantle source. Bulk partition coefficients for the batch melting equation were calculated using the source modal mineralogy of Norman and Garcia (1999): 65% spinel lherzolite (90% olivine + opx, 10% cpx) and 35% garnet lherzolite (80% olivine +opx, 10% cpx, 10% garnet). We used olivine and clinopyroxene partition coefficients measured in this study, while orthopyroxene and

garnet D values were taken from Liu et al. (2014) for Cu, and Salters and Stracke (2004) for Ce and Er, and Adam and Green (2006) for all other elements.

We first modeled a depleted MORB mantle given the average concentrations of Cu, Ga, Ge, As, Mo, Ag, Cd, In, Sn, Sb, La, Er, W, Tl, Pb, and Bi in MORB from Jenner and O'Neill (2012). Again, using the batch melting equation we use bulk D values calculated with the modal mineralogy of Workman and Hart (2005) of 57% olivine, 28% cpx, 13% garnet, and 1.99% spinel with 0.01% sulfide given the low melt fraction of 6% (Workman and Hart, 2005). Then this DMM composition was mixed with between 10 and 20% recycled oceanic crust, of which 95% to 99% is MORB (Jenner and O'Neill, 2012) and UCC sediments compose the remaining 5 to 1%.

Subduction effects on model

Lead, As, Sb, and Tl are predicted to partition into the mantle wedge along with a fluid phase during subduction (Noll et al., 1996), thus depleting these elements from the slab and lowering their contribution to the mantle plume source. Copper and Ag may also be enriched in the mantle wedge from the oxidation of slab sulfides (Timm et al., 2012), suggesting that other chalcophile elements like Cd, In, and Bi may also be released from the slab. There is conflicting evidence as to whether Mo, Sn, and W would be removed from or maintained in the slab (Noll et al., 1996; König et al., 2008; Bali, 2012; Timm et al., 2012), and we are not aware of studies of Ga and Ge in subduction zones. However, depletion of these elements from the slab would not greatly affect the mixing model assuming the elements are mostly removed from terrigenous sediments that may melt or release fluids during subduction. In fact, loss of Pb, As, Tl, and Cu from the slab and sediment package would move the mixing lines (gray region, Fig. 9) closer to that of the estimated KI source.

Supplementary tables can be found online at: https://doi.org/10.1016/j.gca.2017.04.033

Appendix B.

**The geochemistry of molybdenum in the continental crust -** Supplementary Materials

Sample Descriptions

<u>Phanerozoic Granites</u>

    Ellicott City Granodiorite (AG1401): Granodiorite consisting of plagioclase, quartz, K-feldspar, biotite, hornblende, epidote, allanite, titanite, zircon, and sulfides. The major phases (feldspars, quartz, biotite, amphibole) are euhedral to subhedral with melanocratic minerals (biotite, amphibole) composing <10% of the sample. Several plagioclase grains show alteration to sericite along concentric zoning boundaries. Several biotite grains contain zircon with pleochroic halos. Accessory phases (epidote, allanite, titanite, zircon, sulfides) comprise ~5% of the sample. The epidote has been determined to be a primary igneous phase (Zen and Hammerstrom, 1984), and is euhedral to subhedral with allanite cores. Sulfides (5-50 um) are ubiquitous throughout the samples and are composed of pyrite and chalcopyrite regions. Many have oxide rims and are mostly found as interstitial phases, although several occur as inclusions in biotite, epidote, and titanite. Mass balance for Mo is attained in this sample. Below: photomicrograph of a typical pyrite grain and scan of a thin section of the granodiorite.


50 µm

Idaho Batholith Tonalite (07RMG52): Extremely leucocratic peraluminous tonalite consisting of quartz, plagioclase, muscovite, garnet, K-feldspar, zircon, and niobite. Quartz, plagioclase, and muscovite are the euhedral major phases with K-feldspar occurring as antiperthite inclusions in some plagioclase grains. Euhedral garnet (spessartine – almandine) is the most common accessory phase (~2%). One grain of niobite/columbite (~50um in diameter) was found. Mass balance of Mo is not attained in this sample, however this may be due to the nugget effect given the presence of small grains of niobite that concentrate Mo. Below: photomicrographs in ppl and xpl showing the extreme leucocratic nature of the sample (horizontal FOV ~6 mm).
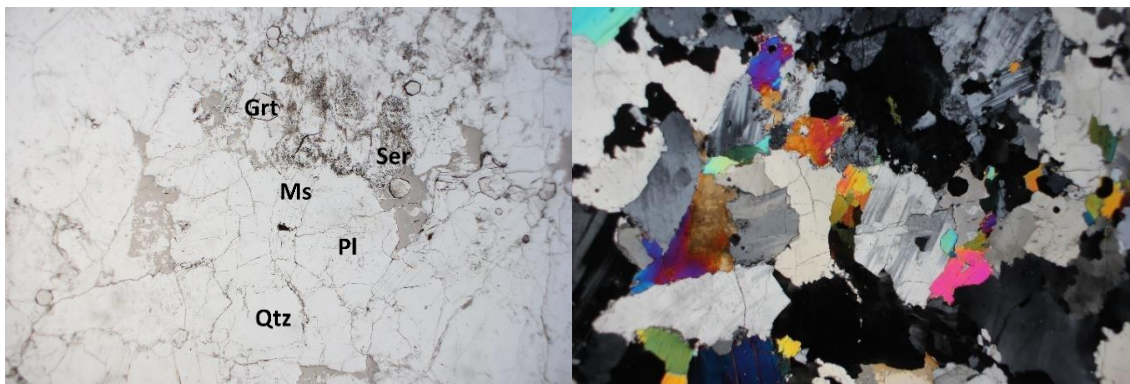
Lookout Mountain Tonalite (10RMG005): Granite consisting of plagioclase, quartz, biotite, hornblende, oxides, sulfides, and apatite. The major phases (plagioclase, quartz, biotite, amphibole) are euhedral to subhedral with several of the plagioclase grains showing zoning and twinning with minor sericite along the twin planes. Melanocratic minerals compose ~30% of the sample. Magnetite with ilmenite exsolution are the most common accessory phases (~3%) with occasional rutile present. Several oxides contain inclusions of chalcopyrite (<20 µm). The apatite occurs predominately within and alongside biotite

grains. Mass balance of Mo is not attained in this sample. Below: photomicrograph of a small sulfide inclusion in magnetite and a thin section scan.
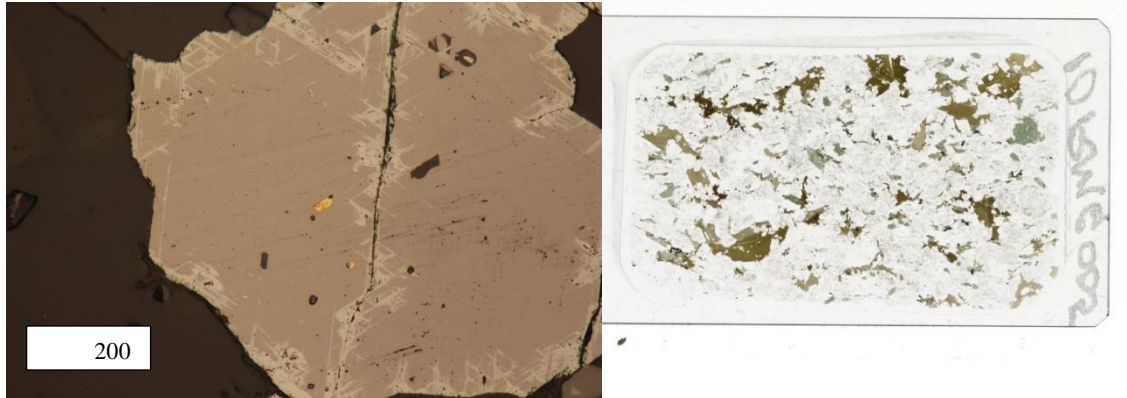

Zimbabwe Craton

Further sample descriptions can be found in Luais and Hawkesworth (1994).

ZB 89-10: Extremely leucocratic, foliated tonalite consisting of plagioclase, quartz, biotite, muscovite, titanite, oxides, and epidote with allanite cores. Recrystallization is evident given fine grain sizes of major and accessory phase minerals (50-100 µm). Melanocratic minerals make up ~5% of the sample. Alteration textures and mineral assemblages are present, including secondary epidote and heavily sericitized plagioclase. Rutile often occurs alongside or within titanite. Mass balance of Mo is not attained in this sample. Below: photomicrographs in ppl and xpl showing the foliation and recrystallized textures (horizontal FOV ~6 mm).
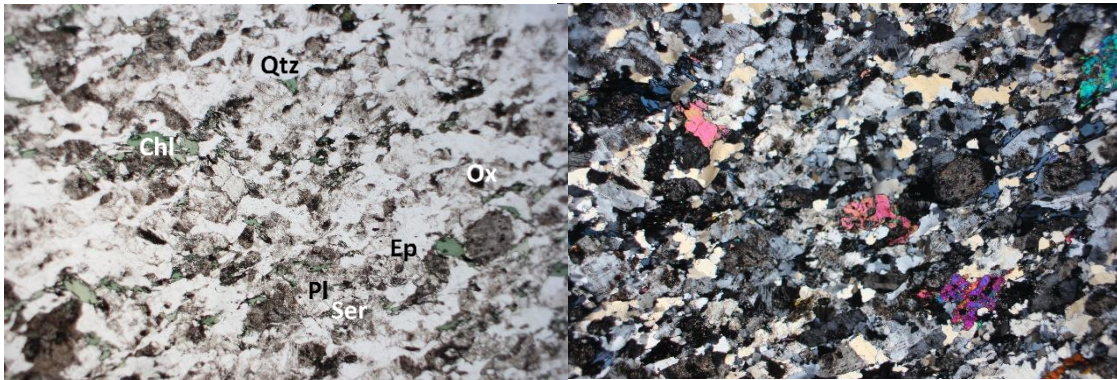
ZB 89-13: Slightly foliated tonalite consisting of plagioclase, quartz, biotite, hornblende, epidote with allanite cores, hornblende, titanite, oxides, and apatite. The apatite forms thin needles that are too small for LA-ICP-MS. Several plagioclase grains are sericitized. Melanocratic minerals comprise ~30% of the sample. Ilmenite typically forms alongside or within biotite. Epidote is probably secondary, but forms extremely large (100 - 500 µm) grains. Mass balance of Mo is attained in this sample. Below: photomicrographs in ppl and xpl showing foliation (horizontal FOV ~6 mm).
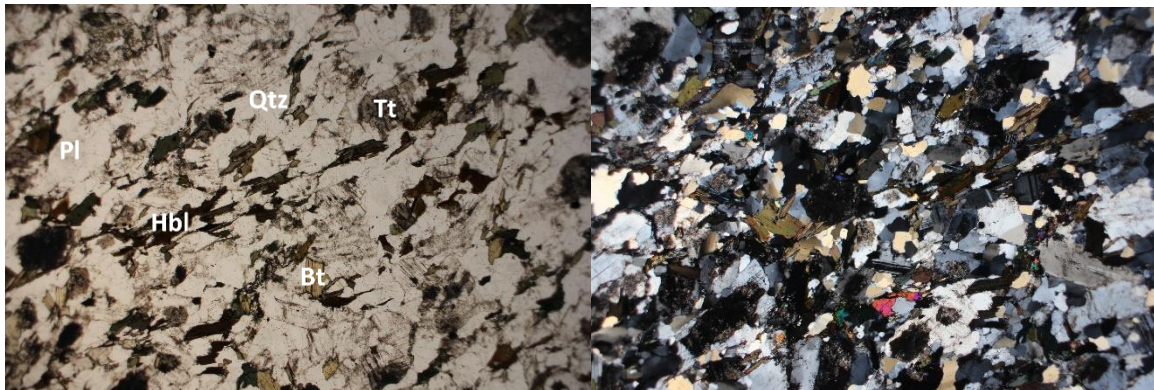

ZB 89-15: Foliated tonalite consisting of plagioclase, quartz, biotite altered to chlorite, epidote with allanite cores, titanite, and oxides. Recrystallization is evident given fine grain sizes of major and accessory phase minerals (50-200 µm). Plagioclase grains are variably sericitized. Melanocratic minerals comprise ~ 5% of the sample. Mass balance of Mo is

attained in this sample. Below: photomicrographs in ppl and xpl showing foliation and recrystallized textures (horizontal FOV ~ 6 mm).

ZB 89-53: Relatively un-foliated tonalite consisting of plagioclase, K-feldspar, quartz, biotite altered to chlorite, epidote with allanite cores, and oxides. Plagioclase grains are variably sericitized. Melanocratic minerals compose ~10% of the sample. Several oxides contain sulfide inclusions. One oxide grain may contain an inclusion of MoS_2 (pictured below, right). Mass balance of Mo is attained in this sample. Below left: photomicrograph showing overall texture/grain size and sericitization of plagioclase (horizontal FOV ~ 6 mm).
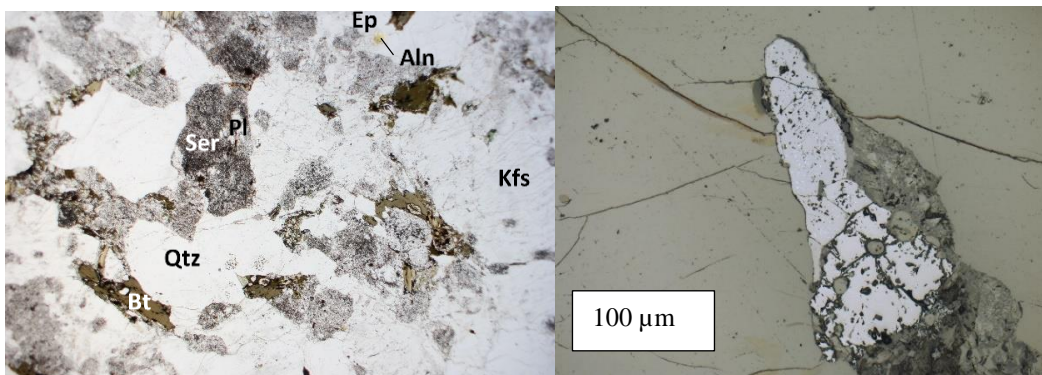
PBA97-23: Unfoliated, coarse grained granite consisting of quartz, plagioclase, K-feldspar, biotite, muscovite, titanite, magnetite, and sulfides. Melanocratic minerals comprise ~10% of the sample. Plagioclase grains are variably sericitized and titanite grains show occasional rutile rims and zoning. Little to no metamorphism or metasomatic alteration is observed. Several small (< 20 µm) pyrite grains rimmed by oxides are observed throughout the sample (photo, below left). Mass balance of Mo can be attained in the sample without the sulfide contribution. Below right: PPL photomicrograph showing overall texture of the sample (horizontal FOV ~ 6 mm).
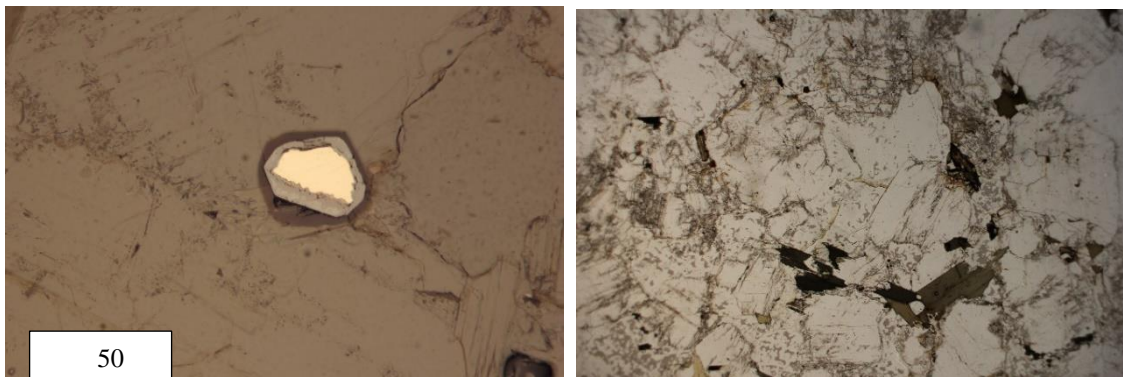
WXP99-123: Relatively foliated and slightly metamorphosed tonalite consisting of plagioclase, amphibole, quartz, biotite, ilmenite, epidote, apatite, and sulfides. Melanocratic phases make up ~ 40% of the sample. Hornblende and cummingtonite are the predominate amphiboles present. The sulfides are pyrite and chalcopyrite and are disseminated throughout the matrix (<30 µm in diameter; photo below, left, RL). The apatite grains form acicular crystals and are too small for laser-ablation analysis. Mass balance of Mo is attained in this sample. Below right: PPL photomicrograph showing overall texture of samples (horizontal FOV ~ 6mm).
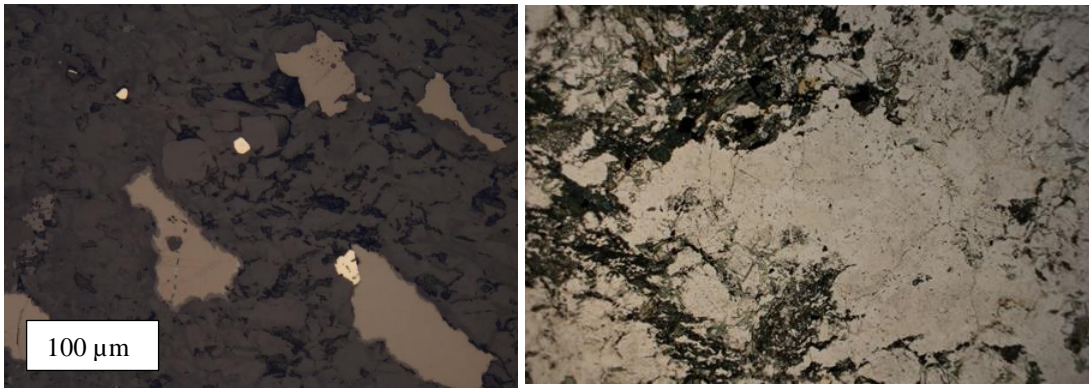
WXP99-176: Metamorphosed but unfoliated leucocratic trondhjemite consisting of plagioclase, quartz, muscovite, epidote, titanite, biotite, oxides, and minor sulfides. Melanocratic minerals make up ~5% of the sample. The epidote and muscovite are like secondary phases, and secondary rutile forms within the titanite. A few grains of pyrrhotite and chalcopyrite ($<20 \mu m$) are found in the matrix. Mass balance of Mo is not attained in this sample. Below: photomicrograph of a sulfide inclusion in plagioclase (RL, left) and a wider view of the thin section to show the leucrocratic nature of the sample (PPL, right, horizontal FOV ~ 6mm).
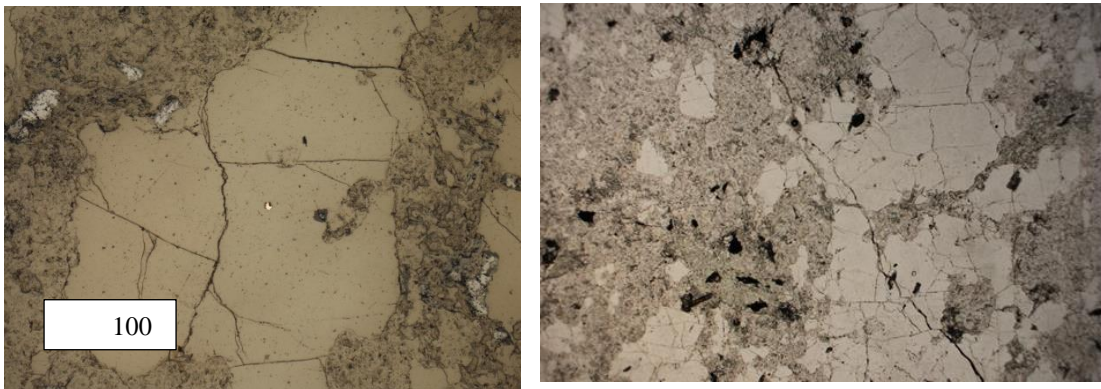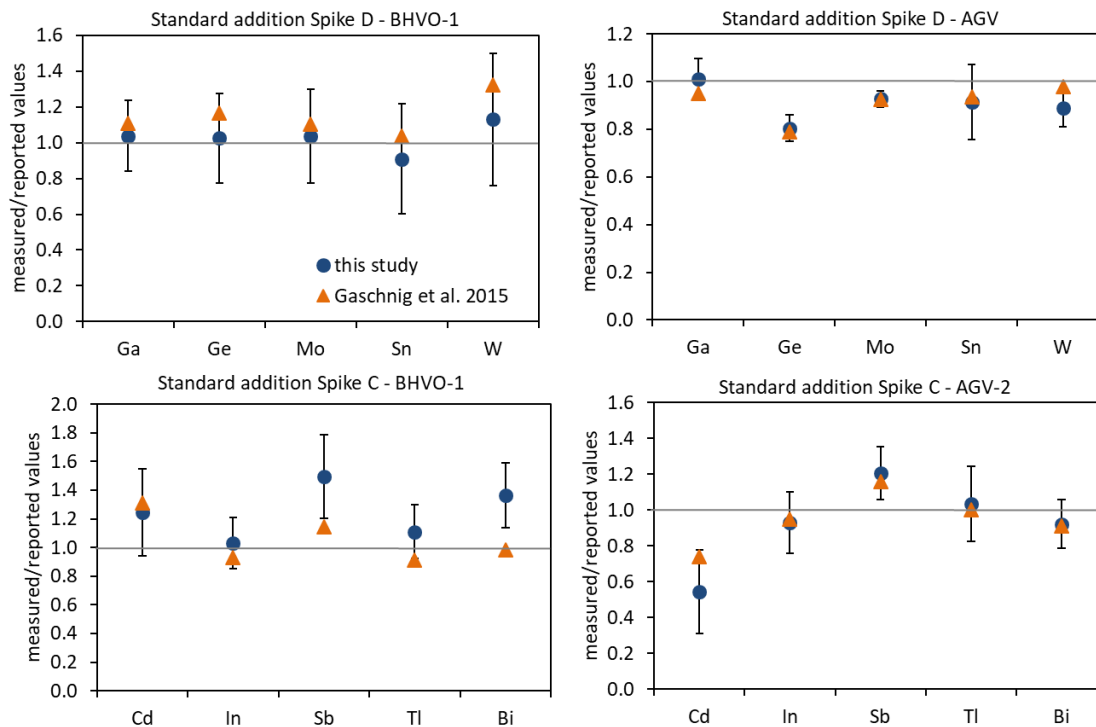
Methods

slightly modified from Greaney et al. (2017)

Whole rock analyses

The powdered granitoids, four USGS rock standards (BHVO-1, W-2, AGV-2, and GSP-1), and a total analytical blank (TAB) were analyzed using standard addition solution inductively-coupled mass spectrometry (ICP-MS) for Mo concentrations and externally calibrated solution ICP-MS for other trace elements. Fifty milligrams of powder were dissolved in high-pressure Teflon Parr bombs with one mL of concentrated HNO_3 and 3 mL of concentrated HF in a furnace (180°C) for ≥72 hours. The solutions were then evaporated to dryness on a hotplate and 2 mL of concentrated HNO_3 were added and subsequently evaporated before adding 1 mL of HNO_3 and 2 mL of 18Ω MilliQ H_2O, resealing the bombs, and replacing them in the furnace overnight (≥12 hours). The bombs were removed the next day and "master solutions" were made, consisting of the dissolved solution (sample + 1 mL of HNO_3 + 2 mL of MilliQ H_2O) diluted to 15 mL with 2% HNO_3 and trace HF. Sample dissolution and standard addition followed the procedures given by Zhang et al. (2012) and Gaschnig et al. (2015).

The standard addition technique involves spiking the solution of unknown concentration with known concentrations of the element of interest, and using the spiked samples to create a calibration curve. For the most accurate results, the spike was prepared so that it contained roughly double the concentration of Mo expected in the samples. Three solutions were created for each sample + spike combination. Solution one contained 1mL of master solution and 1 mL of a purified Rh solution in 2% HNO_3 (~75 ppb) to be used for drift corrections. Solution two contained 1 mL of master solution, 1 mL of Rh, and 0.5 mL of

spike. Solution three contained 1 mL of master solution, 1 mL of Rh, and 1 mL of spike. The three aliquots were diluted to a total volume of 10 mL with 2% HNO_3.

A separate 1 mL aliquot of the master solution was spiked with 1mL of ~800ppb In (drift corrector) and diluted to 15 mL with 2% HNO_3 for trace element analyses. These data were reduced with an external calibration curve created using the USGS standards. The standard addition and In-spiked solutions were run on a Thermo-Finnigan Element2 HR-ICP-MS at the University of Maryland within a week of solution preparation. The instrument was tuned to keep oxide production below 0.8% $^{238}U^{16}O/^{238}U$. Multiple isotopes of Mo were run in both low (LR) and medium (MR) resolution to reduce polyatomic and isobaric interferences: ^{95}Mo (LR, MR), ^{97}Mo (LR, MR), ^{98}Mo (LR, MR). Detection limits range from 0.03 to 0.10 µg/g, but the analytical session for the Barberton samples produced a higher background (0.16 µg/g). Precision was determined using replicate analyses of BHVO-1 and AGV-2 (Table 2, main text). BHVO-1 shows poor reproducibility – likely due to heterogeneities introduced into the powder during crushing – which has been noted in previous studies (Konig et al. 2008; Willbold et al. 2016; Gaschnig et al. 2015). The standard addition data were reduced using an in-house Excel macro created by Ming Tang and errors are calculated from the counting statistics reported by the instrument (average 12% 2RSD), as these are generally more conservative than the error associated with reproducibility of AGV (7% 2RSD).

Figure B1. Elements measured by the standard addition method normalized to values reported in GeoRem.

Three TTGs with extremely low Mo were dissolved and analyzed a second time at Arizona State University using a Thermo Fischer iCAP Quadropole ICP-MS and with isotope dilution on a Thermo Fischer Neptune MC-ICP-MS to ensure data quality. The quadrupole data were reduced using a calibration curve generated by standards created in the ASU Keck Lab for Biogeochemistry. The isotope dilution data were measured using a Mo double spike technique (^{97}Mo-^{100}Mo) and measuring the ratio of 98/95. Two samples (WXP99-143 and STY-1) reproduced extremely well, while the second dissolution of ZB89-10 showed lower values. Mass balance could not be completed in this sample, suggesting minor heterogeneities may exist within the powder due to a "nugget effect" of MoS_2. Indeed, only 50 mg of powder were used for both rounds of dissolution, so this effect is

quite probable. Nevertheless, these replicate analyses provide further evidence for the observation that significant Mo is "missing" from the TTGs and granites studied here.

	SA SC-ICP-MS	2σ	Q-ICP-MS	2σ	ID MC-ICP-MS	2σ
Sample	Dissolution 1		Dissolution 2			
WXP99-143	≤0.10	-	0.10	0.06	0.11	0.01
ZB89-10	0.25	0.02	0.08	0.04	0.13	0.01
STY-1	0.16	0.04	0.13	0.03	0.14	0.01

Table B1. Comparison of Mo (µg/g) measured in three samples with three different methods. The standard addition data reported in this paper were dissolved and run at the University of Maryland. The Q-ICP-MS and MC-ICP-MS data were collected from a separate sample aliquot dissolved and analyzed at Arizona State University and 2σ refers to internal precision.

In-situ analyses

In-situ analyses of silicates, oxides, and sulfides were carried out on petrographic thin sections. The phases were analyzed for major-element compositions using WDS on a JEOL JXA-8900 Electron Probe Micro-analyzer at the University of Maryland. All EPMA analyses were performed with a 5 µm beam, 15 kV accelerating voltage, and 25 nA probe current.

Trace element abundances were determined using LA-ICP-MS at the University of Maryland. The phases were ablated in a He atmosphere using a New Wave UP 213 nm wavelength laser and the resulting sample plume was analyzed with a Thermo-Finnigan Element2 HR-ICP-MS. The instrument was tuned so that the $^{238}U^{16}O/^{238}U$ ratio was below 0.8%. All substrates were ablated with a laser frequency of 7 Hz and fluence was kept between 2.5 and 4 J/cm^2, depending on the substrate being analyzed. Three isotopes of Mo were measured: ^{95}Mo, ^{97}Mo, ^{98}Mo and they generally vary by less than 5%, although some Mn-rich phases (e.g., garnet) can generate significant variance between ^{95}Mo and the other two isotopes due to Mn-argide interferences. Silicate and oxide analyses were performed

using a laser spot size between 55 to 80 µm, and sulfide analyses were performed with a spot size of 25 to 80 µm, depending on the size of the phase being ablated. Data reduction for LA-ICP-MS was performed using NIST 610 as the external calibration standard and the Iolite software created at the University of Melbourne (Paton et al., 2011). Silicon-29 was used as an internal standard for silicate phases, ^{65}Cu or ^{60}Ni for sulfides, and ^{55}Mn or ^{49}Ti for oxides. Reference materials BHVO-2g, NIST-612, and JB sulfide (an in-house reference material created by James Brenan) were used as secondary standards during laser ablation analyses (Table 2 in main text). The values reported in Table 3 in the main text represent average values of multiple analyses (n), with the 2σ representing 2 standard deviations of that mean.

Several low abundance phases (biotite, amphibole, plagioclase, and quartz) were re-analyzed with laser ablation at the University of California Santa Barbara using a Photon Machines 193 nm laser and an Agilent 7700x Q-ICP-MS. A 60 µm spot size was used and three isotopes of Mo (95, 97, and 98) were monitored and returned values that are indistinguishable from those measured at UMD. Detection limits were routinely 0.01 µg/g. These values are included in Table 3 in the main text.
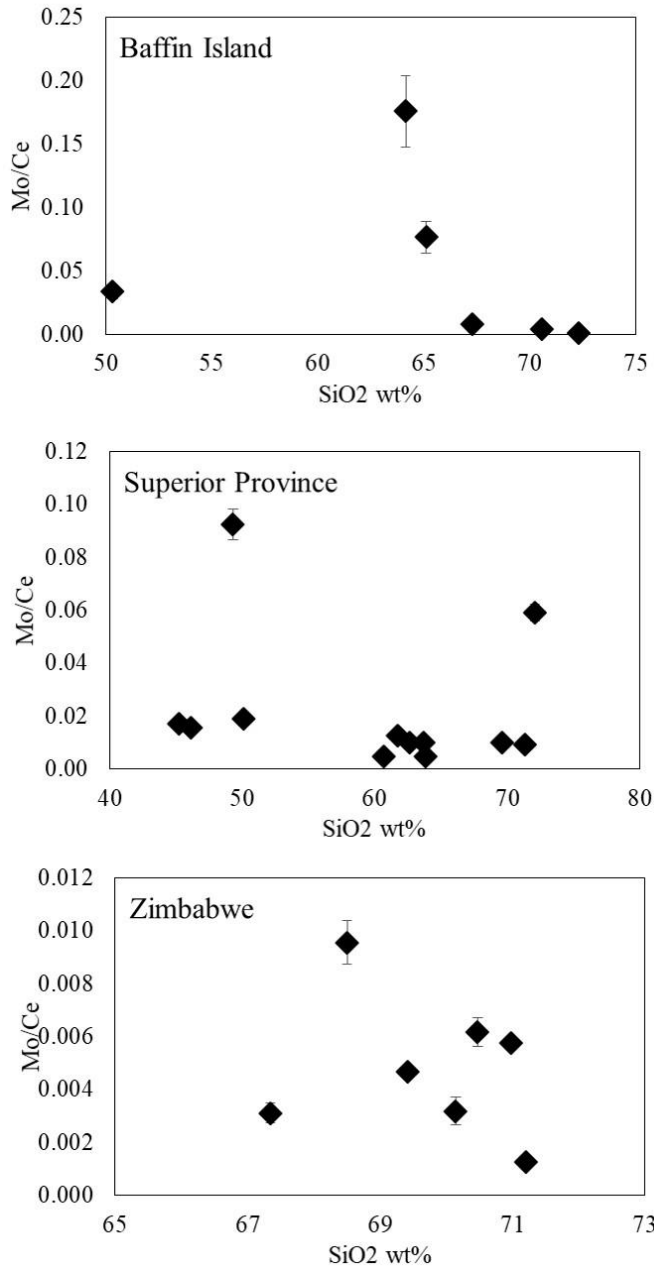
Figure B2. Correlations (or lack thereof) between Mo/Ce and SiO2 in various differentiation suites.
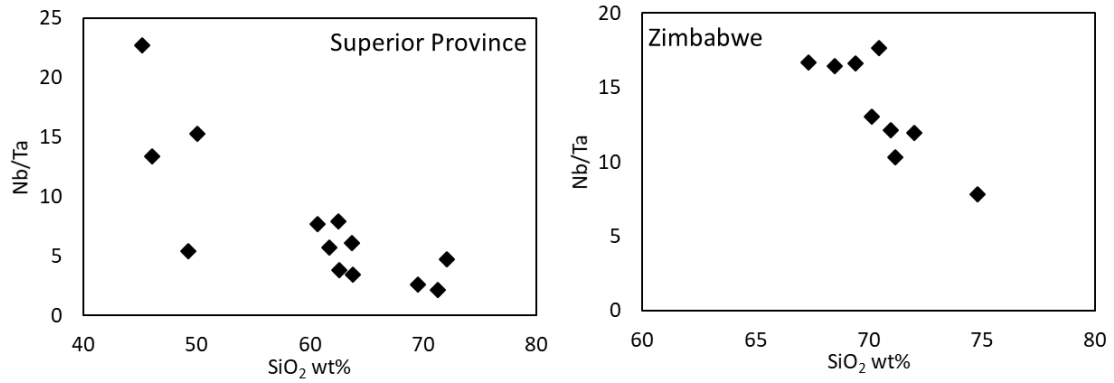
Figure B3. Nb/Ta fractionation observed in the Superior Province and Zimbabwe Craton TTGs, suggesting fractionation of a titaniferous phase like titanite.
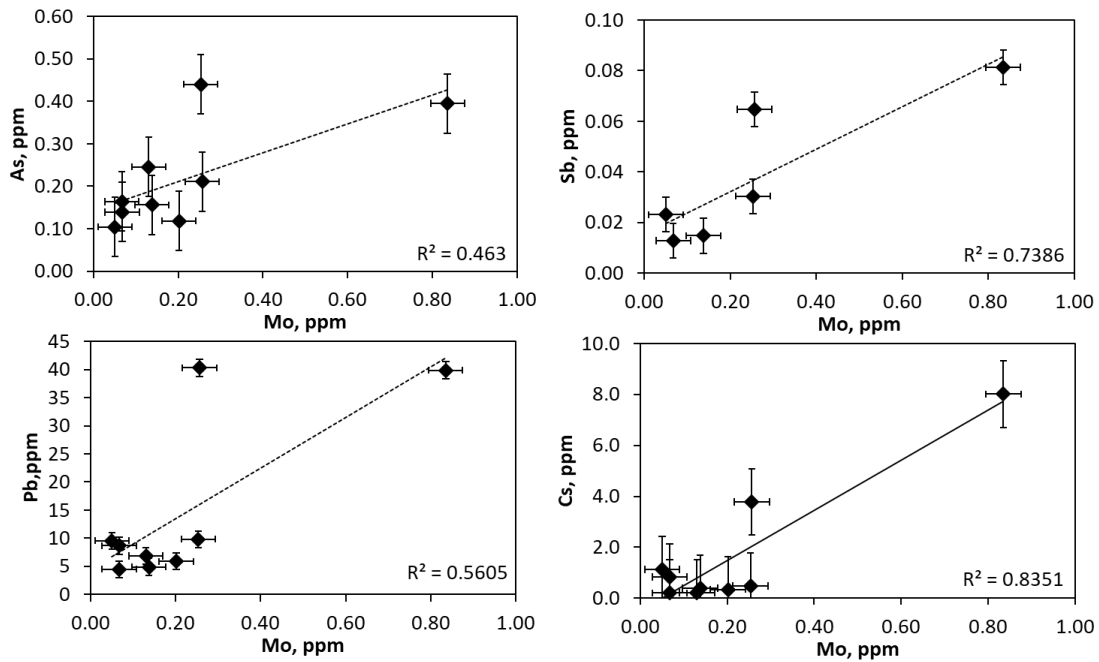
Figure B4. Weak Mo correlations with fluid-mobile elements in the Zimbabwe pluton.

Supplementary tables can be found online at: https://doi.org/10.1016/j.gca.2018.06.039

Appendix C.

Completing the Completing the Molybdenum Isotope Mass Balance in Subduction

Zones - Supplementary Data

Sulfide Photomicrographs
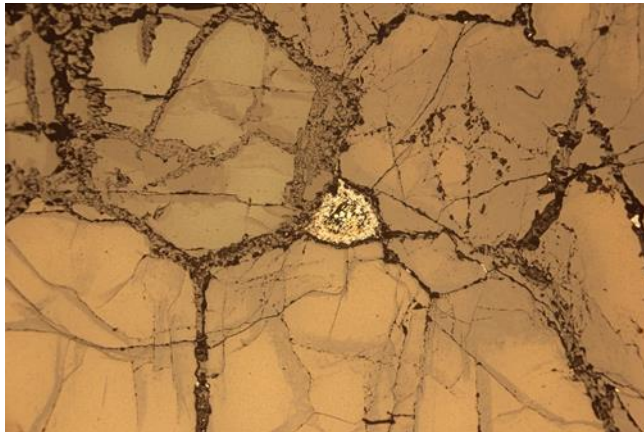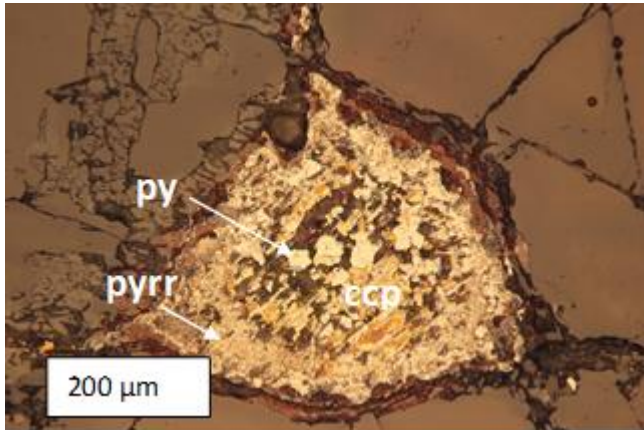
Sample 91-2, Sulfide 01. Fe-hydroxides coat the rim of the sulfide, much of the core has

been significantly altered, and pyrite overgrowths are found throughout the sulfide.

Pyrrhotite can found along the outer edge. The bright orange color is rust on the surface.
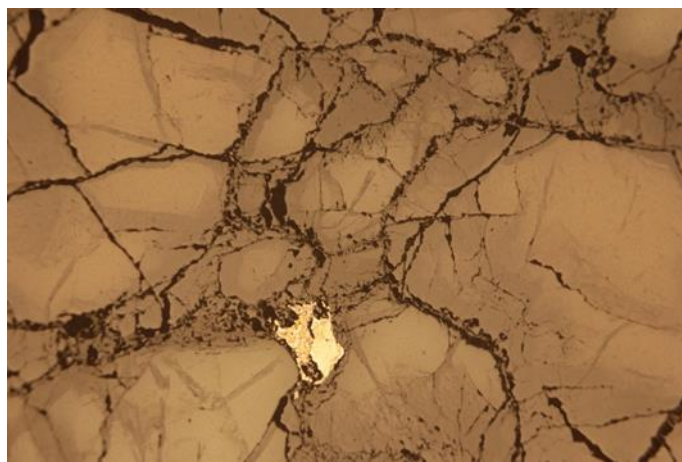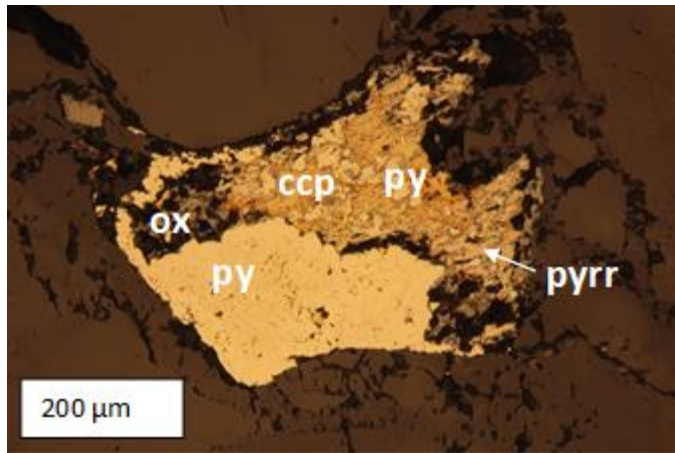
Sample 91-6, Sulfide 03. Pyrite has completely replaced/adhered to one half of the sulfide, while cubic pyrite crystals can be found throughout the other side which is primary composed of chalcopyrite. Some pyrrhotite can be found near the outer edges, along with Fe-hydroxides that coat the rim.
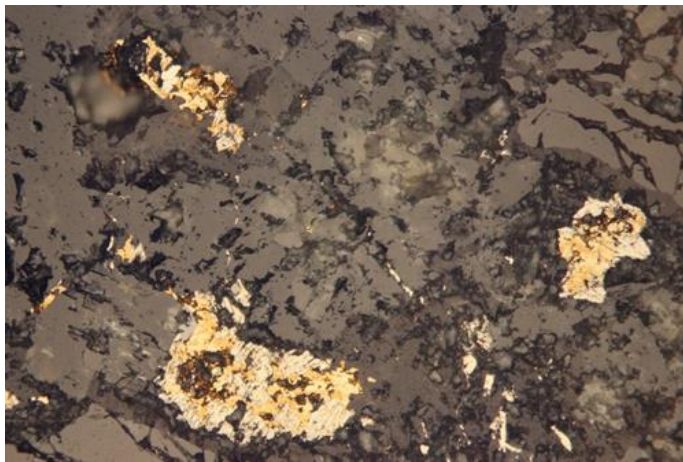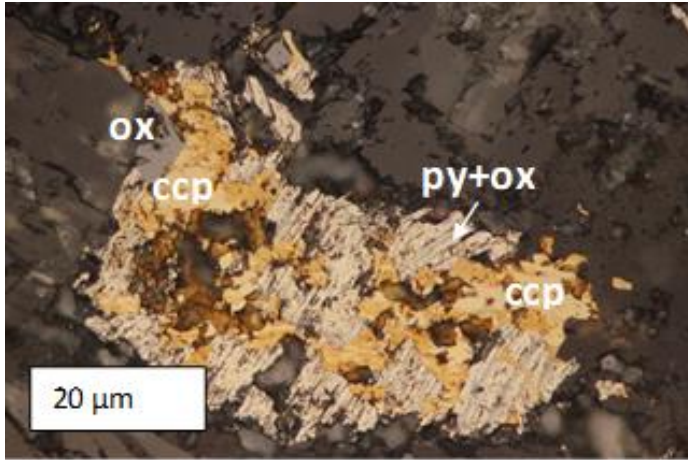
Sample 91-22, Sulfide 02. Chalcopyrite interspersed between fractured pyrite with oxide

exsolution. The bright orange color is rust on the surface.
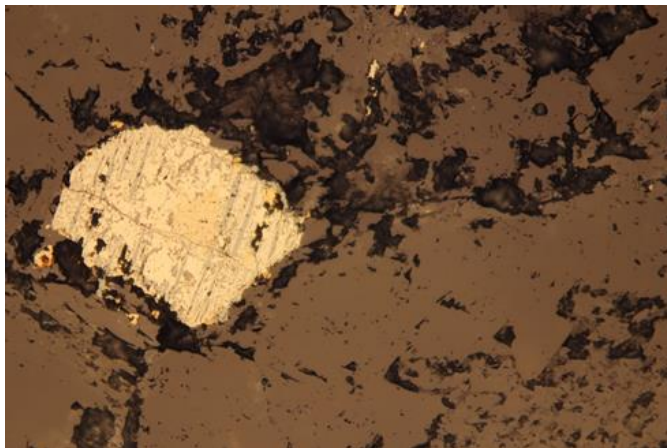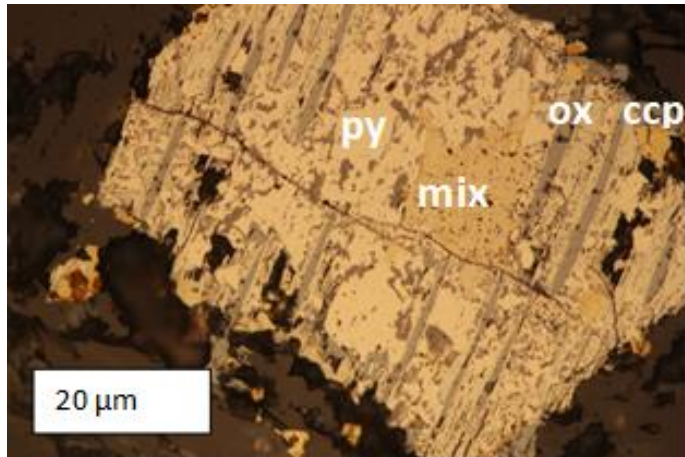
Sample 91-37, Sulfide 17. Mostly pyrite with Fe-oxide exsolution. The region in the center of the sulfide is a heterogenous mix (very fine exsolution) of chalcopyrite and some Fe-sulfide like pyrrhotite or pyrite.

BHVO-2g	V 51	Ga 71	Ge 74	Nb 93	Mo 95	Mo 97	Mo 98	Cd 111	In 115
measured	277	30	2.22	18.0	3.95	3.95	3.97	0.10	0.11
2s	47.7	5.21	0.37	1.01	0.26	0.26	0.19	0.03	0.02
accepted	308	22	1.6	18.3	3.8	3.8	3.8	0.1	0.1
BHVO-2g	Sb 121	La 139	Ce 140	Pr 141	Nd 146	W 184	Tl 205	Pb 208	Bi 209
measured	0.28	15.3	38.5	5.18	22.7	0.23	0.02	1.88	0.03
2s	0.15	4.05	8.15	1.07	0.74	0.03	0.01	0.48	0.02
accepted	0.3	15.2	37.6	5.35	24.5	0.23	0.02	1.7	0.015

Table C1. Secondary standard for LA-ICP-MS. These data represent the mean of 38 replicates of BHVO-2g analyzed multiple times over the course of a year alongside the eclogite analyses.

Rutile		V	Ga	Ge	Nb	Mo	Cd	In	Sb	La	Ce	Pr	Nd	W	Tl	Pb	Bi
91-13	mean	1891	1.31	bdl	1006	17.6	0.12	0.08	0.25	bdl	bdl	bdl	0.03	9.93	bdl	0.09	bdl
	2s	46.4	1.04		537	2.83	0.03	0.01	0.35				0.01	7.32		0.28	
86-6	mean	2213	1.69	bdl	48.8	7.24	0.17	0.19	bdl	bdl	0.01	bdl	0.03	0.2	bdl	0.01	bdl
	2s	123	0.6		2.27	2.71	0.06	0.06			0.02		0.02	0.17		0.02	
91-20	mean	2040	2.8	bdl	4016	12.9	0.24	0.13	0.83	bdl	0.01	bdl	0.03	19	bdl	0.03	bdl
	2s	167	1.72		5514	7.22	0.09	0.02	0.28		0.01		0.01	22.6		0.11	
80-B1	mean	1380	8.68	0.43	104	1.67	0.07	0.12	0.13	0.04	0.08	0.01	0.05	1.5	bdl	0.05	bdl
	2s	72.3	0.79	0.24	8.79	0.23	0.13	0.04	0.05	0.07	0.16	0.03	0.07	0.13		0.09	
81-3	mean	2073	3.27	0.38	1807	16.7	0.13	0.08	1.3	0.02	0.03	bdl	0.04	18.6	bdl	0.01	bdl
	2s	159	2.32	0.12	174	1.55	0.04	0.01	0.16	0.09	0.15		0.07	21.9		0.01	
91-58	mean	1369	10.8	0.25	1953	2.34	0.06	0.15	0.03	0.02	0.04	bdl	0.03	0.42	bdl	0.05	bdl
	2s	23.1	0.64	0.22	46	0.14	0.02	0.01	0.02	0.08	0.16		0.06	0.02		0.17	
86-12	mean	739	1.32	1.55	37.3	4.42	0.14	0.16	0.03	bdl	bdl	bdl	0.03	16.8	bdl	0.01	bdl
	2s	494	1.1	0.99	3.52	0.28	0.04	0.03	0.03				0.01	0.57		0.01	
81-8	mean	1616	1.88	1.17	406	34.1	0.04	0.07	0.29	bdl	bdl	bdl	0.02	20.9	bdl	0.01	0.01
	2s	147	0.9	0.46	128	2.67	0.02	0	0.21				0.02	16.3		0.01	0.04
91-4	mean	2503	5.08	0.66	149	5.22	0.08	0.08	0.23	0.03	0.04	bdl	0.04	1.29	bdl	0.02	bdl
	2s	137	3.16	1.01	33.4	0.24	0.02	0.01	0.14	0.11	0.14		0.05	1.42		0.01	
80-A2	mean	2522	3.04	2.39	2438	6.25	0.09	0.17	0.16	0.83	0.82	0.07	0.26	6.69	bdl	0.03	bdl
	2s	135	1.92	0.33	177	0.52	0.03	0.01	0.1	2.75	2.54	0.21	0.75	5.08		0.05	
80-18	mean	1836	1.73	1.53	341	12	0.08	0.13	0.45	0.34	0.41	0.04	0.14	5.49	bdl	0.05	bdl
	2s	50.8	1.04	1.72	645	1.28	0.02	0.01	0.53	1.54	1.83	0.16	0.44	10.7		0.16	
86-56	mean	1988	1.37	1.17	104	5.26	0.05	0.2	bdl	0.01	0.02	0	0.04	3.48	0	0.01	bdl
	2s	159	1.16	1.24	2.19	0.13	0.03	0.02		0.03	0.05	0.01	0.01	0.2	0	0.01	

Table C2. Trace element abundances in rutile. The mean represents multiple LAICPMS spot analyses on the mineral.

Garnet		V	Ga	Ge	Nb	Mo*	Cd	In	Sb	La	Ce	Pr	Nd	W	Tl	Pb	Bi
91-13	**mean**	**125**	**8.74**	**0.98**	**0.04**	**bdl**	**0.13**	**0.05**	**bdl**	**0.048**	**0.15**	**0.04**	**0.53**	**0.002**	**bdl**	**0.03**	**bdl**
	2s	4.07	0.62	0.12	0.16		0.02	0.01		0.178	0.35	0.03	0.15	0.003		0.01	
86-6	**mean**	**191**	**12.1**	**1.23**	**bdl**	**bdl**	**0.21**	**0.08**	**bdl**	**0.002**	**0.09**	**0.08**	**1.47**	**0.001**	**bdl**	**0**	**bdl**
	2s	7.72	1.4	0.26			0.05	0.01		0.001	0.02	0.01	0	0.001		0.01	
91-20	**mean**	**173**	**11.4**	**0.12**	**bdl**	**bdl**	**0.21**	**0.08**	**bdl**	**0.006**	**0.12**	**0.07**	**1.1**	**0.001**	**bdl**	**0.02**	**bdl**
	2s	15.1	0.56	0.25			0.04	0.01		0.003	0.03	0.01	0.07	0.001		0.02	
80-B1	**mean**	**129**	**11.8**	**1.14**	**bdl**	**bdl**	**0.11**	**0.06**	**bdl**	**0.001**	**0.02**	**0.01**	**0.26**	**0.002**	**bdl**	**0.01**	**bdl**
	2s	23.7	0.93	1.42			0.03	0.01		0.001	0.01	0	0.04	0.002		0.01	
81-3	**mean**	**193**	**11.5**	**2.14**	**bdl**	**bdl**	**0.13**	**0.07**	**0.01**	**0.043**	**0.69**	**0.29**	**3.17**	**0**	**bdl**	**0**	**0.004**
	2s	13.2	0.78	0.3			0.02	0.01	0.03	0.014	0.04	0.02	0.13	0.001		0	0.004
91-58	**mean**	**205**	**14.7**	**2.25**	**bdl**	**bdl**	**0.27**	**0.11**	**0.02**	**0.039**	**0.39**	**0.15**	**1.97**	**0.002**	**bdl**	**0.02**	**0.002**
	2s	9.88	0.44	0.14			0.05	0.01	0.02	0.015	0.11	0.03	0.13	0.001		0.01	0.004
86-12	**mean**	**166**	**9.8**	**2.1**	**bdl**	**bdl**	**0.19**	**0.09**	**0.03**	**0.014**	**0.32**	**0.15**	**1.92**	**0.001**	**bdl**	**0**	**0.003**
	2s	15.4	0.08	0.2			0.04	0	0.02	0.005	0.02	0.03	0.23	0.002		0	0.004
81-8	**mean**	**202**	**11.9**	**2.68**	**bdl**	**bdl**	**0.13**	**0.08**	**0.03**	**0.004**	**0.13**	**0.11**	**1.75**	**0.001**	**bdl**	**0.01**	**0.004**
	2s	4.58	0.87	0.3			0.05	0	0.06	0.002	0.02	0.01	0.11	0.001		0	0.004
91-4	**mean**	**193**	**13.6**	**2.97**	**bdl**	**bdl**	**0.18**	**0.08**	**0.06**	**0.005**	**0.12**	**0.07**	**1.06**	**0.002**	**bdl**	**0**	**0.004**
	2s	12.7	0.3	1.15			0.02	0.01	0.1	0.004	0.01	0.01	0.09	0.004		0.01	0.014
80-A2	**mean**	**222**	**15.1**	**3.1**	**bdl**	**bdl**	**0.21**	**0.1**	**bdl**	**0.006**	**0.17**	**0.12**	**1.54**	**0.002**	**bdl**	**0**	**bdl**
	2s	16.1	1.22	0.05			0.09	0.01		0.003	0.02	0.01	0.15	0.003		0.01	
80-18	**mean**	**216**	**14.3**	**3.32**	**bdl**	**bdl**	**0.24**	**0.08**	**0.03**	**0.007**	**0.21**	**0.14**	**1.83**	**0.001**	**bdl**	**0.01**	**bdl**
	2s	11.1	0.9	0.41			0.05	0.01		0.003	0.03	0.01	0.12	0.003		0.01	
86-56	**mean**	**142**	**14**	**3.06**	**bdl**	**bdl**	**0.08**	**0.07**	**0.02**	**0.008**	**0.09**	**0.09**	**1.46**	**0.005**	**bdl**	**bdl**	**0.002**
	2s	1.34	0.73	1.13			0.02	0.01	0.04	0.021	0.01	0.01	0.08	0.016			0.009

*Reported [98]Mo because [95]Mo has interference of [55]Mn

Table C3. Trace element abundances in garnet. The mean represents multiple LAICPMS spot analyses on the mineral.

Omphacite		V	Ga	Ge	Nb	Mo	Cd	In	Sb	La	Ce	Pr	Nd	W	Tl	Pb	Bi
91-13	**mean**	**404**	**15.8**	**bdl**	**0.63**	**0.01**	**0.08**	**0.08**	**bdl**	**2.99**	**8.69**	**1.22**	**5.97**	**0.01**	**bdl**	**0.85**	**bdl**
	2σ	12	2.28		0.63	0	0.01	0.01		0.73	1.74	0.23	1.04	0.04		0.25	
86-6	**mean**	**382**	**17.2**	**0.38**	**0.07**	**0.01**	**0.08**	**0.08**	**bdl**	**0.99**	**3.46**	**0.7**	**4.52**	**0.01**	**bdl**	**0.14**	**bdl**
	2σ	28	6.31	0.33	0.25	0.01	0.03	0.01		2.57	5.04	0.51	1.74	0.06		0.27	
91-20	**mean**	**410**	**14.4**	**bdl**	**0.01**	**0.01**	**0.12**	**0.09**	**bdl**	**2.28**	**9.31**	**1.55**	**7.97**	**0**	**bdl**	**0.44**	**bdl**
	2σ	7.92	0.51		0.02	0	0.03	0.01		0.25	0.66	0.14	0.73	0.01		0.06	
80-B1	**mean**	**346**	**12.8**	**1.24**	**0.2**	**0.29**	**0.45**	**0.16**	**0.32**	**5.29**	**16.2**	**2.57**	**12.5**	**0.13**	**0.02**	**0.86**	**0.112**
altered	2σ	5.46	1.32	0.03	0.57	0.95	0.84	0.17	0.71	3.19	7.13	1.15	2.29	0.3	0.05	1.02	0.354
81-3	**mean**	**391**	**20.7**	**0.88**	**0.01**	**bdl**	**0.04**	**0.05**	**0.04**	**2**	**7.94**	**1.25**	**5.71**	**bdl**	**bdl**	**0.27**	**0.007**
	2σ	4.57	0.41	0.23	0		0.01	0.01	0.04	0.2	0.6	0.09	0.4			0.02	0.002
91-58	**mean**	**501**	**22.5**	**1.03**	**0.07**	**0.01**	**0.09**	**0.12**	**0.01**	**0.65**	**2.28**	**0.38**	**2.18**	**bdl**	**bdl**	**0.31**	**bdl**
	2σ	3.82	0.3	0.26	0.1	0.01	0.03	0.01	0.03	0.15	0.36	0.04	0.26			0.09	
86-12	**mean**	**410**	**18.3**	**0.95**	**0**	**bdl**	**0.1**	**0.08**	**0.01**	**0.97**	**4.71**	**0.94**	**5.34**	**bdl**	**bdl**	**0.53**	**0.006**
	2σ	5.51	0.22	0.24	0		0.05	0.01	0	0.18	0.44	0.05	0.12			0.05	0.005
81-8	**mean**	**474**	**19.1**	**0.97**	**0.01**	**0.01**	**0.05**	**0.06**	**bdl**	**1.26**	**5.15**	**0.84**	**4.17**	**bdl**	**bdl**	**0.44**	**bdl**
	2σ	118	3.08	0.26	0.02	0.01	0.02	0.01		0.44	1.87	0.27	1.41			0.06	
91-4	**mean**	**468**	**20.6**	**1.6**	**bdl**	**bdl**	**0.1**	**0.09**	**0.04**	**1.27**	**5.57**	**1.14**	**5.78**	**bdl**	**bdl**	**0.23**	**bdl**
	2σ	4.07	0.14	0.56			0.02	0	0.06	0.06	0.08	0.01	0.19			0.08	
80-A2	**mean**	**493**	**21.6**	**1.79**	**bdl**	**bdl**	**0.08**	**0.09**	**0.02**	**0.67**	**3.39**	**0.78**	**4.02**	**bdl**	**bdl**	**0.19**	**bdl**
	2σ	2.95	0.12	0.5			0.01	0.01	0.05	0.02	0.17	0.01	0.19			0.01	
80-18	**mean**	**402**	**18.2**	**1.66**	**bdl**	**bdl**	**0.08**	**0.09**	**0.02**	**1.39**	**5.79**	**1**	**4.39**	**bdl**	**bdl**	**0.29**	**bdl**
	2σ	1.04	0.2	0.69			0.03	0.01	0.08	0.1	0.55	0.1	0.13			0	
86-56	**mean**	**368**	**22.2**	**1.21**	**bdl**	**bdl**	**0.04**	**0.06**	**bdl**	**0.33**	**2.59**	**0.82**	**5.11**	**bdl**	**bdl**	**0.28**	**0.005**
	2σ	10.4	0.61	0.21			0.01	0		0.02	0.11	0.01	0.16			0.05	0.005

Table C4. Trace element abundances in omphacite. The mean represents multiple LAICPMS spot analyses on the mineral.

Appendix D.

Molybdenum isotope fractionation in glacial diamictites tracks the onset of oxidative weathering of the continental crust – Supplementary Materials
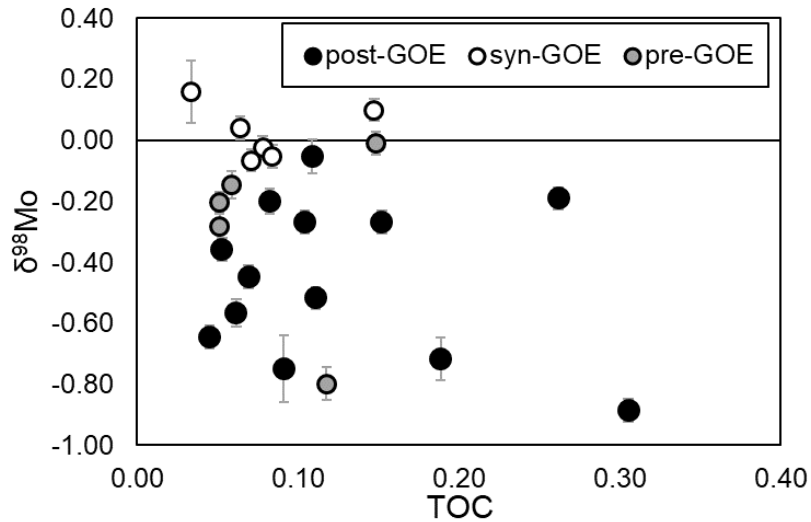
Figure D1. No correlation is observed between δ^{98}Mo and TOC.
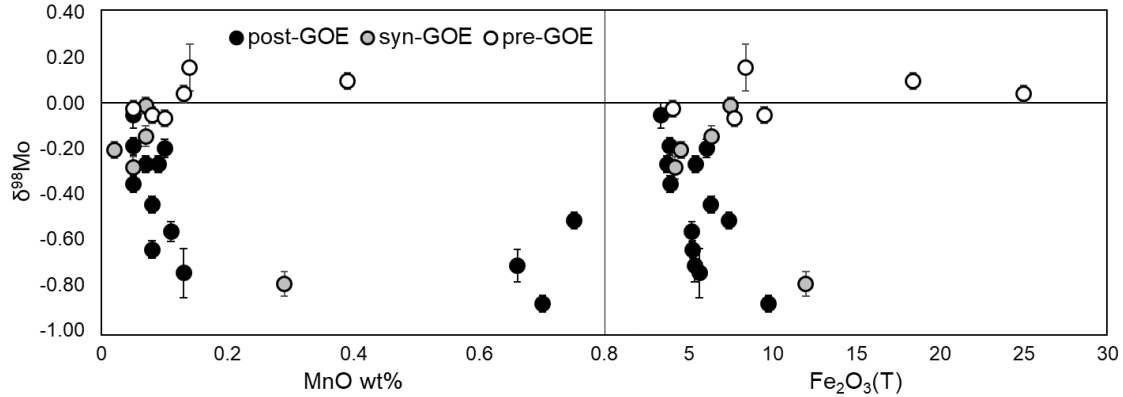
Figure D2. Weak correlation is observed between δ^{98}Mo and Fe and Mn.
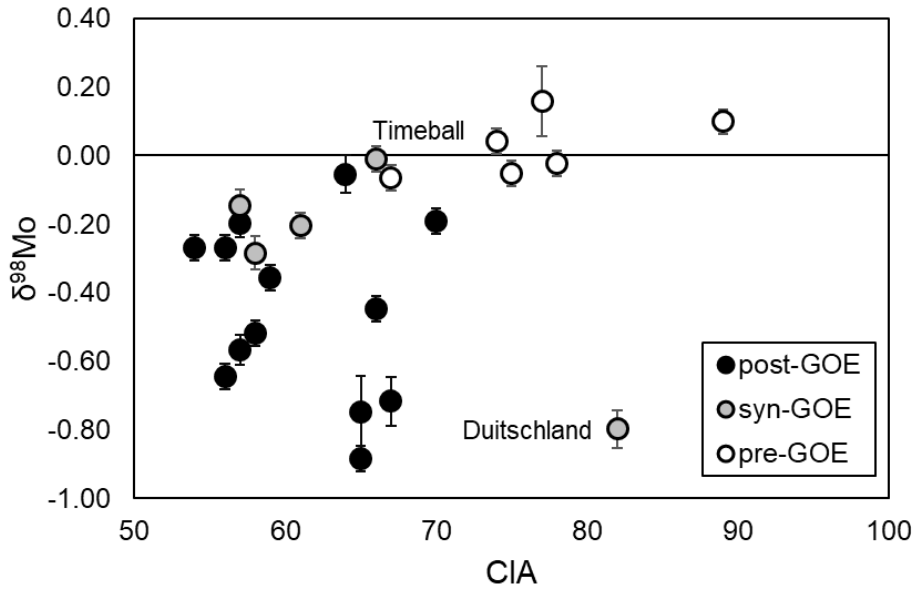
Figure D3. Relationship between d98Mo and chemical index of alteration (CIA).
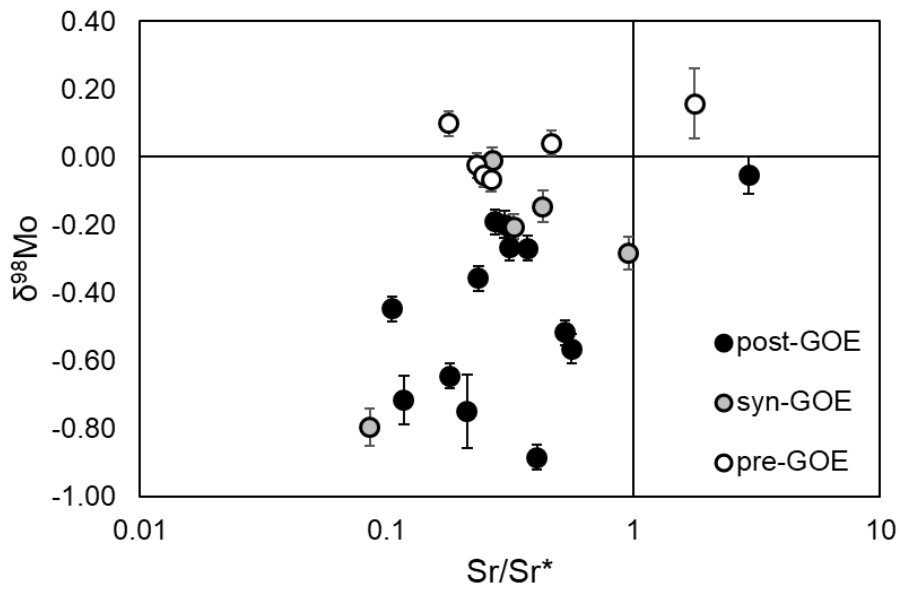
Figure D4. Weak corelation bewteen δ^{98}Mo and Sr/Sr*, implying that samples that are more strongly weathered retain lighter Mo isotopes.
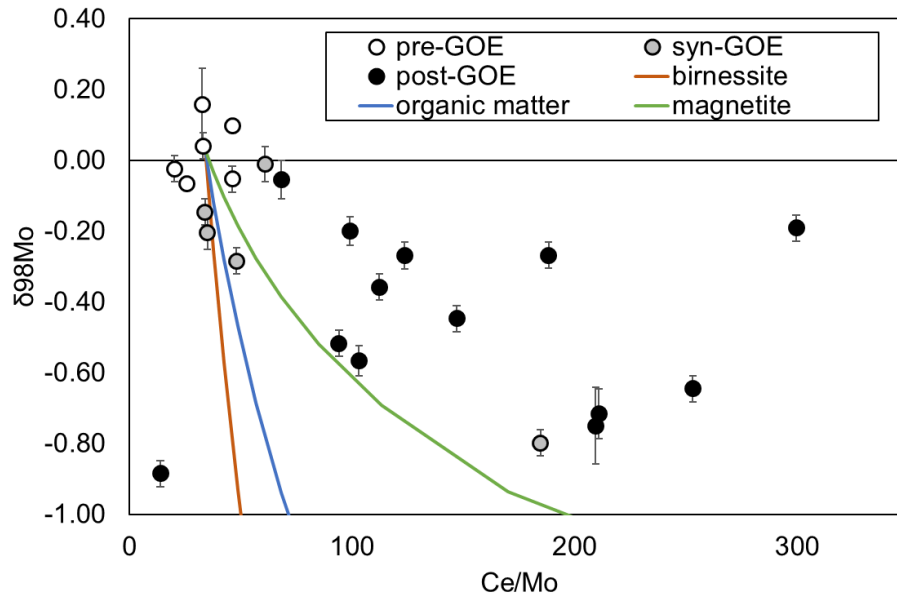
Figure D5. Results of Rayleigh fractionation modeling without adding in the mixing calculation with unfractionated bedrock. The model predicts stronger fractionation than observed in the diamictite, hence the need to mix various proportions of un-weathered to weathered bedrock.
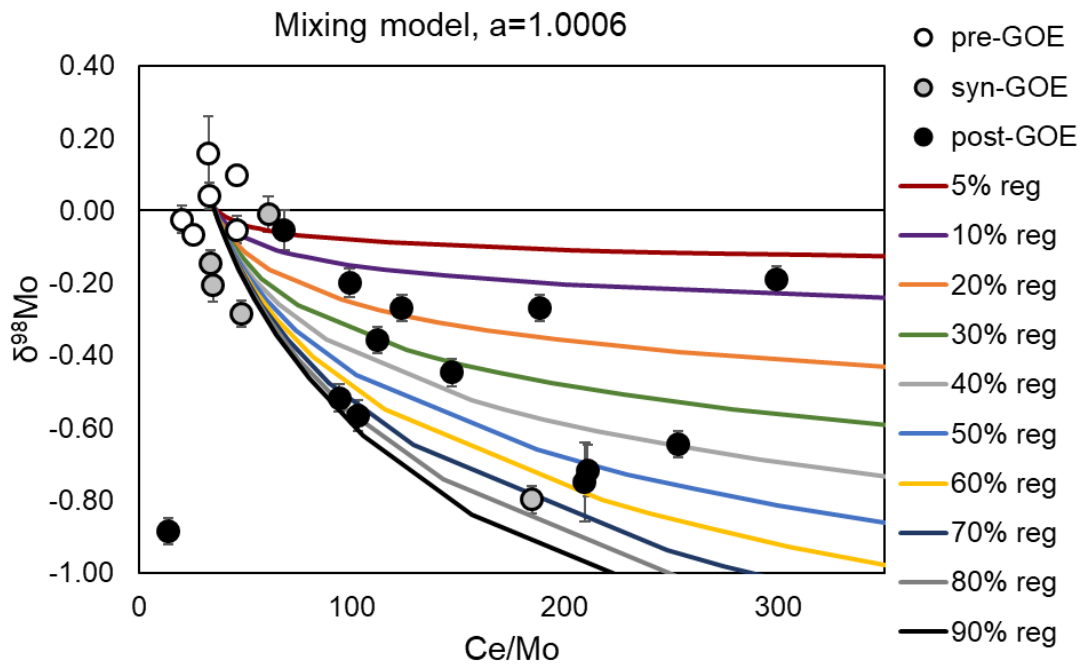
Figure D6. Results of Rayleigh fractionation and mixing models (colored lines) using a fractionation factor of a=1.0006 (magnetite). The proportion of regolith to bedrock that composes the diamictite is noted as X% reg (e.g., 10% reg = 10% regolith, 90% bedrock).
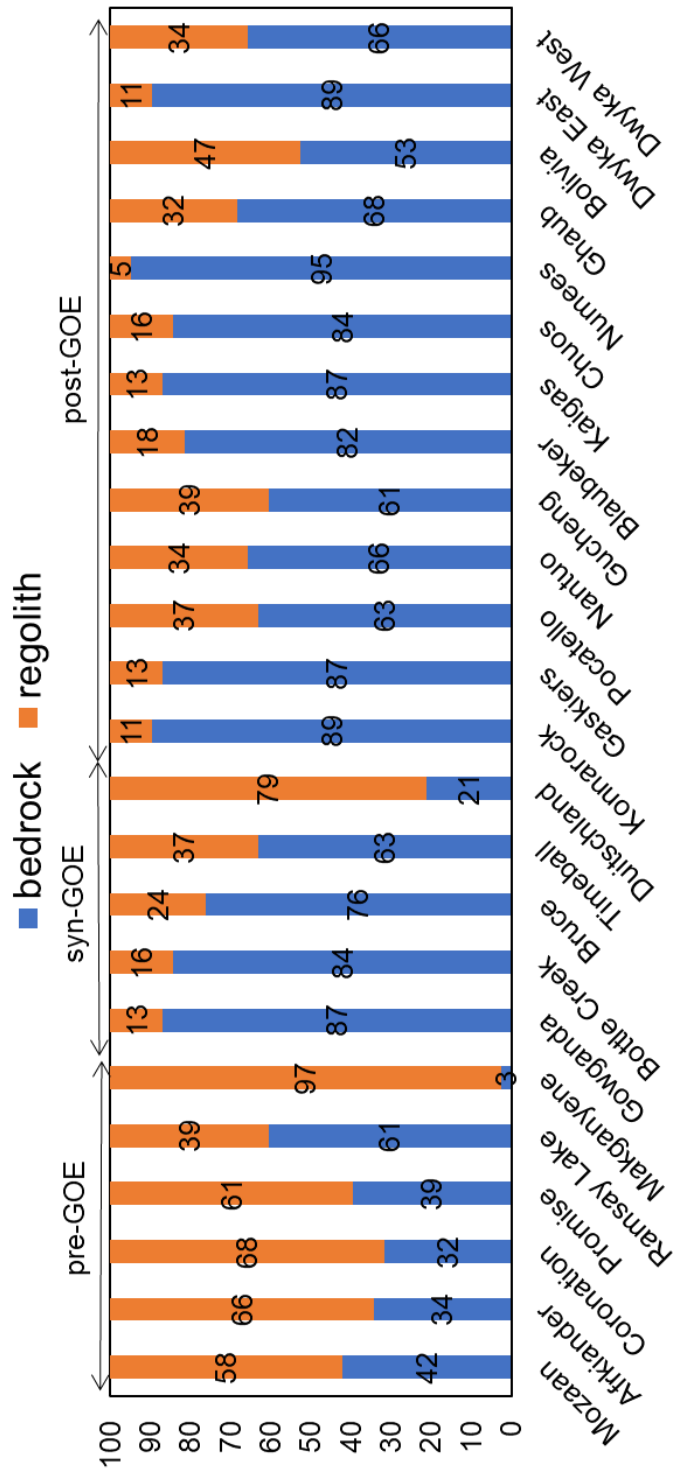
Figure D7. Proportion of un-weathered bedrock to weathered regolith calculated for each diamictite according to the CIA mixing equations in the primary text, assuming a CIA of 90 for the regolith and 52 for un-weathered bedrock.

Appendix E.

Assessing molybdenum isotope fractionation during continental weathering as recorded by saprolites and bauxites - Supplementary Information

Methods

Molybdenum isotope data were collected at the W.M. Keck Laboratory for Environmental Biogeochemistry at Arizona State University. Sample aliquots containing 75 to 100 ng of Mo were ashed at 550°C in a furnace overnight to remove organics. Powders were transferred to Savillex beakers and dissolved on a hotplate using a mixture of concentrated HNO_3, HF, and HCl. Immediately prior to hotplate dissolution, a ^{97}Mo-^{100}Mo double spike was added to the powders to produce a 2:1 ratio between the double-spike and sample-derived Mo. After hot plate dissolution, the solutions were evaporated to near-dryness and re-fluxed with concentrated HCl to produce a clear solution free of precipitates. Finally, the samples were dried down and brought up in 1mL of 6M HCl for column chemistry.

Mo was purified from the sample matrix using a combination of anion and cation exchange chromatography following (Romaniello et al., 2016). For anion chemistry, 2 mL of cleaned Biorad AG1X-8 anion exchange resin was loaded into the columns and rinsed with 10 mL of 1 M HCl. Twenty mL of 6 M HCl was then run through the columns for equilibration before the samples (in 6M HCl) were loaded. Sample elution was achieved using repeated volumes of 1M HCl from 0.5 mL up to 10 mL. Several samples that contained high Zr were brought through anion columns a second time. The elution was dried down and brought in 6M HCl and samples were brought up in 0.5 M HCl. Biorad AG50WX-8 cation exchange resin was used for cation column chemistry. Two mLs of resin

were loaded into the column then cleaned and equilibrated overnight in 10 mL of 0.5 M HCl. Afterwards, 10 mL of 0.5 M HCl + 0.01% H_2O_2 were added to the columns in order to keep Mo oxidized. The samples hosted in 0.5 M HCl were added to the columns and Mo was eluted with repeated volumes of 0.5 M HCl + 0.01% H_2O_2 from 0.5 mL up to 10 mL. The final elution was dried down and brought up in 1 mL of concentrated HNO_3 + 200 µL of H_2O_2 twice to dissolve any remaining organic compounds. Finally, the samples were dried down and brought up in 3 mL of 2% HNO_3.

The isotopes ^{91}Zr, ^{92}Mo, ^{95}Mo, ^{96}Mo, ^{97}Mo, ^{98}Mo, ^{99}Ru, and ^{100}Mo were measured on the Thermo-Neptune Multi-collector ICP-MS on three samples aliquots of ~25 ng Mo. Ruthenium-99 was monitored to check for high organic content that could interfere with Mo measurements. A double spike inversion was performed using an in-house MATLAB script at ASU which uses non-linear optimization to simultaneously solve for the spike-sample ratio, instrument mass bias, and isotopic fractionation of the samples. Mo isotope data are reported as: $\delta^{98}Mo = 1000*[(^{98}Mo/^{95}Mo_{sample})/(^{98}Mo/^{95}Mo_{standard})-1]$ relative to the isotopic composition of NIST 3134 Mo standard. The USGS shale SDO-1 was analyzed as a secondary standard and yielded a value of 0.79‰ (±0.03 2σ), in excellent agreement with published values (Goldberg et al., 2013). Additionally, the RGM-1, a rhyolite, was run as a secondary standard and produced a value of +0.03‰ (±0.04 2σ). Internal run precision and long-term precision are both ~ 0.04‰ (2σ).
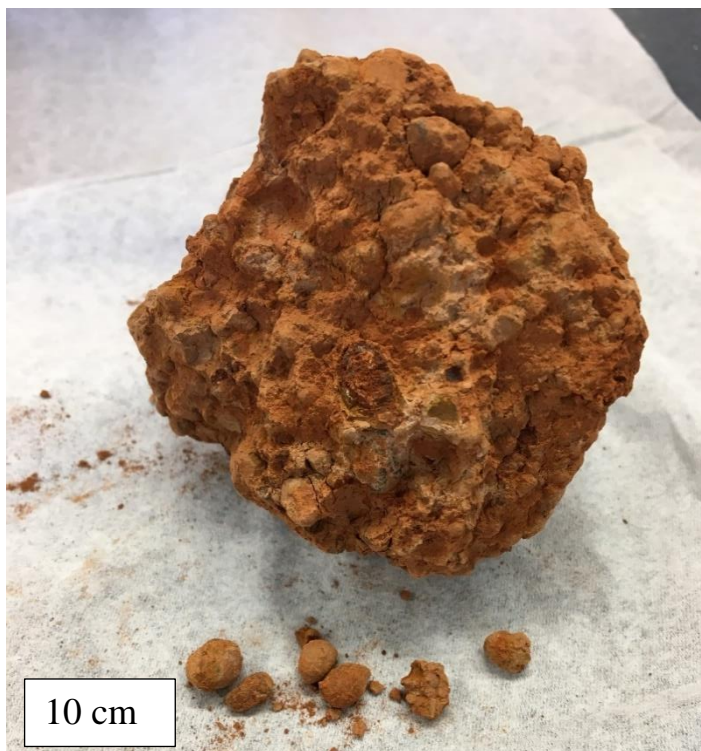
Figure E1. Photo of Fe-pisolite layer that corresponds to sample 5110.
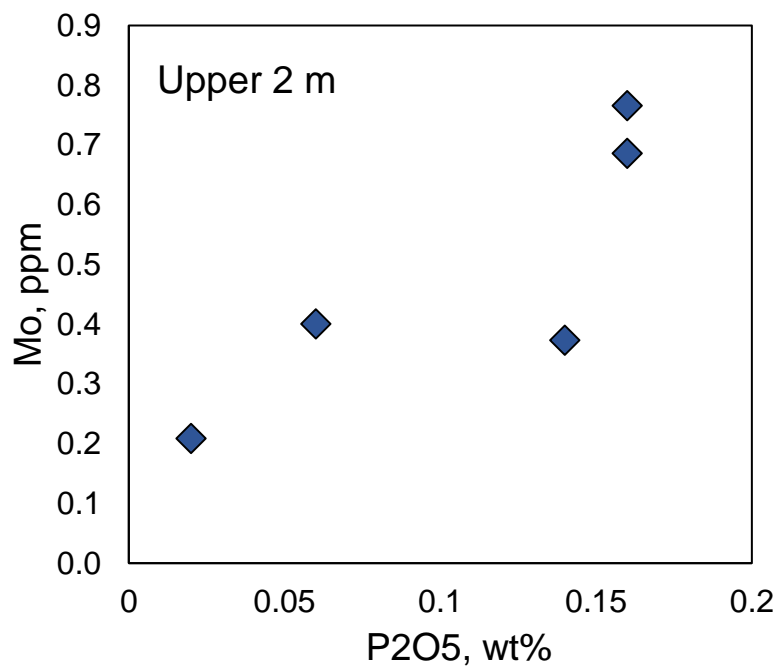
Figure E2. Correlation between Mo and P_2O_5 in the upper 2m of the saprolite profile.

Appendix F.

The distribution of V, Ga, Ge, Mo, Cd, In, Sn, Sb, W, Tl, and Bi in the lithospheric

mantle - Supplementary Information

	Ga	Ge	Mo	Cd	In	Sn	Sb	W	Tl	Bi
BHVO-1	20.3	1.68	1.07	0.12	0.08	1.99	0.21	0.23	0.041	0.015
2σ	1.24	0.14	0.07	0.02	0.01	0.13	0.01	0.03	0.002	0.001
BHVO-1	21.5	1.01	1.02	0.11	0.08	1.87	0.09	0.22	0.044	0.010
2σ	1.86	2.35	0.34	0.01	0.10	0.18	1.35	0.03	0.002	0.022
BHVO reported	21.3	1.57	1.06	0.11	0.09	2.09	0.16	0.21	0.046	0.012
AGV-2	19.7	0.78	1.97	0.14	0.05	1.93	0.71	0.49	0.292	0.054
2σ	0.51	0.12	0.16	0.02	0.02	0.06	0.16	0.02	0.032	0.004
AGV reported	20.4	1.20	2.00	0.18	0.05	1.83	0.46	0.55	0.275	0.052

Table F1. Secondary standards analyzed by SA-ICP-MS

	V	Ga	Ge	Mo	Cd	In	Sn	Sb	W	Tl	Bi
BHVO-2g basaltic glass											
measured	308	26.7	1.74	3.88	0.10	0.10	1.64	0.18	0.22	0.02	0.02
2σ	20.8	13.3	0.80	0.43	0.10	0.03	0.45	0.29	0.04	0.01	0.02
reported	308	22	1.6	3.8	0.1	0.1	2.6	0.3	0.23		0.01
JB-NiS4 synthetic Ni-sulfide											
measured				5.88			330				1898
2σ				2.21			173				372
reported				10.1			416				1998
JB-sulf synthetic Fe-Ni sulfide											
measured				2.66							
2σ				1.15							
reported				2.55							
Ge-7 synthetic sulfur-germanium glass											
measured		4.67		2.91			143		4.33		14.2
2σ		0.91		0.78			39.9		1.32		2.81
reported		7.96		2.58			122		7.26		16.4

Table F2. Secondary standards analyzed by LA-ICP-MS

	SiO$_2$	Al$_2$O$_3$	MnO	Na$_2$O	MgO	FeO	CaO	TiO$_2$	Cr$_2$O$_3$	NiO	total
POR-1											
olivine	39.56	0.00	0.14	BDL	48.94	9.66	0.02	0.00	BDL	0.35	98.65
2σ	0.67	0.02	0.03		0.28	0.20	0.02	0.02		0.03	
opx	52.54	6.13	0.13	0.06	31.45	5.92	0.56	0.17	0.44	0.08	97.49
2σ	4.45	3.93	0.09	0.00	4.18	0.93	0.60	0.12	0.15	0.03	
cpx	50.86	7.28	0.08	1.73	14.02	2.17	21.51	0.56	0.92	0.03	99.17
2σ	0.50	0.10	0.03	0.00	0.15	0.02	0.28	0.07	0.01	0.06	
spinel	0.04	57.22	0.12	BDL	18.97	13.32	BDL	0.04	9.70	0.37	99.75
2σ	0.05	3.15	0.02		0.33	0.41		0.06	0.44	0.04	
POR-2											
olivine	39.39	BDL	0.14	0.00	48.96	9.57	0.01	BDL	BDL	0.38	98.45
2σ	1.65		0.03	0.02	0.59	0.26	0.01			0.07	
opx	54.17	4.15	0.16	0.04	33.22	6.40	0.35	0.10	0.29	0.08	98.96
2σ	0.26	0.17	0.01	0.02	0.70	0.26	0.12	0.04	0.00	0.00	
cpx	51.43	6.80	0.07	1.73	14.42	2.30	21.51	0.62	0.79	0.02	99.72
2σ	0.94	1.04	0.04	0.28	0.76	0.14	0.14	0.03	0.21	0.06	
spinel	0.03	59.64	0.10	BDL	19.00	13.08	BDL	0.02	8.66	0.39	100.9
2σ	0.02	0.71	0.02		0.22	1.04		0.01	0.28	0.03	
71-336											
olivine	39.46	0.00	0.14	BDL	49.01	9.54	0.01	BDL	BDL	0.39	98.55
2σ	0.66	0.01	0.04		0.32	0.23	0.01			0.04	
opx	53.69	4.43	0.15	0.05	33.10	6.25	0.35	0.10	0.29	0.09	98.51
2σ	0.64	1.30	0.01	0.02	0.53	0.20	0.05	0.02	0.11	0.03	
cpx	50.61	6.99	0.08	2.05	14.31	2.23	20.79	0.61	0.71	0.03	98.41
2σ	0.75	0.40	0.03	0.10	0.21	0.14	0.36	0.04	0.06	0.03	
spinel	0.03	60.82	0.11	BDL	19.62	11.71	BDL	0.01	8.11	0.41	100.8
2σ	0.02	0.67	0.06		0.12	0.60		0.01	0.22	0.05	
POR-3											
olivine	39.39	BDL	0.14	BDL	48.87	9.84	0.01	BDL	BDL	0.37	98.62
2σ	0.32		0.03		0.45	0.33	0.03			0.03	
opx	53.93	4.35	0.16	0.05	33.13	6.55	0.37	0.09	0.33	0.07	99.04
2σ	0.34	0.74	0.01	0.01	0.52	0.13	0.10	0.03	0.09	0.03	
cpx	51.12	6.22	0.09	1.59	14.79	2.34	21.68	0.44	0.67	0.03	98.98
2σ	0.45	0.16	0.03	0.05	0.57	0.20	0.68	0.02	0.07	0.03	
spinel	0.02	58.28	0.10	BDL	18.78	13.11	0.01	0.03	10.02	0.37	100.7
2σ	0.04	0.48	0.03		0.15	0.53	0.03	0.03	0.61	0.07	

Table F3. Major element data for silicate and spinel phases in the Pyrenees Massif peridotites. Similar data for phases in the Hannuoba basalts can be found in Rudnick et al. (2004).

Table 4	Sulf	Morph	Co	V	Mn	Ga	Ge	Mo	Cd	In	Sn	Sb	W	Tl	Pb	Bi
Pyrenees Massif Sulfides																
POR2_S03	pent	Type i	2027	154	5300	5.50	BDL	1.90	0.70	0.14	3.80	8.90	0.04	0.67	84	0.53
POR2_SO2	pent	Type i	11950	2.30	127	BDL	BDL	BDL	0.85	0.03	4.60	4.78	BDL	65.3	315	7.00
POR3_S04	pent	Type i	4630	43.1	183	0.33	5.30	BDL	6.84	0.02	1.28	2.10	0.01	1.98	332	3.97
POR3_S09	pent	Type i	4180	48.0	680	1.00	7.70	0.08	2.71	0.01	0.93	3.58	0.04	1.15	137	4.67
POR3_S12	pent	Type i	5760	0.20	27.0	BDL	1.60	BDL	2.46	BDL	1.29	1.37	0.00	0.99	115	4.25
POR3_S13	pent	Type i	4250	17.0	346	0.36	1.50	BDL	6.11	BDL	0.48	1.26	0.01	0.45	385	1.13
POR3_S14	pent	Type i	3511	0.38	28.6	0.02	1.40	BDL	1.70	BDL	0.39	2.04	0.01	8.74	104	0.78
POR3_S15	pent	Type i	2440	0.14	40.5	0.09	1.20	BDL	0.08	BDL	0.16	0.33	BDL	0.21	2.5	BDL
POR3_S11b	pent	Type i	3820	7.30	290	0.23	BDL	0.14	0.02	BDL	0.73	0.53	0.01	1.00	20	2.95
POR3_S16	pent	Type i	5450	5.43	357	0.61	4.70	0.06	1.31	BDL	1.46	4.30	0.04	1.91	309	7.58
POR3_S07	pent	Type i	9650	24.0	118	0.60	3.20	2.90	1.34	0.06	2.38	1.36	0.05	0.79	108	1.21
71336_S05	pent	Type i	5930	0.17	26	0.09	0.60	0.07	0.55	BDL	0.58	0.06	BDL	0.02	45	0.36
71336_S06	pent	Type i	7100	0.82	197	0.51	0.90	0.37	0.39	BDL	1.04	0.08	BDL	0.02	14	0.64
71336_S07	pent	Type i	874	0.17	7	BDL	0.30	0.05	0.01	BDL	0.38	BDL	BDL	0.01	3.0	0.02
71336_S16	pent	Type i	3527	0.16	102	0.10	BDL	0.03	1.47	BDL	0.98	0.09	BDL	0.04	36	0.36
71336_S12	pent	Type i	4290	0.62	117	0.21	2.40	BDL	0.27	0.02	1.03	0.26	0.01	0.03	34	0.13
71336_S18	pent	Type i	1980	3.71	330	0.02	BDL	BDL	1.08	BDL	0.34	0.10	BDL	0.07	2.9	0.01
71336_S10	pent	Type iv	4490	0.04	69	0.14	BDL	BDL	1.37	BDL	0.65	0.26	BDL	0.07	71	1.00
71336_S13	pent	Type iv	1860	3.60	219	BDL	BDL	0.04	0.39	BDL	1.30	BDL	BDL	0.02	19	0.11
71336_S25	pent	Type i	4700	95.1	396	20.6	BDL	BDL	1.50	0.12	BDL	BDL	0.02	0.07	13	0.41
71336_S20	pent	Type iv	4290	1.60	131	0.20	BDL	0.50	0.38	0.01	0.45	BDL	BDL	0.13	7.8	0.52
71336_S19	pent	Type iv	8710	5.04	182	BDL	BDL	1.36	0.55	0.05	0.61	BDL	0.04	0.02	26	0.39
POR1_S19	pent	Type i	11490	0.91	50.1	0.41	4.10	0.16	21.3	0.01	0.61	0.11	0.02	16.6	4310	7.89
POR1_S15	pent	Type iv	3840	0.48	127	BDL	0.60	0.15	1.85	BDL	1.73	0.22	0.02	6.56	505	1.00
POR1_S13	pent	Type i	7560	12	67	0.11	1.50	0.08	5.26	0.02	1.32	0.13	0.01	3.41	665	4.71
POR1_S09	pent	Type i	5970	1.95	13.3	BDL	1.60	0.09	0.73	BDL	2.11	0.17	BDL	0.15	71	0.15
POR1_S21	pent	Type i	4850	0.37	45.1	0.07	1.50	0.17	0.35	0.02	0.85	0.13	BDL	3.29	513	2.33

Table 4 cont	Sulf	Morph	Co	V	Mn	Ga	Ge	Mo	Cd	In	Sn	Sb	W	Tl	Pb	Bi
POR1_S22	pent	Type e	6000	23.2	47.7	0.17	3.30	0.03	0.78	0.00	3.87	0.55	0.01	9.10	298	8.01
POR1_S04	pent	Type i	9000	4.87	66.5	0.27	BDL	0.06	1.31	0.01	1.59	BDL	0.02	10.6	767	1.20
POR1_S20	pent	Type i	7120	0.26	113	BDL	5.30	BDL	3.54	BDL	0.16	BDL	BDL	2.42	82	2.50
POR1_S17	pent	Type i	11980	0.80	29.6	0.05	2.60	0.07	11.1	0.04	1.26	BDL	BDL	13.5	4500	3.37
POR1_S05	pent	Type i	16480	159	402	6.20	9.00	1.60	2.01	0.13	0.60	BDL	0.02	6.20	1590	17.7
POR2_S17	pent	Type i	9870	71	105	0.32	2.6	BDL	11.8	0.01	2.2	2.02	BDL	2.59	87	2.09
POR2_S05	pent	Type f	6540	BDL	6.23	BDL	4.00	BDL	0.46	0.02	2.86	1.44	BDL	6.85	216	15.3
POR2_S18	pent	Type e	3840	23.0	386	0.29	2.90	0.08	1.28	0.01	6.90	1.75	BDL	3.11	61	3.37
POR2_S19	pent	Type i	7840	74.0	1880	2.50	3.10	BDL	1.06	0.16	4.40	4.04	BDL	103	640	5.00
POR2_S06	pent	Type iv	19100	0.49	144	BDL	BDL	0.33	59.0	BDL	4.90	0.86	BDL	44.0	1590	1.71
POR3_S01	pent	Type i	5090	0.23	65.0	0.23	1.50	0.02	2.73	BDL	0.96	0.43	0.01	1.17	114	2.02
POR3_S02	pent	Type i	4990	0.56	72.0	0.19	0.40	0.04	0.57	BDL	0.31	0.18	0.01	0.75	122	1.70
POR1_S19	pyrr	Type i	13500	0.30	119	0.12	5.00	0.22	7.90	0.01	0.30	0.29	0.02	10.0	2180	2.55
POR1_S21	pyrr	Type i	1770	0.57	67.9	0.11	BDL	0.40	1.01	BDL	0.48	BDL	BDL	2.00	29.6	BDL
POR1_S17	pyrr	Type i	3210	0.56	115	BDL	5.60	0.25	3.18	BDL	BDL	BDL	0.04	21.3	8.10	0.05
POR1_S17	py	Type i	12500	0.87	27.2	0.88	5.60	0.37	1.22	0.03	BDL	BDL	0.02	0.40	0.16	0.05
POR2_S02	py	Type i	16500	210	158	1.31	4.80	0.20	1.25	0.06	0.63	0.61	BDL	7.10	22.4	13.8
POR3_S11	py	Type i	18900	1.44	99.0	0.20	BDL	BDL	0.70	0.07	BDL	1.09	0.01	0.34	0.93	0.10
POR3_S13	py	Type i	14400	0.87	6.90	BDL	3.90	BDL	0.15	BDL	0.00	0.51	0.01	0.09	7.40	0.18
POR3_S15	py	Type i	27100	1.47	36.0	BDL	2.80	0.59	1.73	BDL	0.91	0.71	0.59	0.10	11.3	0.83
POR2_S06	MSS	Type i	4980	0.07	141	BDL	1.10	0.40	15.8	0.01	1.82	2.80	BDL	18.9	590	11.3
POR2_S04	MSS	Type e	6980	1.80	7.60	BDL	BDL	0.27	5.60	BDL	2.40	8.72	BDL	0.30	440	28.2
POR2_S04	ccp	Type e	2010	4.30	19.0	BDL	BDL	BDL	13.6	0.71	5.40	BDL	0.02	0.57	55.6	0.17
71336_S07	ccp	Type i	2430	0.17	14.7	0.16	BDL	BDL	0.51	BDL	1.11	0.17	BDL	0.01	4.21	0.03
POR3_S15	ccp	Type i	16.0	14.8	470	1.40	BDL	BDL	1.01	0.33	0.85	1.60	BDL	0.04	3.10	BDL
POR3_S13	ccp	Type i	3790	3.70	44.1	0.01	4.10	0.08	5.10	0.03	2.80	1.90	0.00	0.55	499	1.64
POR2_S07	pent + ccp	Type e	6890	8.60	290	0.10	11.0	BDL	4.90	0.35	2.10	0.09	0.06	18.8	620	14.0

Table 4 cont	Sulf	Morph	Co	V	Mn	Ga	Ge	Mo	Cd	In	Sn	Sb	W	Tl	Pb	Bi
POR1_S05	pyrr + pent	Type i	27300	2.36	306	0.44	1.80	0.19	47.0	0.02	0.88	BDL	0.04	33.8	5960	5.70
71336_S23	altered pent	Type i	1860	0.32	72	0.36	BDL	7.00	0.20	BDL	4.60	0.38	BDL	0.04	1.72	0.32
71336_S23	ccp + pent	Type i	4100	0.32	202	0.39	BDL	0.01	3.11	0.03	0.11	0.15	BDL	0.31	2.80	0.12
71336_S14	ccp + pent	Type i	2670	11.3	132	0.14	0.71	BDL	1.06	0.00	0.47	0.09	BDL	0.02	10.0	0.51
71336_S08	ccp + pent	Type i	2270	23.5	146	0.31	BDL	BDL	1.11	0.11	0.30	0.14	BDL	0.02	34.9	0.40
POR2_S16	ccp + pent	Type i	24600	22.6	570	1.50	14.0	2.30	16.2	BDL	BDL	0.90	BDL	4.50	120	1.78
POR2_S08	pent + MSS2	Type e	11700	BDL	30.0	BDL	27.1	BDL	9.90	BDL	23.0	5.10	BDL	7.20	1130	60.9
POR2_S15	py + pent	Type i	3710	2.00	13.3	0.60	0.50	BDL	0.09	BDL	0.93	0.39	BDL	0.75	43	6.57
POR1_S14	pent + MSS2	Type iv	4450	1.15	143	BDL	BDL	0.39	1.22	BDL	0.91	BDL	0.01	1.94	917	4.30
POR1_S06	pent + pyrr	Type e	15050	0.37	39.0	0.03	BDL	0.05	4.00	0.01	4.20	0.27	0.01	2.58	389	7.11

Table F4. All sulfide analyses from the Pyrenees Massif peridotites.

283

Table 5	Sulf	Morph	Co	V	Mn	Ga	Ge	Mo	Cd	In	Sn	Sb	W	Tl	Pb	Bi
Hannuoba Xenolith Sulfides																
DMP23a_S03	pent	Type i	5070	300	2700	19.0	9.00	154	4.80	BDL	8.10	BDL	0.24	7.4	146	3.20
DMP41_S03	pent	Type i	7200	88	1050	490	89.0	3.00	3.30	BDL	1.90	35.0	0.81	0.82	73.0	2.44
DMP41_S02	pent	Type i	5520	1.23	169	31.5	25.1	3.07	0.16	BDL	0.39	9.8	0.02	0.09	32.0	1.02
DMP41_S01-1	pent	Type i	7700	6.3	320	17.9	5.00	14.5	0.01	0.23	1.10	BDL	0.07	0.07	74.0	BDL
DMP41_S01-2	pent	Type i	5700	75	1300	42.0	BDL	9.40	0.06	1.10	BDL	61.0	0.05	1.0	370	3.40
DMP41_S01-3	pent	Type i	5000	260	4400	59.0	BDL	2.40	BDL	BDL	BDL	BDL	0.04	0.13	120	BDL
DMP19_S02	pent	Type i	28000	BDL	BDL	589	560	18.0	5.40	0.8	8.00	BDL	BDL	2.2	112	3.10
DMP19_S01	pent	Type i	5700	0.43	10.4	0.06	4.00	11.2	0.71	0.07	0.26	BDL	0.04	0.35	7.60	0.19
DMP56_S02	pent	Type i	1900	1.33	14.9	0.21	5.60	32.0	4.20	0.18	4.50	0.89	0.29	0.3	114	8.30
DMP57_s6	pent	Type i	9100	1.22	498	1.64	3.69	51.0	2.90	0.03	BDL	3.50	0.1	27.8	4.10	0.22
DMP59_s4	pent	Type i	12400	12.4	1090	4.60	BDL	187	6.30	0.08	2.40	9.90	BDL	2.03	150	1.54
DMP57_s2	pent	Type i	1120	9.9	6700	220	110	141	74.0	4.00	11.1	2.90	0.22	81	70.0	0.26
DMP60n_s1	pent	Type i	1440	1060	134000	2200	BDL	120	0.00	16.0	320	BDL	330	1.6	1200	0.60
DMP60n_s50	pent	Type i	9330	588	3900	92.0	11.0	453	3.10	0.10	0.60	0.55	2.4	0.45	40.0	0.66
DMP60n_s15-1	pent	Type i	6130	13	240	1.14	5.25	1210	1.90	0.07	0.49	0.97	0.12	0.24	28.0	0.80
DMP60n_s15-2	pent	Type i	6940	56	387	2.69	5.28	1260	1.52	0.16	0.57	1.19	0.20	0.31	31.4	0.49
DMP60n_s16	pent	Type i	12000	360	54000	8.2	1.00	430	BDL	0.06	4.20	0.34	4.5	0.13	9.60	0.41
DMP60n_s44-1	ccp ss	Type i	2940	7.3	370	2.20	4.28	254	0.52	0.01	0.36	0.23	0.42	0.11	2.71	0.31
DMP60n_s44-2	ccp ss	Type i	2300	31.1	246	1.01	3.07	254	0.38	0.03	0.26	0.18	0.07	0.11	1.81	0.29
DMP60n_s53	pent	Type i	6860	8.6	2000	4.50	7.00	161	2.90	0.53	2.70	8.00	0.07	0.56	28.2	1.92
DMP60n_s43-1	pent	Type i	7300	8.1	570	2.70	8.20	236	1.31	0.28	BDL	6.10	0.2	0.59	27.3	1.23
DMP60n_s43-2	pent	Type i	11600	48	4600	3.70	5.90	890	2.00	0.12	0.90	1.50	3.6	0.55	26.0	0.76
DMP60n_s21	pent	Type i	5600	470	140000	1300	30.0	2200	BDL	BDL	BDL	600	2.3	BDL	5.60	1.20
DMP60n_s28	pent	Type i	5910	11.8	3000	3.50	11.0	520	0.80	0.69	BDL	15.0	0.34	0.18	15.0	2.90
DMP60n_s30-2	pent	Type i	6670	17.6	430	0.66	12.1	1570	BDL	0.09	0.50	61.0	0.33	0.34	6.20	0.15
DMP60n_s30-1	pent	Type i	6910	1.52	223	0.75	4.9	690	0.29	0.05	BDL	52.0	0.06	0.21	18.9	0.65
DMP60n_s29	pent	Type i	6400	4.3	720	1.63	5.8	649	8.10	0.85	0.10	5.80	0.48	1.39	19.2	0.96

Table 5 cont	Sulf	Morph	Co	V	Mn	Ga	Ge	Mo	Cd	In	Sn	Sb	W	Tl	Pb	Bi
DMP60n_s27	pent	Type i	33700	BDL	620000	2110	BDL	50.0	BDL	BDL	BDL	BDL	BDL	BDL	BDL	BDL
DMP60n_s32	pent	Type i	7500	82	6900	2.70	17.2	550	6.90	1.55	0.9	5.70	0.6	1.8	34.0	0.66
DMP04n_s4	pent	Type i	14800	570	169000	260	310	380	7.00	2.8	32.0	19.0	80	3	6.00	4.30
DMP04n_s1-1	pent	Type i	3250	3.7	830	1.93	4.50	43.0	1.30	0.13	0.49	1.22	0.69	0.72	5.2	0.17
DMP04n_s1-2	pent	Type i	4580	270	2600	31.0	13.0	61.0	4.40	0.34	BDL	0.80	0.38	0.58	10.3	0.14
DMP60_s17_1	pent	Type i	3800	7.1	2000	10.7	0.40	910	BDL	0.15	1.60	0.66	1.5	0.11	6.60	0.82
DMP60n_s47	pent	Type i	400000	5	1680	4.40	16.2	41.0	0.25	0.16	BDL	3.70	0.04	0.3	32.9	1.36
DMP60n_s45-1	pent	Type i	9400	0.93	100	0.33	8.10	1160	BDL	BDL	0.59	0.80	0.11	0.13	12.4	0.74
DMP60n_s45-2	pent	Type i	5400	3.92	500	0.44	5.40	1760	BDL	BDL	0.40	0.73	0.04	0.14	9.40	0.31
DMP60n_s45-3	pent	Type i	3570	2.05	431	0.92	6.00	1383	0.55	0.01	0.09	0.43	0.42	0.05	3.13	0.26
DMP60n_s22-2	ccp ss	Type i	1050	0.29	393	0.05	5.30	6.80	21.7	2.10	1.40	39.0	BDL	0.33	2.31	BDL
DMP60n_s22-1	pent	Type i	3740	1.26	215	0.14	5.46	840	0.09	0.07	0.77	34.0	0.46	0.06	2.70	0.39
DMP60n_S22-3	pent	Type i	4010	0.98	201	0.28	5.59	781	0.09	0.18	0.75	35.0	0.45	0.11	4.30	0.39
DMP60n_S22-4	pent	Type i	3860	21.2	263	0.47	4.84	903	0.01	0.17	0.89	31.0	0.37	0.13	4.60	0.48
DMP59_s7	pent	Type i	7370	1.72	389	1.32	4.65	51.8	12.9	0.98	BDL	9.07	0.12	6	17.1	0.47
DMP60n_s36	pent	Type i	4970	11.7	331	2.30	4.10	551	0.93	0.06	0.17	3.70	0.29	0.31	2.64	0.61
DMP04_S01-1	pent	Type f	8570	14.5	175	0.72	0.80	10.4	20.7	0.47	BDL	BDL	0.15	0.00	577	41.0
DMP04_S01-2	pent	Type f	8800	5.7	73	0.35	37.0	6.76	11.0	0.42	BDL	11.8	0.08	0.02	295	7.58
DMP56_S04	pent	Type f	3406	0.56	17.1	1.37	4.10	25.0	5.60	0.41	BDL	BDL	0.36	0.18	85.0	0.88
DMP56_S01	pent	Type f	6310	0.45	790	0.18	BDL	8.40	0.51	0.16	BDL	BDL	0.03	0.16	3.90	0.30
DMP23a_S01	pent	Type f	5550	4.76	69	0.16	4.25	10.3	0.33	0.01	0.54	0.32	0.04	19.6	1.46	0.26
DMP60_S01	ccp	Type f	3820	9.02	180	0.38	5.53	3.20	1.03	0.40	6.00	0.30	0.03	0.28	6.90	0.60
DMP56_S08a	pent	Type f	630	480	2400	19.0	45.0	58.0	23.4	0.56	10.3	30.0	0.77	0.24	41.0	0.90
DMP56_S08b	ccp	Type f	260	52	370	3.40	12.8	28.0	32.0	0.48	17.6	11.2	0.4	0.38	31.6	0.38
DMP59_s3-1	pent	Type f	3330	2.86	492	0.50	9.8	213	9.30	4.20	0.44	6.70	0.29	1.78	16.7	0.71
DMP59_s3-2	ccp	Type f	1420	3.4	250	1.16	35.0	260	24.0	2.10	BDL	2.50	0.57	2.26	26.0	0.48
DMP59_s3-3	ccp	Type f	3600	0.78	21.1	0.23	5.60	59.0	6.20	2.00	BDL	7.20	0.13	0.26	4.80	0.97
DMP57_s5	pent	Type f	2210	0.4	568	0.05	2.41	4.76	0.06	BDL	0.1	0.67	0.08	BDL	0.62	0.05

| Table 5 cont	Sulf	Morph	Co	V	Mn	Ga	Ge	Mo	Cd	In	Sn	Sb	W	Tl	Pb	Bi
DMP59_s6	MSS1	Type f	3140	0.24	174	0.02	2.75	2.85	BDL	BDL	BDL	6.53	BDL	0.03	0.74	0.07
DMP04n_S2	pent	Type f	BDL	4.1	930	9.10	12.8	16.5	3.00	BDL	BDL	1.29	0.34	0.36	4.30	0.47
DMP57_s1	pent	Type f	4910	0.53	215	1.28	4.93	56.0	0.97	BDL	0.16	0.46	0.08	14.9	0.37	0.09
DMP04_S02	pent	Type e	4570	164	790	2.80	35.9	19.2	0.65	0.03	BDL	5.20	0.18	0.11	2.96	0.20
DMP56_S03	pent	Type e	4070	1.2	1030	0.17	23.4	15.0	0.55	0.06	0.61	3.40	0.07	0.04	4.60	0.14
DMP56_S07	pent	Type e	2800	470	6400	19.6	26.6	36.0	0.18	BDL	2.8	BDL	BDL	0.29	3.10	BDL
DMP56_S06	pent	Type e	3620	4.7	228	0.26	4.70	8.60	0.11	BDL	2.03	BDL	BDL	0.05	1.30	0.09
DMP60n_s5_1	pent	Type iv	6120	0.47	108	0.29	4.56	307	0.27	BDL	0.75	0.2	0.08	0.49	7.90	0.24
DMP60n_s17_2	pent	Type iv	2460	16.6	2070	8.50	5.00	84.0	6.50	0.88	BDL	10	0.94	0.23	17.8	0.42
DMP60n_s18	pent	Type iv	####	109	350	2.30	8.80	111	3.20	0.18	0.09	15	BDL	0.30	41.0	2.90

Table F5. All sulfide analyses from the Hannuoba Xenolith peridotites. Note sulfides in samples DMP-23a and DMP-57 were analyzed, but a mass balance was not completed for these samples.

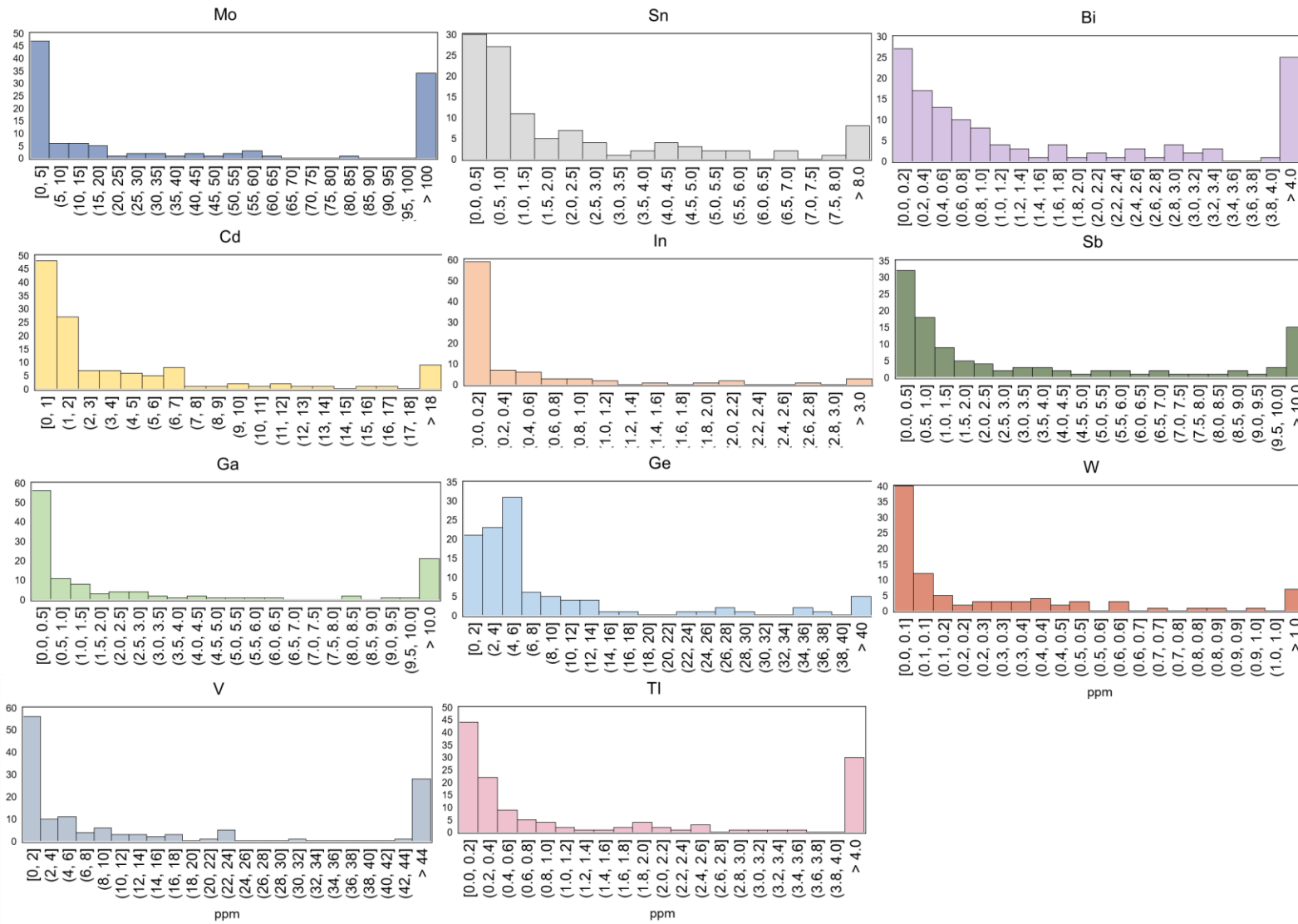| Sample	T(°C)
DMP-04	1098
DMP-19	1080
DMP-23a	1043
DMP-25	1055
DMP-41	1051
DMP-51	1087
DMP-56	1108
DMP-58	1105
DMP-59	1052
DMP-60	1079
DMP-67c	1052
POR-1	936
POR-2	947
POR-3	916
71-336	966

Table F6. Equilibration temperature of the peridotites calculated from the opx-cpx thermometer of Brey and Kohler (1990) and assuming a pressure of 1.5 GPa.
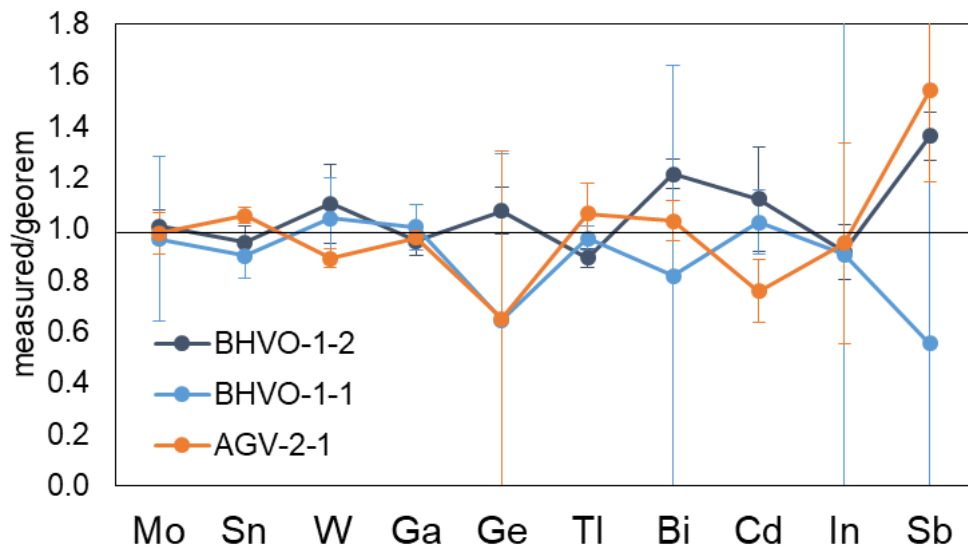

Figure F1. Secondary standards run with standard addition solution ICP-MS.
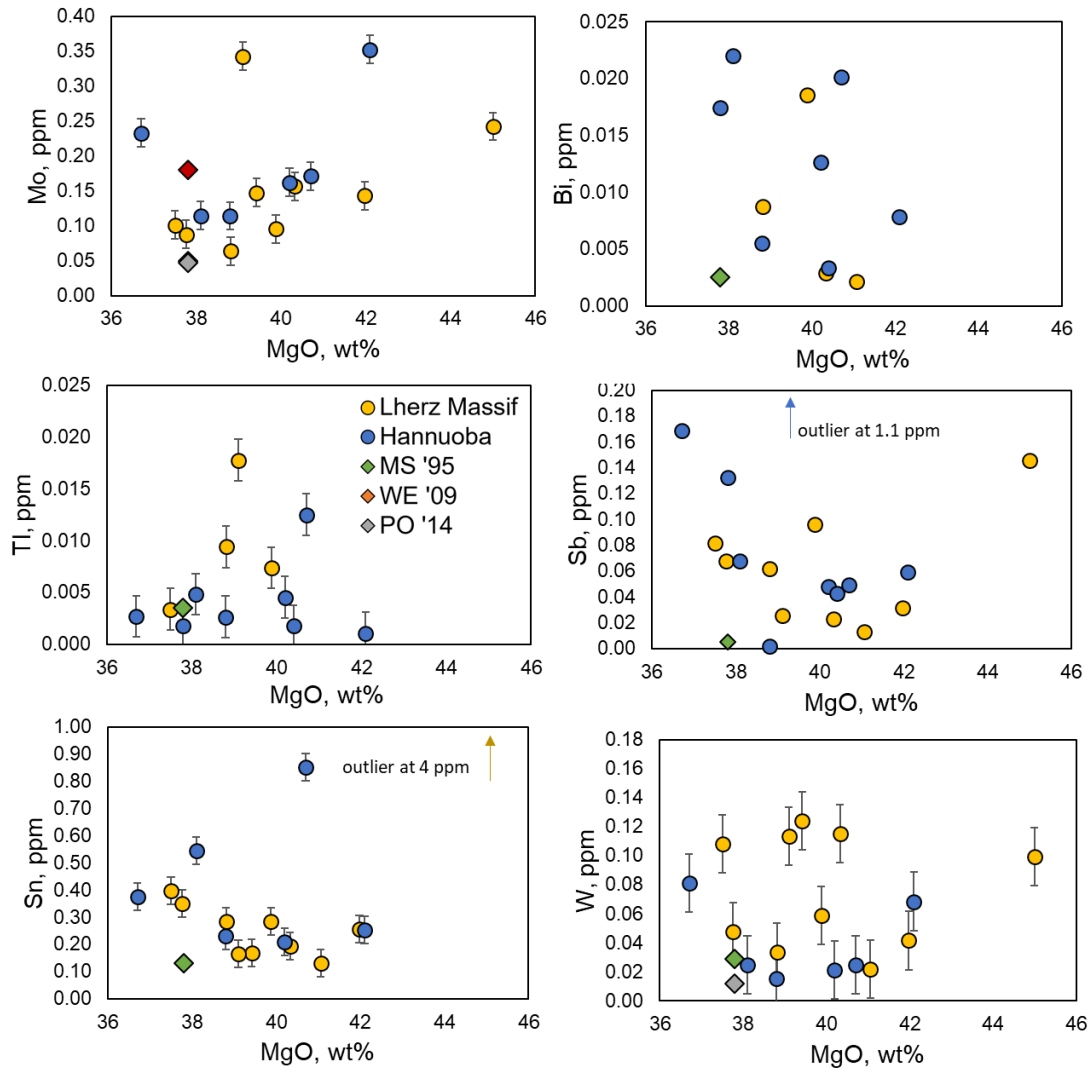
Figure F2. Whole rock abundances of the elements (ppm) that don't show a trend when plotted against MgO (wt%). The Mo chart also contains the primitive mantle estimate of Liang et al. (2017) in red.
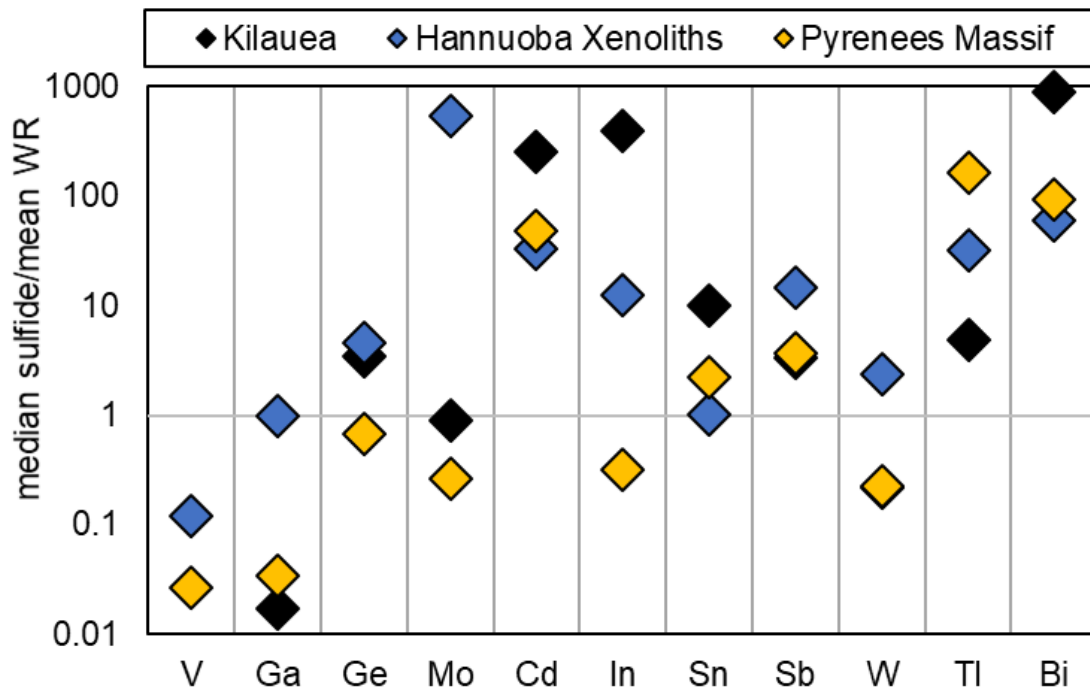
Figure F3. Histograms of element concentrations in sulfides. Bins are in ppm and bin sizes vary depending on the sample.
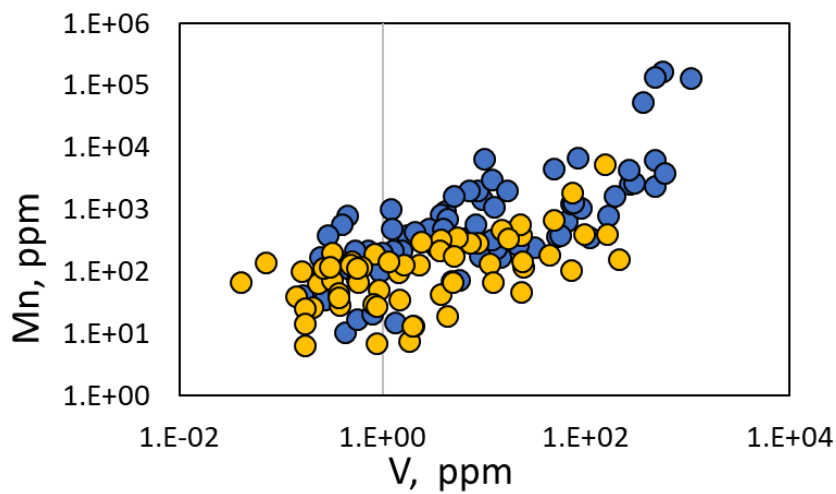
Figure F4. Correlation between V and Mn in sulfide minerals in the Hannuoba (blue) and Lherz Massif (yellow) peridotites.
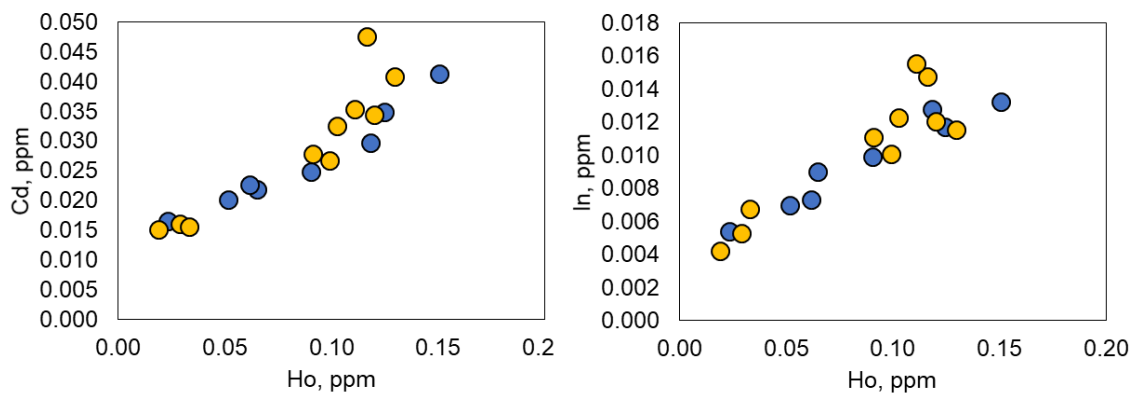
Figure F5. Correlation between Cd – Ho and In – Ho. Both elements correlate strongly ($R^2>0.8$) with the MREE to HREE.

Figure F6. Modified partition coefficients for each element calculated as the median sulfide value divided by the average whole rock value of each suite of samples. The peridotite suites are compared to similar data from Kilauea Iki lava lake in Hawaii (Greaney et al., 2017). Vanadium was not analyzed in the Kilauea samples, and the Pyrenees W value overlaps the Kilauea value.

Appendix G.

Causes of Molybdenum Depletion in Granites

Magali Toc[1], Allison T. Greaney[1], Roberta L. Rudnick[1], John D. Foden[2]

[1]University of California – Santa Barbara, Santa Barbara, California, USA 93106

[2]University of Adelaide, South Australia

As presented at Goldschmidt Meeting 2018

Molybdenum is an important trace element that serves as a proxy for atmospheric oxygen contents of early Earth. During the Great Oxidation Event (GOE), which occurred ~2.3 billion years ago, an increase in atmospheric oxygen caused redox-sensitive Mo to be removed from the crust at the onset of oxidative weathering. Mo residence in typical upper crustal rocks: Archean and Proterozoic granites from North America and South Africa, show systematic depletion of Mo relative to the LREE[1], whereas Mo in basaltic rocks has normalized concentrations similar to those of the LREE. One hypothesis to explain this depletion is that, due to their similar atomic radii, Mo^{6+} substitutes for Ti^{4+} in Fe-Ti bearing oxides during differentiation of calc-alkaline igneous rocks in arc settings.

We tested this hypothesis by measuring Mo concentrations in a calc-alkaline differentiation suite from Rindjani Volcano, Indonesia, in the western part of the east Sunda Arc[2]. LA-ICP-MS on Li-tetraborate-fused glass beads was used to determine Mo content within the suite, which ranges from relatively primitive high-Al basalts to dacite. The differentiation suite shows clear fractionation of Fe-Ti-oxides at 4.4 MgO wt%. The mafic samples exhibit low Mo concentrations (minimum 0.27 ppm), whereas the felsic samples exhibit higher Mo concentrations (maximum 6.1 ppm). Thus, Mo behaves as an incompatible element throughout the suite. When normalizing the samples to UCC values, Mo shows

consistent enrichment relative to LREE. The incompatible behavior of Mo therefore suggests that significant Mo does not substitute into Ti-bearing minerals during calc-alkaline igneous differentiation. Thus, the depletion of Mo in granites may reflect removal of Mo from granitic plutons in a late-stage magmatic vapor phase. If this is the dominant process responsible for Mo removal from granites, then much of the Mo in the upper continental crust may be contained within molybdenite-bearing veins that precipitate from such vapors.